Doctoral Dissertation

Development of functionalized organosilica membranes with high NH_3 permselectivity and their application to green NH_3 production

（NH_3 選択透過性を有するオルガノシリカ膜の開発とグリーン NH_3 製造への応用）

YAN WEIWEI

Chemical Engineering Program,

Graduate School of Advanced Science and Engineering,

Hiroshima University

(広島大学 先進理工系科学研究科 化学工学プログラム)

September 2024

Abstract of dissertation

Ammonia (NH_3) plays a vital role in population growth, agricultural production and even the development of human society, which has made it one of the most in-demand chemicals in the world. Since the advent of Haber-Bosch process at the beginning of the last century, NH_3 has been mass-produced as a revolutionary product for artificial nitrogen fixation, and its annual output has exceeded 230 million metric tons. However, the harsh NH_3 production conditions such as high temperature (400-500 °C) and intense pressure (20-50 MPa) via Haber-Bosch process bring many problems including high energy consumption, high pollution, and high cost, especially in NH_3 separation process by a condenser. The gas membrane separation technology, which has the advantages of low energy consumption, environmental friendliness, and continuous operation, would be expected to be used for NH_3 separation in NH_3 synthesis process.

Firstly, based on the Lewis acid-base interaction between NH_3 and transition metal, a strategy was proposed to improve NH_3 affinity through the coordination of transition metal with aminosilica structure. Notably, Ni-doped bis[3-(trimethoxysilyl)propyl] amine (BTPA) showed the highest NH_3 adsorption amount (1.77 mmol g^{-1}) compared with Fe, Co, Cu, and Ag-doped BTPA by metal-induced coordination and hydrogen bonds and/or van der Waals interactions caused by *N-H*, *N=O*, and *Si-OH* groups via characterizations and molecular simulations. Furthermore, after optimizing the amount of nickel doping (Ni/*N-H* molar ratios of 0, 0.125, 0.25, 0.50, and 1.00), 0.50 Ni-BTPA membrane showed a superior NH_3 separation performance, i.e., NH_3 permeance of ~2.8×10^{-6} mol m^{-2} s^{-1} Pa^{-1} with ideal NH_3/H_2 selectivity of 11 and NH_3/N_2 selectivity

of 102 at 200 °C. It was ascribed to the sufficient molecular sieving owing to the enlarged pore size by metal coordination as well as high NH_3 adsorption-diffusion due to improved NH_3 affinity by doped nickel.

Additionally, based on the Brønsted acid-base interaction between NH_3 and acidic groups, the organosilica precursor with sulfonic acid group would be expectantly used to fabricate NH_3 separation membranes. In the first stage, the (3-mercaptopropyl)trimethoxysilane (MPTMS) containing mercaptan group (-*SH*) was used and further oxidized to sulfonic acid groups by H_2O_2 to improve NH_3 adsorption amount (~1.41 mmol g^{-1}). Owing to the enhanced acid-base interactions including intensified acidity and more acidic sites, oxidized MPTMS membrane showed an excellent NH_3/H_2 selectivity of 6 and NH_3/N_2 selectivity of 18 with an NH_3 permeance of ~1.4×10^{-7} mol m^{-2} s^{-1} Pa^{-1} at 300 °C. For another, 3-(trihydroxysilyl)-1-propanesulfonic acid (TPS) which contains -*SO_3H* groups in the chemical structure was used to fabricate TPS-derived membrane by directly coating TPS solutions, that was diluted to 0.1 wt% with ethanol, on SiO_2-ZrO_2 intermediate layer. Owing to the inherently stronger proton-acidic -*SO_3H* groups in TPS, TPS-EtOH membranes showed a superior NH_3 permeance of ~2.6 and ~1.8×10^{-7} mol m^{-2} s^{-1} Pa^{-1} with an excellent NH_3/H_2 selectivity of 7 and 165, and NH_3/N_2 selectivity of 266 and 18700 at 300 and 50 °C, respectively.

Finally, a green NH_3 production system was proposed and carried out, namely reactor combined with membrane separator with recycle flow, which enables the temperature of reactor and membrane separator controlled independently. The Ru (10 wt%)/Cs/MgO catalyst and two types of membranes (Aquivion/ceramic composite and

oxidized MPTMS membranes have different permeation properties and NH_3 selectivity) were used to produce NH_3 and selectively extract the synthesized NH_3 from feed side to permeate side, respectively. For recycle membrane reactor, NH_3 mole fraction of permeate side can be greatly increased to 0.1-0.45, which is ten to forty times higher than 0.01 of equilibrium state without using membrane separator. A mathematical model with one-dimension, isothermal, and plug-flow was proposed and successfully applied to simulate recycle membrane reactor, which is beneficial to understand NH_3 mole fraction, recovery, and recycle parameters as a function of membrane length, membrane performance, feed pressure, and feed flow rate, respectively.

In this dissertation, three types of organosilica membranes were fabricated for selective NH_3 separation over a wide temperature range (50-300 °C) and a recycle membrane reactor process was developed for green NH_3 production with efficient and low energy consumption.

CONTENTS

Chapter 1

General introduction

1.1 NH_3 synthesis

1.1.1 Current situation for NH_3 synthesis

Ammonia (NH_3) is of critical importance as one of the most demanded chemicals all over the world and is the second-most produced chemical based on the International Renewable Energy Agency (IRENA) report in 2022. The annual production of NH_3 in energy-intensive manufacturing plants via Haber-Bosch process [1] worldwide has exceeded 230 million metric tons and has been rising year by year as indicated in Fig. 1-1, [2] and the main producers are China (30%), Russia (12%), India (9%) and other countries as displayed in Fig. 1-2. [3] Noteworthily, 80% of NH_3 produced globally is used in fertilizer production, and the production of plastics, explosives, nitric acid, and intermediates for pharmaceuticals produced using NH_3 also have a non-negligible specific gravity.

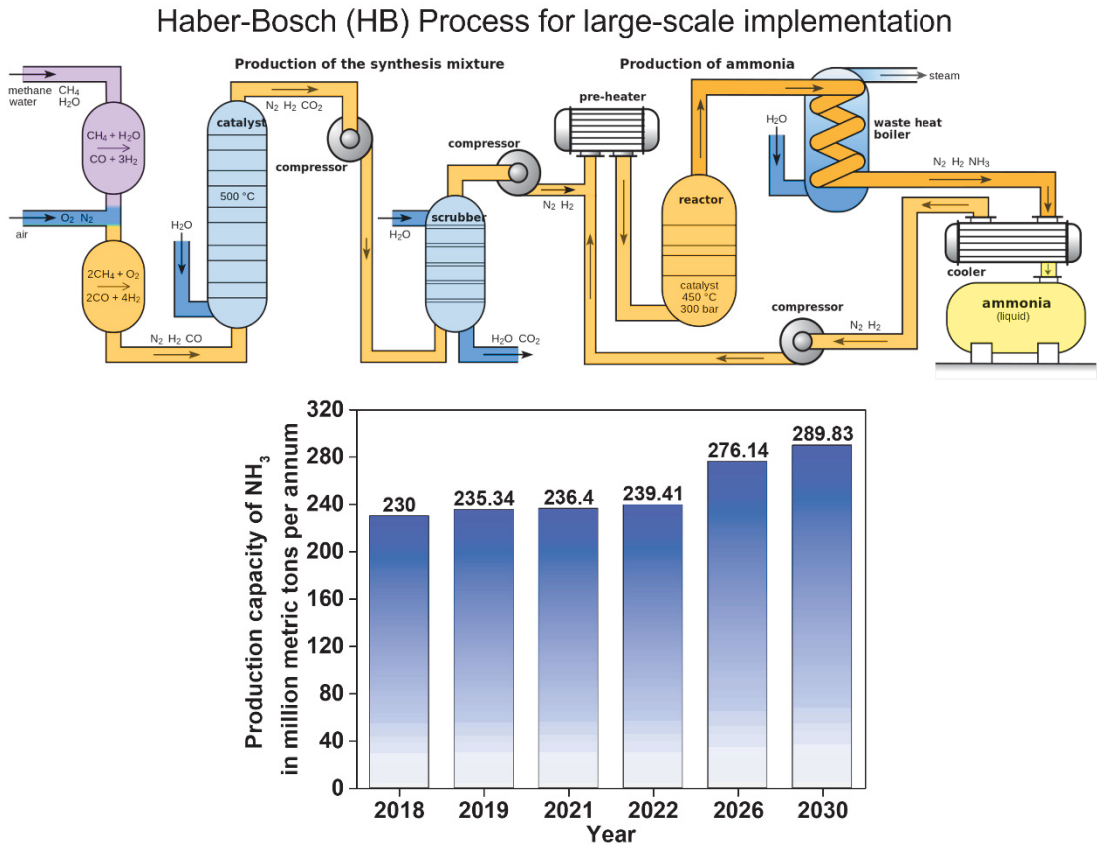

Fig. 1-1. Haber-Bosch process for large-scale (above, https://en.wikipedia.org/wiki/Haber_process.); production capacity of ammonia worldwide from 2018 to 2022, with a forecast for 2026 and 2030 (below). [2]

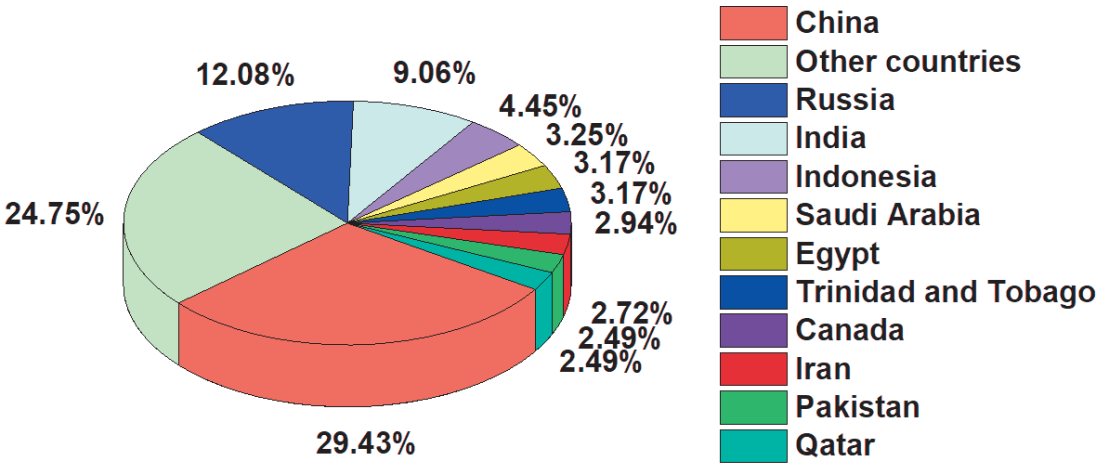

Fig. 1-2. Distribution of world ammonia production, Year 2021. [3]

Conventional Haber-Bosch process using Fe-based catalysts was applied to NH_3 production ($N_2 + 3\ H_2 \rightleftharpoons 2\ NH_3$ ΔH= -91.8 kJ mol^{-1}) under harsh conditions including

high temperature (400-500 °C) and intense pressure (20-50 MPa). Nonetheless, only ~15% of NH_3 conversion was obtained due to kinetic and thermodynamic constraints. An overall conversion of ~98% can be achieved through NH_3 condensation and recycling of unreacted H_2 and N_2, [4] which would consume around 1.8% of global energy output each year and cause 500 million tonnes of global CO_2 emission. [5] In recent years, the concept of "clean NH_3" [6], "renewable NH_3" [7], "NH_3 economy" [8] is gradually being established and induced NH_3 as a potential fuel, which also causes NH_3 to have many practical applications as shown in Fig. 1-3. Furthermore, since synthetic NH_3 has increasingly become one of the important factors determining the national and global energy and grain security, [9] therefore, the search for more efficient and sustainable NH_3 synthesis process has been the trend of the times.

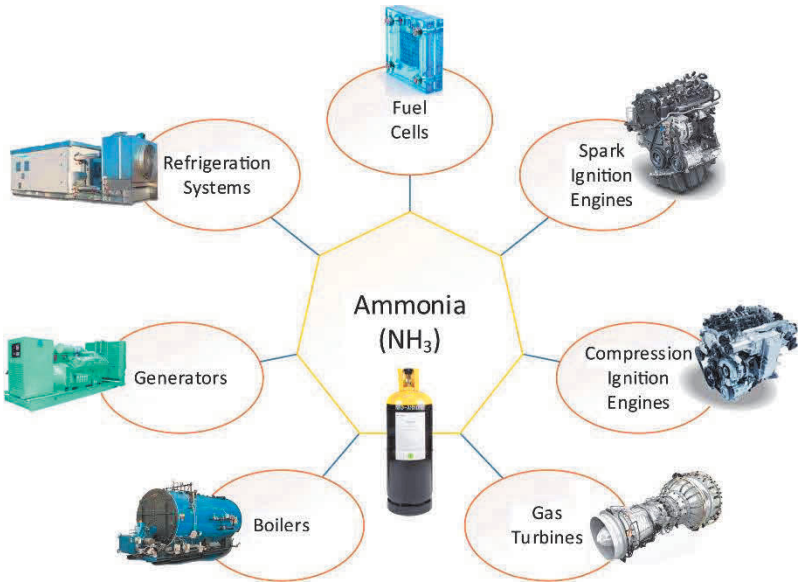

Fig. 1-3. Uses of ammonia in various practical applications. [6]

1.1.2 Catalysts and reaction conditions for NH_3 synthesis

As exhibited in Fig. 1-4, catalysts are the key to overcome the reaction barrier and improve the reaction efficiency, among which typical Fe-based, Ru-based, and Co-Mo

metallic catalysts play a distinctly important role for NH_3 synthesis. [10] Fe-based catalysts, which are the first generation and already commercially available, are still being ameliorated due to low cost and reliably catalytic activity, for example, K-Fe/C [11] and iron pyrite [12]. Furthermore, the second-generation Ru-based catalysts were developed and expressed superior reaction activity even at milder conditions including low temperature, medium pressure, and low H_2/N_2 ratio, [13,14] which were also not susceptible to poisoning under conditions with high NH_3 concentrations. Either the activation of N≡N bonds or the formation of N-H bonds that could be regarded as the rate-determining step always requires the abundant energy for synthesizing NH_3, [15,16] resulting in the harsh reactive conditions. Consequently, some supports that can promote or enrich electron density for Ru metals, such as hydrides, [17] electrides, [18] oxides, [19] and nitrides, [20] would be considered, which is highly expected to further enhance the catalytic activity.

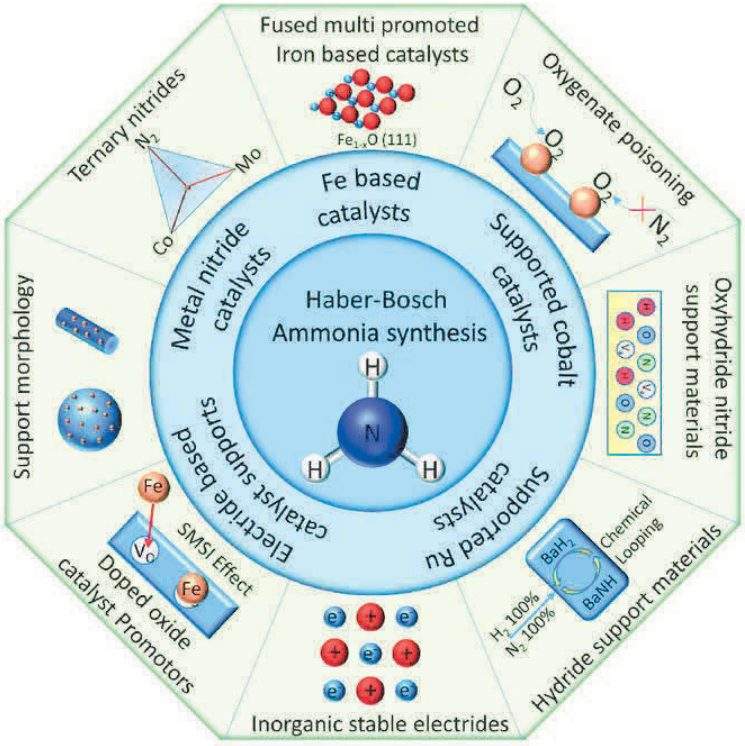

Fig. 1-4. Graphical overview of strategies to improve Haber-Bosch NH_3 synthesis. [10]

Impressively, a stable electron-donating Ru/CaFH catalyst was reported and used to NH_3 synthesis at low temperature (50 °C), which could be ascribed to the fact that ionic bonds between Ca^{2+} and H^- was weakened by introducing F^- into CaH_2, resulting in the facile release of H atoms from H^- sites. [21] However, most catalysts currently under development still require high temperatures for efficiently improving NH_3 conversion, even though high thermodynamic conversion can be achieved at low temperatures due to exothermic NH_3 reactions. In addition, although highly active catalysts have been reported successively, catalyst cost also deserves further consideration because it possibly be restricted their large-scale application.

1.1.3 Green NH_3 production

Fig. 1-5 [22] shows the volumetric energy density of various fuel options. NH_3, because of high hydrogen-storage capacity of 17.6 wt%, volumetric energy density of 4.32 kWh L^{-1} in liquid, and volumetric density of 107.7 kg_{H2} m^{-3}, as well as facile liquefication and safe storage at moderate conditions, can be regarded as a CO_x-free hydrogen-carrier and also considered as a future potentially industrial fuel, for example, NH_3-based fuel cells by direct-using as fuel [23].

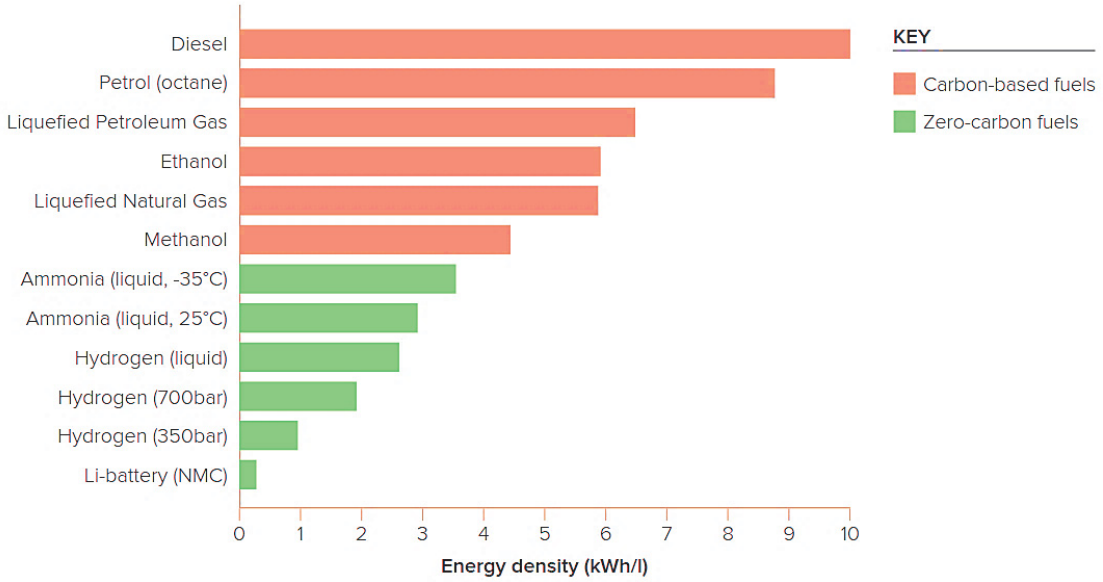

Fig. 1-5. The volumetric energy density of various fuel options. [22]

Green NH_3 can be scientifically described as a sustainable NH_3 production pattern that emits no or little CO_2 into the atmosphere [24], which primarily means that H_2 feedstock can be produced and supplied through eco-friendly routes, such as steam methane reforming (SMR) with carbon capture and storage, biomass gasification, or water electrolysis via renewable power [25], because the main energy consumption and CO_x emissions in Haber Bosch (HB) process come from the H_2 production. This has also driven the technological revolution in the small-scale and distributed process of NH_3 production such as biological, electrochemical, photochemical, [26] photothermal technologies, although they are still at the stage of basic technical or feasibility studies. [27] Additionally, it is particularly necessary to rigorously analyze the NH_3 production and transport costs of the emerging technology [28]. Advisedly, biomass gasification [29] and water electrolysis via renewable power [30-32] that can be used to obtain H_2 have been widely explored for NH_3 production and usually named for biomass-to-ammonia and power-to-ammonia, [33] respectively.

As shown in Fig. 1-6 (left), NH_3 production can actively transit from current HB process to SMR-HB process with carbon capture and storage, and H_2O electrolysis-HB, as well as finally long-term NH_3 electrosynthesis [34] for realizing the transition to the second NH_3 revolution with carbon-free, energy efficient, and low-cost. With the global boom in renewable energy, the favorable HB process coupling with H_2O electrolysis would improve energy efficiency of the synthesis loop by 50% (4.2 GJ $t_{NH_3}^{-1}$) and greatly decrease CO_2 emissions of ~78% [35]. Consequently, green NH_3 production using renewable energy is increasingly bursting the potential to become economically competitive, implying that replacing energy-intensive HB process to significantly reduce greenhouse gas emissions is no longer a dream. [36] As shown in Fig. 1-6 (right), the evolution from brown NH_3 to blue NH_3 and finally green NH_3 [37] offers a fingerpost to safely phase out fossil fuels [38] to pioneer its “bottle” role for storing energy in the form of a liquid-fuel. However, NH_3 separation is inseparable in NH_3 production, and the current physical condensation not only has high energy consumption but also low separation efficiency. Therefore, novel adsorption and membrane separation technologies have been wildly developed due to low energy consumption, especially membrane separation that can continuously operate compared to adsorption-desorption process.

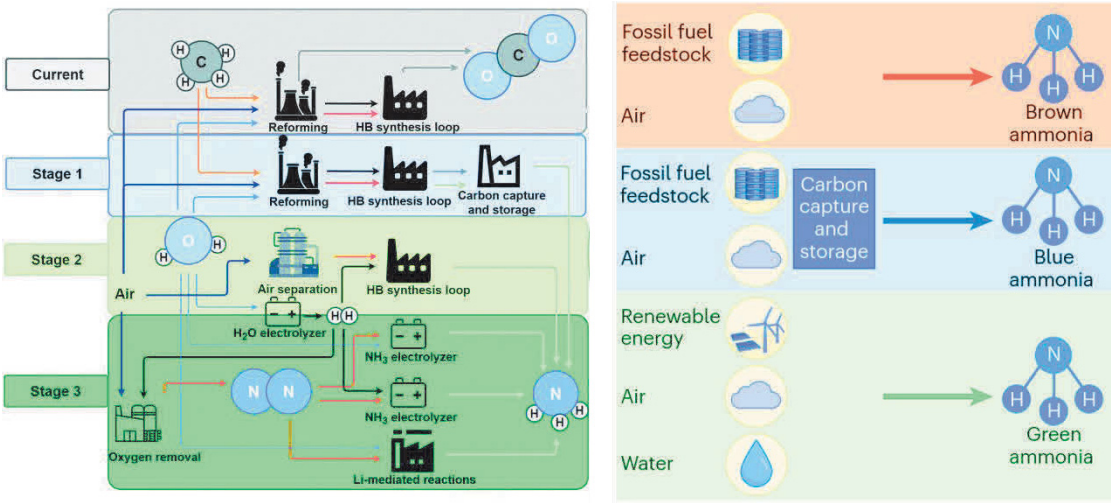

Fig. 1-6. Outlook of stages along a transition from the present-day SMR-HB process towards sustainable NH_3 (left) [34]; definition of green NH_3 (right) [37].

1.2 Membrane separation and membrane for NH_3 separation

Since the 1980s, membrane technology has applied to various separation processes, such as H_2, N_2, CO_2, and gaseous hydrocarbon separation. A membrane is commonly made of organic (like polymer), inorganic (like ceramic and zeolite), or composite material. Table 1-1 briefly summarizes the different materials for fabricating membranes and their advantages and disadvantages.

Table 1-1. Various membrane materials.

Type	Membrane	Advantage	Disadvantage
Organic	Polymeric membrane	✓ Low cost ✓ Easiness for large scale manufacture	☐ Large swelling ☐ Low permeability
	Ionic liquids/deep eutectic solvent-based membrane	✓ On-demand design ✓ Easiness for fabrication	☐ Large swelling ☐ Low permeability ☐ High cost
Inorganic	Crystalline Zeolite	✓ Perfect shape selectivity ✓ High mechanical and thermal stability	☐ Rigid and Fragile ☐ High cost ☐ Unstable in acid conditions

		Metal–organic framework (MOF)	✓ High microporosity ✓ Tunable channel structure	☐ Interface defect ☐ Rigid and Fragile
	Amorphous	Carbon molecular sieve (CMS)	✓ Narrow pore sizes ✓ High separation for isomers	☐ Rigid and Fragile ☐ High cost
		Organosilica or ceramic	✓ Do not swell ✓ High mechanical and thermal stability	☐ The formation of micropores is limited by the structure of the precursor
Organic–Inorganic hybrid	Various membranes		Combine the advantages of organic and inorganic membranes	Difficultly combine organic and inorganic materials

1.2.1 Gas transport mechanism in porous materials

Porous materials including metal-organic frameworks (MOFs), covalent-organic frameworks (COFs), zeolites, and porous polymers are becoming growingly attractive for molecular separation, adsorption, catalysis, and energy storage, as shown in Fig. 1-7. [39] The rise of membrane technology can not only exploit the practical application of porous materials especially in the field of molecular separation, but also reduce its application cost. For example, the support layer prepared using a low-cost material can occupy the most bulk of a multilayer composite membrane and maintain favorable mechanical strength, therefore, only a small number of porous materials are used to fabricate the separation layer. [40] Furthermore, the mechanism of molecule permeation through membranes has received continuous attention, such as pore-flow model and solution-diffusion model established as early as the 1950s and 1960s.

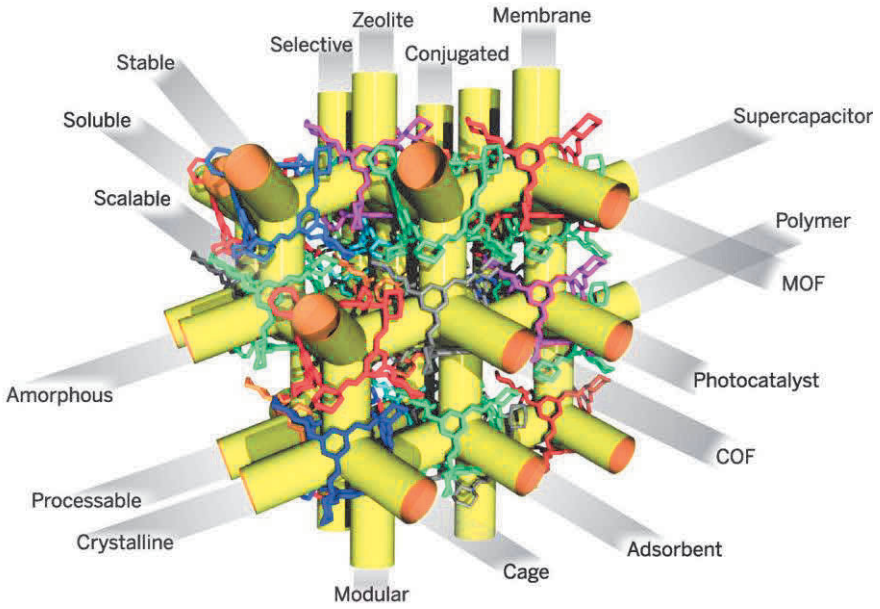

Fig. 1-7. Porous materials defined by type or by function. [39]

As illustrated in Fig. 1-8, according to the physicochemical properties of membrane materials and the internal pore structure they can form, membrane materials can be generally classified as flexible polymers, semirigid polymers, and rigid molecular sieve. [41] Flexible polymer materials exhibit a feeble diffusion selectivity because the thermal movement of the polymer segment within the activation region are inaccurately controlled. [42] Moreover, high diffusion selectivity based on the molecular sieving mechanism can be acquired from membrane prepared from rigid materials owing to uniform size of micropores, and semirigid polymer materials with flexibility and sieving properties not only express comparable separation performance, but also are alternative to rigid molecular sieve materials. [41,43]

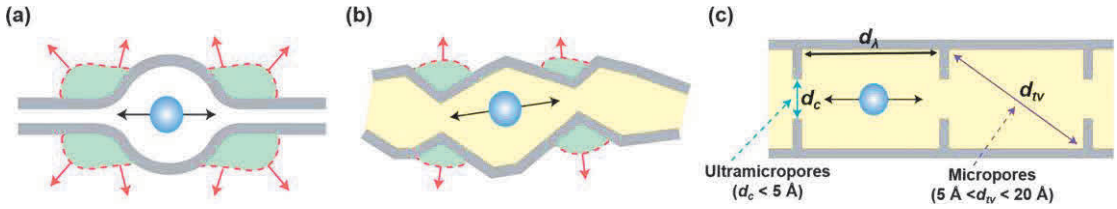

Fig. 1-8. Three major classes of membrane materials: (a) Flexible polymers with

characteristic transient gaps created by segmental packing and motion. (b) Semirigid polymers with interconnected micropores created by inefficient segmental packing. (c) Molecular sieves with rigid ultramicropores and micropore morphology. The yellow shaded areas in semirigid polymers and molecular sieves represent intrinsic and measurable porosity, which is not present in flexible polymers. The green shaded areas represent motion-enabled zones of activation required for diffusion. [41]

Precise molecule/ion separation depends not only on the pore morphology and chemical composition of the membrane but also on the properties of the target molecule/ion. Ideally, the pore size of the membrane should be between sizes of two or more molecules to be separated, so that smaller molecules can selectively and rapidly permeate through the microporous membrane, namely molecular sieve mechanism as displayed in Fig. 1-9. [44] As shown in Fig. 1-9 (a_1-a_4), the most classic molecular sieving, Knudsen diffusion, surface diffusion, and capillary condensation, should be assigned to the diffusion-selectivity separation mechanism. Based on molecular-cross-section size differentiation (Fig. 1-9 (b)) and shape-based molecular sieving mechanism (Fig. 1-9 (c)), a gallate-based MOF with zigzag channels and pore sizes of ~3.5 Å and a rigid MOF with precise shape matching, respectively, can be used for precisely separating ethylene/ethane. Interestingly, an ultrathin cyclodextrin-based POC membrane with trefoil-shaped aperture was used for organic solvent nanofiltration, it can achieve high precision separation of dye molecules based on conformation-controlled molecular sieving, as shown in Fig. 1-9 (d).

Moreover, because of the specific affinity between the target molecule/ion and the membrane matrix, the solution-diffusion mechanism was frequently utilized to interpret the permeation behavior of molecules/ions in ultramicropore or dense membranes. In

addition, the permeation of molecules/ions in membrane would be greatly promoted due to the transport effect that can be ascribed to the carrier substrates contained in the membrane, for example, diffusion of CO_2 through a micropore or dense membrane containing functional groups of amines. [45] Noteworthily, the diffusion of molecules/ions in the membrane hardly depends on one permeation mechanism completely, and often requires the synergistic effect of different permeation behaviors to enhance the molecule/ion permeance and selectivity.

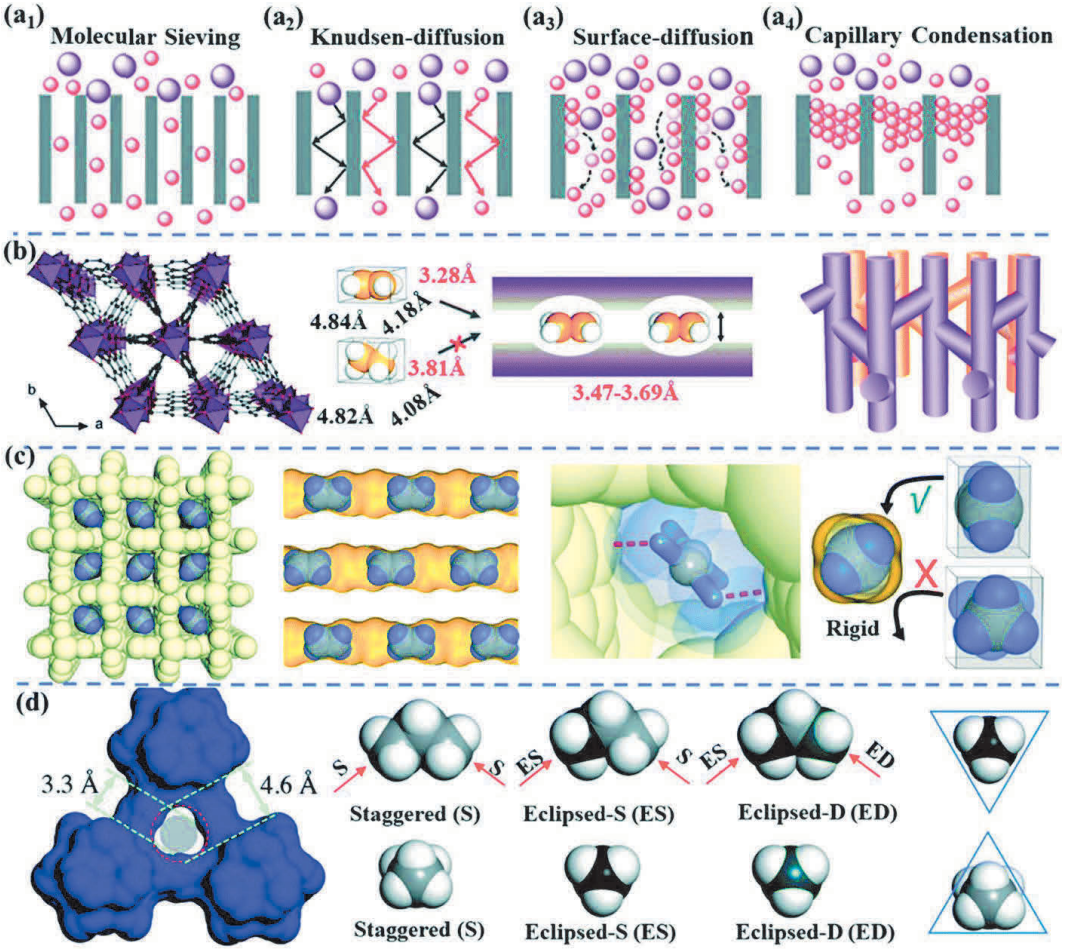

Fig. 1-9. Separation mechanisms of microporous framework membranes. (a) Diffusion mechanisms: molecular sieving (a_1), Knudsen diffusion (a_2), surface diffusion (a_3), and capillary condensation (a_4); (b) Molecular sieving based on molecular-cross-section size differentiation; (c) Shape-based molecular sieving; (d) Conformation-controlled molecular sieving. [44]

After extensive reviewing of the reference and thorough consideration, the

mechanism of membrane separation can be summarized in detail in Fig. 1-10. Firstly, the most common and diffusion-dominated selective separations can be classified as: size-based molecular sieving, Knudsen diffusion, surface diffusion, and capillary condensation, which mainly rely on the pore morphology of the membrane. Considering the synergistic effect of the pore morphology and functionalized matrix of membranes as well as the physicochemical properties of separated molecules, the solution-diffusion mechanism can be further subdivided into diffusion- and adsorption-selectivity separation and their synergies. [44] Additionally, some emerging separation mechanisms deserves to be emphasized, such as shape-based molecular sieving, [46] molecular-cross-section size-based sieving, [47] molecular configuration sieving, [48] and so on.

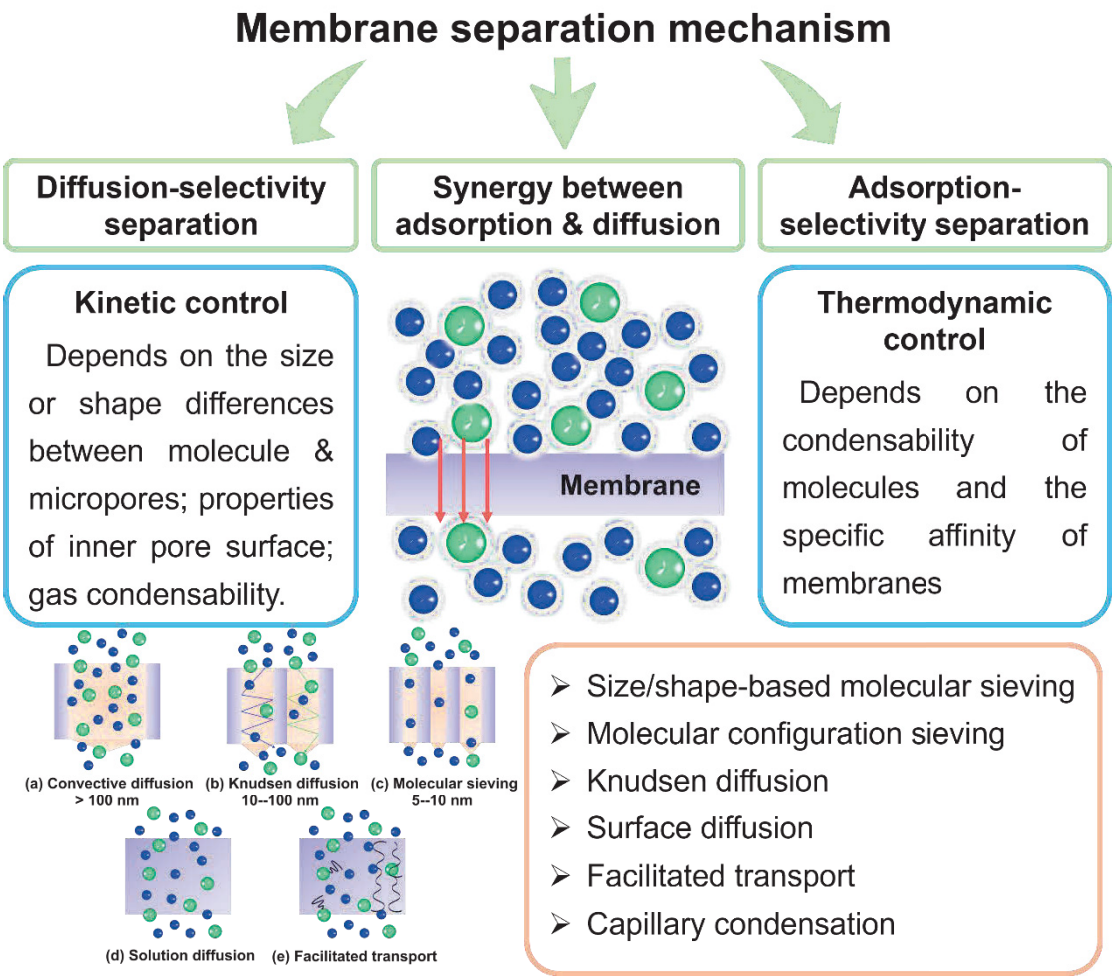

Fig. 1-10. Summary of separation mechanism of membranes.

1.2.2 Polymeric membrane for NH_3

Table 1-2 summarizes the NH_3 selectivity and permeance of the reported polymeric membranes for NH_3 separation at low and high temperatures. Generally, most of polymeric membranes showed considerable NH_3 selectivity around room temperature but inferior NH_3 permeance. Among them, polymers containing sulfoacid groups were of particular interest.

Table 1-2. Data for the selectivity and permeance of various polymeric membranes.

Name	Temp. [°C]	NH_3 permeance [mol m^{-2} s^{-1} Pa^{-1}]	NH_3/H_2	NH_3/N_2	Ref.
Poly(vinylammonium thiocyanate)	24.0	1.67E-08	6000.0	3600.0	50
	50.0	6.70E-08	1390.0	2000.0	
H^+-Nafion	21.0	2.57E-07		3000.0	51
	200.0	3.47E-08		3000.0	
Ag^+-Nafion	21.0	1.54E-07		600.0	
	200.0	3.14E-08		300.0	
Polypropylene/Nafion	25.0	3.35E-06	500.0	2000.0	52
Sulfonated block copolymers	25.0	2.01E-07	90.0	100.0	53
Cellulose acetate	25.0	9.80E-08	9.3	111	54
2D-MXene	25.0	6.20E-07	50.0	-	63
Prussian blue	25.0	3.72E-08	40.0	100.0	64

Poly(vinylammonium thiocyanate) membranes prepared from poly(vinyl alcohol) impregnated with ammonium thiocyanate were used for selective NH_3 transport in 1990. The high NH_3 selectivity was primarily attributed to the chemical interaction between NH_3 and NH_4^+/SCN^- carrier ions (solution-diffusion mechanism), but this chemical interaction also possibly resulted in the plasticization of the membrane, especially at high temperatures. [49,50] Subsequently, perfluorosulfonic acid (PFSA) membranes such as Nafion were developed, showing a high NH_3 permeance of ~2.1×10^{-7} mol m^{-2} s^{-1} Pa^{-1} with a NH_3/N_2 selectivity of >3000 at 21 °C due to the reversible reactions between NH_3 and sulfonic groups, [51,52] superior than poly(vinylammonium thiocyanate)

membranes. Nevertheless, both membranes showed an obvious decrease in NH_3 permeance with the increase of temperature. Furthermore, a membrane containing 7-23 nm polystyrene sulfonate domains was designed to improve NH_3 permeance and resistance by variating the sulfonated phase domain size and the degree of crosslinking. [53] Cellulose acetate membranes with good strength and low cost also expressed a favorable NH_3 permeance of ~9.5×10^{-8} mol m^{-2} s^{-1} Pa^{-1} with a NH_3/N_2 selectivity of 100 and NH_3/H_2 selectivity of 10 at 21 °C owing to hydrogen bonds between NH_3 and the polymer. [54]

Moreover, the cellulose acetate-multiwalled carbon nanotubes composite membrane [55] and Nafion-PTFE hollow fiber composite membrane [56] were also fabricated for NH_3 permeation and recovery. The fine-tuned design of porous polymer materials with potentially strong affinity for NH_3 based on chemical and structural properties are urgently advocated under different NH_3 concentrations and temperatures. As shown in Fig. 1-11 (a), various fluorinated polymers with different fluorine density exhibited a disappointing NH_3 solubility within more and more fluorinated matrixes (Polydimethylsiloxane (PDMS): 156.7×10^{-3}; Ethylene tetrafluoroethylene copolymer (ETFE): 29.5×10^{-3}; Perfluoroethylene propylene (FEP): 3.9×10^{-3} cm^3(STP) cm^{-3} $cmHg^{-1}$), which could be attributed to the repulsive dipole-dipole interactions between the lone-pair electron of NH_3 molecules and the electronic cloud of fluorine atoms. [57] Additionally, Brønsted acidic functional groups including -SO_3H, [58] -NH_3Cl, [59] -PO_3H_2, [59] -CO_2H, [59,60] as well as pyridine, imidazole, and Lewis acidic metal nanoclusters [58] can be elaborately decorated into the polymer in order to strengthen the adsorption capacity

and separation potential of NH_3 based on reversible base-acid interactions, hydrogen bonding interactions, and/or proton transfer.

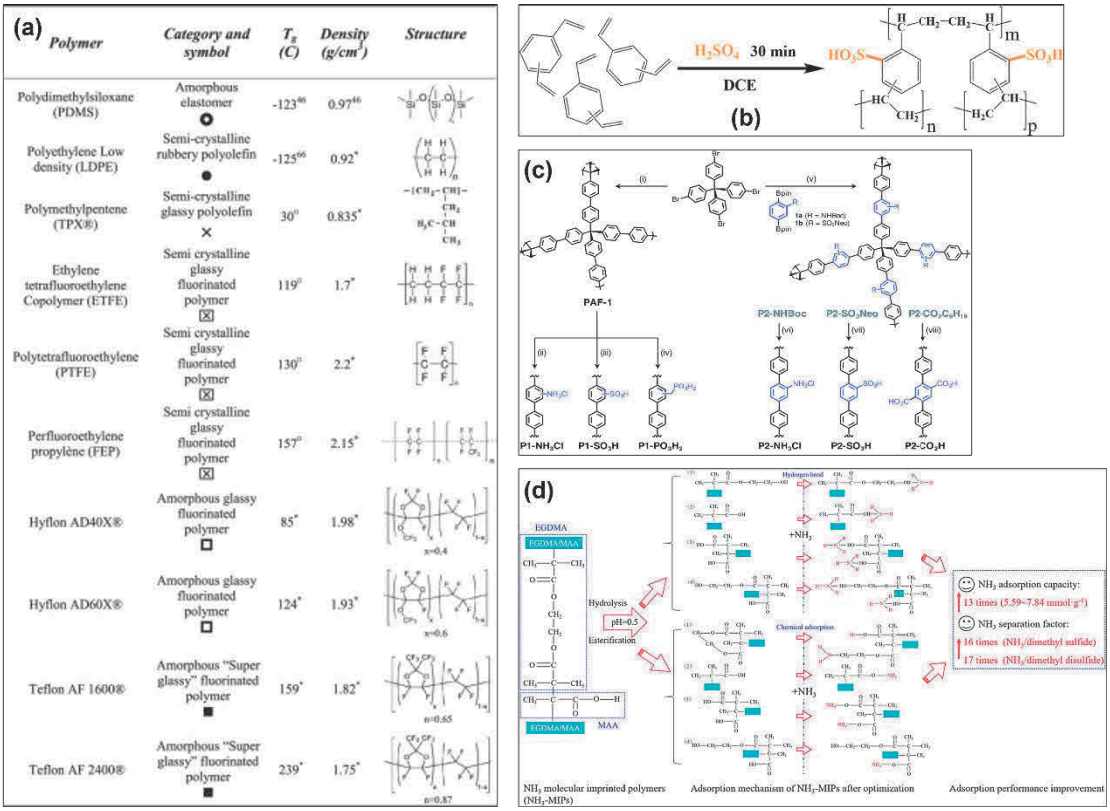

Fig. 1-11. The characteristics of the different fluorinated polymers (a), [57] synthetic route of MPOP-x-SO_3H Using H_2SO_4 as both the initiator and sulfonated agent (b), [58] General scheme for the syntheses of P1 and P2 polymers incorporating various Brønsted acid groups (c), [59] NH_3 adsorption in an NH_3 molecularly imprinted polymer (NH_3-MIP) (d). [60]

1.2.3 Zeolite and metal-organic framework membrane for NH_3

Table 1-3 lists the NH_3 selectivity and permeance of the reported zeolite membranes for NH_3 separation. MFI-type membrane showed both remarkable NH_3 permeance and excellent NH_3 selectivity at room temperature, while an impressive NH_3 selectivity was found in Na^+-grafted nanochannels membrane even at 200 °C.

Table 1-3. Data for the selectivity and permeance of various zeolite membranes.

Name	Temp. [°C]	NH_3 permeance [mol m^{-2} s^{-1} Pa^{-1}]	NH_3/H_2	NH_3/N_2	Ref.
ZIF-21	25.0	5.79E-07	12.0	35.0	61

MFI	25.0	2.30E-06	307.0	2236.0	62
Na^+-grafted nanochannels	200.0	2.24E-08	328.0	1106	65

LTA-type zeolitic imidazolate framework membranes, [61] named for ZIF-21, were synthesized via secondary seeded growth for NH_3 separation from H_2 and N_2, which represents a comparable NH_3 permeance of ~5.8×10^{-7} mol m^{-2} s^{-1} Pa^{-1} with NH_3/N_2 and NH_3/H_2 selectivities of 35 and 12, respectively, at room temperature. This is due to the polar-polar interactions between NH_3 and the linker polar channels and particularly the favorable thermodynamic action. [61] Moreover, nanosheet-based MFI membranes exhibited an high NH_3/N_2 selectivity of 2236 with NH_3 permeance of 1.1×10^{-6} mol m^{-2} s^{-1} Pa^{-1} and high NH_3/H_2 selectivity of 307 with NH_3 permeance of 2.3×10^{-6} mol m^{-2} s^{-1} Pa^{-1} in their respective mixed-gas separation at room temperature, which was attributed to the inhibitory effect of preferentially adsorbed NH_3 in membrane on H_2 and N_2 permeation at low temperatures, but not applicable to high temperatures. [62]

Additionally, ultrathin 2D-MXene nanosheet membranes with terminal -*OH* surface groups revealed different permeation mechanism for absorbed and non-adsorbed gases, namely Knudsen diffusion for permanent gases and labyrinthine hopping transport for condensing vapors, resulting in a favorable NH_3 permeance of 6.2×10^{-7} mol m^{-2} s^{-1} Pa^{-1} and medium NH_3/H_2 selectivity of 50 that can be improved in humid atmosphere. [63] Surprisingly, ultrathin Prussian Blue membranes with protonic carrier can be prepared by cyclic electrodeposition and resulted in a potential NH_3 permeance of 3.7×10^{-8} mol m^{-2} s^{-1} Pa^{-1} and ideal NH_3/H_2 and NH_3/N_2 selectivities of 40 and 100, respectively, which can be ascribed to the proton carrier's promotion on NH_3 diffusion and the Prussian Blue channel's size-exclusion effect on H_2 and N_2 transport. [64] Noticeably, NH_3

transport in the form of ammonium in the membrane can not only hold the electroactivity of the selected layer, but also can be reversibly converted in an electrochemical framework, [64] showing a promoted NH_3 transport. Recently, Na^+-gated nanochannel membranes were fabricated by secondary NaA seed-growth on α-Al_2O_3 hollow fiber supports. After optimizing the membrane preparation process, the optimal membrane displayed the highest NH_3/H_2 and NH_3/N_2 selectivities of ~328 and ~1106, respectively, with NH_3 permeance of 3.0×10^{-8} mol m^{-2} s^{-1} Pa^{-1} at 200 °C and 21 bar. [65]

Metal-organic framework (MOF) and its derived membrane can also be recognized as a superior candidate for NH_3 adsorption, removal, and permeation owing to its tunable structure, convenient functionalization, scalable two- and three-dimensional arrays, and excellent sorption properties. [66] As manifested in Fig. 1-12, the functionalized Zr-MOF by *Cl* ion [67] and -NH_2 [68] appeared remarkable NH_3 capture and reversible/irreversible NH_3 uptake in both dry and humid conditions because of the strong and diverse interactions between NH_3 and functional groups, for instance, van der Waals forces, proton transfer, coordination, hydrogen bonding, chemical bonding, and *NH*-π interactions.

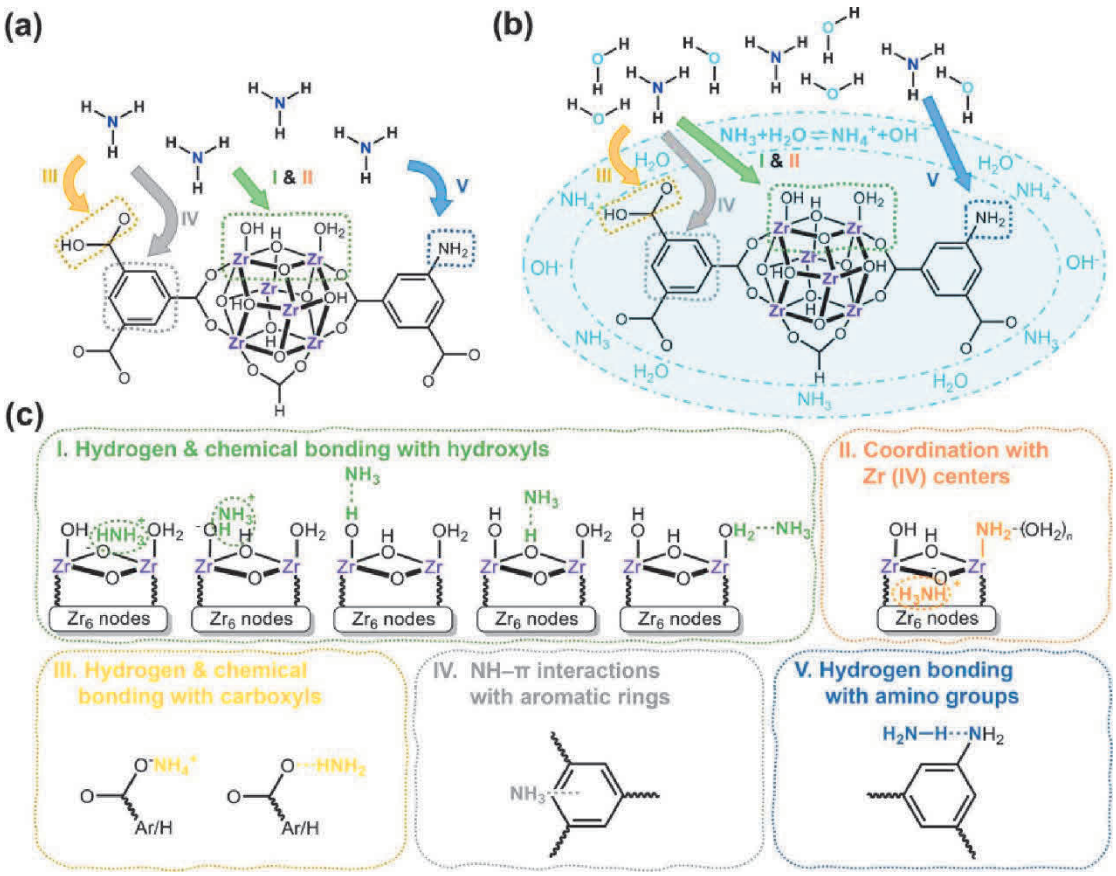

Fig. 1-12. Illustration of the interactions of NH_3 with amino-functionalized Zr-MOFs xerogels under (a) dry and (b) extremely moist conditions in addition to physisorption, and (c) proposed NH_3 binding configurations. [68]

Although the customary grafting of acid functional groups to MOF can significantly enhance NH_3 affinity and increase NH_3 uptake, it seriously challenged the recyclability of MOF. Ligand -functionalized Al-MOFs in Fig. 1-13 were reported and screened to show a superior NH_3 adsorption capacity, among them, a robust MOF-303(Al) with Al^{3+} was fabricated using pyrazole-3,5-dicarboxylate with multiple sites and showed a as high as NH_3 adsorption capacity of 19.7 mmol g^{-1} at 25.0 °C and 1.0 bar due to hydrogen bonding interactions of multiple sites and also verified fully reversible after 20 cycles of NH_3 adsorption-desorption. [69]

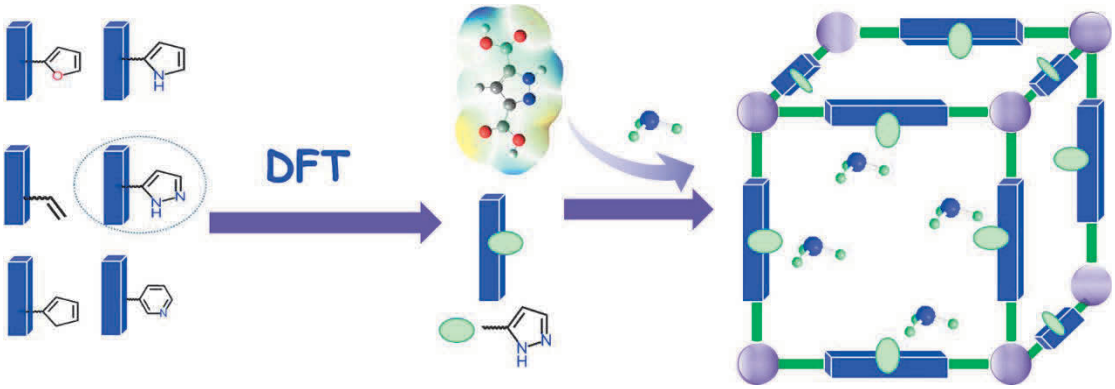

Fig. 1-13. Ligand-grafted Al-MOFs for reversible ammonia adsorption. [69] Ligand includes furan, pyrrole, propylene, pyrazole, cyclopentadiene, and pyridine.

1.2.4 Ionic liquid or Deep eutectic solvent-based membrane for NH_3

Table 1-4 lists the NH_3 selectivity and permeance of two ionic liquid membranes for NH_3 separation. Although ionic liquid membranes can be flexibly designed by using different types of anion/cations and also show good performance at room temperature, their NH_3 separation performance at different temperatures and pressures remains to be investigated.

Table 1-4. Data for the selectivity and permeance of two ionic liquid membranes.

Name	Temperature [°C]	NH_3 permeance [mol m^{-2} s^{-1} Pa^{-1}]	NH_3/H_2	NH_3/N_2	Ref.
Nexar/[Eim][NTf_2]	25.0	9.28E-07	264.0	1407.0	71
Neat Pebax	25.0	1.99E-07	70.1	406.7	72

Nexar/[Eim][NTf_2]: middle-sulfonated pentablock copolymer (Nexar^{TM})/1-ethylimidazolium bis(trifluoromethylsulfonyl)imide ([Eim][NTf_2]); Neat Pebax: poly(ether-block-amide) copolymer (Pebax).

Functionalized ionic liquids with high NH_3 affinity were designed and further incorporated into the commercial middle-sulfonated pentablock copolymer (Nexar^{TM}) or poly(ether-block-amide) copolymer (Pebax) to fabricate Nexar/ionic liquid or Pebax/ionic liquid hybrid membranes, [70-72] combining the respective advantages of ionic liquids and polymers. Consequently, the self-assembled and interconnected

channels can be regarded as an NH_3 transport highways, which was thankful to the continuous ionic domains formed by the incorporation of ionic liquids into copolymers with well-defined nanochannels. [70-72] Usually, ionic liquid-derived hybrid membranes exhibited a comparable NH_3 permeance of 0.5-1.0×10^{-6} mol m^{-2} s^{-1} Pa^{-1} and favorable NH_3/H_2 and NH_3/N_2 selectivities of 100-360 and 500-1800, respectively, at room temperature, [70-72] which can be ascribed to multiple-site hydrogen bonding, proton transfer, metallic coordination, and acid-base interactions as well as interconnected channels, as demonstrated in Fig. 1-14. [73-75]

Compared to the expensive precursors, complex synthesis process, and high viscosity of ionic liquids, the readily available deep eutectic solvents can be not only simply synthesized but also have a strong NH_3 affinity comparable to ionic liquids. Imidazole/resorcinol, [76] glycolic acid/xylitol, [77] ethylamine chloride/resorcinol, [78] LiCl/ethylene glycol [79] can be prepared by simply mixing and used to selectively capture NH_3 and reversibly desorb NH_3, which benefits by relatively low viscosity to reduce the mass-transfer barrier and multiple weak-acidic groups. [80] Therefore, deep eutectic solvents have the dramatical potential to be prepared into membranes for the NH_3 separation.

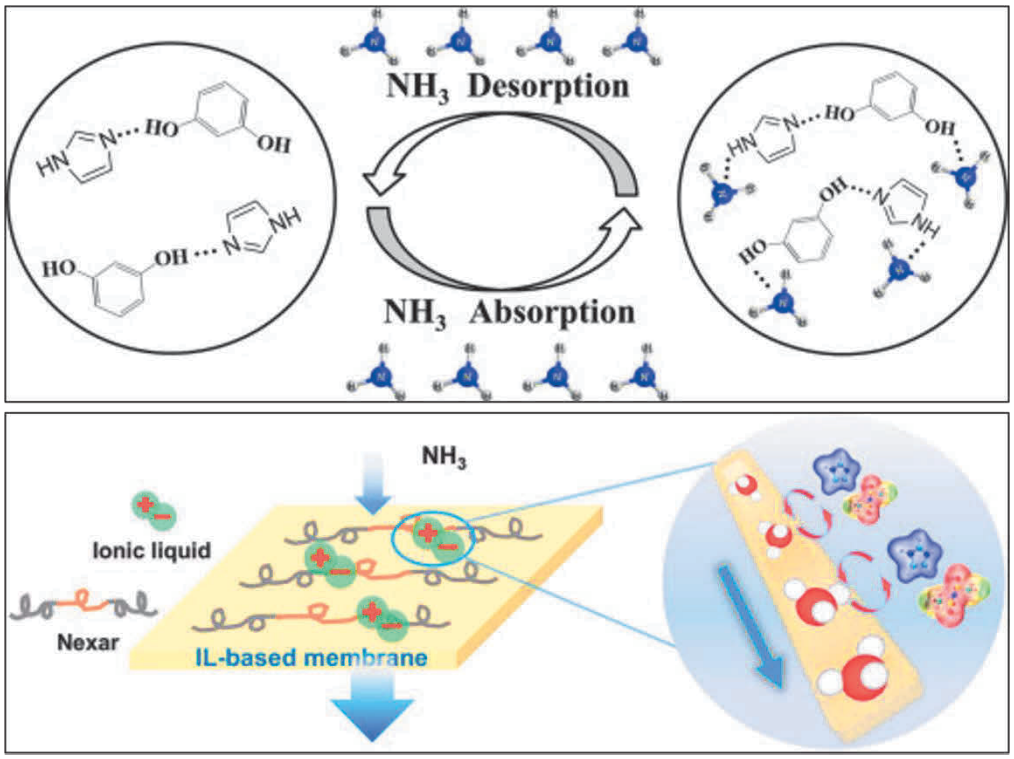

Fig. 1-14. Schematic NH_3 adsorption [76] and permeation [70] on ionic liquids or deep eutectic solvents and their membranes, respectively.

1.3 Organosilica membrane

1.3.1 Organosilica precursor

Organotrialkoxysilanes ($RSi(OR')_3$) as silica-based precursors in Fig. 1-15 (above) have been widely investigated to prepare organosilica-based membranes due to high thermal stability, favorable chemical-stability, comparable mechanical-strength, and tunable network structures, especially for the additional functionalities by grafting various organic groups (R). [81-84] Commonly, organosilica precursors can be divided into bridge-type (namely "spacer") and pendant-type (namely "template") precursors, depending on where the organic group is grafted around the silicon atom. Furthermore, the grafted organic groups can not only modify the pore morphology of the membrane to increase the gas permeances and molecular sieving, [85,86] but also enhance their

affinity to polar molecules such as CO_2 to improve the adsorption-diffusion, [87,88] which depends on the nature of the organic groups themselves.

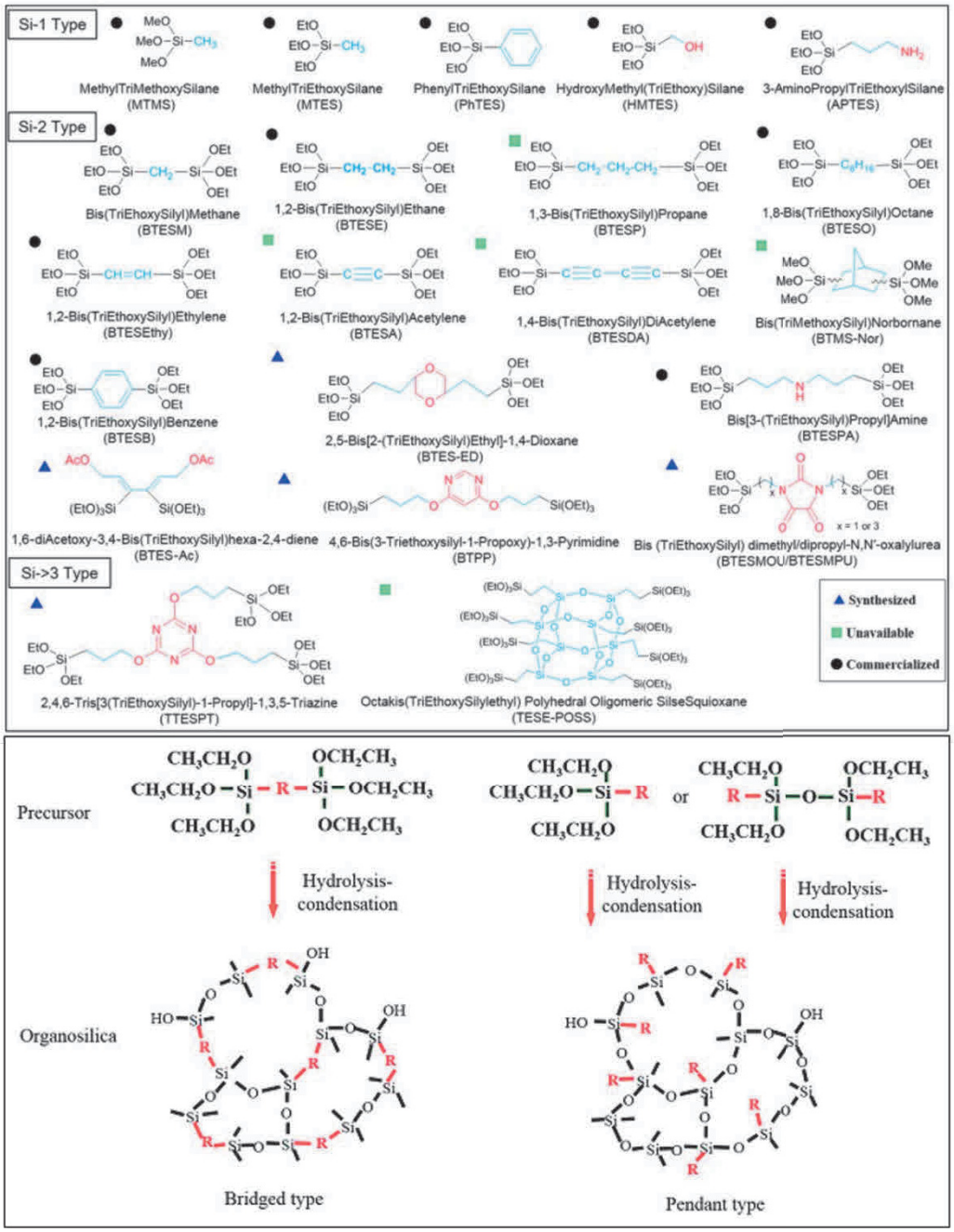

Fig. 1-15. Most of the organoalkoxysilane materials along with their chemical structures. (Et: ethyl; Me: methyl) (above) and the represented bridge-type and pendant-type precursors and their organosilica structures formed (below). [81]

For the membranes prepared by organosilica precursor containing alkyl chains such as ethane, ethene, ethynylene, and octane bridges, as shown in Fig. 1-16, the pore size

of membranes increased from ethane and ethene to ethynylene due to the increased bond angles of Si-O-Si and Si-C-C groups and the construction of a looser structure. [89,90] Moreover, bis(triethoxysilyl)acetylene (BTESA) membranes showed a C_3H_6 separation potential from C_3H_8 owing to the enlarged porosity as well as the improved polarity caused to the π-π interaction between C_3H_6 molecules and ethynylene groups. [91,92] However, bis(triethoxysilyl)octane (BTESO) membranes exhibit a dense structure and more hydrophobicity, nearly a nonporous organosilica membrane, because of the striking flexibility of the octylene units as a longer linking-bridge group. [93,94] Amine functionalized organosilicas have been widely used for separating CO_2 based on the "membrane affinity". As indicated in Figs. 1-17 (a) and (b), the primary amines and secondary amines belong to unhindered amines while tertiary amines should be sterically hindered amines obviously in the three selected aminosilica precursors, according to the definition of unhindered and sterically hindered amines. [95] After summarizing the performances of all membranes in Figs. 1-17 (c) and (d), the TA-Si membrane with sterically hindered amines can not only decrease CO_2 binding energy but also improved the reaction rates between amine and CO_2, which greatly promotes the CO_2 transport in aminosilica membranes. [96]

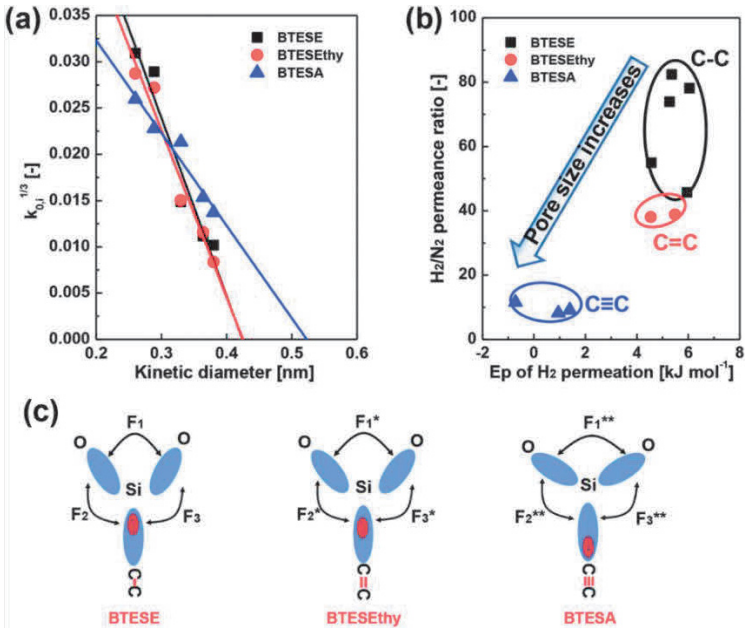

Fig. 1-16. The relationship between kinetic diameters and $k_{0,i}^{1/3}$ for BTESE, BTESEthy, and BTESA membranes (a), H_2/N_2 permeance ratio at 200 °C as a function of the activation energy of H_2 permeation for BTESE, BTESEthy, and BTESA membranes (b), the bonding structure model for BTESE, BTESEthy, and BTESA (c).[91]

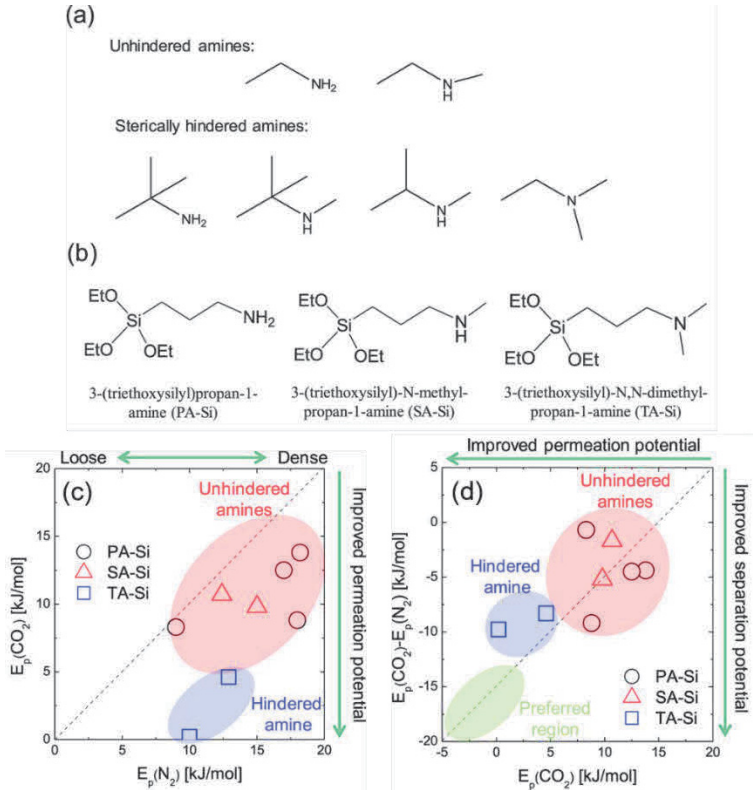

Fig. 1-17. Illustration of the chemical structures of unhindered and sterically hindered amines (a), chemical structures of organoalkoxysilane precursors employed in the present study (b), relationships of *Ep(N2) vs. Ep(CO2)* (c) and *Ep(CO2) vs. Ep(CO2)-Ep(N2)*

(d) of amine-silica membranes. [96]

In addition to the organic group functionalized organosilica precursors, as shown in Fig. 1-18, metal-doped organosilica membranes, such as bis[3-(trimethoxysilyl)propyl] amine (BTPA) membranes doped with Ni, Cu, and Ag, can also express the improved gas permeance and selectivity due to the enlargement of pore size through the transition metal coordination with propylamines. [97] Owing to the difference in coordination strength between the metal and propylamine, gas permeation was increased following the order of Ni-BTPA > Cu-BTPA > Ag-BTPA > BTPA. Furthermore, doping transition metal into the BTPA network structure can not only control the pore size but also adjust the open sites of the metal by controlling the doping amount to promote the specific adsorption of the molecules to be separated. [98]

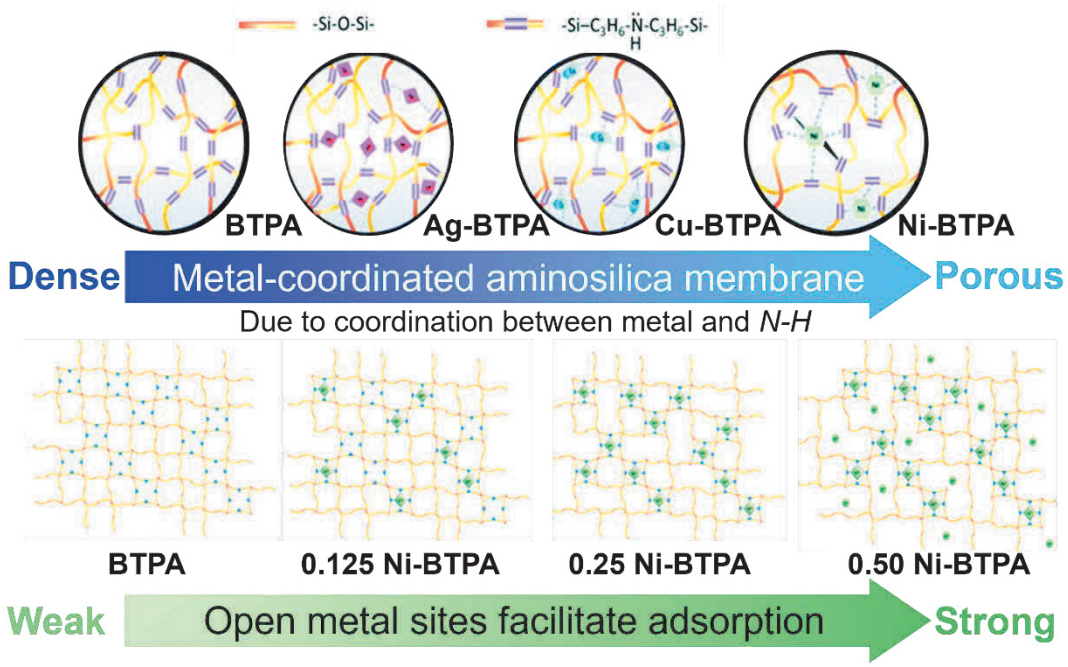

Fig. 1-18. Metal-doped aminosilica membrane with high gas permeation by enlarging pore sizes. [97,98]

1.3.2 Fabrication approach of organosilica membrane

Table 1-5 summaries the NH_3 selectivity and permeance of various silica-based

membranes for NH_3 separation. Compared with pure silica membrane (TEOS), perfluorosulfonic acid/ceramic composite membranes showed superior NH_3 permeance and selectivity at low temperatures, but NH_3 selectivity decreased rapidly with the increase of temperature.

Table 1-5. Data for the selectivity and permeance of various silica-based membranes.

Name	Temperature [°C]	NH_3 permeance [mol m^{-2} s^{-1} Pa^{-1}]	NH_3/H_2	NH_3/N_2	Ref.
TEOS	50.0	1.02E-07	28.7		100
	400.0	1.04E-07	0.1		
Nafion/ceramic	50.0	2.85E-06	40.3	730.9	
	200.0	1.93E-06	2.6	24.8	
Aquivion-H^+/ceramic	50.0	2.71E-06	118.6	2085.9	108
	200.0	1.68E-06	6.3	73.9	
Aquivion-Li^+/ceramic	50.0	1.88E-06	44.7	465.6	
	200.0	9.05E-07	1.9	22.3	

The silica-based membranes were usually fabricated by sol-gel and chemical vapor deposition (CVD) process. Typically, the alkoxysilanes can be firstly hydrolyzed with H_2O to obtain silanol (*Si-OH*) and further condensed to build *Si-O-Si* network, namely the most feasible and low-cost sol-gel method. As displayed in Fig. 1-19 (a), both polymeric sols and colloidal sols can be prepared by controlling the reaction conditions and be used to construct an intermediate layer and/or a separation layer through the subsequent gelation process on the porous supports, [99] for silica-based membrane. [100]

Importantly, the new-type atmospheric-pressure plasma-enhanced CVD process (AP-PECVD), as schematically exhibited in Figs. 1-19 (b), (c), and (d), was also used to fabricate silica-based membranes owing to its simple and continuous operation under atmospheric pressure rather than vacuum systems. [101,102] Moreover, one-side and counter-diffusion CVDs were classified based on differences in feeding behavior of reactants, particularly counter-diffusion CVD can help to form internal pores and lessen

pinholes. [99]

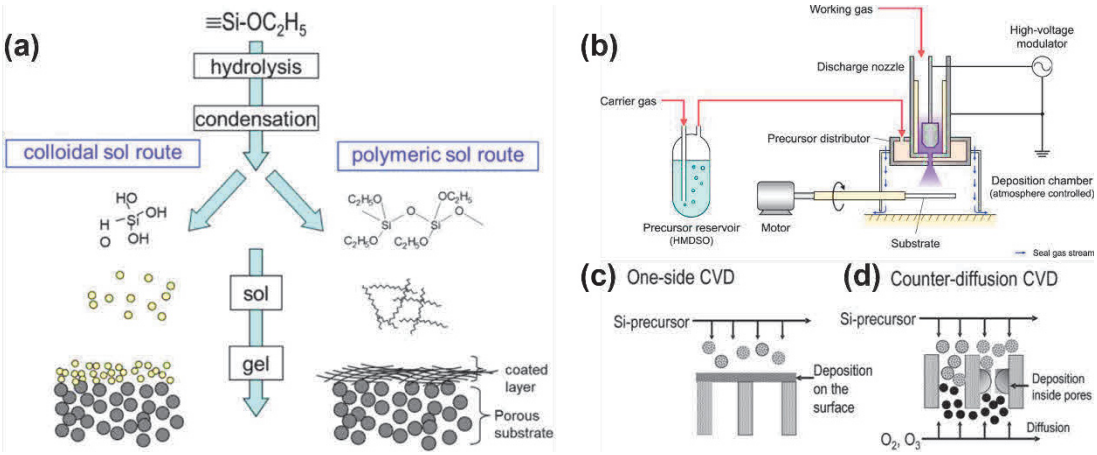

Fig. 1-19. Sol-gel processing of SiO_2 membranes (a); [99] Schematic illustration of the membrane fabrication via AP-PECVD (b), [101] different types of CVD (c,d). [99]

As demonstrated in Fig. 1-20 (a), organosilica top-separation layer was formed by coating their sols on the intermediate layer. [103] However, if the pore size of the intermediate layer is larger than the particle size of the sol, the sol can penetrate into the large pore of the intermediate layer, resulting in a dense gas permeation membrane. [104] Consequently, the size and shape of the sol particle should be controlled by adjusting the pH to affect the hydrolysis and condensation rate, since the sol-gel process is usually pH dependent. [104]

In addition to sol-gel and CVD process, the interfacial polymerization, [105] flow-induced deposition, [106] and photo-induced sol-gel [107] were also utilized to fabricate inorganic/organosilica membranes for gas and liquid separation. Furthermore, the calcination temperature of the membrane preparation is also one of the key factors for controlling the pore size of the membrane and adjusting the affinity of organic groups to polar molecules. [108]

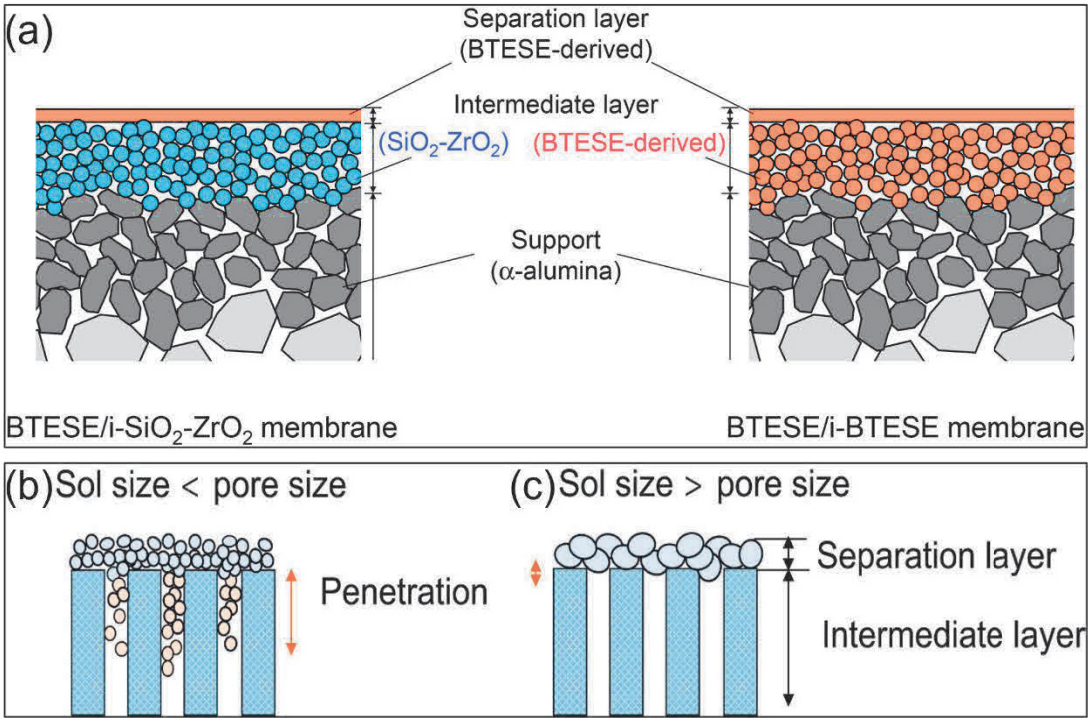

Fig. 1-20. Schematic images of a BTESE/i-SiO_2-ZrO_2 membrane and a BTESE/i-BTESE membrane, [103] schematic structure of small and large size sols-derived membranes. [104]

1.4 Catalytic membrane reactors (CMRs)

1.4.1 Theoretical concept of CMRs

Compared to packed bed reactor (PBR), as shown in Fig. 1-21 (left), CMRs have attracted increasing interest as an integrated unit that combines catalytic reaction and membrane separation, which would provide inherent advantage that can achieve a higher reaction conversion even under mild conditions owing to the shift of the reaction equilibrium towards the product side through membrane extraction. [109] As shown in Fig. 1-21 (right), the mathematical model with one-dimensional, isothermal, and plug-flow characters was proposed to understand the CMR mechanism and facilitate the CMR design as well as optimize the CMR performance. [110] Selectively permeative separation using membranes can undoubtedly improve the reaction yield and rate and

increase the concentration of the product in the permeated side of membrane. [111] In addition, the reaction parameters (temperature, pressure, reactor length, flowrate, and catalyst weight) and the membrane performances (permeance and selectivity) can be reasonably investigated to deeply understand the mechanism and nature of CMR. [110]

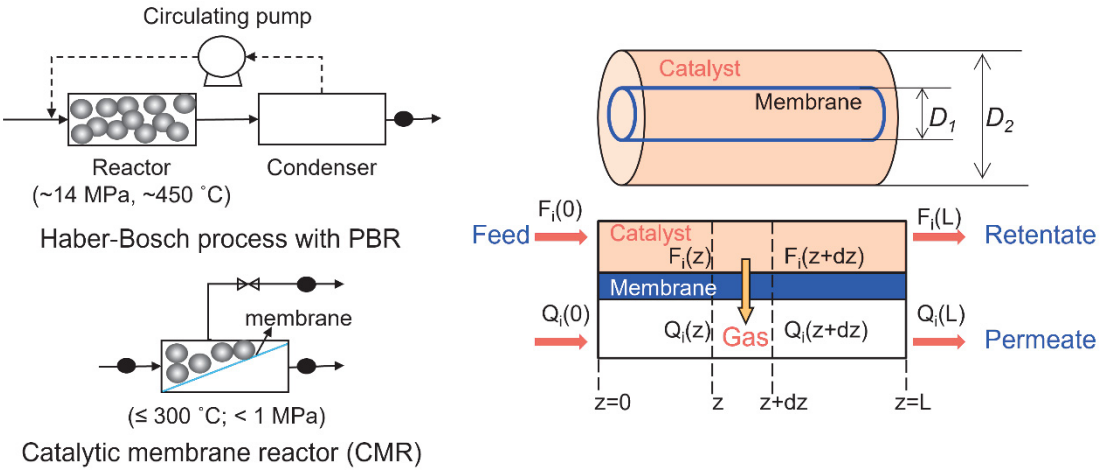

Fig. 1-21. Schematic diagram of the Haber-Bosch and membrane reactor process (left); schematic diagram of the CMR mechanism (right). [110]

1.4.2 Application of CMRs

Table 1-6 shows some microporous membrane reactors from the representative experimental results of H_2 production. Obviously, the product conversion can be improved by using CMRs because membranes can selectively transfer the product from reaction to permeate side that can break the reaction equilibrium. Among them, silica and hybrid silica membranes were widely used in steam reforming of methane, methylcyclohexane dehydrogenation, and NH_3 decomposition, which much attracts attention.

Table 1-6. Experimental results of some practical applications via a CMR. [122]

Reaction system	Membranes	Reaction temperature [°C]	Feed pressure [MPa]	Catalysts	Conversion [%]
Steam reforming of methane	Carbon molecular sieve	250	0.2	$CuO/ZnO/Al_2O_3$	55
	Silica	500	0.1	Rh	65
	Hybrid silica	500	0.1	Ni	80

Water gas shift reaction	Silica	500	0.2	Ni/Al_2O_3	80
	MFI zeolite	550	0.6	Fe/Ce	98
	MFI zeolite	550	0.15	Fe/Ce	82
	MFI zeolite	300	0.2	$CuO/ZnO/Al_2O_3$	95
Methylcyclohexane dehydrogenation	Carbon molecular sieve	220	0.1	Pt/Al_2O_3	62
	Hybrid silica	220	0.1	Pt/Al_2O_3	80
	Hybrid silica	230	0.12	Pt/Al_2O_3	77
NH_3 decomposition	Hybrid silica	450	0.3	Ru/Al_2O_3	74
	Hybrid silica	450	0.1	Ru/Al_2O_3	95

1.4.2.1 Methane steam reforming via CMRs

A CMR consisting of silica membrane with H_2 perm-selectivity and Ni catalyst was fabricated and used for methane steam reforming. The methane conversion could be increased from a conversion of 0.44 (equilibrium conversion) to 0.8 by transferring H_2 from the reaction side to the permeation side where 500 °C, and feed and permeate pressures of 100 and 20 kPa, respectively. [112] Moreover, the CMR for methane steam reforming can be stably operated for 30 h using Ni catalyst and hexamethyldisiloxane-derived membrane with H_2/N_2 selectivity of ~10^3 under the hydrothermal conditions. [113]

1.4.2.2 Water gas shift reaction via CMRs

The MFI-type zeolite membrane with a H_2/CO_2 selectivity of 68.3 and H_2 permeance of 2.94×10^{-7} mol m^{-2} s^{-1} Pa^{-1} at 550 °C was packed with a cerium-doped ferrite catalyst, which was designed to be a CMR for high temperature water gas shift reaction. [114] The CO conversion of 81.7% was acquired by removing H_2 from catalytic reactor, which was much higher than the conversion via PBR (62.5%) and the equilibrium conversion (65%). [114] Furthermore, the results of the reaction conversion were further explored at 400-500 °C and 0.2-0.6 MPa. [115] Besides, a CMR for low temperature water gas shift

reaction was designed by loading commercial $CuO/ZnO/Al_2O_3$ catalysts on modified zeolite membranes (H_2/CO_2 selectivity: 42.6 and H_2 permeance: 2.82×10^{-7} mol m^{-2} s^{-1} Pa^{-1} at 550 °C), showing a greatly improved CO conversion of 95.4% at relatively low temperature such as 300 °C. [116]

1.4.2.3 Methylcyclohexane dehydrogenation via CMRs

A bimodal CMR, as indicated in Fig. 1-22, equipped with Pt/Al_2O_3 catalyst and bis(triethoxysilyl) ethane (BTESE) derived organosilica membrane (H_2/toluene selectivity: 16000 and H_2 permeance: 10^{-6} mol m^{-2} s^{-1} Pa^{-1} at 200 °C) for the dehydrogenation of methylcyclohexane to produce H_2, which increased the conversion over the equilibrium conversion (0.44-0.86) at 250 °C and recovers 99% H_2 from the reaction stream into the permeation stream with H_2 purity of 99.8%. [117] Additionally, a 2D axial symmetric model was utilized to simulate several parallel and small CMRs and a single CMR with the same volume for methylcyclohexane dehydrogenation, indicating that the parallel CMR has a high H_2 production rate, that is 3-5 times higher than that of a single CMR. [118]

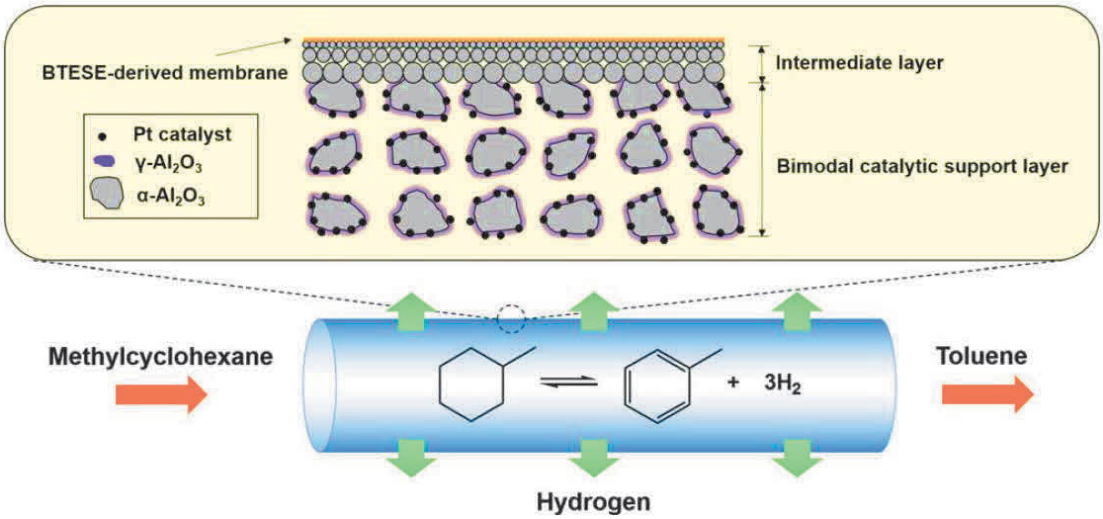

Fig. 1-22. Schematic diagram of the bimodal CMR for methylcyclohexane

dehydrogenation. [117]

1.4.2.4 SO_3/H_2SO_4 decomposition via CMRs

A CMR simulation for SO_3 decomposition in Iodine-Sulfur thermochemical cycle revealed that the SO_3 decomposition temperatures can be greatly decreased from 900-1100 °C to ~600 °C through using membrane extraction due to a shift of thermodynamic equilibrium. [110] SO_3 conversion of 0.93 at ~600 °C, that vastly surpasses the equilibrium conversion of 0.28, could be achieved using a porous membrane with O_2/SO_3 selectivity of > 50 and O_2/SO_2 selectivity of < 10. [110] Afterward, microporous BTESE-derived membranes with O_2/SO_3 selectivity of 10 at 550 °C and O_2 permeance of 2.5×10^{-8} mol m^{-2} s^{-1} Pa^{-1} was developed and highly expected for the SO_3 decomposition via a CMR. [119]

1.4.2.5 NH_3 decomposition via CMRs

As shown in Fig. 1-23, Ru/γ-Al_2O_3/α-Al_2O_3 catalyst was supported on a homogenous polyhedral oligomeric silsequioxane layer, that showed a high H_2 permeance of 2.6×10^{-7} mol m^{-2} s^{-1} Pa^{-1} with H_2/NH_3 and H_2/N_2 selectivities of 120 and 180, respectively, at 500 °C, to obtain a bimodal CMR for NH_3 decomposition. [120] Conventionally, NH_3 conversion can rapidly decrease from 50.8 to 35.5% using PBR under the reaction conditions (NH_3 feed flow rate of 40 ml min^{-1}, 450 °C, and 0.1-0.3 MPa) because of the increased H_2 inhibition effect, but NH_3 conversion gradually increased from 68.8 to 74.4% using CMR because the H_2 selective permeation breaks through the reaction equilibrium. [120] In addition, it has also been demonstrated that the CMR can stably conduct for 120 h due to the favorable thermal-stability and NH_3 resistance of

membranes. [121]

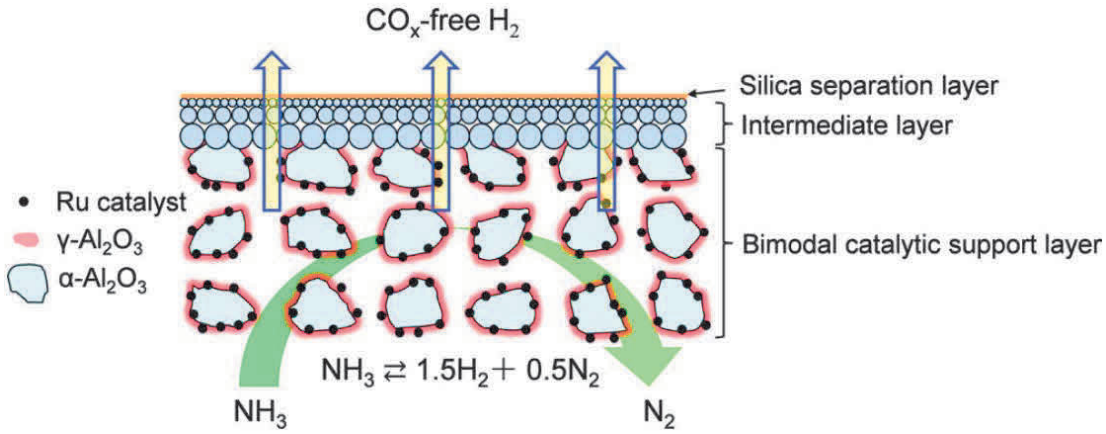

Fig. 1-23. Schematic diagram of the bimodal CMR for NH_3 decomposition. [121]

CMR technologies have been successfully applied to a variety of reactions to promote reaction conversion through membrane extraction of target molecules. As displayed in Fig. 1-24, various membranes such as zeolite and ZIF membranes, silica membranes, carbon molecular sieve (CMS) membranes, and graphene oxide (GO) membrane [122] would also be bound to play a pivotal role as the core of CMR, and not just for H_2 production.

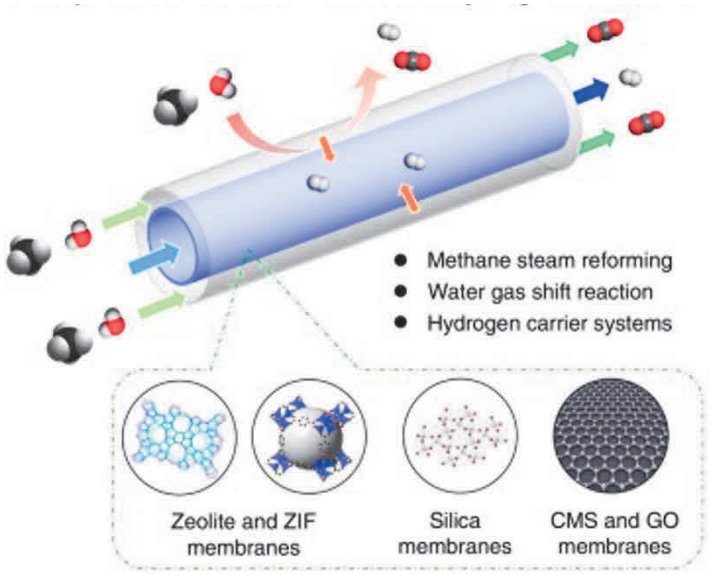

Fig. 1-24. Microporous CMR for H_2 production. [122]

1.5 Scope of this thesis

The overall objective of this dissertation research is to exploit advanced organosilica membranes for NH_3 separation and their application for NH_3 synthesis catalytic membrane reactors. Given the intrinsic limitations of the currently used membranes, this study has been focusing on the development of novel organosilica membranes with excellent molecular sieving, NH_3 adsorption-diffusion, and NH_3 resistance at high temperatures, which can be applied to enhance the NH_3 separation performance and improve synthetic NH_3 conversion via catalytic membrane reactors. The main work is as follows.

(1) Development and optimization of metal-doped bis[3-(trimethoxysilyl)propyl] amine (BTPA) membranes for NH_3 separation. (**Chapter 2 and 3**, metal-coordinated organosilica membranes)

(2) Development of sulfonated (3-Mercaptopropyl)trimethoxysilane and sulfonic 3-(trihydroxysilyl)-1-propanesulfonic acid membranes for NH_3 permeation. (**Chapter 4 and 5**, sulfoacid-containing organosilica membranes)

(3) To investigate the performance of recycle catalytic membrane reactors for NH_3 synthesis using the above organosilica membranes. (**Chapter 6**, green NH_3 production via membrane reactors)

This dissertation consists of 6 chapters, as follows:

Chapter 1 is "**General introduction**", which introduces the research background and purpose of this study.

Chapter 2 is "**Enhanced NH_3 permeation of bis[3-(trimethoxysilyl)propyl] amine**

membranes via coordination with metals". Bis[3-(trimethoxysilyl)propyl] amine (BTPA) membranes doped with different metals, including Fe, Ni, and Ag, were applied to evaluate the permeation properties of H_2, N_2, and NH_3. All metal-coordinated BTPA gels showed superior NH_3 adsorption and desorption capacity via NH_3 temperature-programmed desorption (NH_3-TPD), which benefits from the coordination between metal and NH_3. The single-gas permeation and activation energy of permeance were measured to evaluate NH_3 separation performance, which occurred in the following order: Ni-BTPA > Fe-BTPA > Ag-BTPA > BTPA. These results are consistent with NH_3-TPD data. The Ni-BTPA membrane showed NH_3 permeance at ~2.8×10^{-6} and ~1.5×10^{-6} mol m^{-2} s^{-1} Pa^{-1} with ideal NH_3/H_2 selectivities of 11 and 27, and NH_3/N_2 selectivities of 102 and 277 at 200 and 50 °C, respectively. Intermolecular interaction energies and types between Ni-BTPA and NH_3 were calculated by Density functional theory and Independent gradient model based on Hirshfeld partition in order to uncover the affinity mechanism for NH_3. The results indicate that the interaction of Ni-BTPA with NH_3 is significantly enhanced *via* metal-induced coordination and hydrogen bonds and/or van der Waals interactions caused by *N-H*, *Si-OH*, and *N=O* functional groups.

Chapter 3 is "**Optimization of Ni-amine coordination for improving NH_3 permeation through nickel-doped bis[3-(trimethoxysilyl)propyl] amine membranes**". Nickel-coordinated bis[3-(trimethoxysilyl)propyl] amine (BTPA) xerogels and membranes reportedly showed excellent NH_3 adsorption, permeance, and permselectivity. To study the H_2, N_2, and NH_3 permeation properties of Ni-BTPA membranes in detail, the nickel doping amount in BTPA should be optimized. In this work, Ni-BTPA

sols/gels with nickel/propylamine (Ni/*N-H*) mole ratios of 0, 0.125, 0.25, 0.50, and 1.00 were prepared and characterized via DLS, FT-IR, UV-vis, TG-MS, and XRD, indicating that the sol size and the interactions between nickel and *N-H*/*N=O* were increased with an increase in the Ni/*N-H* mole ratio. The large NH_3 adsorption and desorption amounts were obtained with 0.50 and 1.00 Ni-BTPA xerogels via NH_3-TPD measurement, additionally, the competitive interactions between nickel and NH_3/other functional groups, such as *N-H* and *N=O*, were found in 1.00 Ni-BTPA, which could negatively affect the NH_3 affinity. The pore sizes of membranes were gradually enlarged in Ni-BTPA with increases in the nickel content, which improved gas permeation. Due to the enlargement of the pore size and the sufficient NH_3 affinity, the 0.50 Ni-BTPA membrane recorded the optimal performance with a NH_3 permeance of ~2.8×10^{-6} mol m^{-2} s^{-1} Pa^{-1}, an ideal NH_3/H_2 selectivity of 11, and NH_3/N_2 selectivity of 102 at 200 °C.

Chapter 4 is "**Development of sulfonated (3-Mercaptopropyl)trimethoxysilane membranes with thermal stability and excellent NH_3 perm-selectivity at 300 °C**". (3-Mercaptopropyl)trimethoxysilane (MPTMS) sols, xerogels, and membranes with and without H_2O_2 oxidation were prepared to improve NH_3 affinity and selectivity and is expected to be used in synthetic NH_3 catalytic membrane reactors due to its favorable high-temperature tolerance. Mercaptan (*S-H*) in MPTMS precursor can be completely oxidized to to transform *S=O* originated from various sulfur oxidization groups by mixing H_2O_2 to sol solution for enhancing NH_3 affinity, as proven by FT-IR and XPS analyses. Thermogravimetric mass spectrometer (TG-MS) and N_2 adsorption verified the thermal stability and non-porous structure of unoxidized and oxidated MPTMS

xerogels around 300 °C. Furthermore, NH_3 temperature-programmed desorption (NH_3-TPD) revealed that oxidated MPTMS xerogels showed a strong NH_3 affinity (NH_3 adsorption amount of ~1.41 mmol g^{-1}), twice higher than that of unoxidized MPTMS xerogels (0.75 mmol g^{-1}) owing to the strengthened acidity and increased acidic sites. Finally, oxidated MPTMS membranes expressed an excellent selectivity for NH_3/H_2 of 6 and NH_3/N_2 of 18 with an NH_3 permeance of ~1.4×10^{-7} mol m^{-2} s^{-1} Pa^{-1} at 300 °C for single gas permeation. NH_3 permeance and selectivity at 300 °C in NH_3/H_2 and NH_3/N_2 mixed gas permeation were almost constant without any mixing-effects, consistent with those in single gas permeation.

Chapter 5 is "**Fabrication of 3-(trihydroxysilyl)-1-propanesulfonic acid membranes with superior affinity and selectivity for NH_3 permeation over H_2 and N_2 at 50-300 °C**". The 3-(trihydroxysilyl)-1-propanesulfonic acid (TPS) was applied, for the first time, to fabricate sulfonic silica-based membranes and evaluated for NH_3 selective permeation. The amorphous siloxane network can be formed by simple condensation of silanol (*Si-OH*) under sulfonic acid (*-SO_3H*) self-catalysis, as confirmed by the results of Fourier transform infrared spectroscopy and X-Ray diffractometry. Moreover, TPS xerogel powders dried from TPS sols showed excellent thermal stability and dense structure via thermogravimetric and N_2 adsorption analyses. Importantly, an intensive NH_3 adsorption amount of ~3.0 mmol g^{-1} for TPS xerogels from NH_3 adsorption and temperature-programmed desorption was twice higher than the reported oxidized (3-mercaptopropyl)trimethoxysilane xerogels (~1.41 mmol g^{-1}), which was ascribed to the inherently stronger proton-acidic *-SO_3H* groups in TPS. Finally, TPS membranes

prepared using TPS solutions diluted with ethanol expressed superior NH_3-selective permeation based on favorable molecular sieving and NH_3 adsorption-diffusion via single and binary gas permeation, especially remarkable NH_3 permeance of ~2.6×10^{-7} mol m^{-2} s^{-1} Pa^{-1} and excellent NH_3/N_2 selectivity of 266 at 300 °C.

Chapter 6 is "**Green ammonia production via recycle membrane reactor: Experiment and process simulation**". With the increasing demand for ammonia (NH_3) and the environmental benefits, green and sustainable NH_3 production has been urgently developed and is expected to replace the traditional Haber-Bosch (HB) process with high energy consumption and CO_x emission. In this work, a recycle membrane reactor (RMR) process where a catalytic reactor relates to a membrane separator in series and the retentate stream is recycled to the reactor was designed and executed to produce NH_3, in which a Ru (10 wt%)/Cs/MgO catalyst and two membranes with different permeation properties and NH_3 selectivity were used. By independently controlling the temperature of the reactor and membrane separator, the synthesized NH_3 was selectively extracted from feed side to permeate side by Aquivion/ceramic composite and sulfonated (3-mercaptopropyl)trimethoxysilane membranes. Impressively, NH_3 mole fraction was greatly increased from 0.01 of equilibrium state to 0.1-0.45 in permeate stream, which is ascribed to the permeation properties and NH_3 selectivity of membrane at different temperatures. Moreover, a one-dimensional, isothermal, and plug-flow model was proposed to simulate RMR, which can be successfully applied to deeply understand the mechanism of RMR. Furthermore, a green NH_3 production process based on RMR was simulated to give rationalized suggestions for the NH_3 synthesis

under mild conditions.

Chapter 7 is “**Conclusions and outlook**”. Main conclusions presented in this thesis were summarized and outlook for future work were provided.

References

[1] The Haber-Bosch Process and the Development of Chemical Engineering. A Century of Chemical Engineering. New York: *Plenum Press. Appl, M.* (1982) 29-54. ISBN 978-0-306-40895-3.

[2] Global ammonia annual production capacity, https://www.statista.com/statistics/1065865/ammonia-production-capacity-globally/.

[3] U.S. Geological Survey, Mineral Commodity Summaries, NITROGEN (FIXED)-AMMONIA, January 2022. https://pubs.usgs.gov/periodicals/mcs2022/mcs2022-nitrogen.pdf.

[4] Tamaru K, (1991) in: J. R Jennings (Ed.). Catalytic Ammonia Synthesis. Plenum Press, New York, (Chapter 1).

[5] Poppy Puspitasari, Noorhana Yahya, Development of Ammonia Synthesis, IEEE, January 2012. DOI: 10.1109/NatPC.2011.6136449.

[6] A. Yapicioglu, I. Dincer, A review on clean ammonia as a potential fuel for power generators, *Renew. Sust. Energ. Rev.* 103 (2019) 96-108.

[7] S. Giddey, S.P.S. Badwal, C. Munnings, M. Dolan, Ammonia as a renewable energy transportation media, *ACS Sustainable Chem. Eng.* 5 (2017) 10231-10239.

[8] D.R. MacFarlane, P.V. Cherepanov, J. Choi, B.H.R. Suryanto, R.Y. Hodgetts, J.M. Bakker, F.M. F. Vallana, A.N. Simonov, A roadmap to the ammonia economy, *Joule* 4 (2020) 1186-1205.

[9] K.H.R. Rouwenhorst, A.S. Travis, L. Lefferts, 1921-2021: A century of renewable ammonia synthesis, *Sustain. Chem.* 3 (2022) 149-171.

[10] J. Humphreys, R. Lan, S. Tao, Development and recent progress on ammonia synthesis catalysts for Haber–Bosch process, *Adv. Energy Sustainability Res.* 2 (2021) 2000043.

[11] P. Yan, W. Guo, Z. Liang, W. Meng, Z. Yin, S. Li, M. Li, M. Zhang, J. Yan, D. Xiao, R. Zou, D. Ma, Highly efficient K-Fe/C catalysts derived from metal-organic frameworks towards ammonia synthesis, *Nano Res.* 12 (2019) 2341-2347.

[12] I. Temprano, T. Liu, S.J. Jenkins, Activity of iron pyrite towards low-temperature

ammonia production, *Catal. Today* 286 (2017) 101-113.

[13] G. Prieto, F. Schüth, The Yin and Yang in the development of catalytic processes: catalysis research and reaction engineering, *Angew. Chem. Int. Ed.* 54 (2015) 3222-3239.

[14] N. Saadatjou, A. Jafari, S. Sahebdelfar, Ruthenium nanocatalysts for ammonia synthesis: A review, *Chem. Eng. Commun.* 202 (2015) 420-448.

[15] V.S. Marakatti, E.M. Gaigneaux, Recent advances in heterogeneous catalyst for ammonia synthesis, *ChemCatChem* 12 (2020) 5838-5857.

[16] H.P. Jia, E. A. Quadrelli, Mechanistic aspects of dinitrogen cleavage and hydrogenation to produce ammonia in catalysis and organometallic chemistry: relevance of metal hydride bonds and dihydrogen, *Chem. Soc. Rev.* 43 (2014) 547-564.

[17] M. Kitano, Y. Inoue, H. Ishikawa, K. Yamagata, T. Nakao, T. Tada, S. Matsuishi, T. Yokoyama, M. Hara, H. Hosono, Essential role of hydride ion in ruthenium-based ammonia synthesis catalysts, *Chem. Sci.* 7 (2016) 4036-4043.

[18] Y. Inoue, M. Kitano, S.W. Kim, T. Yokoyama, M. Hara, H. Hosono, Highly dispersed Ru on electride $[Ca_{24}Al_{28}O_{64}]^{4+}(e^{-})_4$ as a catalyst for ammonia synthesis, *ACS Catal.* 4 (2014) 674-680.

[19] Z. Zhang, C. Karakaya, R.J. Kee, J. D. Way, C.A. Wolden, Barium-promoted ruthenium catalysts on yittria-stabilized zirconia supports for ammonia synthesis, *ACS Sustainable Chem. Eng.* 7 (2019) 18038-18047.

[20] J.S.J. Hargreaves, Heterogeneous catalysis with metal nitrides, *Coord. Chem. Rev.* 257 (2013) 2015-2031.

[21] M. Hattori, S. Iijima, T. Nakao, H. Hosono, M. Hara, Solid solution for catalytic ammonia synthesis from nitrogen and hydrogen gases at 50 °C, *Nat. Commun.* 11 (2020) 2001.

[22] Ammonia: zero-carbon fertilizer, fuel and energy store. February 2020 DES5711, The Royal Society. ISBN: 978-1-78252-448-9.

[23] Congressional Research Service. (7 December 2022). Ammonia's Potential Role in a Low-Carbon Economy. https://crsreports.congress.gov/product/pdf/IF/IF12273.

[24] A.G. Olabi, M.A. Abdelkareem, M. Al-Murisi, N. Shehata, A.H. Alami, A. Radwan, T. Wilberforce, K.J. Chae, E.T. Sayed, Recent progress in green ammonia: Production, applications, assessment; barriers, and its role in achieving the sustainable development goals, *Energ. Convers. Manage.* 277 (2023) 116594.

[25] S.C. D'Angelo, S. Cobo, V. Tulus, A. Nabera, A.J. Martín, J. Pérez-Ramírez, G. Guillén-Gosálbez, Planetary boundaries analysis of low-carbon ammonia production routes, *ACS Sustainable Chem. Eng.* 9 (2021) 9740-9749.

[26] P.W. Huang, M.C. Hatzell, Prospects and good experimental practices for photocatalytic ammonia synthesis, *Nat. Commun.* 13 (2022) 7908.

[27] O.A. Ojelade, S.F. Zaman, B.J. Ni, Green ammonia production technologies: A review of practical progress, *J. Environ. Manage.* 342 (2023) 118348.

[28] N. Salmon, R. Bañares-Alcántara, Green ammonia as a spatial energy vector: a review, *Sustain. Energ. Fuels* 5 (2021) 2814-2839.

[29] P. Arora, A.F.A. Hoadley, S.M. Mahajani, A. Ganesh, Small-scale ammonia production from biomass: A techno-enviro-economic perspective, *Ind. Eng. Chem. Res.* 55 (2016) 6422-6434.

[30] D. Yao, C. Tang, P. Wang, H. Cheng, H. Jin, L.X. Ding, S.Z. Qiao, Electrocatalytic green ammonia production beyond ambient aqueous nitrogen reduction, *Chem. Eng. Sci.* 257 (2022) 117735.

[31] J. Sousa, W. Waiblinger, K.A. Friedrich, Techno-economic study of an electrolysis-based green ammonia production plant, *Ind. Eng. Chem. Res.* 61 (2022) 14515-14530.

[32] R. Lan, J.T.S. Irvine, S. Tao, Synthesis of ammonia directly from air and water at ambient temperature and pressure, *Sci. Rep.-UK* 3 (2013) 1145. DOI: 10.1038/srep01145.

[33] H. Zhang, L. Wang, J. Van herle, F. Maréchal, U. Desideri, Techno-economic comparison of green ammonia production processes, *Appl. Energ.* 259 (2020) 114135.

[34] M. Wang, M.A. Khan, I. Mohsin, J. Wicks, Alexander H. Ip, K.Z. Sumon, C.T. Dinh, E.H. Sargent, I.D. Gates, M.G. Kibria, Can sustainable ammonia synthesis pathways compete with fossil-fuel based Haber-Bosch processes? *Energy Environ.*

Sci. 14 (2021) 2535-2548.

[35] C. Smith, A.K. Hill, L. Torrente-Murciano, Current and future role of Haber–Bosch ammonia in a carbon-free energy landscape, *Energy Environ. Sci.* 13 (2020) 331-344.

[36] B. Lee, L.R. Winter, H. Lee, D. Lim, H. Lim, M. Elimelech, Pathways to a green ammonia future, *ACS Energy Lett.* 7 (2022) 3032-3038.

[37] Green ammonia synthesis. *Nat. Synth*. 2 (2023) 581-582. https://doi.org/10.1038/s44160-023-00362-y

[38] Green Ammonia-Brighten two horizons at once, https://www.topsoe.com/processes/green-ammonia.

[39] A.G. Slater, A.I. Cooper, Function-led design of new porous materials, *Science* 348 (2015) 8075. DOI:10.1126/science.aaa8075.

[40] R.W. Baker, B.T. Low, Gas separation membrane materials: A perspective, *Macromolecules* 47 (2014) 6999-7013.

[41] Q. Qian, P.A. Asinger, M.J. Lee, G. Han, K.M. Rodriguez, S. Lin, F.M. Benedetti, A.X. Wu, W.S. Chi, Z.P. Smith, MOF-based membranes for gas separations, *Chem. Rev.* 120 (2020) 8161-8266.

[42] B.D. Freeman, Basis of permeability/selectivity tradeoff relations in polymeric gas separation membranes, *Macromolecules* 32 (1999) 375-380.

[43] A.R. Kamble, C.M. Patel, Z.V.P. Murthy, A review on the recent advances in mixed matrix membranes for gas separation processes, *Renew. Sust. Energ. Rev.* 145 (2021) 111062.

[44] H. Dou, M. Xu, B. Wang, Z. Zhang, G. Wen, Y. Zhen, D. Luo, L. Zhao, A. Yu, L. Zhang, Z. Jiang, Z. Chen, Microporous framework membranes for precise molecule/ion separations, *Chem. Soc. Rev.* 50 (2021) 986-1029.

[45] Y. Dai, Z. Niu, W. Luo, Y. Wang, P. Mu, J. Li, A review on the recent advances in composite membranes for CO_2 capture processes, *Sep. Purif. Technol.* 307 (2023) 122752.

[46] R.B. Lin, L. Li, H.L. Zhou, H. Wu, C. He, S. Li, R. Krishna, J. Li, W. Zhou,

B. Chen, Molecular sieving of ethylene from ethane using a rigid metal-organic framework, *Nat. Mater.* 17 (2018) 1128-1133.

[47] T. Ke, Q. Wang, J. Shen, J. Zhou, Z. Bao, Q. Yang, Q. Ren, Molecular sieving of C_2-C_3 alkene from alkyne with tuned threshold pressure in robust layered metal-organic frameworks, *Angew. Chem. Int. Ed.* 59 (2020) 12725-12730.

[48] Y. Liu, Z. Chen, G. Liu, Y. Belmabkhout, K. Adil, M. Eddaoudi, W. Koros, Conformation-controlled molecular sieving effects for membrane-based propylene/propane separation, *Adv. Mater.* 31 (2019) 1807513.

[49] D.V. Laciak, R. Quinn, G.P. Pez, J.B. Appleby, P.S. Puri, Selective permeation of ammonia and carbon dioxide by novel membranes, *Sep. Sci. Technol.* 25 (1990) 1295-1305.

[50] A. Bhown, E.L. Cussler, Mechanism for selective ammonia transport through poly(vinylammonium thiocyanate) membranes, *J. Am. Chem. Soc.* 113 (1991) 742-749.

[51] Y. He, E.L. Cussler, Ammonia permeabilities of perfluorosulfonic membranes in various ionic forms, *J. Membrane Sci.* 68 (1992) 43-52.

[52] V. Tricoli, E.L. Cussler, Ammonia selective hollow fibers, *J. Membrane Sci.* 104 (1995) 19-26.

[53] W.A. Phillip, E. Martono, L. Chen, M.A. Hillmyer, E.L. Cussler, Seeking an ammonia selective membrane based on nanostructured sulfonated block copolymers, *J. Membrane Sci.* 337 (2009) 39-46.

[54] I.V. Vorotyntsev, P.N. Drozdov, N.V. Karyakin, Ammonia permeability of a cellulose acetate membrane, *Inorg. Mater.* 42 (2006) 231-235.

[55] A. Raza, S. Farrukh, A. Hussain, Synthesis, characterization and NH_3/N_2 gas permeation study of nanocomposite membranes, *J. Polym. Environ.* 25 (2017) 46-55. DOI: 10.1007/s10924-016-0783-6.

[56] S. Yu, Y. Qin, Q. Zhao, M. Li, H. Yu, G. Kang, Y. Cao, Nafion-PTFE hollow fiber composite membranes for ammonia removal and recovery using an aqueous-organic membrane contactor, *Sep. Purif. Technol.* 271 (2021) 118856.

[57] C. Makhloufi, D. Roizard, E. Favre, Reverse selective NH_3/CO_2 permeation in

fluorinated polymers using membrane gas separation, *J. Membrane Sci.* 441 (2013) 63-72.

[58] J. Mi, W. Peng, Y. Luo, W. Chen, L. Lin, C. Chen, Q. Zhu, F. Liu, A. Zheng, L. Jiang, A Cationic polymerization strategy to design sulfonated micro-mesoporous polymers as efficient adsorbents for ammonia capture and separation, *Macromolecules* 54 (2021) 7010-7020.

[59] G. Barin, G.W. Peterson, V. Crocellà, J. Xu, K.A. Colwell, A. Nandy, J.A. Reimer, S. Bordig, J.R. Long, Highly effective ammonia removal in a series of Brønsted acidic porous polymers: investigation of chemical and structural variations, *Chem. Sci.* 8 (2017) 4399-4409.

[60] Z. Han, Y. Xu, H. Tian, J. Liang, D. Sun, Enhanced ammonia adsorption and separation by a molecularly imprinted polymer after acid hydrolysis of its ester cross-linker, *J. Hazard. Mater.* 412 (2021) 125145.

[61] Q. Wei, J.M. Lucero, J.M. Crawford, J. Douglas Way, C.A. Wolden, M.A. Carreon, Ammonia separation from N_2 and H_2 over LTA zeolitic imidazolate framework membranes, *J. Membrane Sci.* 623 (2021) 119078.

[62] X. Duan, D. Kim, K. Narasimharao, S. Al-Thabaiti, M. Tsapatsis, High-performance ammonia-selective MFI nanosheet membranes, *Chem. Commun.* 57 (2021) 580-582.

[63] D.I. Petukhov, A.S. Kan, A.P. Chumakov, O.V. Konovalov, R.G. Valeev, A.A. Eliseev, MXene-based gas separation membranes with sorption type selectivity, *J. Membrane Sci.* 621 (2021) 118994.

[64] M.A. Komkova, I.S. Sadilov, V.A. Brotsman, D.I. Petukhov, A.A. Eliseev, Facilitated transport of ammonia in ultra-thin Prussian Blue membranes with potential-tuned selectivity, *J. Membrane Sci.* 639 (2021) 119714.

[65] S. Padinjarekutt, B. Sengupta, H. Li, K. Friedman, D. Behera, R. Lecaros, M. Yu, Synthesis of Na^+-gated nanochannel membranes for the ammonia (NH_3) separation, *J. Membrane Sci.* 674 (2023) 121512.

[66] K. Vikrant, V. Kumar, K.H. Kim, D. Kukkar, Metal–organic frameworks (MOFs): potential and challenges for capture and abatement of ammonia, *J. Mater. Chem. A*

5 (2017) 22877-22896.

[67] J. Liu, Z. Chen, R. Wang, S. Alayoglu, T. Islamoglu, S.J. Lee, T.R. Sheridan, H. Chen, R.Q. Snurr, O.K. Farha, J.T. Hupp, Zirconium metal−organic frameworks integrating chloride ions for ammonia capture and/or chemical separation, *ACS Appl. Mater. Interfaces* 13 (2021) 22485-22494.

[68] X. Wang, Z. Liu, G. Li, G. Jiang, Y. Zhao, L. Li, K. Li, G. Liang, S. Gao, H. Xi, S. Li, R. Zou, High-efficiency capture of ammonia using hierarchically porous Zr-MOF nanoarchitectures under ambient conditions: Thermodynamics, kinetics, and mechanisms, *Chem. Eng. J.* 440 (2022) 135764.

[69] Z. Wang, Z. Li, X.G. Zhang, Q. Xia, H. Wang, C. Wang, Y. Wang, H. He, Y. Zhao, J. Wang, Tailoring multiple sites of metal−organic frameworks for highly efficient and reversible ammonia adsorption, *ACS Appl. Mater. Interfaces* 13 (2021) 56025-56034.

[70] B. Yang, L. Bai, T. Li, L. Deng, L. Liu, S. Zeng, J. Han, X. Zhang, Super selective ammonia separation through multiple-site interaction with ionic liquid-based hybrid membranes, *J. Membrane Sci.* 628 (2021) 119264.

[71] B. Yang, L. Bai, S. Zeng, S. Luo, L. Liu, J. Han, Y. Nie, X. Zhang, S. Zhang, NH_3 separation membranes with self-assembled gas highways induced by protic ionic liquids, *Chem. Eng. J.* 421 (2021) 127876.

[72] B. Yang, L. Bai, Z. Wang, H. Jiang, S. Zeng, X. Zhang, X. Zhang, Exploring NH_3 transport properties by tailoring ionic liquids in Pebax-based hybrid membranes, *Ind. Eng. Chem. Res.* 60 (2021) 9570-9577.

[73] L. Zhang, H. Dong, S. Zeng, Z. Hu, S. Hussain, X. Zhang, An overview of ammonia separation by ionic liquids, *Ind. Eng. Chem. Res.* 60 (2021) 6908-6924.

[74] S. Zeng, Y. Cao, P. Li, X. Liu, X. Zhang, Ionic liquid-based green processes for ammonia separation and recovery, *Curr. Opin. Green Sust.* 25 (2020) 100354.

[75] L. Luo, Z. Wu, Z. Wu, Y. Liu, X. Huang, R. Ling, L. Ye, X. Luo, C. Wang, Role of structure in the ammonia uptake of porous polyionic liquids, *ACS Sustainable Chem. Eng.* 10 (2022) 4094-4104.

[76] Q. Luo, Q. Wang, X. Sun, H. Wu, J. Hao, L. Wei, S. Zhai, Z. Xiao, Q. An, Dual-

active-sites deep eutectic solvents based on imidazole and resorcinol for efficient capture of NH_3, *Chem. Eng. J.* 416 (2021) 129114.

[77] B. Liu, J. Tian, Investigation of glycolic acid natural deep eutectic solvents with strong proton donors for ammonia capture and separation, *Ind. Eng. Chem. Res.* 60 (2021) 11600-11610.

[78] N.N. Cheng, Z.L. Li, H.C. Lan, W.L. Xu, W.J. Jiang, K. Huang, H.L. Peng, Deep eutectic solvents with multiple weak acid sites for highly efficient, reversible and selective absorption of ammonia, *Sep. Purif. Technol.* 269 (2021) 118791.

[79] K. Li, K. Zong, Z. Zhou, D. Deng, Highly efficient absorption and separation of NH_3 by simple lithium deep eutectic solvents, *Sep. Purif. Technol.* 279 (2021) 119763.

[80] Y. Cao, J. Zhang, Y. Ma, W. Wu, K. Huang, L. Jiang, Designing low-viscosity deep eutectic solvents with multiple weak-acidic groups for ammonia separation, *ACS Sustainable Chem. Eng.* 9 (2021) 7352-7360.

[81] X. Ren, T. Tsuru, Organosilica-based membranes in gas and liquid-phase separation, *Membranes* 9 (2019) 107. Doi: 10.3390/membranes9090107.

[82] G. Gong, H. Nagasawa, M. Kanezashi, T. Tsuru, Tailoring the separation behavior of polymer-supported organosilica layered-hybrid membranes via facile post-treatment using HCl and HN_3 vapors, *ACS Appl. Mater. Interfaces* 8 (2016) 11060-11069.

[83] M. Kanezashi, T. Sasaki, H. Tawarayama, H. Nagasawa, T. Yoshioka, K. Ito, T. Tsuru, Experimental and theoretical study on small gas permeation properties through amorphous silica membranes fabricated at different temperatures, *J. Phys. Chem. C* 118 (2014) 20323-20331.

[84] M. Kanezashi, R. Matsugasako, H. Tawarayama, H. Nagasawa, T. Yoshiok, T. Tsuru, Tuning the pore sizes of novel silica membranes for improved gas permeation properties via an in-situ reaction between NH_3 and Si-H groups, *Chem. Commun.* 51 (2015) 2551-2554.

[85] G. Li, H.R. Lee, H. Nagasawa, M. Kanezashi, T. Yoshioka, T. Tsuru, Pore-size evaluation and gas transport behaviors of microporous membranes: An

experimental and theoretical study, *AIChE J.* 61 (2015) 2268-2279.

[86] M. Kanezashi, Y. Yoneda, H. Nagasawa, T. Tsuru, K. Yamamoto, J. Ohshita, Gas permeation properties for organosilica membranes with different Si/C ratios and evaluation of microporous structures, *AIChE J.* 63 (2017) 4491-4498.

[87] M. Kanezashi, T. Matsutani, T. Wakihara, H. Tawarayama, H. Nagasawa, T. Yoshioka, T. Okubo, T. Tsuru, Tailoring the subnano silica structure via fluorine doping for development of highly permeable CO_2 separation membranes, *ChemNanoMat* 2 (2016) 264-267.

[88] L. Yu, M. Kanezashi, H. Nagasawa, J. Oshita, A. Naka, T. Tsuru, Pyrimidine-bridged organoalkoxysilane membrane for high-efficiency CO_2 transport via mild affinity, *Sep. Purif. Tech.* 178 (2017) 232-241.

[89] N. Moriyama, H. Nagasawa, M. Kanezashi, K. Ito, T. Tsuru, Bis(triethoxysilyl)ethane (BTESE)-derived silica membranes: pore formation mechanism and gas permeation properties, *Journal of Sol-Gel Science and Technology* 86 (2018) 63-72.

[90] X. Yu, H. Nagasawa, M. Kanezashi, T. Tsuru, Improved thermal and oxidation stability of bis(triethoxysilyl)ethane (BTESE)-derived membranes, and their gas-permeation properties, *J. Mater. Chem. A* 6 (2018) 23378-23387.

[91] M. Guo, M. Kanezashi, H. Nagasawa, L. Yu, K. Yamamoto, T. Gunji, J. Ohshita, T. Tsuru, Tailoring the microstructure and permeation properties of bridged organosilica membranes via control of the bond angles, *J. Membrane Sci.* 584 (2019) 56-65.

[92] M. Guo, M. Kanezashi, H. Nagasawa, L. Yu, K. Yamamoto, T. Gunji, T. Tsuru, Fine-tuned, molecular-composite, organosilica membranes for highly efficient propylene/propane separation via suitable pore size, *AIChE J.* 66 (2020) e16850.

[93] X. Ren, K. Nishimoto, M. Kanezashi, H. Nagasawa, T. Yoshioka, T. Tsuru, CO_2 permeation through hybrid organosilica membranes in the presence of water vapor, *Ind. Eng. Chem. Res.* 53 (2014) 6113-6120.

[94] K. Yamamoto, J. Ohshita, T. Mizumo, M. Kanezashi, T. Tsuru, Synthesis of organically bridged trialkoxysilanes bearing acetoxymethyl groups and applications to

reverse osmosis membranes, *Appl. Organometal. Chem.* 31 (2017) e3580.

[95] L. Yu, M. Kanezashi, H. Nagasawa, Toshinori Tsuru, Role of amine type in CO_2 separation performance within amine functionalized silica/organosilica membranes: A review, *Appl. Sci.* 8 (2018) 1032.

[96] L. Yu, M. Kanezashi, H. Nagasawa, T. Tsuru, Fabrication and CO_2 permeation properties of amine-silica membranes using a variety of amine types, *J. Membrane Sci.* 541 (2017) 447-456.

[97] U. Anggarini, L. Yu, H. Nagasawa, M. Kanezashi, T. Tsuru, Metal-induced microporous aminosilica creates a highly permeable gas-separation membrane, *Mater. Chem. Front*. 5 (2021) 3029-3042.

[98] U. Anggarini, L. Yu, H. Nagasawa, M. Kanezashi, T. Tsuru, Microporous nickel-coordinated aminosilica membranes for improved pervaporation performance of methanol/toluene, *ACS Appl. Mater. Interfaces* 13 (2021) 23247-23259.

[99] T. Tsuru, Silica-based membranes with molecular-net-sieving properties: Development and applications, *Journal of chemical engineering of Japan* 51 (2018) 713-725.

[100] M. Kanezashi, A. Yamamoto, T. Yoshioka, T. Tsuru, Characteristics of ammonia permeation through porous silica membranes, *AIChE J.* 56 (2010) 1204-1212.

[101] H. Nagasawa, Y. Yamamoto, N. Tsuda, M. Kanezashi, T. Yoshioka, T. Tsuru, Atmospheric-pressure plasma-enhanced chemical vapor deposition of microporous silica membranes for gas separation, *J. Membrane Sci.* 524 (2017) 644-651.

[102] J. Xu, H. Nagasawa, M. Kanezashi, T. Tsuru, UV-protective TiO_2 thin films with high transparency in visible light region fabricated via atmospheric-pressure plasma-enhanced chemical vapor deposition, *ACS Appl. Mater. Interfaces* 10 (2018) 42657-42665.

[103] N. Moriyama, H. Nagasawa, M. Kanezashi, T. Tsuru, Improved performance of organosilica membranes for steam recovery at moderate-to-high temperatures via the use of a hydrothermally stable intermediate layer, *J. Membrane Sci.* 620 (2021) 118895.

[104] X. Yu, L. Meng, T. Niimi, H. Nagasawa, M. Kanezashi, T. Yoshioka, T. Tsuru,

Network engineering of a BTESE membrane for improved gas performance via a novel pH-swing method, *J. Membrane Sci.* 511 (2016) 219-227.

[105] F.T. Zheng, K. Yamamoto, M. Kanezashi, T. Gunji, T. Tsuru, J. Ohshita, Preparation of hybrid organosilica reverse osmosis membranes by interfacial polymerization of bis[(trialkoxysilyl)propyl]amine, *Chemistry Letters* 47 (2018) 1210-1212.

[106] G. Gong, H. Nagasawa, M. Kanezashi, T. Tsuru, Facile and scalable flow-induced deposition of organosilica on porous polymer supports for reverse osmosis desalination, *ACS Appl. Mater. Interfaces* 10 (2018) 14070-14078.

[107] H. Nagasawa, M. Nishibayashi, M. Kanezashi, T. Yoshioka, T. Tsuru, Photo-induced sol-gel synthesis of polymer-supported silsesquioxane membranes, *RSC Adv.* 7 (2017) 7150-7157.

[108] K. Wakimoto, W.W. Yan, N. Moriyama, H. Nagasawa, M. Kanezashi, T. Tsuru, Ammonia permeation of fluorinated sulfonic acid polymer/ceramic composite membranes, *J. Membrane Sci.* 658 (2022) 120718.

[109] L. Paturzo, A. Basile, E. Drioli, High temperature membrane reactors and integrated membrane operations, *Rev. Chem. Eng.* 18 (2002) 511-552.

[110] L. Meng, M. Kanezashi, T. Tsuru, Catalytic membrane reactors for SO_3decomposition in Iodine-Sulfur thermochemical cycle: A simulation study, *Int. J. Hydrogen Energ.* 40 (2015) 12687-12696.

[111] S. Battersby, M.C. Duke, S. Liu, V. Rudolph, J.C. Diniz da Costa, Metal doped silica membrane reactor: Operational effects of reaction and permeation for the water gas shift reaction, *J. Membrane Sci.* 316 (2008) 46-52.

[112] T. Tsuru, K. Yamaguchi, T. Yoshioka, M. Asaeda, Methane steam reforming by microporous catalytic membrane reactors, *AIChE J.* 50 (2004) 2794-2805.

[113] K. Akamatsu, T. Murakami, T. Sugawara, R. Kikuchi, S.I. Nakao, Reforming in membrane reactors with hydrogen-selective silica membranes, *AIChE J.* 57 (2011) 1882-1888.

[114] Z. Tang, S.J. Kim, G.K. Reddy, J. Dong, P. Smirniotis, Modified zeolite membrane reactor for high temperature water gas shift reaction, *J. Membrane Sci.* 354

(2010) 114-122.

[115] S.J. Kim, Z. Xu, G.K. Reddy, P. Smirniotis, J. Dong, Effect of pressure on high-temperature water gas shift reaction in microporous zeolite membrane reactor, *Ind. Eng. Chem. Res.* 51 (2012) 1364-1375.

[116] Y. Zhang, Z. Wu, Z. Hong, X. Gu, N. Xu, Hydrogen-selective zeolite membrane reactor for low temperature water gas shift reaction, *Chem. Eng. J.* 197 (2012) 314-321.

[117] L. Meng, X. Yu, T. Niimi, H. Nagasawa, M. Kanezashi, T. Yoshioka, T. Tsuru, Methylcyclohexane Dehydrogenation for hydrogen production via a bimodal catalytic membrane reactor, *AIChE J.* 61 (2015) 1628-1638.

[118] Y.R. Chen, T. Tsuru, D.Y. Kang, Simulation and design of catalytic membrane reactor for hydrogen production via methylcyclohexane dehydrogenation, *Int. J. Hydrogen Energ.* 42 (2017) 26296-26307.

[119] X. Yu, L. Meng, H. Nagasawa, M. Kanezashi, M. Machida, T. Tsuru, Evaluating the chemical stability of metal oxides in SO_3 and applications of SiO_2-based membranes to O_2/SO_3 separation, *J. Am. Ceram. Soc.* 102 (2019) 6946-6956.

[120] G. Li, M. Kanezashi, H.R. Lee, M. Maeda, T. Yoshioka, T. Tsuru, Preparation of a novel bimodal catalytic membrane reactor and its application to ammonia decomposition for CO_x-free hydrogen production, *Int. J. Hydrogen Energ.* 37 (2012) 12105-12113.

[121] G. Li, M. Kanezashi, T. Yoshioka, T. Tsuru, Ammonia decomposition in catalytic membrane reactors: Simulation and experimental studies, *AIChE J.* 59 (2013) 168-179.

[122] M. Lie, T. Tsuru, Microporous membrane reactors for hydrogen production, *Curr. Opin. Chem. Eng.* 8 (2015) 83-88.

Chapter 2

Enhanced NH_3 permeation of bis[3-(trimethoxysilyl)propyl] amine membranes *via* coordination with metals

2.1 Introduction

Ammonia (NH_3) is synthesized industrially from N_2 and H_2 via the Haber-Bosch process at temperatures ranging from 400-500 °C and under pressures ranging from 20-40 MPa, and 80% of produced NH_3 is used in fertilizer production and chemicals. [1] At present, NH_3 is also promising as an energy carrier that can be used to store hydrogen (storage capacity of 17.6 wt% and storage density of 108 g L^{-1}). [2] Green NH_3, that is produced by N_2 separated from air and H_2 obtained from sustainable H_2O electrolysis, currently is attracting much attention, but the reversible NH_3 synthesis reaction with limited conversion (10-20%) even under harsh conditions, which increases the difficulty of NH_3 separation and utilization. [3] Therefore, the separation and purification technologies for various mixtures of NH_3 have been widely studied, particularly the reversible adsorption-desorption and membrane separation techniques. [4-6]

It has been reported that adding NH_3 affinity sites on the matrix surface can effectively increase the adsorption rate and capacity for gas molecules. [7-9] The surfaces of most polymer membranes have oxygen-containing and polar functional groups, either self-contained or functionalized, and tend to exhibit moderate NH_3 permeance and selectivity through hydrogen bond for improving NH_3 affinity and solubility. [10-12] Additionally, polar-polar interactions of the linker polar channels in zeolite on NH_3 greatly improve NH_3 diffusivity. [13] Generally, operating conditions under low temperature and

high pressure are beneficial to NH_3 adsorption on the membrane surface as well as to permeation-driving forces, resulting in increasing the NH_3 separation potential of the membrane. [14] Aquivion-Li^+/ceramic composite membrane showed high NH_3 permeance of 1.88×10^{-6} mol m^{-2} s^{-1} Pa^{-1} with comparable NH_3/H_2 and NH_3/N_2 selectivity of 44.7 and 466 at 50 °C, respectively. At 200 °C, however, those values are greatly decreased to 9.05×10^{-7} mol m^{-2} s^{-1} Pa^{-1} with NH_3/H_2 and NH_3/N_2 selectivity of 2 and 22, respectively. [15] Since NH_3 reaction requires high temperature, achieving NH_3 permselectivity through membranes at high temperatures (~200 °C) will undoubtedly extend membrane applications, such as membrane reactors, which combine reaction and separation into one unit to enhance the limited equilibrium reaction.

Importantly, metal is expected to play an important role in NH_3 affinity, which is similar to that of carbon dioxide (CO_2) [16,17]. Metal oxides [18], metal-containing ionic liquids [19,20], metal-organic framework [21], and metal-doped perfluorosulfonic acid (PFSA) [22] were used to selectively separate NH_3 from other gases by Lewis acid, coordination, charge-transfer, and hydrogen bond. The elaborate modification strategies, such as incorporating metal ionic liquids/metal halide into silica gels [23,24] and integrating chloride ions into Zr-MOF [25], have been applied to disperse the metal evenly among the ligands to better exploit the affinity of the metal to NH_3. Although to use metal-containing compounds for reversible adsorption-desorption of NH_3 is promising, [26,27] the separation process using metals has been focused on adsorption, that require batch-wise operation, lacks some convenience compared to membrane separation that can be operated continuously.

Bis[3-(trimethoxysilyl)propyl] amine (BTPA) has been reported to anchor transition metals by coordination between the donor pairs of electrons in the amine and the empty *d* orbital in the transition metals, [28] which also reportedly improves CO_2 permeance in the membrane. Similarly, the adsorption, diffusion, and permselectivity of NH_3 as a polar gas in BTPA-based membranes is expected to increase. Particularly, exploring the interaction types and strengths between NH_3 and metal-doped BTPA by density functional theory (DFT) and molecular dynamics could provide a theoretical basis for subsequent development in excellent metal-doped ligand membranes. [29,30]

Herein, the undoped and metal-doped BTPA sols and xerogels are characterized *via* FT-IR, TG-MS, XRD, and NH_3-TPD to elucidate the role of metals in the BTPA structure. Undoped BTPA, Fe-, Ni-, and Ag-doped BTPA membranes were fabricated to measure the gas permeance and NH_3 permselectivity, indicating excellent performance at 200 °C, superior to PSFA-based membranes. Finally, the interaction types and intensities between NH_3 and Ni-doped BTPA were calculated by DFT and Independent gradient model based on Hirshfeld partition (IGMH).

2.2 Experimental and computational

2.2.1 Sol preparation and membrane fabrication

Details of sol preparation and membrane fabrication can be found elsewhere. [28] Briefly, the BTPA-based sols were prepared *via* the sol-gel method, including hydrolysis, condensation, and coordination reactions, using BTPA precursors, metal nitrate, H_2O, and HNO_3 or HCl as the catalyst in ethanol. Firstly, the mixture of HNO_3 (or HCl) and water was added to BTPA dissolved in ethanol that had been mixed in advance and

stirred continuously. After stirring at room temperature for 12 h, the BTPA-derived sols, that are BTPA (HNO_3) and BTPA (HCl), were obtained. To prepare the metal-doped BTPA sol (BTPA/H_2O/HNO_3/metal nitrate = 1/300/1/0.5), $Fe(NO_3)_3 \cdot 9H_2O$, $Co(NO_3)_2 \cdot 6H_2O$, $Ni(NO_3)_2.6H_2O$, $Cu(NO_3)_2 \cdot 3H_2O$, or $AgNO_3$ was added into the BTPA sol at ambient temperature and stirred for 1 h; each sol was labelled as Fe-BTPA, Co-BTPA, Ni-BTPA, Cu-BTPA, and Ag-BTPA, respectively. The concentration of BTPA precursor in each of the sol solutions was maintained at 5 wt% using ethanol, and the synthetic sols were finally diluted to 0.1 wt% with H_2O for membrane fabrication.

The α-alumina particles (0.2 and 2 μm) dispersed in 2 wt% SiO_2-ZrO_2 sol were coated on the surface of porous α-alumina tubes (length: 100 mm, average pore size: 1 μm, porosity: 50%, kindly supplied by Nikkato Cor. (Japan) as the support) to decrease the pore size, and then calcined at 550 °C for 15 min. This process was repeated 3-4 times to cover all the macropores of the porous α-alumina tube. Thereafter, 0.5 wt% SiO_2-ZrO_2 sol was further coated on the particle layers and calcined at 550 °C for 15 min to obtain the intermediate layer with a pore size of approximately 1 nm. Finally, the top separation layer was constructed with BTPA and metal-doped BTPA sol (diluted to 0.1 wt% using H_2O), followed by calcination at 150 °C for 30-40 min under a N_2 atmosphere. Pure BTPA membranes were fabricated, in addition to 150 °C, at 200 and 250 °C that were marked as BTPA (200) and BTPA (250), respectively.

2.2.2 Characterization

The colloidal sizes of the BTPA and metal-doped BTPA sols were analysed using a Malvern Zetasizer (ZEN 3600) with dynamic light scattering (DLS). The obtained sols were coated onto KBr plates and then calcined at different temperatures under a N_2 atmosphere to detect the chemical structures and the thermal stability by a Fourier transform infrared spectrometer (FT-IR-4100, JASCO, Japan). The BTPA-based xerogel powders that were calcined at different temperature under a N_2 atmosphere were characterized by an X-Ray diffractometer (XRD) D2 PHASER (Bruker, Germany) with Cu-Kα radiation in a 2θ range of from 5 to 80º. A thermogravimetric mass spectrometer (TG-MS, TGA-DTA-PIMS 410/S, Rigaku, Japan) was used to detect the thermal properties of the BTPA-based xerogel powders. The NH_3 temperature-programmed desorption (NH_3-TPD) of the xerogel powders was measured using a BELCAT-AT with BELMASS-HT (BELL Cor., Japan) from 50 to 150 °C, and the details of the program as well as the time courses of the mass signals and temperatures are summarized in the Supplementary Material (SI-1). The xerogel powders were pre-calcined at 150 °C under a N_2 atmosphere and thereafter evacuated at 130 °C under vacuum conditions for 12 h and were then used for the N_2 sorption measurement (BELMAX Inc., Japan).

2.2.3 Single- and binary-gas permeation measurement

High-purity single components of He, H_2, NH_3, N_2, and CH_4 were fed into the outside of the membrane at upstream pressures of 50-300 kPa, whereas the permeate stream was maintained at atmospheric pressure. The experimental apparatus is schematically depicted in Fig. 2-S2. Before the gas permeation test, the membrane was pre-treated under a He flow at 150 °C overnight to remove the molecules adsorbed in the membrane,

especially H_2O. The permeation test was performed at temperatures ranging from 200 to 50 °C. When the permeation reached a steady state, the film-flow meter (Horiba, Co. Ltd., Japan) was used to measure the flow rate data of gases, except for NH_3, but the flow rate of NH_3 was measured using a mass-flow meter (Horiba, Co. Ltd., Japan) calibrated via binary measurement (NH_3/H_2 and NH_3/N_2) from a gas chromatograph (GC). Furthermore, the permeance of binary gas, equimolar NH_3/N_2 and NH_3/H_2 mixtures under a constant NH_3 flow rate of 600 ml min^{-1}, was measured using a feed side pressure of 250 kPa and an permeate pressure maintained at atmosphere. The NH_3 and H_2 (or N_2) concentrations were analyzed using Ar as the carrier gas in two gas chromatographs, which are equipped with a Porapack N column (GC-1) and a Molecular Sieve X column (GC-2), respectively. The film-flow meter was used to measure the H_2 and N_2 flow rates in the permeate side after absolving NH_3 in water for the removal. The NH_3 permeate flow rate was measured using a calibrated mass flow controller by closing the retentate valve and allowing all feed to permeate.

According to the H_2, N_2, and NH_3 perameance from 200 to 50 °C, the activation energies of H_2, N_2, and NH_3 were calculated based on the slope of the regression curve obtained by using the following equation, which was derived from the modified gas translation (m-GT) model. [31,32]

$$P_i = \frac{k_{0,i}}{\sqrt{M_i RT}} exp\left(-\frac{E_{P,i}}{RT}\right)$$

P_i: permeance; M_i: molecular weight; R: gas constant; $E_{P,i}$: activation energy of permeation; $k_{0,i}$:permeation constant.

2.2.4 DFT calculation

The interaction between NH_3 and metal-doped BTPA is discussed using DFT calculation. Although the structure of BTPA contains methoxy groups, methoxy groups are hydrolyzed to form silanol group after hydrolysis and condensation, so hydroxyl groups are used instead of methoxy groups (SI-3), which can also reduce the computational burden. The structures of H_2, N_2, NH_3, Ni, and the redefined BTPA were drawn with GaussView 05 software and optimized by Gaussian 09 D.01 program [33] together with the TPSSh-D3(BJ) [34] method and the mixed basis set that SDD and 6-311g* were adopted to calculate nickel and other ligands, respectively. The frequency calculation was carried out after the geometric optimization at the same theoretical level to ensure that the obtained minimal point contains no imaginary frequency and then the def2-TZVP [35] basis set was used to calculate the single point energies.

According to the above-obtained *.fchk* file generated from vibration analysis, IGMH [36] was applied to analyze the interaction types between Ni-BTPA and NH_3 via Multiwfn [37] and visualized via Visual molecular dynamics (VMD) [38].

2.3 Results and discussions

2.3.1 Role of metal in the BTPA structure

As shown in SI-4, the size of the metal-doped BTPA sol is larger than that of the BTPA sol, which indicates that the added metal can grow the sol structure due to the coordination between metal and amine moiety in BTPA by the charge-transfer.

The FT-IR spectrum of metal-coordinated BTPA films pretreated with N_2 at different temperatures are shown in Fig. 2-1. The intensity of the characteristic peak of *Si-O-Si* increases while that of *Si-OH* (895 cm^{-1}) decreases as raising the calcination

temperature, which indicates that high temperature can induce *Si-OH* groups to transform *Si-O-Si* framework. [39] Although the retained *Si-OH* could fill the pore structure and impede the permeation of gas molecules, they, as a polar functional group, could be beneficial to increase affinity for polar molecules, such as NH_3. Additionally, the characteristic peak of *N=O* (1385 cm^{-1}) remained in all samples even at 250 °C, implying that *N=O* can be reserved in the BTPA matrix to potentially improve the NH_3 affinity by acid-base interactions. The intensity of the characteristic peak of *N-H* (1585 cm^{-1}) was mildly decreased with increasing the calcination temperature.

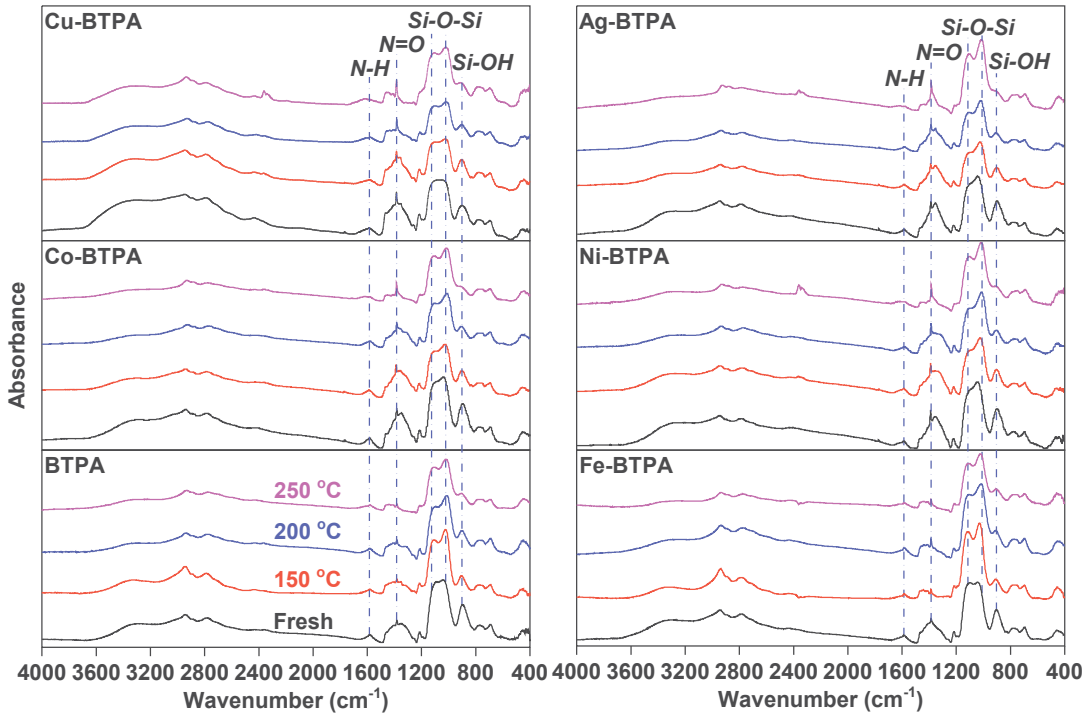

Fig. 2-1. FT-IR spectra of undoped BTPA and various metal-doped BTPA films.

As exhibited in Fig. 2-2, as the temperature increase to 250 °C, the characteristic peak of *N-H* functional group was significantly split and shifted to high wavenumber (blue-shift), which is consistent with previous results [28]. Since sol-gel synthesis is a dynamic process, the water and acid as catalyst in the sol could be removed with higher

temperature, which could improve the interaction type/intensity between *N-H* and metals/other functional groups, particularly the coordination between *N-H* and metals due to the apparent splitting of *N-H* peak in metal-doped BTPA sols compared with that in a BTPA sol.

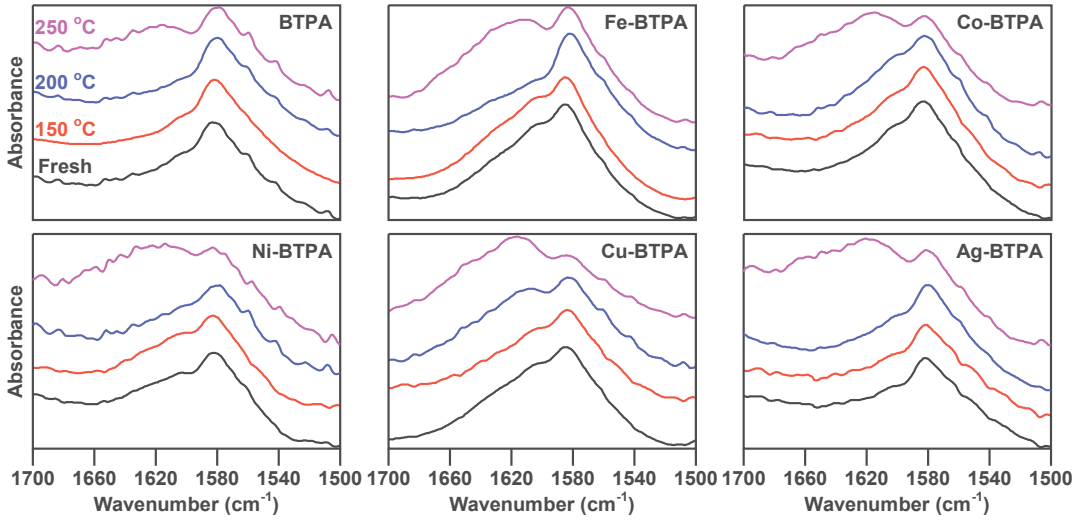

Fig. 2-2. The narrow FT-IR spectra of the *N-H* deformation band ranging from 1700-1500 cm^{-1}.

2.3.2 TG-MS analysis

As displayed in Fig. 2-3, the weight-loss at temperatures higher than 700 °C of BTPA prepared with HCl and HNO_3 as a catalyst are similar, albeit with different weight-loss stages. The m/z=35 could be attributed to chlorine (Cl) for BTPA prepared with HCl. Although it is difficult to categorically assign m/z=35 to a specific weight-loss stages, the removal of chlorine should be mainly ascribed to stage c, suggesting BTPA prepared by HCl has a higher initial decomposition temperature, which is probably due to the formation of stable composites, such as -NH^+Cl^-.

Based on the m/z=30 fragment peaks in Figs. 2-3 (b) and (c), the characteristic peak 3 at high temperature could be attributed to the decomposition of the main body of

BTPA, namely the breakage of the alkyl-amine molecules. [40] Furthermore, peaks 1 and 2 at lower temperature could be ascribed to *N=O* from HNO_3, consistent with the fact that the chlorine decomposes at a higher temperature than *N=O*. As indicate in Figs. 2-3 (d) and (e), the decomposition temperature of *N=O* in $Ni(NO_3)_2$-derived powders, that was dissolved in H_2O and then dried to powder, was slightly lower than that of fresh $Ni(NO_3)_2 \cdot 6H_2O$ probably due to the amorphous structure. Furthermore, because the characteristic peak of *N=O* observed in $Ni(NO_3)_2$-derived powders was shifted to a higher temperature at peak 2 in BTPA (HNO_3), indicating that peak 2 could belong to the coordinated *N=O* (stage b) that have coordination and/or hydrogen bonds with metals/other functional groups, which could be also assigned to the hydrogen bond between *N=O* and *N-H* in BTPA (HNO_3). Therefore, peak 1 should be attributed to the free *N=O* that possible physical adsorbs to BTPA gels located in stage a.

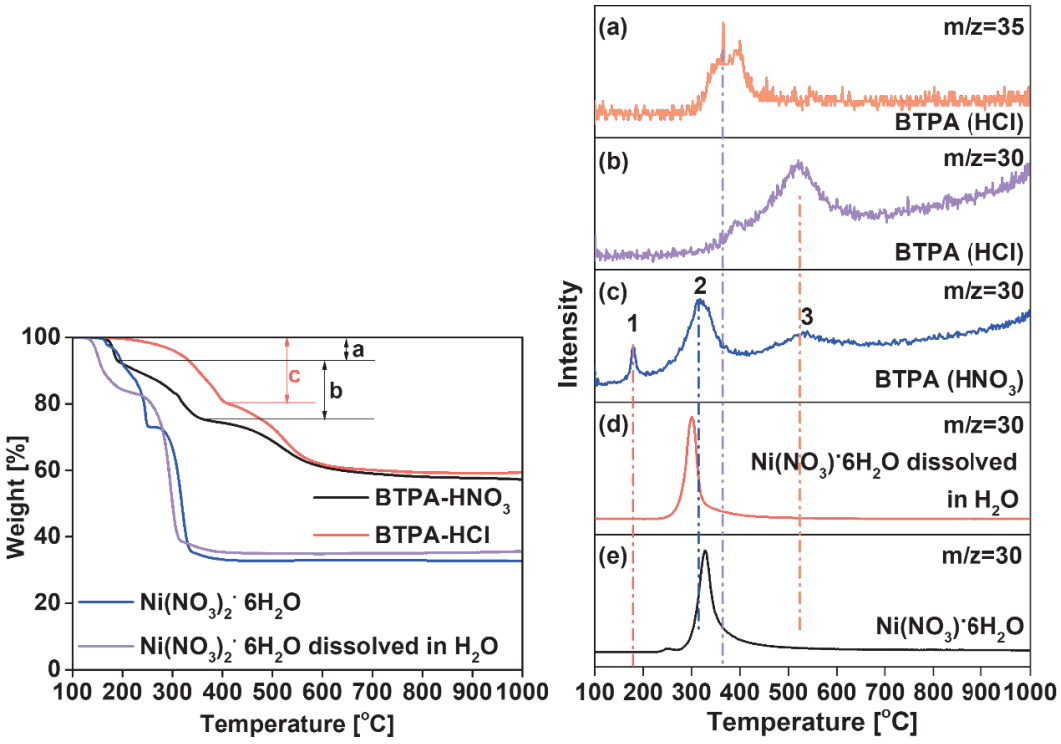

Fig. 2-3. TG-MS analysis of BTPA prepared using HNO_3 and HCl (left); the mass signal of m/z = 30 and m/z = 35 in BTPA prepared using HCl and HNO_3 as a function of

thermal treatment (right).

As demonstrated in Fig. 2-4 (left), although adding metal to BTPA increased the sol size (SI-4), the total weight-loss of all BTPA-based powders was similar without a clearly negative effect. According to the TG-MS analysis of BTPA prepared with HNO_3 and HCl, the characteristic peaks at lower and higher temperatures in the signal curve of m/z=30 could be ascribed to the ion fragments of *N=O* and alkyl-amine molecules, respectively. Peak 1 that belonged to the free *N=O* in BTPA disappeared in metal-doped BTPA and shifted to high temperatures that was most clearly observed for Ni-BTPA, indicating that the metal doping could also contribute to interactions with *N=O* due to its multiple coordination numbers. Moreover, the alkyl-amine functional groups were more easily decomposed at around 200 °C after doping metal into BTPA, which could be ascribed to the competitive interactions caused by the coordination between the metal and *N=O*/*N-H*, the acid-base interaction between *N=O* and *N-H*, and/or the catalytic effect of doped metals on the decomposition. Therefore, both BTPA and metal-doped BTPA can reserve more *N=O* at lower calcination temperature to strengthen the affinity for NH_3 by acid-base interaction.

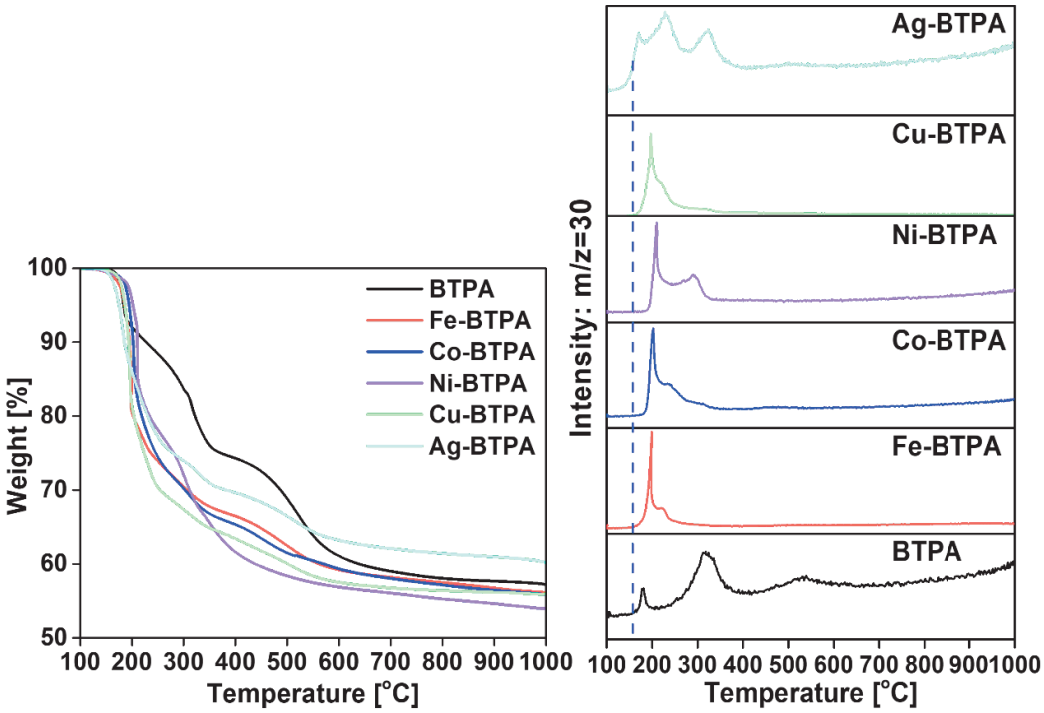

Fig. 2-4. TG-MS analysis of undoped BTPA and BTPA doped with different metals (left); the mass signal of m/z =30 in undoped BTPA and BTPA doped with different metals as a function of thermal treatment (right).

2.3.3 NH_3-TPD and XRD

Fig. 2-5 shows the NH_3 adsorption and desorption amounts of PFSA, such as Nafion and Aquivion, BTPA, and metal-doped BTPA xerogel powders. The details of the measurements appear in SI-1. Firstly, BTPA, as an organosilica species, still has comparable NH_3 adsorption amounts compared with Nafion and Aquivion in Fig. 2-5. It should be noted that PSFA has sulfonic groups of 1.0 meq g^{-1}, indicating approximately one sulfonic group adsorbed one NH_3 in an ion-exchanged manner. All metal-doped BTPA powders have excellent NH_3 adsorption amounts compared with pure BTPA and PFSA due to the affinity/coordination between metal and NH_3, since the coordination could be induced by Lewis-acid/base and/or electrostatic interactions in nature. The Ni-BTPA xerogel powder has the highest NH_3 adsorption amount (1.77 mmol g^{-1}) that is almost 2-4 times higher than BTPA and PFSA, which could be attributed to the fact that nickel

has a six-coordination number and a greater affinity for polar NH_3 than other metals, [41,42] suggesting metal-doped BTPA has the potential to separate NH_3. Although Fe and Co also have six coordination numbers, which have a weaker affinity with NH_3 that could be ascribed their slightly less electronegativity (Fe: 1.80; Co: 1.88) than Ni (1.91) and Cu (1.90). [43] Ag has the smallest coordination number and therefore has a low affinity with NH_3. Previous studies have shown that the binding energy (eV) between Ni and *N-H* from X-ray photoelectron spectroscopy is higher than that for either Cu or Ag. [28] Because of the similarity between NH_3 and *N-H*, these binding energies could also be used to confirm the affinity of metals for NH_3.

Fig. 2-S1 (c) shows the N_2 adsorption-desorption isotherms for BTPA-based xerogel powders at -196 °C. Although the adsorption isotherm of metal-doped BTPA is higher than that of undoped BTPA, all BTPA-based xerogels exhibit near poreless properties of less than 0.5 cm^3 $(STP)g^{-1}$, which could be attributed to alkyl chains in the BTPA monomer. Therefore, the difference in NH_3 adsorption amount for metal-doped BTPA and undoped BTPA could be mainly ascribed to the affinity of the metal and/or functional groups (*Si-OH*, *N=O*, and *N-H*).

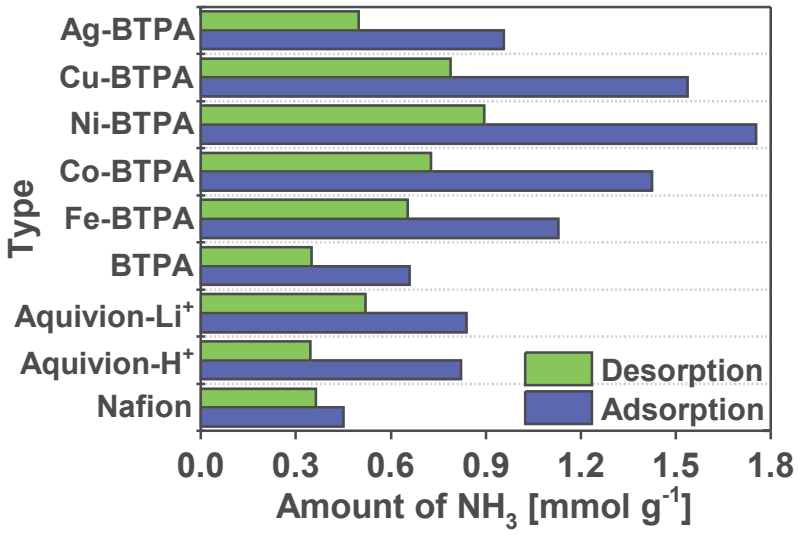

Fig. 2-5. NH_3-TPD of BTPA and different metal-doped BTPA at 150 °C.

Fig. 2-6 shows the XRD patterns of BTPA and metal-doped BTPA xerogel powders at different calcination temperatures. No clear characteristic peak of metal particles was detected in any samples at 150 °C, indicating that the coordination interaction between metal ions and *N-H* is stable at low temperature. [28] When the temperature rises to 200 °C, however, the characteristic peaks of metal particles appears in Ni-, Cu-, and Ag-BTPA powders, especially Ag-BTPA powder showed clear peak due to the weak coordination between Ag and *N-H*. [28] Nonetheless, there was no characteristic peak of metal particles for Fe- and Co-BTPA, indicating doped metals can be distributed in amorphous phase and fewer metal particles were formed, below the detection limit of the instrument. Therefore, Fe-, Ni-, and Ag-BTPA sols were selected to fabricate the membrane to explore the permeance and permselectivity for different gas molecules, particularly for NH_3.

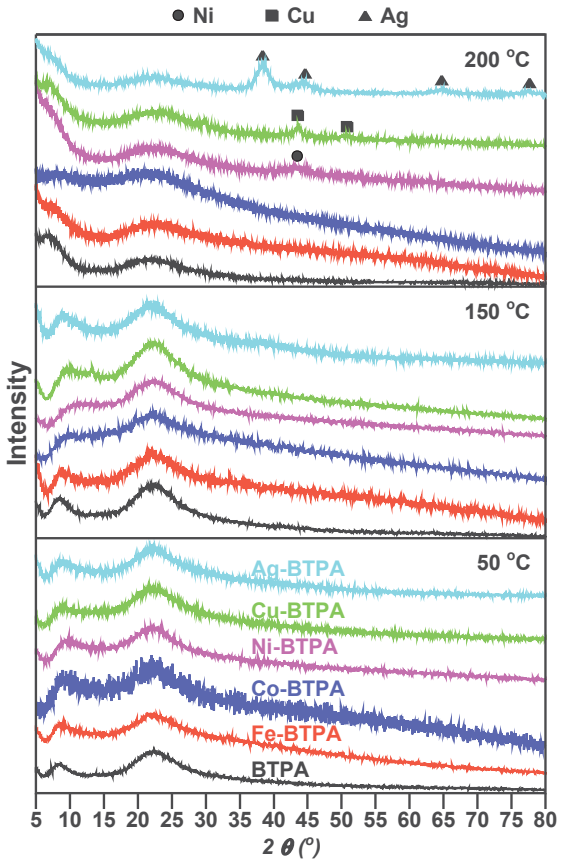

Fig. 2-6. Wide angle XRD patterns for BTPA and different metal-doped BTPA at different calcination temperatures.

Based on the abovementioned characterizations, the formation mechanism for a metal-doped BTPA network is schematically depicted in Fig. 2-7. Uncalcined gel consists of siloxane bonds as the main chain and silanol groups formed by the hydrolysis of methoxides (*Si-O-Me*), showing the loose structural network. After calcination at 150 °C, the silanol groups can be partially condensed to transform siloxane bond compared to fresh silica gel, resulting in the organosilica network. With increasing the calcination temperature, the decomposition of *N=O* could leave more sub-nanometer space and the *Si-OH* group would further condense to transform *Si-O-Si*. Meanwhile, metal particles appear because the coordination between metal and *N-H* can be partially destroyed at high temperature. Unlike the transformations at temperatures of 200 °C or

higher, most *N=O* and *Si-OH* functional groups are retained at lower temperatures, which could increase the affinity and promote adsorption and diffusion of polar molecules and contribute to improve NH_3 adsorption as clearly shown in NH_3-TPD and selective permeate through membranes.

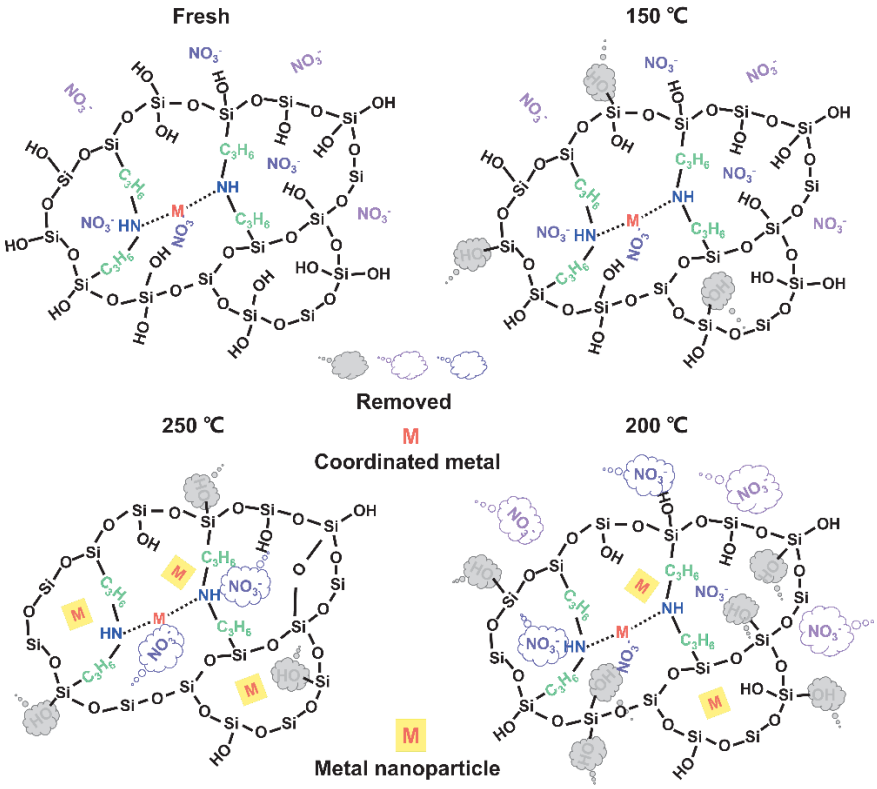

Fig. 2-7. Schematic illustration of the establishment of a metal-doped BTPA network at different calcination temperatures.

2.3.4 Interaction types and energies between Ni-BTPA and NH_3

The metal atoms grafted to the silica by *metal-O-Si* bond were proposed to study NH_3 adsorption sites, such as *metal-OH* and *Si-OH*, in metal-doped silicates. [44] In the present study, the interaction mechanism between metal-doped BTPA and NH_3 was explored. Because of the charge-transfer between the lone pair of electrons of the amine group in BTPA and the empty *d* orbital of the transition metal, the transition metal coordinated with the amine group and the metallic nanoparticles could be considered as

the most favorable form in this case. Therefore, the following three types of interaction scenarios between Ni-doped BTPA and NH_3 as shown in SI-5 have been simulated: (a) interaction between Ni-coordinated BTPA and NH_3; (b) interaction between Ni nano-particles and NH_3; and (c) interaction between amine in Ni-coordinated BTPA and NH_3.

Fig. 2-8 shows the interaction type/intensity of intersegments (δg_{inter}) by projecting functions ($sign[\lambda_2(r)\rho(r)]$) onto the IGMH isosurface with different colors. The more negative region of vertical axis (blue area), the more attractive interaction with NH_3, while the green negative region corresponds to van der Waals forces. The distance of Ni···N (*N-H*) of 1.8776 Å in Fig. 2-8 (c) was stretched to 1.9146 Å in Fig. 2-8 (a) since nickel interacts with both *N-H* and NH_3, implying a competitive coordination between nickel and *N-H/NH₃*. The length of Ni···N(*NH₃*) (1.8901 Å in Fig. 2-8 (a)) was shorter than that of Ni···N (*N-H*) (1.9146 Å in Fig. 2-8 (a)), which indicates that compared with the interaction of *N-H*, NH_3 interacts more strongly with nickel. Likewise, the distance between the Ni nanoparticle and NH_3 is shorter than that between the Ni-coordinated BTPA and NH_3 as shown in Figs. 2-8 (a) and (b). Regarding the interaction energy, both coordinated nickels and nickel particles in Ni-doped BTPA have the large interaction energy for NH_3 (-40.06 and -50.24 kcal mol^{-1}) [45] by the synergy between coordination and hydrogen bond, which significantly surpasses the interaction energy between *N-H* and NH_3 (-7.77 kcal mol^{-1} in Fig. 2-8 (c)). This means that compared with *N-H* groups, nickel has a stronger affinity for NH_3: Ni-BTPA >> BTPA.

Among the three types of interaction shown in the isosurface plots, both the nickel coordinated with *N-H* and nickel particles will anchor NH_3 through the coordination

with strong affinity. In addition, nickel nanoparticles, which were confirmed to be formed under a high Ni/*N-H* molar ratio and/or a high calcination temperature, has a stronger coordination with NH_3 than Ni coordinated to the amine group from the scatter plots in Fig. 2-8 (b) due to the shorter interaction distance (1.8500 Å) and hydrogen bonds between amine and NH_3. Additionally, the acid *N=O* groups from HNO_3 and/or metal nitrates remained in the organosilica network even at higher temperatures as discussed in FT-IR and TG-MS, so the hydrogen bond between *N=O* and NH_3 caused by acid-base interaction is also not negligible.

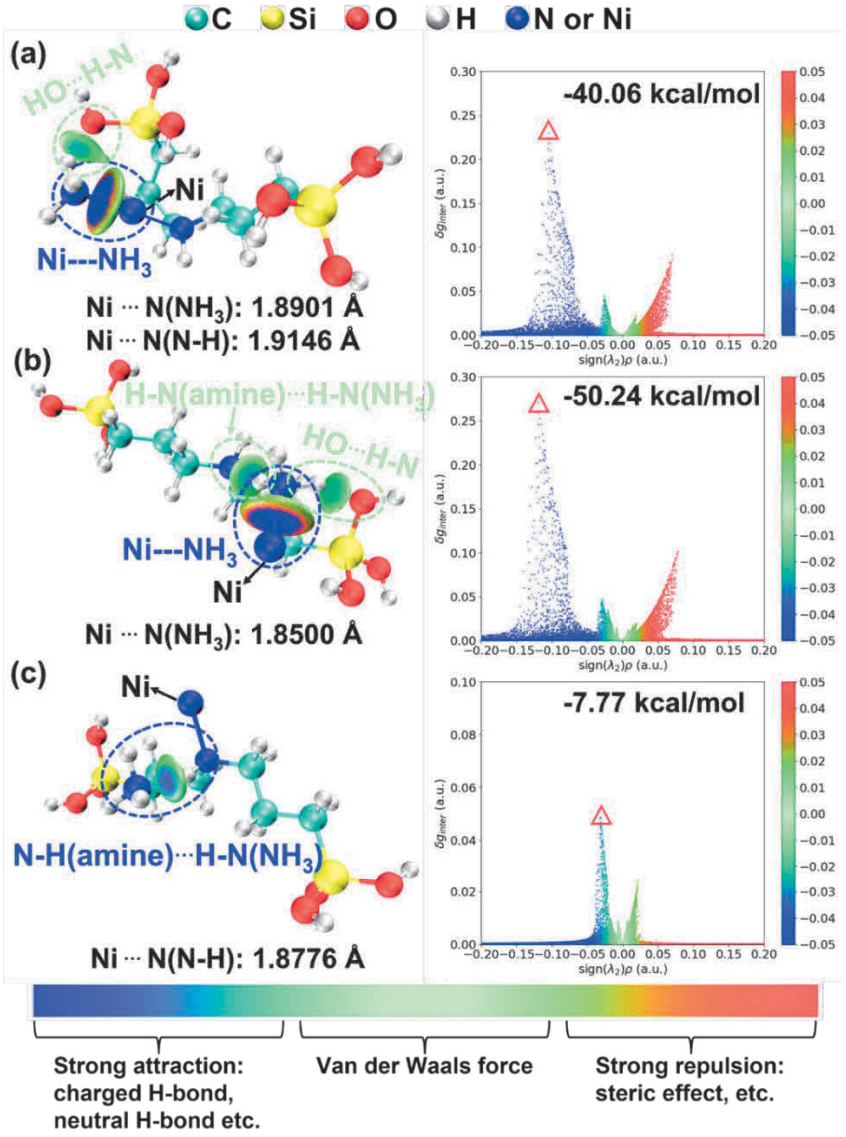

Fig. 2-8. Color-filled IGM isosurface and scatter plots depicting the average interaction regions for Ni-BTPA.

2.3.5 Gas permeation properties of metal-doped BTPA membranes

As demonstrated in SI-6, BTPA membranes calcined at 150, 200, and 250 °C have different performance for H_2, N_2, and NH_3 permeation due to the structural differences obtained at different calcination temperatures. According to the gas permeance and the activation energies of H_2 and N_2 permeation, BTPA membranes calcined at 200 and 250 °C have higher gas permeance, that is lower permeation resistance than that at 150 °C, which could be attributed to the removal of *N=O* and the condensation of *Si-OH* to transform *Si-O-Si*, leaving more sub-nanometer space for gas permeation.

Interestingly, NH_3 had the highest 1.5×10^{-6} mol m^{-2} s^{-1} Pa^{-1} in BTPA (250) and was always more permeable than H_2 and N_2, which could be explained by selective adsorption and diffusion of NH_3 through these membranes. However, the NH_3 selectivity gradually decreases with calcination temperature, as shown in Fig. 2-S7, indicating that enlarging pore size at high temperatures cannot be useful to NH_3 selective permeation by molecular sieving and the reduction of *N=O* and *Si-OH* would decrease the surface affinity for NH_3. BTPA membrane calcined at 150 °C showed NH_3 permeance at 9.6×10^{-7} mol m^{-2} s^{-1} Pa^{-1} with ideal NH_3/H_2 selectivity of 12 and NH_3/N_2 selectivity of 129 at 150 °C due to the appropriate pore size and retaining as much polar functional groups (*Si-OH*, *N=O*, and *N-H*) as possible.

Fig. 2-9 shows the time courses for H_2, N_2, and NH_3 permeance through Ni-BTPA membrane calcined at 150 °C. The measurement was initiated at 150 °C, followed by temperature dependency in the range from 50 to 200 °C. After permeating H_2, N_2, and

NH_3 at 200 °C, the H_2, N_2, and NH_3 permeance and H_2/N_2 selectivity at 150 °C were approximately the same as the initial values, indicating that BTPA-based membranes have considerable thermal stability and adequate NH_3 resistance. The BTPA-based membranes calcined at 150 °C retained the optimum number of functional groups, such as *Si-OH*, *N=O*, and *N-H*, and also demonstrated optimum stability at higher temperature.

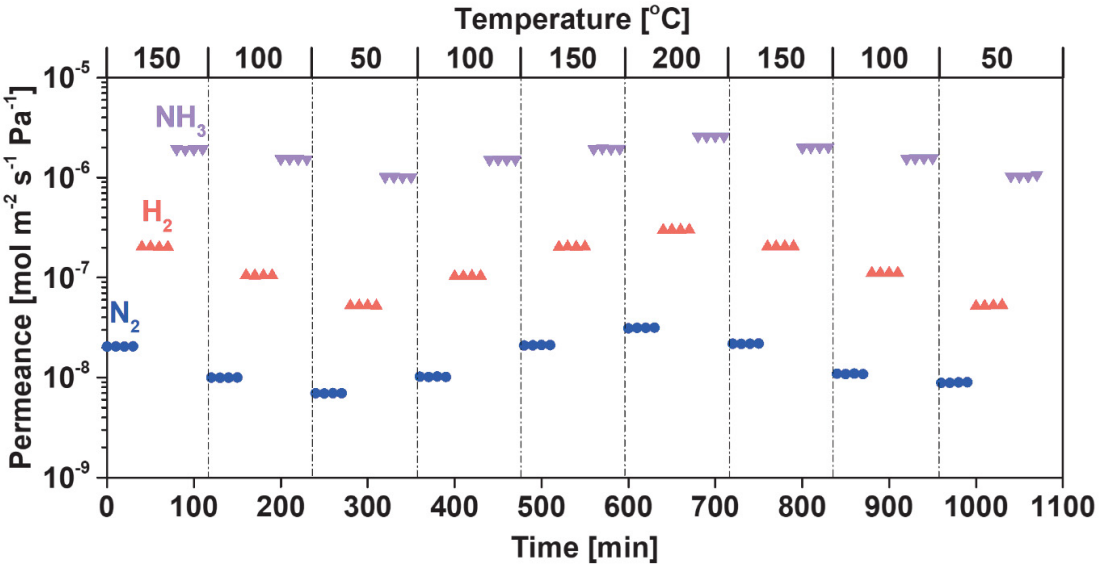

Fig. 2-9. Time course for single H_2, N_2, and NH_3 permeance at temperatures ranging from 50 to 200 °C for Ni-BTPA membrane calcined at 150 °C.

Fig. 2-10 shows single-gas permeance (left) and dimensionless permeance normalized with He permeance (right) for BTPA, Fe, Ni, and Ag-BTPA membranes. Permeance of the gases followed the order of Ni-BTPA > Fe-BTPA ≈ Ag-BTPA > undoped BTPA, which is consistent with previous results, but the gas permeance was not significantly increased compared with membranes calcinated at 250 °C. [28] The permeance of the gases decreased as the molecular diameter increased, showing the molecular sieving effect. The dimensionless permeance of the gases indicates that the gases permselectivity decreased following the doping of metal ions into BTPA, which is consistent

with the higher permeance for He, H_2, N_2, and CH_4 molecules due to the enlargement of pore size by the coordination between the metals and the *N-H* groups.

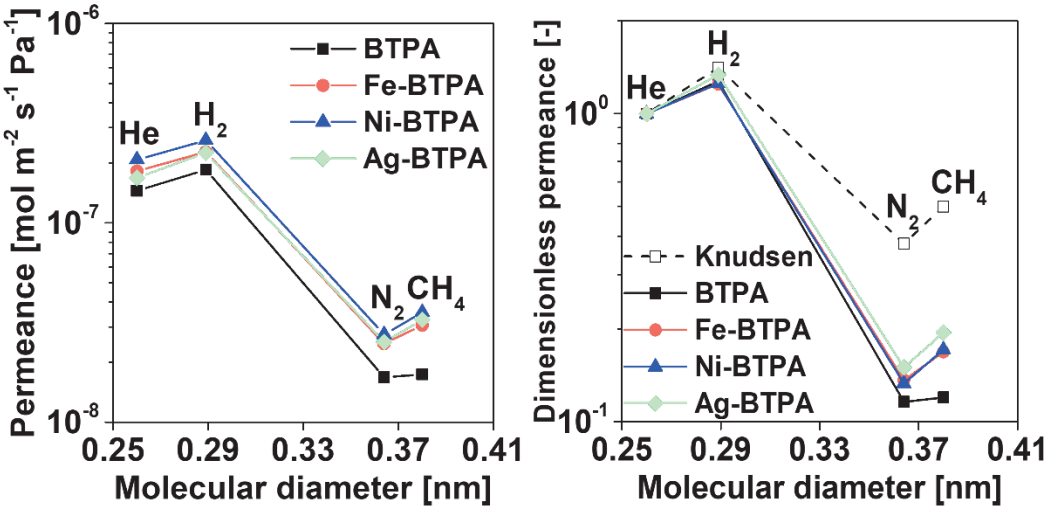

Fig. 2-10. Kinetic diameter dependence of single-gas permeance at 200 °C for BTPA and different metal-doped BTPA.

Fig. 2-11 shows the temperature dependency of H_2, N_2, and NH_3 permeances of BTPA and metal-coordinated BTPA membranes. NH_3 had the highest permeance and increased with increasing temperature for all BTPA-based membranes, which is different from the Nafion and Aquivion membrane that exhibited the highest NH_3 permeance but decreased NH_3 permeance with temperature arise from 50 to 200 °C. [27] BTPA membrane showed the lowest H_2 and N_2 permeance among all types of BTPA-based membranes due to the dense structure formed by the flexible bridged-BTPA monomer, but the higher NH_3 permeance than H_2 and N_2 further confirms that NH_3 permeation was dominated by a solution-diffusion mechanism induced by the adsorption of NH_3.

The H_2 and N_2 permeance, as the non-adsorptive gases, of all metal-doped membranes were higher than those of BTPA, indicating that metal doping into BTPA enlarged the pore size and increased porosity of the organosilica network, resulting in an

increasing gas permeance as discussed in Fig. 2-10 (left). Additionally, the efficient affinity of the metal to NH_3 also greatly improves the selective adsorption and permeation of NH_3 through the membrane. Although the kinetic diameter of NH_3 can be assumed to be 0.326 nm [6,27] that is larger than that of H_2 and smaller than that of N_2, so that NH_3 permeance is always higher than N_2 or even H_2. This can be explained by the fact that the adsorption and diffusion of NH_3 contributed to membrane permeation, and an increase in temperature is beneficial to the permeation of NH_3 within the membrane even if it would reduce the NH_3 adsorption amount. It should be noted that the enlarged pore size for all metal-doped membranes could increase the permeance, but an excessive expansion of pores would reduce NH_3 selectivity. [6]

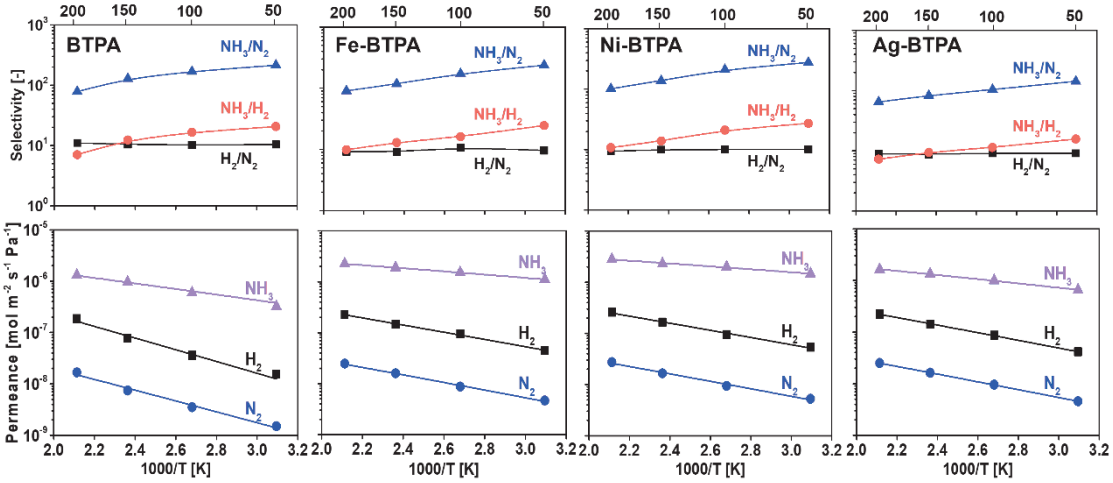

Fig. 2-11. Temperature dependence of single-gas permeance for BTPA and different metal-doped BTPA membranes range from 50 to 200 °C.

Metal-coordinated BTPA membranes exhibit superior NH_3 permselectivity compared with undoped BTPA membrane even at high temperature due to the strong affinity between metal and NH_3 as shown in Fig. 2-12. Generally, the low temperature tends to promote NH_3 adsorption in a membrane but decreases the diffusivity of NH_3 within the membrane matrix, while the high temperature accelerates the transport of NH_3 through

the membrane, irrespective of the decrease in NH_3 adsorption. Therefore, the temperature dependency of permeance is determined by the balance of adsorption and diffusion. BTPA-based membranes show activated-diffusion permeance since the activation energy of diffusion surpasses the adsorption enthalpy due to the strong affinity with metal and to the limited vibration of organosilica networks. Among the BTPA-based membranes, Ni-BTPA membrane showed the best performance, that single-component NH_3 permeance of ~2.8×10^{-6} mol m^{-2} s^{-1} Pa^{-1} was obtained with an ideal NH_3 selectivity of 11 for NH_3/H_2 and 102 for NH_3/N_2 at 200 °C, while the NH_3 permeance was 1.3×10^{-6}, 2.2×10^{-6}, and 1.6×10^{-6} mol m^{-2} s^{-1} Pa^{-1} for BTPA, Fe-BTPA, and Ag-BTPA, respectively.

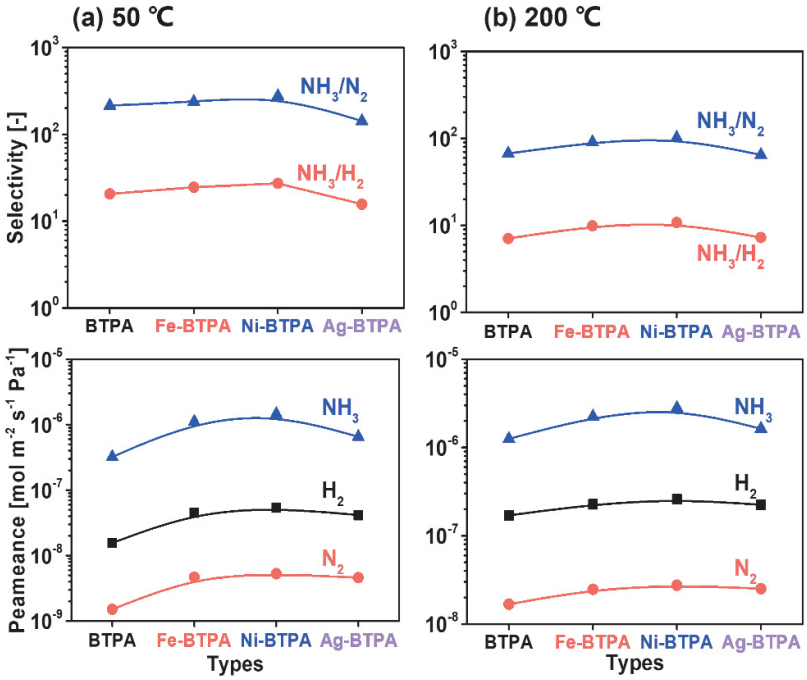

Fig. 2-12. NH_3 permeance and selectivity at 50 (left) and 200 °C (right) as a function of metal affinity.

SI-7 shows the time courses for H_2 and N_2 permeance before and after NH_3 permeation at 50 and 200 °C, indicating that Ni-BTPA membrane has sufficient thermal stability and NH_3 resistance. Moreover, Fig. 2-13 shows the single-gas and binary-gas

selectivities and permeance for NH_3, H_2, and N_2 for Ni-BTPA membrane with a negligible mixing effect at 50 °C. The permeance of $H_2/N_2/NH_3$ and NH_3 selectivity in binary gas permeation were almost constant and almost consistent with that in single gas permeation, meaning that NH_3 permeation was not almost decreased/blocked the H_2 and N_2 permeance in Ni-BTPA membrane at 50 °C.

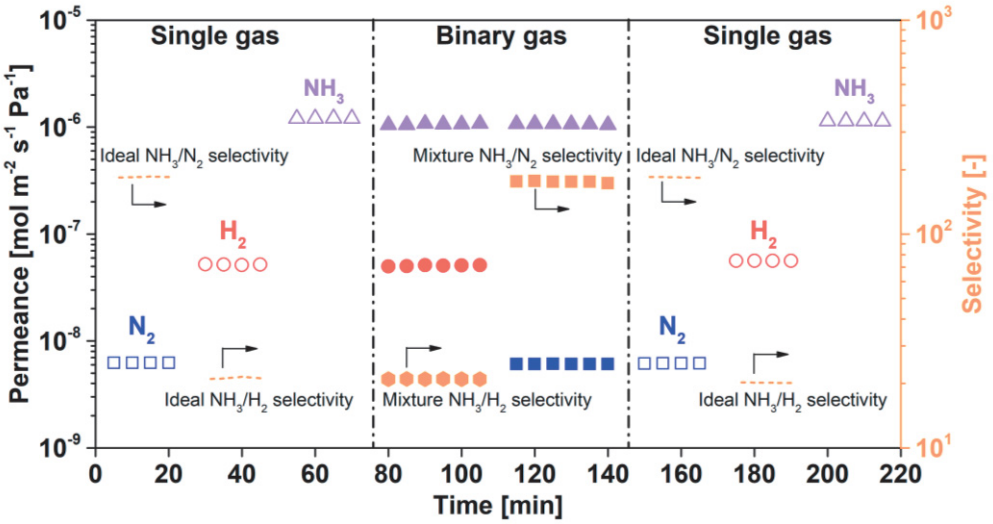

Fig. 2-13. Time courses of selectivity and permeance of NH_3, H_2, and N_2 in single gas and binary gas for Ni-BTPA membrane at 50 °C, the binary gases were equimolar NH_3/H_2 and NH_3/N_2, respectively.

Since green NH_3 has begun to attract a great deal of attention, many types of membranes have been developed. SI-8 summarizes the H_2, N_2, and NH_3 permeation properties of different membranes. Recently, we developed PSFA/ceramic composite membranes, and reported the high NH_3 separation performance which surpassed conventional membranes that could be ascribed to the thin separation layer, and the excellent selectivity that can be attributed to the sulfonic acid functional groups in PSFA. The comparison of the permeation properties of PSFA/ceramic and the present BTPA-based membranes is summarized for permeation temperatures of 200 and 50 °C in the top and bottom of Fig. 2-14, respectively. The high H_2/N_2 selectivity reaching 18 for PFSA-

based membranes exceeds the H_2/N_2 selectivity of ~10 for BTPA-based membranes at 50 °C as indicated in Fig. 2-14 (d), indicating that its pore size is much smaller than that of BTPA-based membranes, which could be beneficial to improve the NH_3/H_2 and NH_3/N_2 selectivity by molecular sieving. [6] Secondly, the strong coordination of the metal for NH_3 (-40-50 kcal mol^{-1} in Fig. 2-8 and ref. 45) could slow NH_3 diffusion (large activation energy of diffusion) through the membrane, irrespective of NH_3 adsorption amount, consistent with NH_3-TPD. Previous studies [46,47] have confirmed that the coordination between metal and NH_3 is too large to easily release NH_3 from the adsorption state of NH_3. Thus, at 50 °C (Figs. 2-14 (e) and (f)), PSFA-based membranes, such as Nafion that displays an NH_3 permeance of 2.9×10^{-6} mol m^{-2} s^{-1} Pa^{-1} and NH_3/N_2 selectivity of 731 and NH_3/H_2 selectivity of 40, are superior to BTPA-based membranes, such as Ni-BTPA with NH_3 permeance of 1.5×10^{-6} mol m^{-2} s^{-1} Pa^{-1} and NH_3/N_2 selectivity of 277 and NH_3/H_2 selectivity of 27.

On the other hand, under high operation temperature, the flexible membranes tend to enlarge the pore size induced by thermal vibration and reduce the adsorption amounts of polar gases. The increased N_2 permeance and decreased H_2/N_2 selectivity at 200 °C were observed, especially for PFSA, as the polymers that have extremely flexible structures, as evidenced by H_2/N_2 selectivity from 18 at 50 °C down to ~10 at 200 °C as shown in Figs. 2-14 (a) and (d). On the other hand, BTPA, as an organosilica membrane, has a relatively rigid structure because the alkyl-amine chain can be constrained by two silicon and/or metals. Therefore, the pore size can be only slightly affected by thermal vibration, which has been confirmed by the approximately constant H_2/N_2 selectivity

of ~10. The NH_3 permeance in PFSA-based membranes decreased with rising temperature, for example, from 1.9×10^{-6} at 50 °C down to 9.1×10^{-7} mol m^{-2} s^{-1} Pa^{-1} at 200 °C together with dramatic decrease in NH_3/H_2 selectivity from ~40 to ~2 for Aquivion-Li^+ membrane in Figs. 2-14 (b) and (e). On the contrary, the NH_3 permeance in BTPA-based membrane increased at high temperature, such as, from 1.5×10^{-6} at 50 °C rise to 2.8×10^{-6} mol m^{-2} s^{-1} Pa^{-1} at 200 °C with a slight decrease in NH_3/H_2 selectivity from ~20 to ~10 for Ni-BTPA membrane. Therefore, metal-doped BTPA membranes show superior NH_3/H_2 and NH_3/N_2 selectivity and NH_3 permeance at 200 °C compared with PSFA-based membranes as shown in Fig. 2-14 (c), which could be ascribed to the fact that the higher temperature can promote NH_3 diffusion through the membrane. In addition to controlling the pore size of the membrane, the NH_3 adsorption/affinity on the membrane surface and the solution-diffusion of NH_3 within the membrane should be reasonably controlled, which can be more beneficial to NH_3 permselectivity. [48]

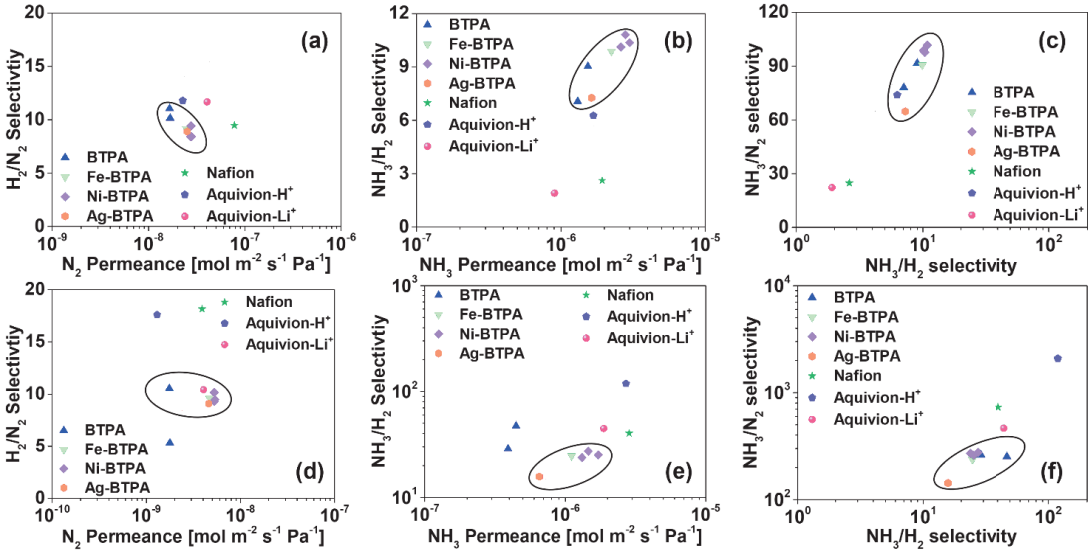

Fig. 2-14. Trade-off of the selectivity and permeance at 200 (above) and 50 °C (below) for BTPA and different metal-doped BTPA membranes; Each point indicates the permeance of the different membranes for H_2 and N_2 (a, d), and for NH_3 and H_2 (b, e), and the relationship between NH_3/H_2 and NH_3/N_2 (c, f).

BTPA-based membranes with higher NH_3 permeance and selectivity at higher temperatures also provide preferable solutions for NH_3 synthesis or decomposition membrane reactors that have attracted a great deal of attention in recent years, [49,50] because higher synthesis or decomposition temperatures are more conducive to the efficient utilization of NH_3.

2.4 Conclusions

The gels obtained by doping metal into BTPA with the coordination between metal and amine groups showed remarkable NH_3 adsorption and desorption capacity. The affinity for NH_3 was greatly enhanced by metal-induced coordination and hydrogen bonds and/or van der Waals interactions caused by *N-H*, *N=O*, and *Si-OH* functional groups by analyzing intermolecular interaction type. The Ni-BTPA membrane showed the highest NH_3 permeance of ~2.8×10^{-6} mol m^{-2} s^{-1} Pa^{-1} with ideal NH_3/H_2 and NH_3/N_2 selectivity that reached 11 and 102 at 200 °C, respectively. Finally, the competitive coordination interaction between metal and nitrogen species (NH_3 and *N-H*) that results from the charge-transfer tends to promote NH_3 adsorption and permeation.

References

[1] A. Klerke, C.H. Christensen, J.K. Nørskovb, T. Vegge, Ammonia for hydrogen storage: challenges and opportunities, *J. Mater. Chem.* 18 (2008) 2304-2310.

[2] J.W. Erisman, M.A. Sutton, J. Galloway, Z. Klimont, W. Winiwarter, How a century of ammonia synthesis changed the world, *Nat. Geosci.* 1 (2010) 636-639.

[3] M. Wang, M.A. Khan, I. Mohsin, J. Wicks, A.H. Ip, K.Z. Sumon, C.T. Dinh, E.H. Sargent, I.D. Gates, M.G. Kibria, Can sustainable ammonia synthesis pathways compete with fossil-fuel based Haber-Bosch processes? *Energy Environ. Sci.* 14 (2021) 2535-2548.

[4] T.T. Zhu, B.Y. Pei, T. Di, Y.X. Xia, T.S. Li, L. Li, Thirty-minute preparation of microporous polyimides with large surface areas for ammonia adsorption, *Green Chem.* 22 (2020) 7003-7009.

[5] H.R. Tang, C. Gunathilake, X.Z. Zhou M. Jaroniec, Polymer-templated mesoporous hybrid oxides of Al and Cu: highly porous sorbents for ammonia, *RSC Adv.* 6 (2016) 38662-38670.

[6] M. Kanezashi, A. Yamamoto, T. Yoshioka, T. Tsuru, Characteristics of ammonia permeation through porous silica membranes, *AIChE J.* 56 (2010) 1204-1212.

[7] A.J. Rieth, M. Dincă, Programming framework materials for ammonia capture, *ACS Cent. Sci.* 4 (2018) 666-667.

[8] S.J. Zeng, L. Liu, D.W. Shang, J.P. Feng, H.F. Dong, Q.X. Xu, X.P. Zhang, S.J. Zhang, Efficient and reversible absorption of ammonia by cobalt ionic liquids through Lewis acid-base and cooperative hydrogen bond interactions, *Green Chem.* 20 (2018) 2075-2083.

[9] N.A. Rogozhnikov, A study of ammonia adsorption on gold face (111), *Materials Today: Proceedings* 31 (2020) 473-475.

[10] I.V. Vorotyntsev, P.N. Drozdov, N.V. Karyakin, Ammonia permeability of a cellulose acetate membrane, *Inorg. Mater.* 42 (2006) 231-235.

[11] W.A. Phillip, E. Martono, L. Chen, M.A. Hillmyer, E.L. Cussler, Seeking an ammonia selective membrane based on nanostructured sulfonated block copolymers,

J. Membr. Sci. 337 (2009) 39-46.

[12] B. Yang, L. Bai, Z. Wang, H. Jiang, S. Zeng, X. Zhang, X. Zhang, Exploring NH_3 transport properties by tailoring ionic liquids in Pebax-based hybrid membranes, *Ind. Eng. Chem. Res.* 60 (2021) 9570-9577

[13] Q. Wei, J.M. Lucero, J.M. Crawford, J. Douglas Way, C.A. Wolden, M.A. Carreon, Ammonia separation from N_2 and H_2 over LTA zeolitic imidazolate framework membranes, *J. Membr. Sci*. 623 (2021) 119078.

[14] X.Duan, D. Kim, K. Narasimharao, S. Al-Thabaitic, M. Tsapatsis, High-performance ammonia-selective MFI nanosheet membranes, *Chem. Commun.* 57 (2021) 580-582.

[15] K. Wakimoto, W.W. Yan, N. Moriyama, H. Nagasawa, M. Kanezashi, T. Tsuru, Ammonia permeation of fluorinated sulfonic acid polymer/ceramic composite membranes, *J. Membr. Sci.* 658 (2022) 120718.

[16] H. Kim, M. Sohail, K. Yim, Y.C. Park, D.H. Chun, H.J. Kim, S.O. Han, J.H. Moon, Effective CO_2 and CO separation using [M_2(DOBDC)] (M = Mg, Co, Ni) with unsaturated metal sites and excavation of their adsorption sites, *ACS Appl. Mater. Interfaces* 11 (2019) 7014-7021.

[17] L. Li, J. He, W. Xu, K. Zhang, T. Xing, Z. Li, D. Zhen, B. Xiong, Z. Ge, X. Zhang, S. Wang, F. Zhang, X. Gu, P. Dai, D. Liu, L. Yang, X. Zhao, High CO_2 separation performance on a metal- organic framework composed of nano-cages lined with an ultra-high density of dual-side open metal sites, *Mater. Adv.* 3 (2022) 493-497.

[18] E. Rezaei, B. Schlageter, M. Nemati, B. Predicala, Evaluation of metal oxide nanoparticles for adsorption of gas phase ammonia, *J. Environ. Chem. Eng.* 5 (2017) 422-431.

[19] F.T.U. Kohler, S. Popp, H. Klefer, I. Eckle, C. Schrage, B. Böhringer, D. Roth, M. Haumann, P. Wasserscheid, Supported ionic liquid phase (SILP) materials for removal of hazardous gas compounds-efficient and irreversible NH_3 adsorption, *Green Chem.* 16 (2014) 3560-3568.

[20] L. Luo, Z.H. Wu, Z.X. Wu, Y.B. Liu, X.Y. Huang, R.H. Ling, L. Ye, X.Y. Luo, C.M. Wang, Role of structure in the ammonia uptake of porous polyionic liquids, *ACS*

Sustainable Chem. Eng. 10 (2022) 4094-4104.

[21] Y.Y. Zhang, X. Zhang, Z.J. Chen, K. Otake, G.W. Peterson, Y.W. Chen, X.J. Wang, L.R. Redfern, S. Goswami, P. Li, T. Islamoglu, B. Wang, O.K. Farha, A flexible interpenetrated zirconium-based metal-organic framework with high affinity toward ammonia, *ChemSusChem* 13 (2020) 1710-1714.

[22] Y. He, E.L. Cussler, Ammonia permeabilities of perfluorosulfonic membranes in various ionic forms, *J. Membr. Sci.* 68 (1992) 43-52.

[23] S.J. Zeng, J.L. Wang, P.F. Li, H.F. Dong, H. Wang, X.C. Zhang, X.P. Zhang, Efficient adsorption of ammonia by incorporation of metal ionic liquids into silica gels as mesoporous composites, *Chem. Eng. J.* 370 (2019) 81-88.

[24] X.X. Pan, M. Zhu, H. Mei, Z.S. Liu, T.Y. Shen, Ammonia absorption enhancement by metal halide impregnated hollow mesoporous silica spheres, *ChemistrySelect* 5 (2020) 5720-5725.

[25] J. Liu, Z.J. Chen, R. Wang, S. Alayoglu, T. Islamoglu, S.J. Lee, T.R. Sheridan, H.Y. Chen, R.Q. Snurr, O.K. Farha, J.T. Hupp, Zirconium metal-organic frameworks integrating chloride ions for ammonia capture and/or chemical separation, *ACS Appl. Mater. Interfaces* 13 (2021) 22485-22494.

[26] T.N. Nguyen, I.M. Harreschou, J.H. Lee, K.C. Stylianou, D.W. Stephan, A recyclable metal-organic framework for ammonia vapour adsorption, *Chem. Commun.* 56 (2020) 9600-9603.

[27] D.W. Shang, S.J. Zeng, X.P. Zhang, X.C. Zhang, L. Bai, H.F. Dong, Highly efficient and reversible absorption of NH_3 by dual functionalized ionic liquids with protic and Lewis acidic sites, *J. Mol. Liq.* 312 (2020) 113411.

[28] U. Anggarini, L. Yu, H. Nagasawa, M. Kanezashi, T. Tsuru, Metal-induced microporous aminosilica creates a highly permeable gas-separation membrane, *Mater. Chem. Front.* 5 (2021) 3029-3042.

[29] Y. Cao, J. Zhang, Y. Ma, W. Wu, K. Huang, L. Jiang, Designing low-viscosity deep eutectic solvents with multiple weak-acidic groups for ammonia separation, *ACS Sustainable Chem. Eng.* 9 (2021) 7352-7360.

[30] B. Liu, J. Tian, Investigation of glycolic acid natural deep eutectic solvents with

strong proton donors for ammonia capture and separation, *Ind. Eng. Chem. Res.* 60 (2021) 11600-11610.

[31] T. Yoshioka, M. Kanezashi, T. Tsuru. Micropore size estimation on gas separation membranes: A study in experimental and molecular dynamics. *AIChE J.* 59 (2013) 2179-2194.

[32] H.R. Lee, T. Shibata, M. Kanezashi, T. Mizumo, J. Ohsita, T. Tsuru, Pore-size-controlled silica membranes with disiloxane alkoxides for gas separation. *J. Membr. Sci.* 383 (2011) 152-158.

[33] M.J. Frisch, G.W. Trucks, H.B. Schlegel, G.E. Scuseria, M.A. Robb, J.R. Cheeseman, G. Scalmani, V. Barone, B. Mennucci, G.A. Petersson, H. Nakatsuji, M. Caricato, X. Li, H.P. Hratchian, A.F. Izmaylov, J. Bloino, G. Zheng, J.L. Sonnenberg, M. Hada, M. Ehara, K. Toyota, R. Fukuda, J. Hasegawa, M. Ishida, T. Nakajima, Y. Honda, O. Kitao, H. Nakai, T. Vreven, JA Jr Montgomery, J.E. Peralta, F. Ogliaro, M. Bearpark, J.J. Heyd, E. Brothers, K.N. Kudin, V.N. Staroverov, R. Kobayashi, J. Normand, K. Raghavachari, A. Rendell, J.C. Burant, S.S. Iyengar, J. Tomasi, M. Cossi, N. Rega, J.M. Millam, M. Klene, J.E. Knox, J.B. Cross, V. Bakken, C. Adamo, J. Jaramillo, R. Gomperts, R.E. Stratmann, O. Yazyev, A.J. Austin, R. Cammi, C. Pomelli, J.W. Ochterski, R.L. Martin, K. Morokuma, V.G. Zakrzewski, G.A. Voth, P. Salvador, J.J. Dannenberg, S. Dapprich, A.D. Daniels, Ö. Farkas, J.B. Foresman, J.V. Ortiz, J. Cioslowski, D.J. Fox, Gaussian 09, revision D.01; Gaussian, Inc., Wallingford CT, 2009.

[34] K.P. Jensen, Bioinorganic chemistry modeled with the TPSSh density functional, *Inorg. Chem.* 47 (2008) 10357-10365.

[35] K.L. Schuchardt, B.T. Didier, T. Elsethagen, L. Sun, V. Gurumoorthi, J. Chase, J. Li, T.L. Windus, Basis Set Exchange: A community database for computational sciences, *J. Chem. Inf. Model.* 47 (2007) 1045-1052.

[36] T. Lu, Q.X. Chen, Independent gradient model based on Hirshfeld partition: A new method for visual study of interactions in chemical systems, *J. Comput. Chem.* 43 (2022) 539-555.

[37] T. Lu, F.W. Chen, Multiwfn: A multifunctional wavefunction analyzer, *J. Comput.*

Chem. 33 (2012) 580-592.

[38] W. Humphrey, A. Dalke, K. Schulten, VMD: Visual Molecular Dynamics, *J. Mol. Graph.* 14 (1996) 33-38.

[39] H. Song, Y. Wei, H. Qi, Tailoring pore structures to improve the permselectivity of organosilica membranes by tuning calcination parameters, *J. Mater. Chem. A* 5 (2017) 24657-24666.

[40] U. Anggarini, L. Yu, H. Nagasawa, M. Kanezashi, T. Tsuru, Microporous nickel-coordinated aminosilica membranes for improved pervaporation performance of methanol/toluene separation, *ACS Appl. Mater. Interfaces* 13 (2021) 23247-23259.

[41] T. Aoki, H. Miyaoka, H. Inokawa, T. Ichikawa, Y. Kojima, Activation on ammonia absorbing reaction for magnesium chloride, *J. Phys. Chem. C* 119 (2015) 26296-26302.

[42] Y. Zhou, Z. Wu, D. Ding, T. He, B. Wang, S. Rong, Tunnel structured manganese dioxides for the gaseous ammonia adsorption and its regeneration performance, *Sep. Purif. Technol.* 284 (2022) 120252.

[43] T.F. Zhang, H. Miyaoka, H. Miyaoka, T. Ichikawa, Y. Kojima, Review on ammonia absorption materials: metal hydrides, halides, and borohydrides, *ACS Appl. Energy Mater.* 1 (2018) 232-242.

[44] A.M. Jystad, A. Biancardi, M. Caricato, Simulations of ammonia adsorption for the characterization of acid sites in metal-doped amorphous silicates, *J. Phys. Chem. C* 121 (2017) 22258-22267.

[45] B. Sharma, Y. Indra Neela, G. Narahari Sastry, Structures and energetics of complexation of metal ions with ammonia, water, and benzene: A computational study, *J. Comput. Chem.* 37 (2016) 992-1004.

[46] J. Liu, Z.Y. Lu, Z.J. Chen, M. Rimoldi, A.J. Howarth, H.Y. Chen, S. Alayoglu, R.Q. Snurr, O.K. Farha, J.T. Hupp, Ammonia capture within zirconium metal-organic frameworks: reversible and irreversible uptake, *ACS Appl. Mater. Interfaces* 13 (2021) 20081-20093.

[47] J.L. Wang, S.J. Zeng, F. Huo, D.W. Shang, H.Y. He, L. Bai, X.P. Zhang, J.W. Li, Metal chloride anion-based ionic liquids for efficient separation of NH_3, *J. Clean.*

Prod. 206 (2019) 661-669.

[48] L. Yu, M. Kanezashi, H. Nagasawa, T. Tsuru, Fabrication and CO_2 permeation properties of amine-silica membranes using a variety of amine types, *J. Membr. Sci.* 541 (2017) 447-456.

[49] Z.Y. Zhang, J. Douglas Way, C.A. Wolden, Design and operational considerations of catalytic membrane reactors for ammonia synthesis, *AIChE J.*, 67 (2021) e17259.

[50] L. Meng, T. Tsuru, Hydrogen production from energy carriers by silica-based catalytic membrane reactors, *Catal. Today* 268 (2016) 3-11.

Supplementary Material

---------- SI-1: NH_3 temperature-programmed desorption (NH_3-TPD) ----------

The xerogel powders were pre-treated at 150 °C to remove any adsorbed molecules under dry helium (He) at 30 ml min^{-1} for 120 min, followed by temperature decreases from 150 to 35 °C, and were then cooled and maintained at 28 °C for 60 min. After pretreatment of the xerogel powders, 5% NH_3/95% He mixture gas was fed into the system at 30 ml min^{-1} for 90 min together with Ar as non-adsorption gas at 1 ml min^{-1} at 30 °C, Then pure He was fed at 30 ml min^{-1} for 120 min. After that, NH_3 desorption was performed at 40 °C for 120 min, then the temperature was raised from 40 to 150 °C at 10 °C min^{-1}, and held 150 °C for 60 min. The NH_3 adsorption and desorption amounts were calculated using the following equations (Eq-1 and Eq-2), repectively:

$$NH_3 \text{ adsorption amount} = \frac{1}{m}\int_{t1}^{t2}\left(\frac{I_{Ar,t}\frac{I_{NH_3,in}}{I_{Ar,in}} - I_{NH_3,t}}{I_{NH_3,in}}\right) Q_{NH_3}\,dt \qquad \text{Eq-1}$$

$$NH_3 \text{ desorption amount (50}\rightarrow\text{150 °C)} = \frac{1}{m}\int_{t3}^{t4}\left(\frac{I_{NH_3,t}}{I_{NH_3,in}}\right) Q_{NH_3}\,dt \qquad \text{Eq-2}$$

m: weight of sample (g); $I_{i,in}$: intensity of the feed i-th component; $I_{i,t}$: intensity of the feed i-th component at each moment; Q_{NH_3}: flow rate of NH_3.

Each sample was measured 3 times to calculate the average amount of NH_3 adsorption and desorption.

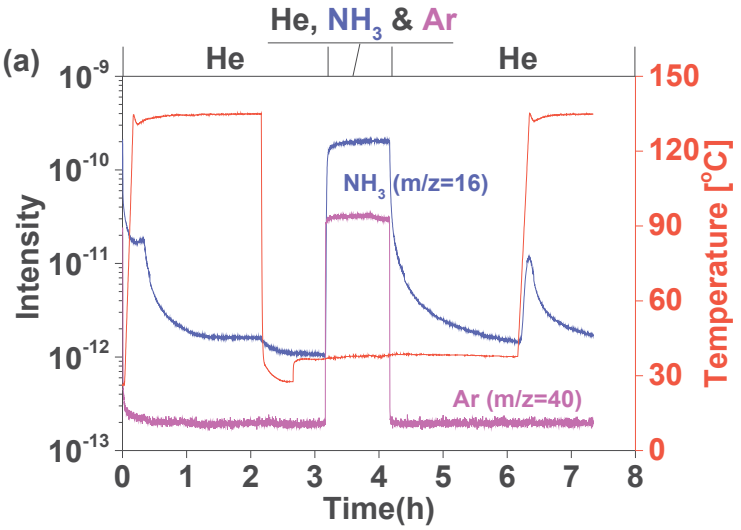

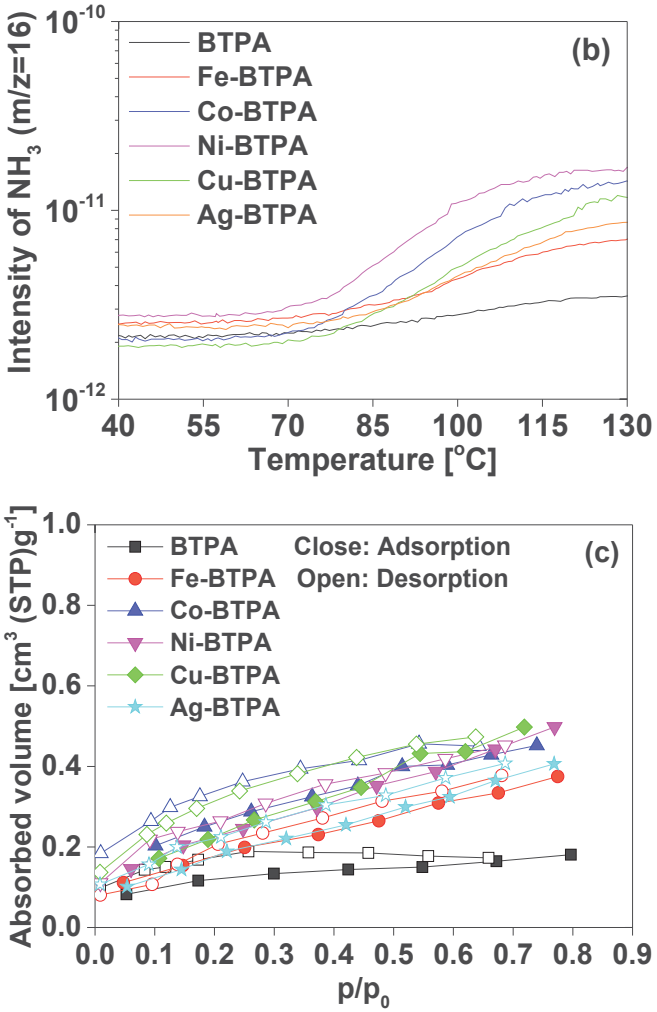

Fig. 2-S1. Time course of mass intensity and temperature during NH_3-TPD measurements for Ni-BTPA powder (a); Intensity of NH_3 (m/z=16) during NH_3 desorption measurements for BTPA and metal-doped BTPA powders (b); N_2 adsorption-desorption isotherms for BTPA-based xerogel powders at -196 °C, where the powder was obtained at a calcination temperature of 150 °C (c).

----------SI-2----------

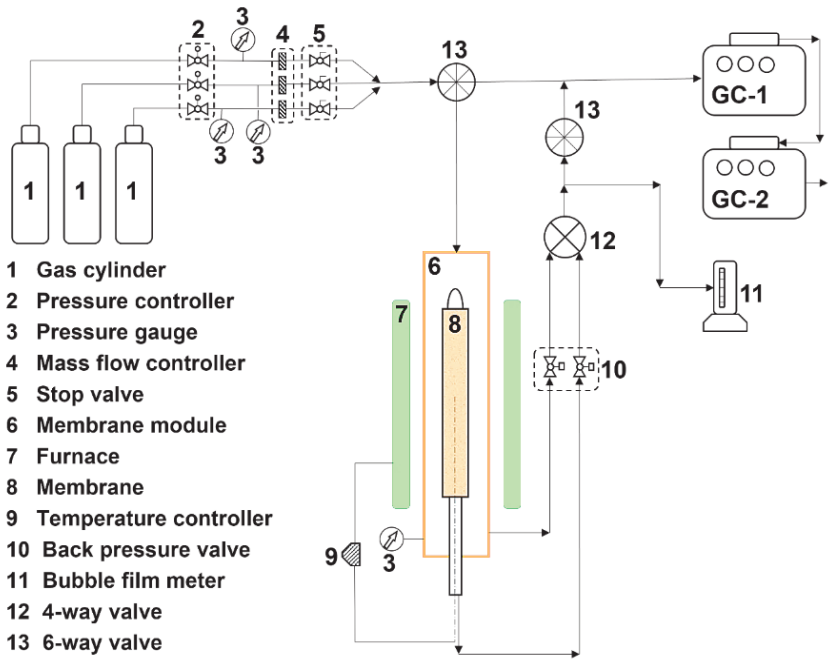

Fig. 2-S2. Schematic diagram of the single- and binary-gas permeation measurement.

----------SI-3----------

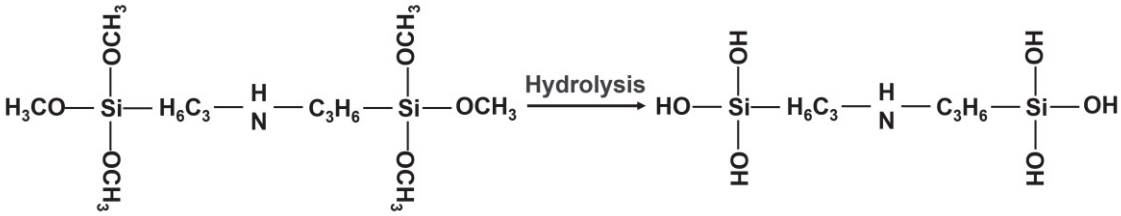

Fig. 2-S3. The chemical structure of BTPA precursors before and after hydrolysis.

----------SI-4----------

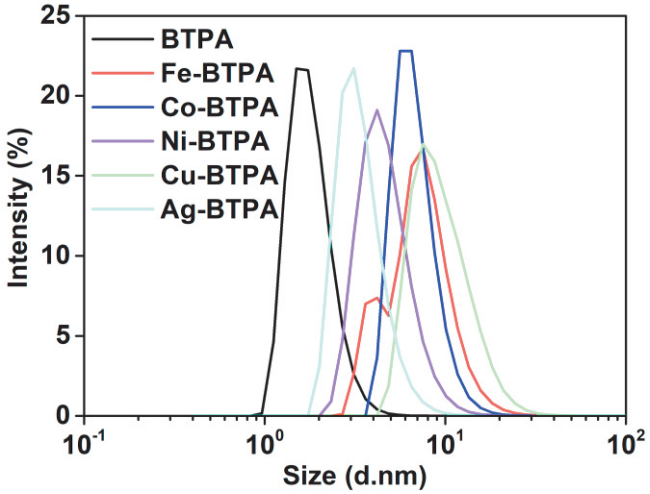

Fig. 2-S4. Size distribution of undoped BTPA and BTPA sol doped with different metals.

----------SI-5----------

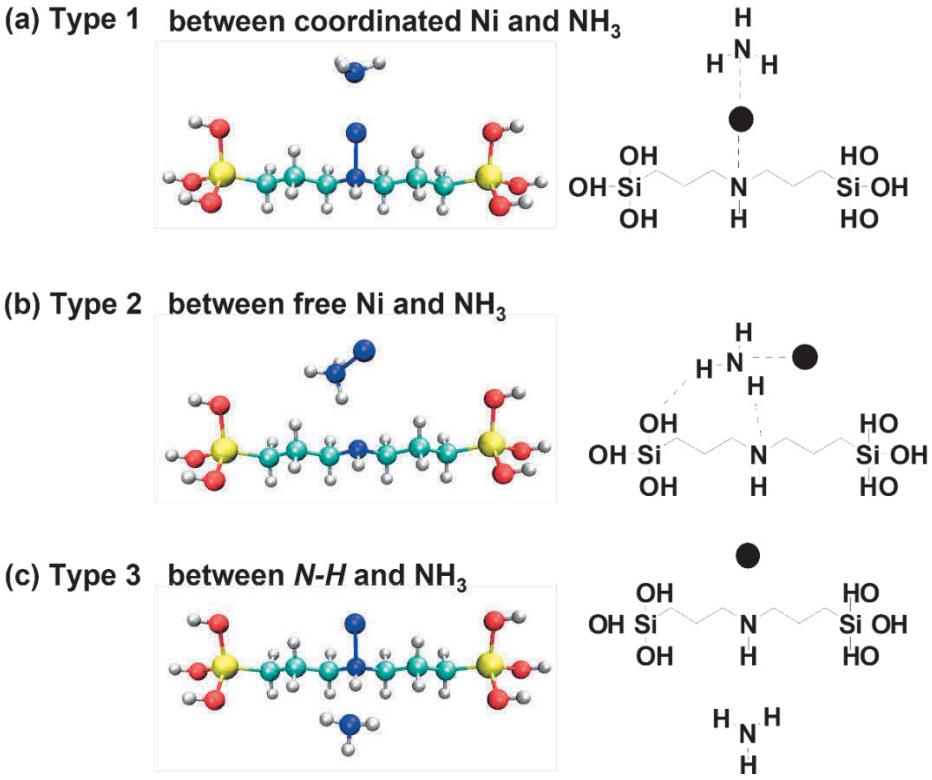

Fig. 2-S5. Interaction types between Ni-BTPA and NH_3.

----------SI-6----------

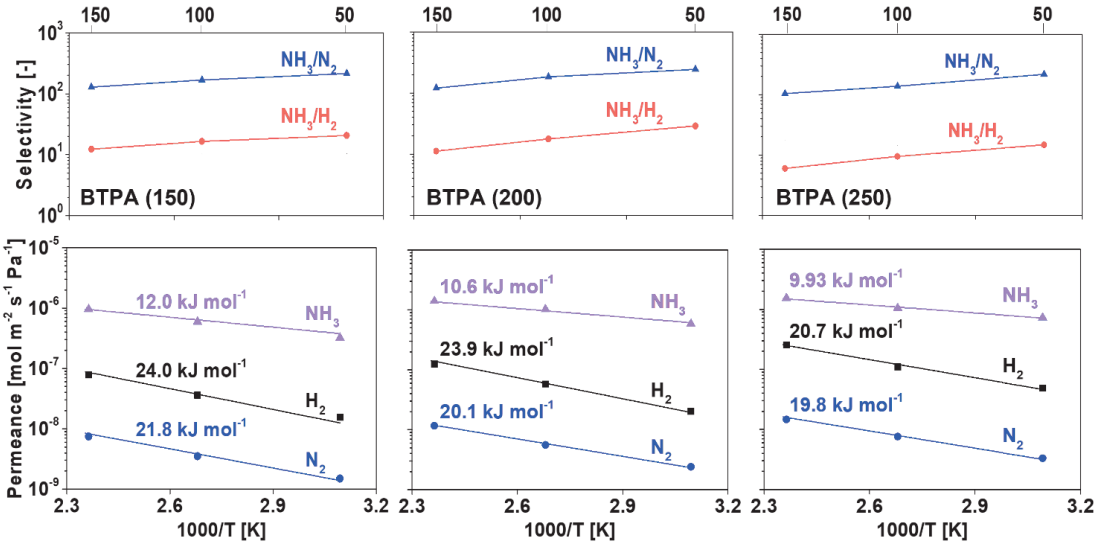

Fig. 2-S6. Temperature dependence of single-gas permeance for BTPA calcined at 150, 200, and 250 °C. Gas permeance was measured at temperatures ranging from 50 to 150 °C.

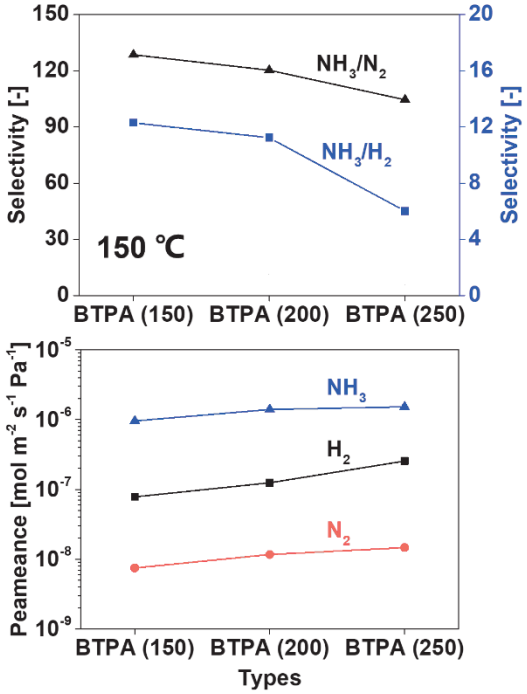

Fig. 2-S7. NH_3 permeance and selectivity at 150 °C as a function of calcination temperature.

----------SI-7----------

As exhibited in Fig. 2-S8, the H_2 and N_2 permeance before and after NH_3 permeation at 50 °C were similar or slightly decreased for all membranes. At 200 °C, the H_2 and N_2 permeance and the H_2/N_2 selectivity were approximately the same before and after NH_3 permeation of 3 h, meaning that the pore size and structure of the membrane could not be clearly changed. Therefore, the BTPA-based membranes showed sufficient stability under NH_3 even at 200 °C.

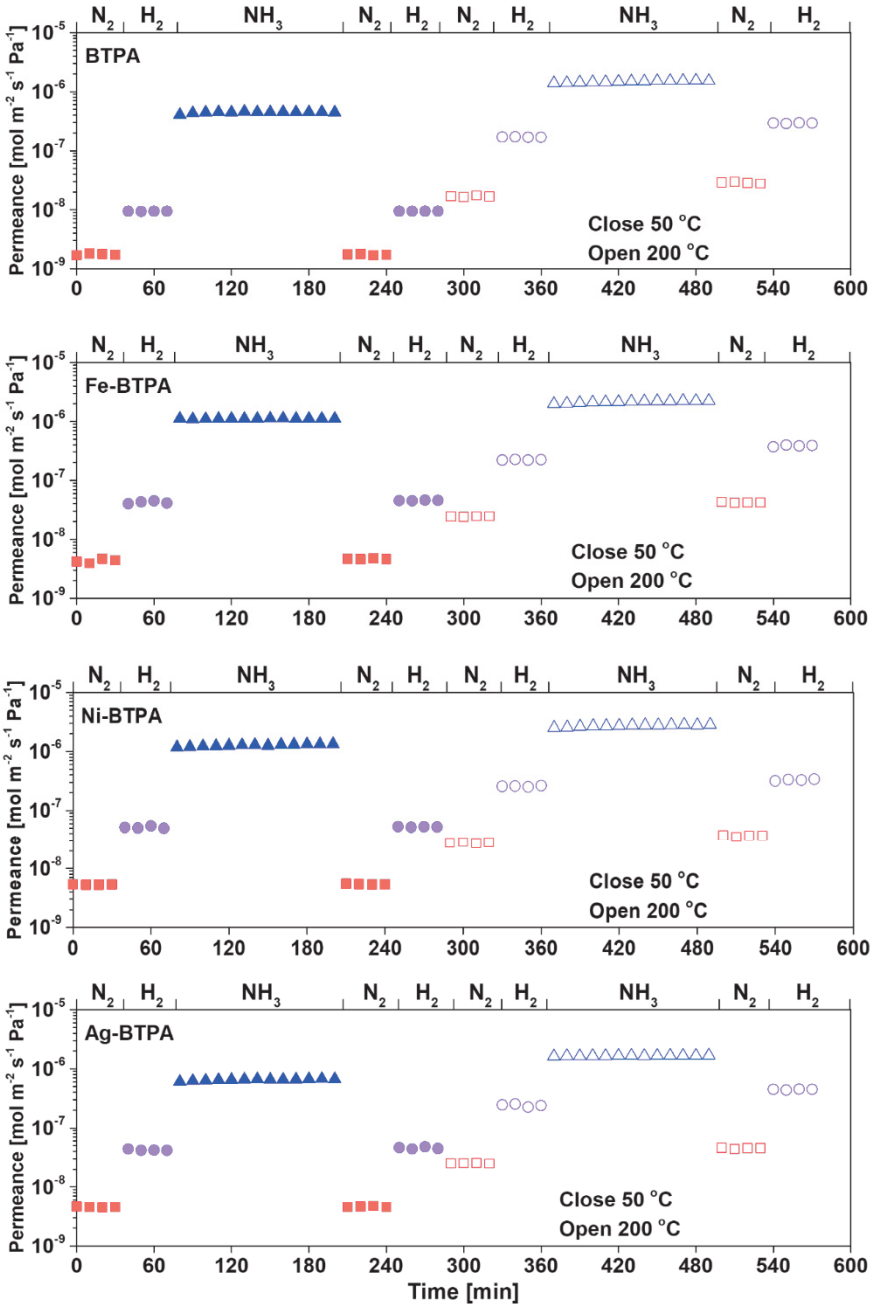

Fig. 2-S8. Time courses for the gas permeance of undoped BTPA and BTPA gels doped with different metals at 200 and 50 °C.

----------SI-8----------

Figs. 2-S9 and S10, all data of which are summarized in Table 2-S1, show the permeation properties of NH_3/H_2 and NH_3/N_2, respectively, for various types of membranes including polymer, inorganic, and hybrid materials in a wide range of permeation temperatures. Several polymers-, such as sulfonated block copolymer membranes, and zeolite-based membranes, such as ZIF-21 membrane, exhibited comparable NH_3 permeance ($>10^{-7}$ mol m^{-2} s^{-1} Pa^{-1}) and remarkable NH_3/H_2 (>100) and NH_3/N_2 (>1000) permselectivity at approximately room temperature, which could be attributed to the excellent NH_3 affinity by hydrogen bonds, acid-base interaction, dipole-dipole interaction, and coordination. However, these membranes using at high temperatures clearly cannot meet the growing demand for NH_3 separation, and only a few of these membranes showed NH_3 permeance exceeding 10^{-6} mol m^{-2} s^{-1} Pa^{-1}. For PFSA-based membranes, such as H^+-Nafion, Ag^+-Nafion, Nafion/ceramic, or Aquivion/ceramic membranes, both NH_3 permeance and permselectivity greatly decreased with increases in the temperature. In this work, metal-doped BTPA membranes showed considerable NH_3 permeance that increases with raising temperatures and acceptable permselectivity even at 200 °C, which could be ascribed to the enlarged pore size *via* the coordination between metal and *N-H* and the improved NH_3 affinity through metal, *N=O*, *N-H*, and *Si-OH*. Increasing the operating temperature of membranes in NH_3 separation will undoubtedly broaden membrane applications, such as membrane reactors, but NH_3 permselectivity would always decrease under high temperatures.

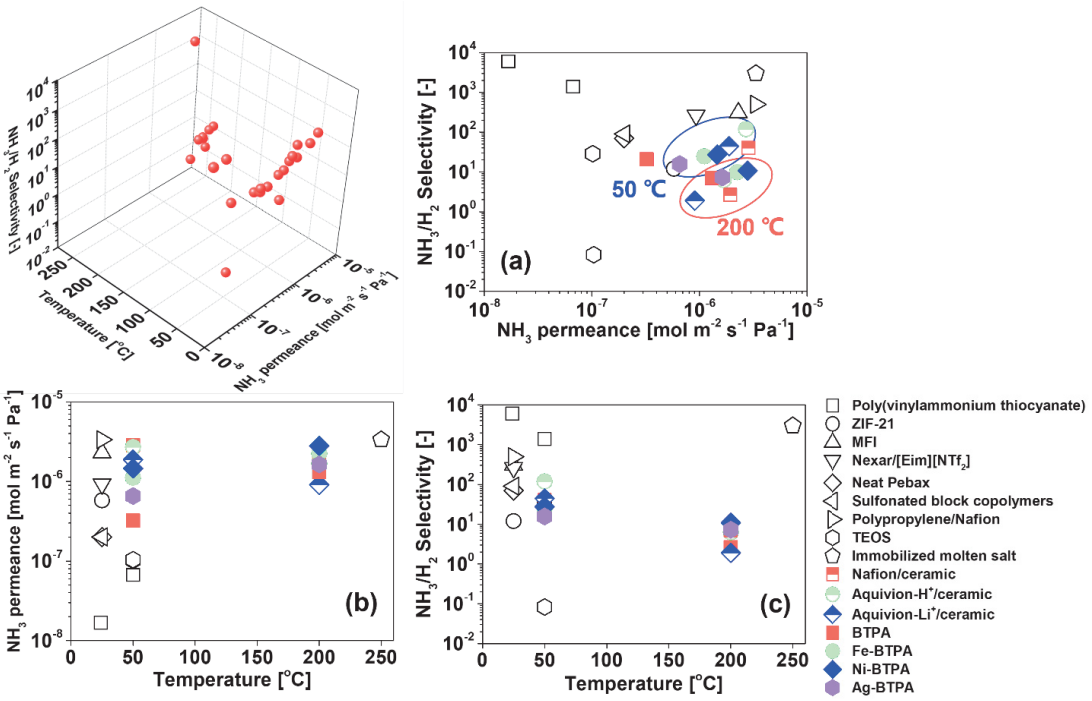

Fig. 2-S9. Trade-off of the NH_3/H_2 selectivity and NH_3 permeance at different temperatures for various membranes.

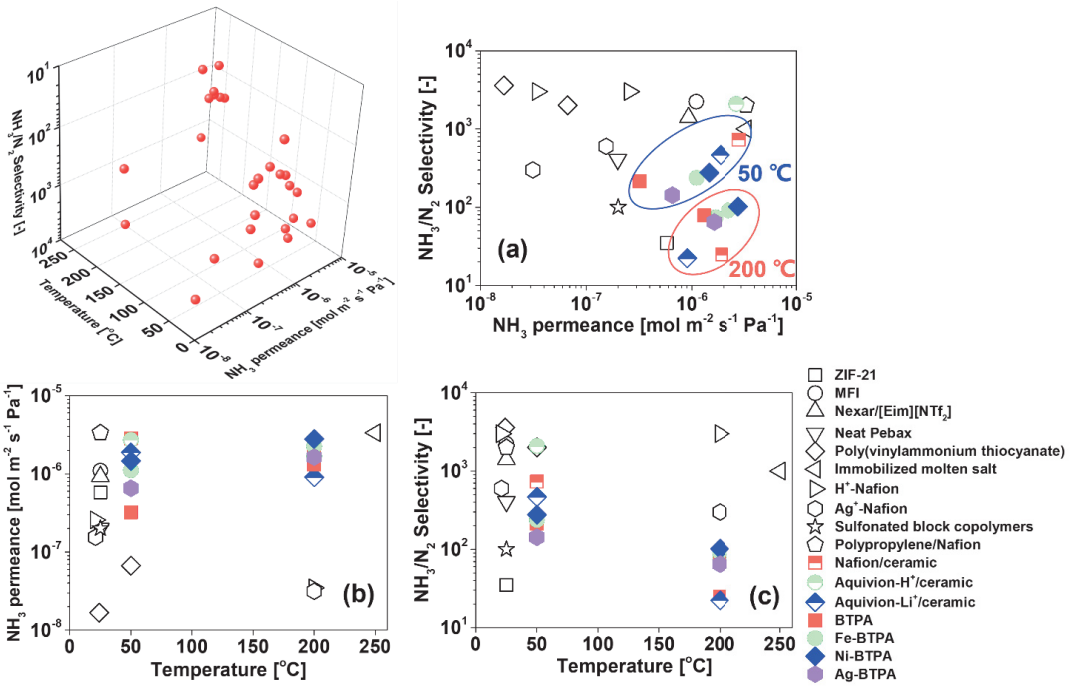

Fig. 2-S10. Trade-off of the NH_3/N_2 selectivity and NH_3 permeance at different temperatures for various membranes.

Table 2-S1. Data for the selectivity and permeance of various membranes.

Name	Temperature [°C]	NH_3 permeance [mol m^{-2} s^{-1} Pa^{-1}]	NH_3/H_2	NH_3/N_2	Ref
Poly(vinylammonium thiocyanate)	24.0	1.6750E-08	6000.0	3600.0	1
	50.0	6.7000E-08	1390.0	2000.0	
ZIF-21	25.0	5.7900E-07	12.0	35.0	2
MFI	25.0	2.3000E-06	307.0	2236.0	3
Nexar/[Eim][NTf_2]	25.0	9.2829E-07	264.0	1407.0	4
Neat Pebax	25.0	1.9959E-07	70.1	406.7	5
Sulfonated block copolymers	25.0	2.0100E-07	90.0	100.0	6
Polypropylene/Nafion	25.0	3.3500E-06	500.0	2000.0	7
TEOS	50.0	1.0200E-07	28.7		8
	50.0	1.0400E-07	0.1		
Nafion/ceramic	50.0	2.8544E-06	40.3	730.9	9
	200.0	1.9355E-06	2.6	24.8	
Aquivion-H^+/ceramic	50.0	2.7100E-06	118.6	2085.9	9
	200.0	1.6800E-06	6.3	73.9	
Aquivion-Li^+/ceramic	50.0	1.8800E-06	44.7	465.6	9
	200.0	9.0500E-07	1.9	22.3	
Immobilized molten salt	250.0	3.3500E-06	3000.0	1000.0	10
H^+-Nafion	21.0	2.5735E-07		3000.0	11
	200.0	3.4743E-08		3000.0	
Ag^+-Nafion	21.0	1.5441E-07		600.0	11
	200.0	3.1434E-08		300.0	
BTPA	50.0	3.2208E-07	20.6	214.2	This
	200.0	1.3107E-06	7.1	78.1	work
Fe-BTPA	50.0	1.1110E-06	24.6	237.6	This
	200.0	2.2437E-06	9.9	90.6	work
Ni-BTPA	50.0	1.4614E-06	27.3	276.7	This
	200.0	2.7995E-06	10.8	101.7	work
Ag-BTPA	50.0	6.5437E-07	15.7	142.6	This
	200.0	1.6300E-06	7.3	64.7	work

References

[1] D.V. Laciak, R. Quinn, G.P. Pez, J.B. Appleby, P.S. Puri, Selective permeation of ammonia and carbon dioxide by novel membranes, *Sep. Sci. Technol.* 25 (1990) 1295-1305.

[2] Q. Wei, J.M. Lucero, J.M. Crawford, J. Douglas Way, C.A. Wolden, M.A. Carreon, Ammonia separation from N_2 and H_2 over LTA zeolitic imidazolate framework membranes, *J. Membr. Sci.* 623 (2021) 119078.

[3] X. Duan, D. Kim, K. Narasimharao, S. Al-Thabaitic, M. Tsapatsis, High-performance ammonia-selective MFI nanosheet membranes, *Chem. Commun.* 57 (2021) 580-582.

[4] B. Yang, L. Bai, S. Zeng, S. Luo, L. Liu, J. Han, Y. Nie, X. Zhang, S. Zhang, NH_3 separation membranes with self-assembled gas highways induced by protic ionic liquids, *Chem. Eng. J.* 421 (2021) 127876.

[5] B. Yang, L. Bai, Z. Wang, H. Jiang, S. Zeng, X. Zhang, X. Zhang, Exploring NH_3 Transport Properties by Tailoring Ionic Liquids in Pebax-Based Hybrid Membranes, *Ind. Eng. Chem. Res.* 60 (2021) 9570-9577.

[6] W.A. Phillip, E. Martono, L. Chen, M.A. Hillmyer, E.L. Cussler, Seeking an ammonia selective membrane based on nanostructured sulfonated block copolymers, *J. Membr. Sci.* 337 (2009) 39-46.

[7] V. Tricoli, E.L. Cussler, Ammonia selective hollow fibers, *J. Membr. Sci.* 104 (1995) 19-26.

[8] M. Kanezashi, A. Yamamoto, T. Yoshioka, T. Tsuru, Characteristics of Ammonia Permeation Through Porous Silica Membranes. *AIChE J.* 56 (2010) 1204-1212.

[9] K. Wakimoto, W.W. Yan, N. Moriyama, H. Nagasawa, M. Kanezashi, T. Tsuru, Ammonia permeation of fluorinated sulfonic acid polymer/ceramic composite membranes, *J. Membr. Sci.* 658 (2022) 120718

[10] D.V. Laciak, G.P. Pez, P.M. Burban, Molten salt facilitated transport membranes. Part 2. Separation of ammonia from nitrogen ana hydrogen at high temperatures, *J. Membr. Sci.* 65 (1992) 31-38.

[11] Y. He, E.L. Cussler, Ammonia permeabilities of perfluorosulfonic membranes in various ionic forms, *J. Membr. Sci.* 68 (1992) 43-52.

Chapter 3

Optimization of Ni-amine coordination for improving NH_3 permeation through nickel-doped bis[3-(trimethoxysilyl)propyl] amine membranes

3.1 Introduction

Ammonia (NH_3), in addition to increasingly being promoted as one of the most important chemicals, is highly expected to act as the energy carrier for hydrogen storage (theoretical H content of 17.6 wt%) and transportation due to its easy liquefication. [1,2] Because of the limited reaction rate of reversible NH_3 synthesis, the NH_3 separation would be a pre-requisite for using a technique and/or materials with sufficient separation factors to promote/move the reaction during NH_3 synthesis, which would improve NH_3 synthesis efficiency. [3,4] Technologies such as condensation, adsorption-desorption, biofiltration, and membrane separation have been used to separate and purify NH_3 from the mixtures through physical transformation and/or chemical affinity. [5-8]

Gas membrane separation technologies that couple controllable pore size, selective adsorption, and thermal stability have received much attention for CO_2 [9,10] and NH_3 [11,12] separation. Polymer membranes [13], zeolite/metal-organic framework membranes [14], ionic liquids/deep eutectic solvent-based membranes [15,16], and silica-based membranes [17] were recently developed to increase NH_3 permeance with high selectivity. Among them, some fluorinated polymer membranes with sulfonic groups have shown excellent NH_3 selective permeation due to the adsorptive interactions between NH_3 and sulfonic groups. [18] Membranes fabricated by introducing ionic liquids/deep eutectic

solvents into polymers have exhibited excellent NH_3 solubility, diffusivity, and selectivity via hydrogen bond. [19,20] Moreover, the remarkable NH_3 permeance ($1.1\text{-}2.3\times10^{-6}$ mol m^{-2} s^{-1} Pa^{-1}) and selectivity (NH_3/H_2: 307 and NH_3/N_2: 2236) [21] have been obtained *via* metal affinity with NH_3 when using zeolite framework membranes at room temperature under high pressure [22].

Besides, the NH_3 permselectivity is known to be enhanced via preferentially adsorbing NH_3 on silica-based membrane to hinder H_2 permeation under low temperatures. [23] Organosilica membranes, such as pyrimidine-bridged organosilica and bis[(trialkoxysilyl)propyl]amine-based, [24,25] have been used for polar gas separation and reverse osmosis. Introducing different functional groups and/or side-links into the silica precursor can also effectively adjust the network pore size and the affinity with the molecules targeted for separation. [26,27] Therefore, amorphous silica-based microporous membranes, which have high thermal stability, sufficient chemical stability, and flexibility, can be strengthened by fine-tuning the structure.

Recently, metal-doped bis[3-(trimethoxysilyl)propyl] amine (BTPA) membranes have shown comparable NH_3 permeance and high NH_3 permselectivity even at 200 °C. [28] Transition metals such as iron, nickel, and silver were anchored in the structure of BTPA via coordination between metal and amine groups (*N-H*) to enlarge the pore size [29] and improve NH_3 affinity. NH_3 temperature-programmed desorption (NH_3-TPD) and single-gas permeation have stablished in Ni-coordinated BTPA as having the strongest NH_3 adsorption capacity and the highest NH_3 permeance with excellent NH_3 permselectivity among different metal ions (Fe, Ni, and Ag). The effect of doping

amount of nickel deserves to be investigated for Ni-doped BTPA membranes in detail, which can optimize the NH_3 affinity based on Lewis acid-base interaction between nickel and NH_3, and improve the selective permeation properties.

In this work, Ni-doped BTPA sols and xerogels with nickel/propylamine (Ni/*N*-*H*) molar ratios of 0, 0.125, 0.25, 0.50, and 1.00 were prepared and characterized through FT-IR, UV-vis, TG-MS, XRD, and NH_3-TPD to account for the affinity of nickel with NH_3. Both single- and binary-gas permeation was measured using Ni-doped BTPA membranes with varying nickel content to evaluate the NH_3 permselectivity. Particularly, the existence form and permeation mechanism of NH_3 in BTPA-based membranes were detailedly expounded by comparing NH_3 permeation in perfluorosulfonic acid (PFSA)-based membranes. Molecular dynamics simulations were applied to visualize and explain the action mechanism between molecules and/or the organosilica network as well as both the interaction types and intensity between H_2/N_2/NH_3 and Ni-doped BTPA.

3.2 Experimental and computational

3.2.1 Sol preparation and membrane fabrication

Fig. 3-S1 displays the sol and membrane preparation processes that can be found elsewhere. [24,28] Briefly, BTPA precursors, $Ni(NO_3)_2{\cdot}6H_2O$, H_2O, ethanol, and HNO_3 as the catalyst were used to prepare the BTPA-based sols *via* the sol-gel method. The molar compositions of the reagents were as follows: BTPA/H_2O/HNO_3 = 1/300/1 with Ni/*N*-*H* molar ratios of 0, 0.125, 0.25, 0.50, and 1.00. A specific amount of BTPA was firstly dissolved in ethanol and then a pre-prepared mixture of H_2O and HNO_3 was

added under continuous stirring. After hydrolysis and condensation reactions for 12 h, the undoped BTPA sol was obtained. Furthermore, Ni-doped BTPA sols with different nickel contents were prepared by dissolving different weights of $Ni(NO_3)_2.6H_2O$ in water and then placing the mixtures into the pre-reacted BTPA sol for 1 h, and these were then labelled as 0.125, 0.25, 0.50, and 1.00 Ni-BTPA. During the preparation process, ethanol was used to control the concentration of the BTPA precursor in the sol solution at 5 wt%.

The macropore on the surface of porous α-alumina tubes (length: 100 mm; average pore size: 1 μm; porosity: 50%; kindly supplied by Nikkato Ltd., Japan) as the support were coated using the α-alumina particles (0.2 and 2 μm) dispersed in a 2 wt% SiO_2-ZrO_2 sol, which was calcined at 550 °C for 15 min. The coating-calcination was repeated 3-4 times to cover all the macropores of the support to form the porous α-alumina particle layers. After that, the particle layers were further coated with a 0.5 wt% SiO_2-ZrO_2 sol to reduce the pore size to ~1 nm, which was also calcined at 550 °C for 15 min to acquire the intermediate layer. The pore size of the SiO_2-ZrO_2 intermediate layer was estimated under a N_2 flow via Nanopermporometry, [30] as exhibited in Fig. 3-S2. Finally, the synthesized BTPA-based sol solutions were diluted with water to 0.1 wt%, then the diluted sols were coated on the intermediate layer to construct the top separation layer, which was calcined at 150 °C for 30-40 min under a N_2 atmosphere. A more detailed account of the membrane fabrication process can be found elsewhere. [29]

3.2.2 Characterization

The size distribution of the above-synthesized sols was analysed using dynamic light scattering (DLS, Malvern Zetasizer ZEN 3600). A Fourier transform infrared spectrometer (FT-IR-4100, JASCO, Japan) was used to analyse the chemical structures of the samples that was prepared by coating the sols onto KBr plates, and the samples were calcined at different temperatures under a N_2 atmosphere to examine the thermal stability. All BTPA-based xerogels as well as the fresh $Ni(NO_3)_2{\cdot}6H_2O$ and its derived powders that were obtained after being dissolved in water and dried were analysed utilizing an Ultraviolet-visible spectrometer (UV-570, JASCO, Japan). The thermal properties of xerogels were evaluated using a thermogravimetric mass spectrometer (TG-MS, TGA-DTA-PIMS 410/S, Rigaku, Japan). The xerogel powders were pre-treated at different temperatures under a N_2 atmosphere and characterized using an X-Ray diffractometer (XRD, D2 PHASER Bruker, Germany) in a 2θ range of from 2 to 80^0. The scanning electron microscopy (SEM, HITACHI S-4800, JEOL, Japan) was used to examine the membrane morphology. The xerogel powders were firstly calcined at 150 °C under a N_2 atmosphere and further evacuated at 130 °C under vacuum conditions for 12 h, the pre-treated powders were used for N_2 sorption measurement (BELL Inc., Japan).

The NH_3 adsorption and desorption amounts were analyzed using a BELCAT-AT equipped with BELMASS-HT (BELL Inc., Japan) based on the following proceduce and calculated by the equations (Eq-1 and Eq-2), repectively. The xerogel powders were pre-treated at 150 °C to remove any adsorbed molecules under dry He at 30 ml min^{-1} for 120 min, followed by decreasing the temperature from 150 to ca. 30 °C, and

then maintained at ca. 30 °C for 60 min. Then, a 5% NH_3/95% He mixture gas was fed into the system at 30 ml min^{-1} for 90 min together with Ar as a non-adsorption gas at 1 ml min^{-1} at ca. 30 °C from time t_1 to t_2. After reaching adsorption equilibrium, pure He was continuously fed at 30 ml min^{-1} for 120 min, and at 40 °C for 120 min. Finally, the temperature was raised from 40 (time: t_3) to 150 °C (t_4) at 10 °C min^{-1}, and held at 150 °C for 60 min.

$$NH_3 \text{ adsorption amount} = \frac{1}{m}\int_{t1}^{t2}\left(\frac{I_{Ar,t}\frac{I_{NH_3,in}}{I_{Ar,in}} - I_{NH_3,t}}{I_{NH_3,in}}\right)Q_{NH_3}\,dt \qquad \text{Eq-1}$$

$$NH_3 \text{ desorption amount (40}\rightarrow\text{150 °C)} = \frac{1}{m}\int_{t3}^{t4}\left(\frac{I_{NH_3,t}}{I_{NH_3,in}}\right)Q_{NH_3}\,dt \qquad \text{Eq-2}$$

m: weight of sample (g); $I_{i,in}$: intensity of the feed i-th component; $I_{i,t}$: intensity of the feed i-th component at each moment; Q_{NH_3}: flow rate of NH_3.

The average amount of NH_3 adsorption and desorption was calculated according to the data from the measurements that were repeated 3 times. Fig. 3-S3 in the Supplementary Material (SI-3) shows the temperature-program and the time course of mass signals.

3.2.3. Single- and binary-gas permeation measurements

Fig. 3-1 schematically depicts the experimental apparatus, which was used for the gas permeation. High-purity He, H_2, NH_3, N_2, CH_4, CF_4, and SF_6 were fed to the outside of the membrane under upstream pressures at 50-300 kPa, and the permeate stream was kept at atmospheric pressure. Prior to the measurement of the gas permeation, the membrane was pre-processed under a He flow at 150 °C for least 6 h to remove the adsorbed water molecules. Single-gas measurements, except for NH_3, were performed at 50 to 200 °C using a film flow meter (Horiba, Co. Ltd., Japan) to collect the flow-rate values.

In order to record the flow-rate values of NH_3 permeation, the mass flow meter 4 (Fig. 3-1), that has been calibrated via a gas chromatograph (GC) using Ar as the carrier gas, was used to measure the flow rate of permeated NH_3 by closing the retentate valve (V-10a in Fig. 3-1). For binary-gas permeation, GC-1 and GC-2 equipped with a Porapack N column and a Molecular Sieve X column were used to analyze the NH_3 and H_2 (or N_2) concentrations, respectively. Generally, the flow-rate data of gases were recorded at least 3 times and then averaged when the permeation reached a steady state. And the errors in the flow-rates of the gases were less than 5% when the permeance was larger than 10^{-10} mol m^{-2} s^{-1} Pa^{-1} and less than 50% for a the permeance smaller than 10^{-10} mol m^{-2} s^{-1} Pa^{-1}.

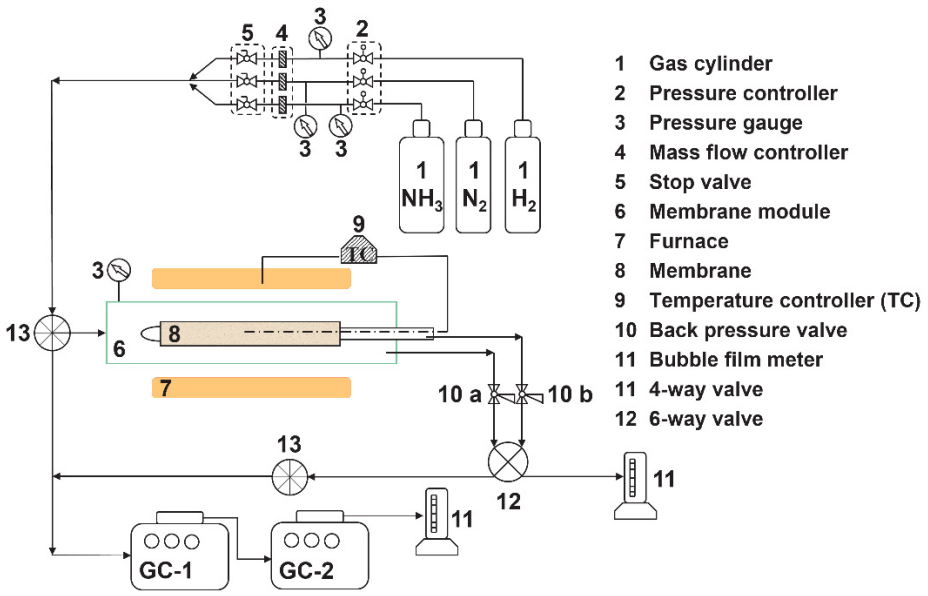

Fig. 3-1. Schematic diagram of the single- and binary-gas permeation measurement.

3.2.4. Molecular dynamics simulation

The Ni-BTPA sols with Ni/*N*-*H* molar ratio of 0.25, 0.5, and 1.0 were prepared, so nickel could be assumed to coordinate with BTPA via the associations of Ni and *N*-*H* in the form of 4 coordination numbers, 2 coordination numbers, and 1 coordination

number, respectively. The structures of H_2, N_2, NH_3, and the Ni-coordinated BTPA were drawn with GaussView 05 software and optimized using the Gaussian 09 D.01 program. [31] The TPSSh-D3(BJ) method [32] combined with the mixed basis set that SDD [33] and 6-311g* were applied to calculate nickel and other compounds, respectively. The details of the structures are shown in Fig. 3-S6.

The Sobtop program, [34] Gromacs 2018.4 package [35] with the Amber14sb-OL15 and generalized AMBER force field, [36] and the Packmol program [37] were used for molecular dynamics simulation. Additionally, the Visual molecular dynamics program [38] was used to analyze the dynamic trajectories, and then the interaction types between H_2/N_2/NH_3 and Ni-coordinated BTPA were analyzed by Multiwfn program [39] combined with the Independent gradient model (IGM) method [40]. Details of the simulation process are described in SI-5.

3.3 Results and discussions

3.3.1 Effect of Ni-doping amounts on sol size and structure

As shown in Fig. 3-2, the size distribution of all Ni-coordinated BTPA sols was larger than that of the undoped BTPA sol because the coordination between nickel and *N-H* that resulted from by the charge transfer induced the growth of sols via cross-linking [41]. The size of Ni-doped BTPA sols gradually increased with increases in Ni/*N-H* molar ratio that is essentially a transformation of the theoretical coordination types between nickel and *N-H*. All BTPA-based sols were transparent without any precipitation and were coated onto the intermediate layer to produce the topmost separation layer. [42]

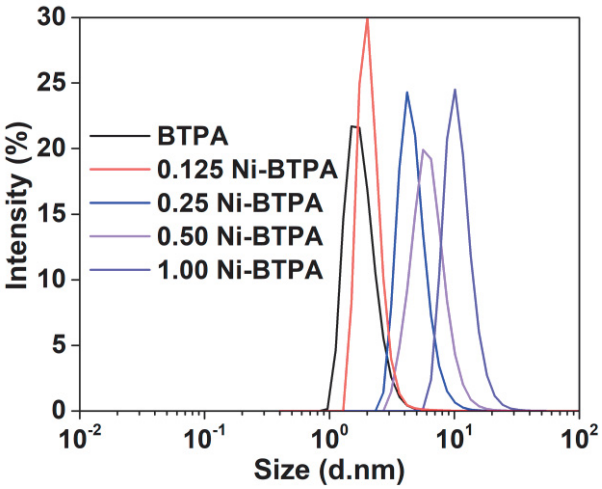

Fig. 3-2. Size distribution of BTPA and different Ni-doped BTPA sols.

Fig. 3-3 shows the FT-IR spectra of BTPA and different Ni-BTPA films with and without calcination at 150 and 200 °C. The intensity of *Si-OH* (895 cm^{-1}) characteristic peaks obviously decreased with increases in the calcination temperature, as illustrated in Fig. 3-3 (left), because of the dynamic transformation of *Si-OH* to *Si-O-Si* and the condensation of the organosilica network after heating films at different temperatures. The *N=O* from either HNO_3, $Ni(NO_3)_2$, or coordinated *N=O* was partially retained in the BTPA structure, which was proven by the sharp peak of *N=O* (1385 cm^{-1}) at 200 °C in all films.

According to the reported results [28,42], the characteristic peak of *N-H* can markedly split in all metal-doped BTPA films fired at 250 °C since the removal of HNO_3 and water enhanced the coordination between the metal and *N-H*. As exhibited in Fig. 3-3 (right), the characteristic peak of *N-H* only in the fresh 1.00 Ni-BTPA film split and blue-shifted to the higher wavenumber, independent of the calcination temperature, indicating that the coordination between nickel and *N-H* was observably enhanced, consistent with the reported XPS data [42]. Therefore, it can be considered that the lone-pair

electrons of the *N* atom on *N-H* could be intensively transferred to the empty *d* orbital of nickel in 1.00 Ni-BTPA, resulting in the strengthening coordination between nickel and propylamine. Additionally, the characteristic peak of *C-H* functional groups (2700-2950 cm^{-1}) still existed clearly even at 200 °C, indicating that the propylamine chain had not decomposed.

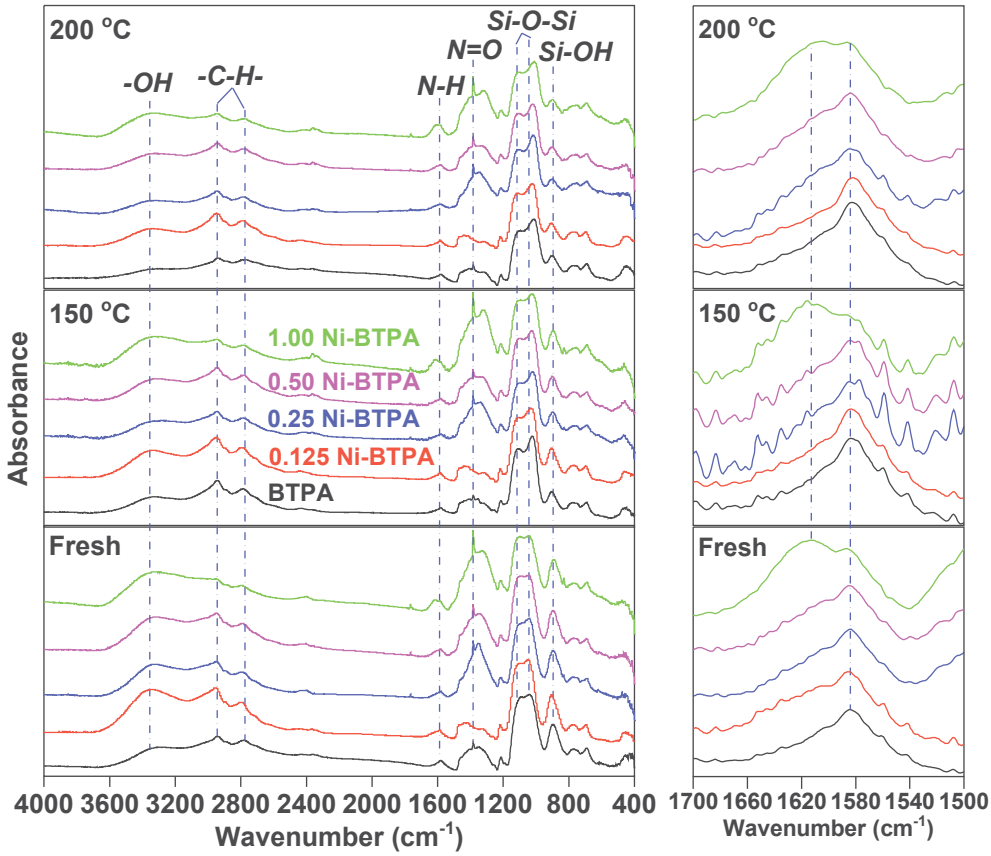

Fig. 3-3. FT-IR spectra of BTPA-based films at different calcination temperatures (left); the narrow FT-IR spectra for the *N-H* deformation band ranging from 1700 to 1500 cm^{-1} (right).

3.3.2 Characterization of different Ni-doped BTPA xerogel powders

Fig. 3-4 displays the UV-vis spectra of different Ni-doped BTPA xerogels (Ni/*N-H*=0, 0.125, 0.25, 0.50, and 1.00), and fresh $Ni(NO_3)_2 \cdot 6H_2O$ and its derived powders which were prepared by dissolving in a mixture of HNO_3 and H_2O and then dried at ~50 °C. The transition types of $n \rightarrow \sigma^*$, $n \rightarrow \pi^*$, and $d \rightarrow d$ correspond to the electron transitions

of *N−H*, *N=O*, and d^8 Ni^{2+}, respectively. [42] The absorption peak at 392 nm from fresh $Ni(NO_3)_2 \cdot 6H_2O$ can be ascribed to the *d-d* transition of the d^8 Ni(II) complex, which was redshifted to 400 nm for its derived powder probably due to the amorphous structure, indicating that nickel can also interact with *N=O* and/or *O-H* by a strong *d-d* transition from the lone-pair electrons in *N=O* and/or *O-H* to the empty *d* orbitals of nickel in Fig. 3-4 (a). Reportedly, the coordination between nickel and *N=O* has also been demonstrated from $Ni(NH_3)_2(NO_3)_2$ obtained from the thermal decomposition of $Ni[(NH_3)_6](NO_3)_2$. [43] After doping $Ni(NO_3)_2$ into BTPA, the absorption peak of the *d-d* transition of d^8 Ni(II) was blue-shifted to 395 nm as shown in Fig. 3-4 (b), which could be ascribed to the coordination between *N=O*/*N-H* and nickel. With an increase in the Ni/*N-H* molar ratio, the transition of $n \rightarrow \sigma^*$ (*N−H*) gradually red-shifted to a higher wavelength, which meant the free electrons from *N−H* could migrate further to the empty *d* orbital of nickel, particularly for 1.00 Ni-BTPA, resulting in the stronger coordination that has been proven via analyzing FT-IR spectra. Inversely, the $n \rightarrow \pi^*$ (*N=O*) blue-shifted to a lower wavelength possibly due to the strong coordination between nickel and *N-H*. A comprehensive analysis of the electron transition of *N=O* and *N-H* indicated that nickel could be more inclined to coordinate with *N-H*.

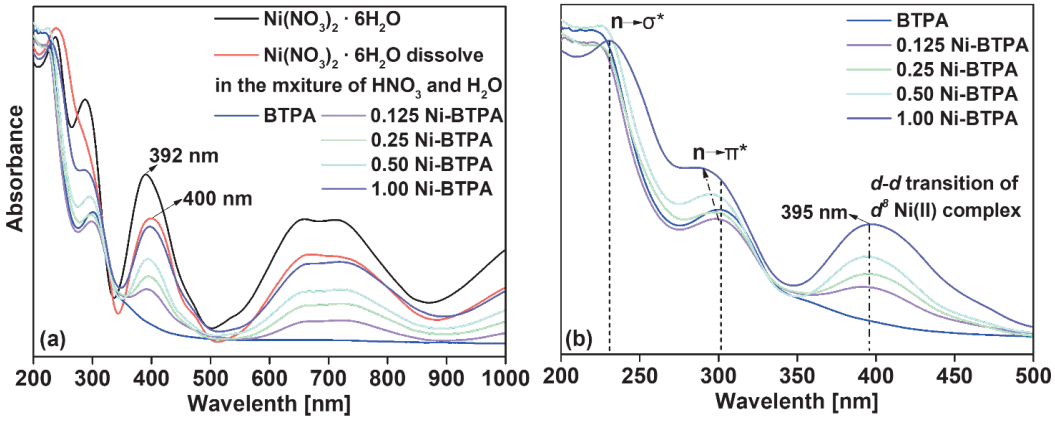

Fig. 3-4. UV-vis spectra of $Ni(NO_3)_2 \cdot 6H_2O$ and its derived powders and different Ni-doped BTPA powders: (a): 200-1000 nm; (b): 200-500 nm.

Fig. 3-5 shows the total weight-residue of Ni-coordinated BTPA xerogel powders increase with raising the Ni/*N-H* molar ratio, which could be ascribed to the decomposition and/or evaporation of the nickel species. As indicated in the inset of Fig. 3-5 in temperature ranges from 100 to 300 °C, and the initial decomposition temperature of Ni-coordinated BTPA xerogel powders (around 200 °C) was increased when Ni/*N-H* molar ratios were from 0.125 to 0.5 higher than that of BTPA xerogel powders, which could be attributed to the increase in the decomposition temperature of the free *N=O* [28] because nickel with a six-coordination number can coordinate with more *N=O*. Moreover, when the Ni/*N-H* molar ratio was increased from 0.125 to 1.0, the powder seemed to be easily decomposed (around 400 °C) and the total weight-residue was decreased gradually, which could be ascribed to a reallocation of the free electrons in amine moieties due to the introduction of nickel and/or the oxidation/hydrogen abstraction of the propylamine with lower *C-H* bond dissociation enthalpies (BDE) by NO_3 radicals [44], resulting in a decrease in the thermal stability of the propylamine chain of BTPA.

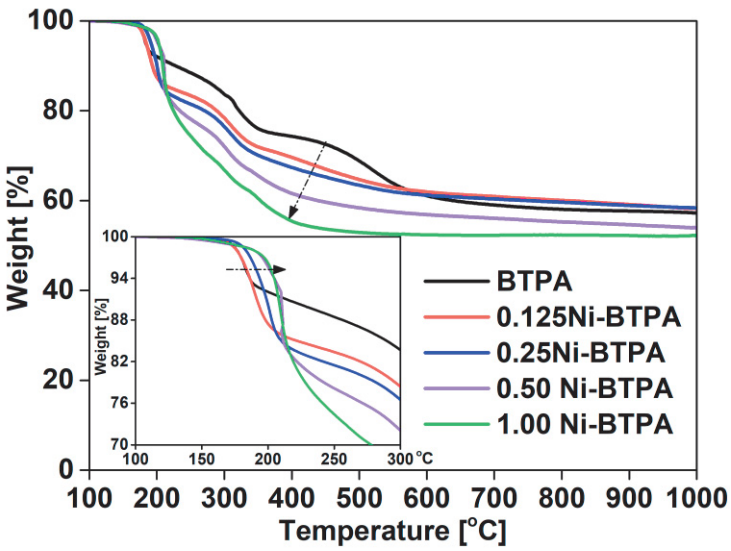

Fig. 3-5. Thermal property analysis of BTPA-based powders by TG-MS.

Based on the previous results [28], in TG-MS singles (m/z=30) exhibited in Fig. 3-6, peaks 1, 2, and 3 in BTPA xerogel powders could be attributed to free *N=O*, coordinated *N=O* with *N-H* or metals, and alkyl-amine molecules, respectively. The peak 1 gradually shifted to a higher temperature after doping nickel into BTPA, and the peak 5 observed in 0.5 Ni-BTPA xerogel powders appeared at high temperatures (ca. 210 °C). As mentioned above, the UV-vis analysis and a published paper [42] show that nickel doped into BTPA structure can not only form the coordination with *N-H*, but also interact with *N=O* certainly via charge transfer. Therefore, the free *N=O* (peak 1) that interacted with nickel probably increased its decomposition temperature and the affinity of nickel to *N=O* increased with raises in the Ni/*N-H* molar ratio from 0.125 to 1.00, consistent with the weight-loss trend around 200 °C (the inset of Fig. 3-5).

According to the theoretical coordination number of nickel and the coordination structure between nickel and BTPA, as shown in Fig. 3-S6, nickel could reserve more coordination sites to bind more *N=O* with increases in the Ni/*N-H* molar ratio, so the

affinity of nickel to *N=O* would increase the initial decomposition temperature of *N=O* in Ni-BTPA xerogel powders. Moreover, the characteristic peak 2 of *N=O* coordinated with *N-H* in BTPA gradually shifted to lower temperatures (peaks 6 and 7), which could be ascribed to the weakening of acid-base interactions between *N-H* and *N=O* due to the enhanced coordination between nickel and *N-H*. Nevertheless, after doping nickel into BTPA, peak 3 in undoped BTPA could be shifted to peak 4 in 0.125 Ni-BTPA and peaks 6 and 7 in 0.25, 0.50, and 1.00 Ni-BTPA, meaning that the alkyl-amine molecules were easily decomposed at temperatures below 300 °C after doping nickel into BTPA because of the oxidation/hydrogen abstraction of the propylamine with NO_3 radicals.

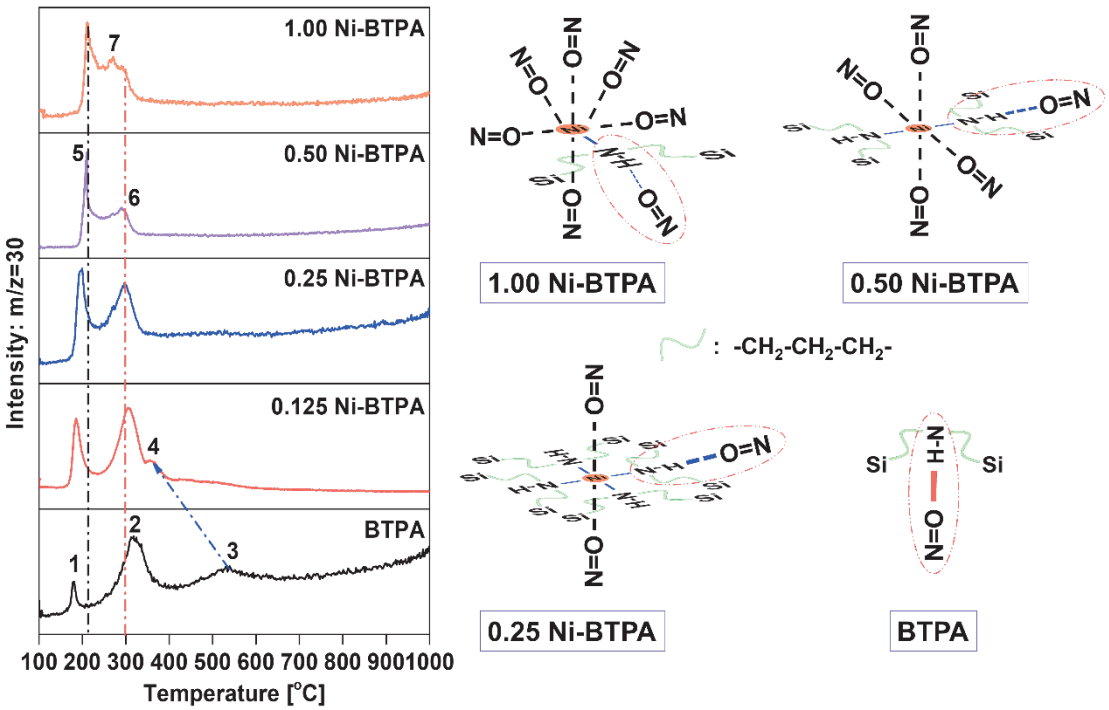

Fig. 3-6. The mass signal of m/z = 30 in BTPA and different Ni-doped BTPA powders as a function of thermal treatment (left) and schematic illustrations of the interactions of different BTPA-based xerogel powders (right).

After calcination at 150 °C, the characteristic peak of nickel particles did not appear in all Ni-BTPA xerogels, as shown in Fig. 3-7, manifesting that the interaction between

nickel and *N-H* was sufficiently stable at 150 °C, even though more nickel (Ni/*N-H*=1.0) was doped into BTPA. As the temperature rose to 200 °C, the characteristic peaks of metallic nickel nanoparticles appeared with different intensities in all Ni-BTPA xerogels. In particular, the 1.00 Ni-BTPA with an excess amount of nickel possibly aggregated and/or segregated to form large particles of 11.2 nm calculated by Scherrer's formula, which could also be confirmed from the peak intensity of the *d-d* transition of the d^8 Ni(II) complex in the UV-vis spectra.

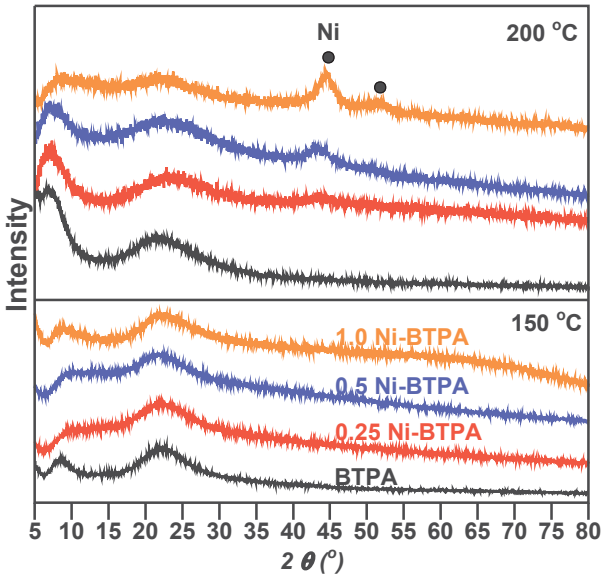

Fig. 3-7. Wide angle XRD patterns for BTPA-based xerogel powders at different calcination temperatures.

3.3.3 NH_3-TPD of different Ni-doped BTPA powders and interaction between Ni-BTPA and NH_3

NH_3 adsorption-desorption measurement was carried out to evaluate the NH_3 affinity for the different BTPA-based powders, as shown in Fig. 3-8, and the typical time courses can be found in SI-3. All nickel-doped BTPA xerogel powders showed a larger NH_3 adsorption capacity than undoped BTPA and PFSA in Fig. 3-8 (a), indicating

nickel with a six-coordination number and efficient electronegativity can greatly improve the NH_3 affinity. With an increase in the Ni/*N*-*H* molar ratio doped in BTPA, the NH_3 adsorption capacity significantly increased from 0.66 (Ni/*N*-*H* = 0), 0.74 (Ni/*N*-*H* = 0.125), and 0.95 (Ni/*N*-*H* = 0.25) to 1.77 mmol g^{-1} (Ni/*N*-*H* = 0.5), but the NH_3 adsorption amount decreased slightly for 1.00 Ni-BTPA (1.75 mmol g^{-1}). Moreover, as displayed in Figs. 3-8 (b) and (c), the temperature where NH_3 desorption was initiated during NH_3 desorption process was lower for 1.00 Ni-BTPA than that for BTPA, 0.125, 0.25 and 0.50 Ni-BTPA, suggesting that the NH_3 affinity of 1.00 Ni-BTPA was possibly weakened. As shown in Fig. 3-S4, the NH_3 adsorption and desorption amount of each sample decreased slightly in turn during repeat testing, indicating that less NH_3 could be irreversibly adsorbed in the xerogel powders.

The N_2 adsorption isotherms of BTPA-based xerogel powders pre-calcined at 150 °C under a N_2 atmosphere were measured, as displayed in Fig. 3-S5. The adsorbed volume of all xerogel powders was less than 0.5 cm^3 (STP)g^{-1}, which corresponds to 0.022 mmol g^{-1}, indicating an approximately nonporous network. Consequently, the affinity of the metal and/or functional groups (*Si*-*OH*, *N*=*O*, and *N*-*H*) to NH_3 could be considered to dominate the NH_3 adsorption amounts of both nickel-doped BTPA and pure BTPA.

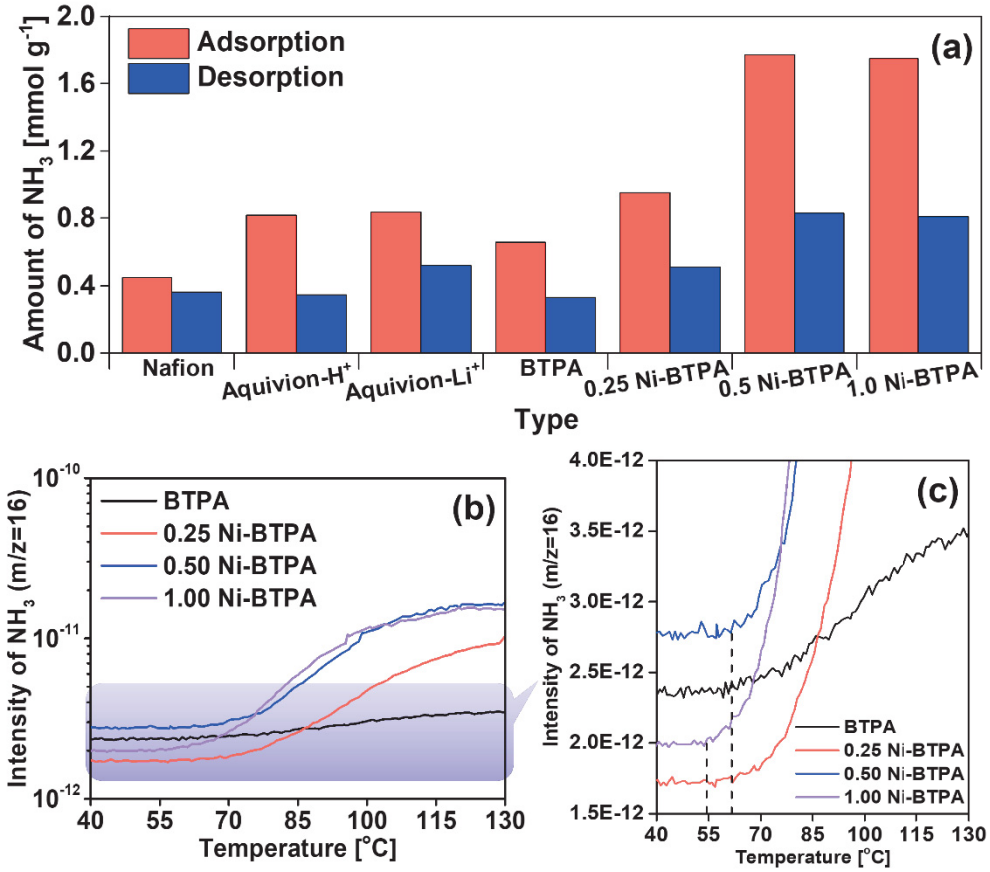

Fig. 3-8. NH_3 adsorption and desorption amounts of BTPA and Ni-doped BTPA at 150 °C (a); intensity of NH_3 (m/z=16) during NH_3-TPD measurements for BTPA and Ni-doped BTPA xerogel powders (b,c).

The coordination types between transition metals and ligands in molecular adsorption have been investigated via molecular simulation, [45] especially, nickel with a six-coordination number, which forms a tetra-coordination with nitrogen ligands, can still coordinate with oxygen ligands. [46] SI-6 describes the simulation results about radial distribution function (RDF) and interaction types for Ni-BTPA with different Ni/*N*-*H* molar ratios. Both NH_3 distribution probability of different Ni-BTPA by RDF analysis and interaction types between NH_3 and different Ni-BTPA by IGM analysis follow this order: 0.5 Ni-BTPA ≥ 1.00 Ni-BTPA > 0.25 Ni-BTPA. This result is consistent with the NH_3-TPD results. The NH_3 affinity can be enhanced by doping nickel into BTPA.

However, because of the binding site (coordination) of nickel being fully occupied by *N-H* and the steric hindrance, the NH_3 affinity did not improve significantly in 0.25 Ni-BTPA. Furthermore, the strengthening of the coordination between nickel and *N-H* in 1.00 Ni-BTPA was also bound to negatively affect the NH_3 affinity through the competitive interactions, as shown in Fig. 3-8 (c). Therefore, for 0.5 Ni-BTPA, nickel has sufficient binding sites (coordination) and considerable interaction intensity to interact with NH_3, which effectively improves the NH_3 affinity.

3.3.4 Gas permeation properties of BTPA-based membranes

Figs. 3-9 (a) and S11 (left) demonstrate that single-gas permeance at 200 °C as a function of the molecular size of permeating gases. It should be noted that Ni-BTPA membranes prepared by calcination at 150 °C were confirmed to be thermally stable at 200 °C by temperature-swing experiments from 150 to 200 °C and back to 150 °C under H_2, N_2, and NH_3, respectively. [28] Permeance was decreased with the molecular size of permeating gases due to the molecular sieving. Importantly, gas permeance generally increased with increases in the Ni/*N-H* molar ratio due to the reduced gas-transport resistance, consistent with previous reports [42].

Dimensionless permeance based on He permeance in Fig. 3-9 (b) shows that all membranes showed better gas permselectivity than that of Knudsen diffusion. In this study, 1.00 Ni-BTPA still performed good gas permselectivity, which is different from previous reports where the 1.00 Ni-BTPA membrane calcined at 250 °C showed a loose structure and gas permselectivity similar to Knudsen diffusion due to the formation of interparticle pores caused by the aggregation of nickel particles. This demonstrated that

the membrane directly calcined at high temperature, such as 250 °C, enhanced aggregation and/or segregation of more nickel particles, resulting in the formation of interparticle pores and in a great reduction in the gas permselectivity of the membrane. The H_2/N_2 and H_2/CH_4 permselectivity was low, however, for 1.00 Ni-BTPA membrane as shown in Fig. 3-S11 (right), implying that the pore size of the membrane was enlarged by excessively increasing in the nickel content. Besides, Fig. 3-S12 shows the morphology of BTPA and 0.50 Ni-BTPA membranes, which confirms that the membranes have the multi-layered structures (top, SiO_2-ZrO_2 intermediate, α-Al_2O_3 particle, and support layers) and shows a smooth top-layer with a thickness of ~100 nm and without any defect.

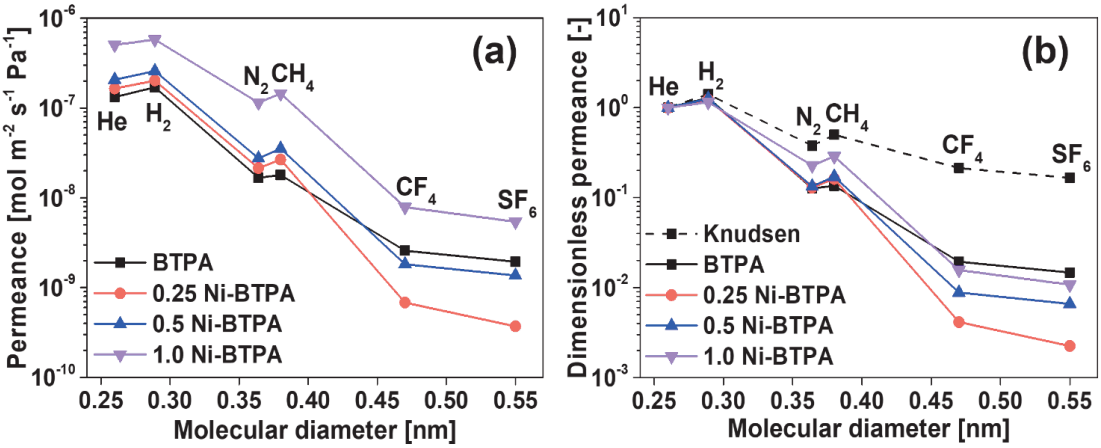

Fig. 3-9. Kinetic diameter dependence of single-gas permeance (a) and dimensionless permeance (b) at 200 °C for BTPA and different Ni-doped BTPA membranes.

Fig. 3-S13 in SI-9 displays the time courses for H_2, N_2, and NH_3 permeance in BTPA and different Ni-doped BTPA membranes at 200 and 50 °C. Although increasing the nickel molar ratio greatly enlarged the pore sizes of the membrane, the H_2 and N_2 permeance were stable with approximately constant values for undoped BTPA and all Ni-BTPA membranes even after NH_3 permeation for 3 h at 50 and 200 °C, as previously

reported superior NH_3 resistance [28].

Fig. 3-10 exhibits H_2, N_2, and NH_3 permeance and NH_3 selectivity at 50 and 200 °C as a function of the Ni/*N-H* molar ratio. The H_2/N_2 permselectivity was gradually decreased with increases in the nickel content in BTPA together with increases in the H_2 and N_2 permeance at both 50 and 200 °C, indicating that the pore size of the membrane was enlarged through increasing nickel content. However, the ideal NH_3/H_2 and NH_3/N_2 selectivity increased as the increase of Ni/N-H molar ratio from 0, 0.25 to 0.5, meaning that NH_3 permeance mainly depends on the affinity of nickel. Furthermore, with an increase in Ni/*N-H* molar ratio from 0, 0.25 to 0.5, the NH_3 permeance increased greatly from 3.2×10^{-7}, 5.8×10^{-7} to 1.5×10^{-6} mol m^{-2} s^{-1} Pa^{-1} at 50 °C, and then slightly increased to 1.6×10^{-6} mol m^{-2} s^{-1} Pa^{-1} in 1.00 Ni-BTPA membrane that could be ascribed to the enlarged pore size of membrane. The NH_3 permeance increased almost linearly as increasing Ni/*N-H* molar ratio from 0 to 0.5 and then increased slightly in 1.00 Ni-BTPA membranes, which is similar to that of NH_3 adsorption amounts tested by NH_3-TPD. This can confirm that the NH_3 affinity/adsorption properties follow this order: BTPA < 0.25 Ni-BTPA < 0.50 Ni-BTPA ≈ 1.00 Ni-BTPA.

The NH_3/H_2 and NH_3/N_2 permeance ratios were gradually increased by raising the Ni/*N-H* molar ratio from 0, 0.25 to 0.5, while decreased clearly for 1.00 Ni-BTPA membrane, independent of the measurement temperature. This indicates that the molecular sieving properties of the membrane were weakened by excessive doping with nickel, and 0.5 Ni-BTPA has optimal NH_3 affinity/adsorption. The balance between molecular sieving (pore size) and membrane affinity plays a prominent role in the gas separation

by microporous aminosilica membranes, especially NH_3 as an adsorptive gas.

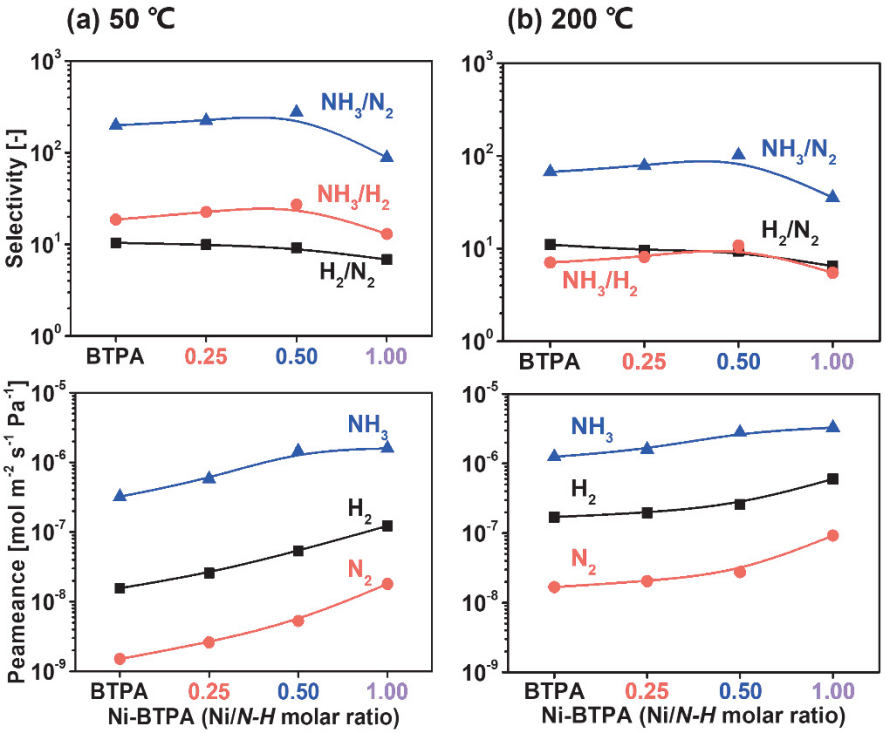

Fig. 3-10. H_2, N_2, and NH_3 permeance and NH_3 selectivity at 50 (a) and 200 °C (b) as a function of different nickel doping amounts.

Fig. 3-11 shows the temperature dependence of single-gas permeance and gas perm-selectivity from 50 to 200 °C for BTPA and Ni-BTPA membranes containing different Ni/*N-H* molar ratios. The permeance of H_2 and N_2, which are the non-adsorptive gases without any special interactions with amine group and/or nickel, as displayed in Figs. 3-S9 and S10, increases for all membranes with increasing temperature, showing the activated transport mechanism. As shown in Fig. 3-11 (d), the H_2/N_2 permselectivity in all membranes is approximately constant regardless of temperature, which can be attributed to a relatively rigid alkyl-amine chain that is constrained by two silicons and/or nickels to similarly affect the effective pore sizes for H_2 and N_2 permeation by thermal vibration. [28] After doping nickel into BTPA, the H_2 and N_2 permeance increased significantly with increasing nickel doping amounts, and meanwhile their temperature-

dependent slopes were decreased compared with undoped BTPA membrane due to the enlarged pore size, particularly 1.00 Ni-BTPA with the interparticle pores formed by the aggregation and/or segregation of nickel nanoparticles.

On the other hand, NH_3 permeance showed smaller slopes (activation energy for permeation) for temperature dependence than H_2 and N_2 permeance, which equates to the smaller values of activation energy for permeation (E_p). The activation energy for permeation (E_p) is expressed as $E_P=\triangle H+E_d$, where $\triangle H$ and E_d are the enthalpy of adsorption (negative) and diffusion energy (positive), respectively. Compared with the negative slope for NH_3 permeation (E_p) in PFSA-based membranes [49], 0.50 Ni-BTPA membrane represented a positive and lower slope for NH_3 permeation (E_p) as shown in SI-10, which was possibly caused by the adsorption of NH_3 in a manner of surface diffusion. Moreover, Fig. 3-S12 shows the morphology of thin and multi-layer for the membranes, so that NH_3 possibly permeates through the membrane by multi-layered adsorption and rapid diffusion under 50-300 kPa. Hence both surface adsorption and diffusion within BTPA-based membranes made a great contribution to NH_3 permeation.

The NH_3/N_2 permselectivity increased with decreasing temperature for all membranes. For 1.00 Ni-BTPA membrane, the enlarged pores also had a negative effect on the NH_3/N_2 permselectivity due to their similar molecular kinetic diameters (NH_3: 0.326 nm [23] and N_2: 0.364 nm). Moreover, NH_3-TPD and computational simulation also proved that an over-incorporation of nickel into BTPA would not improve the NH_3 affinity, which could be ascribed to the competitive interaction between nickel and NH_3/*N-H* and the aggregation and/or segregation of particles.

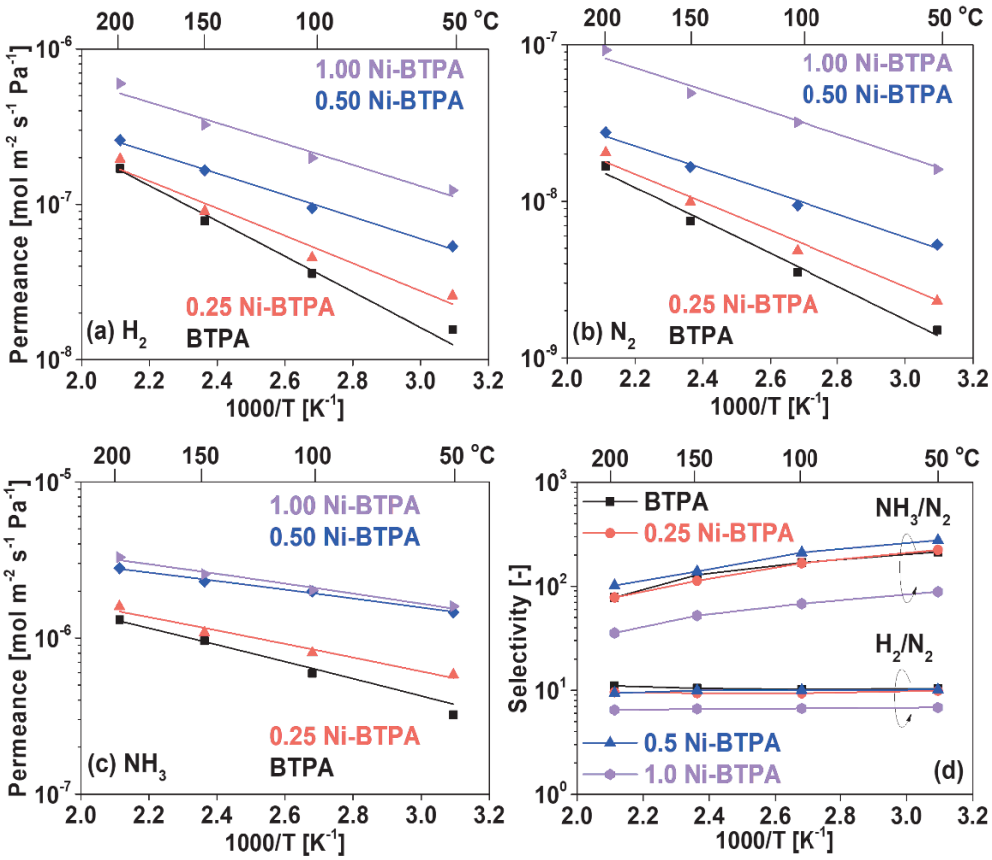

Fig. 3-11. Temperature dependence of single-gas permeance (H_2 (a), N_2 (b), and NH_3 (c)) and permselectivity of H_2/N_2 and NH_3/N_2 (d) for BTPA and different Ni-doped BTPA membranes.

Fig. 3-12 exhibits the pressure dependence of H_2, N_2, and NH_3 permeance for 0.5 Ni-BTPA membrane at 50 °C. The feed pressures of NH_3, and H_2 and N_2 were controlled at around 25-200 and 100-300 kPa, respectively, and the permeance of H_2, N_2, and NH_3 as well as the permselectivity of NH_3 remained approximately constant regardless of the feed pressures of H_2, N_2, and NH_3. This result suggests that the surface diffusion effect is negligible for not only H_2 and N_2 but also for NH_3.

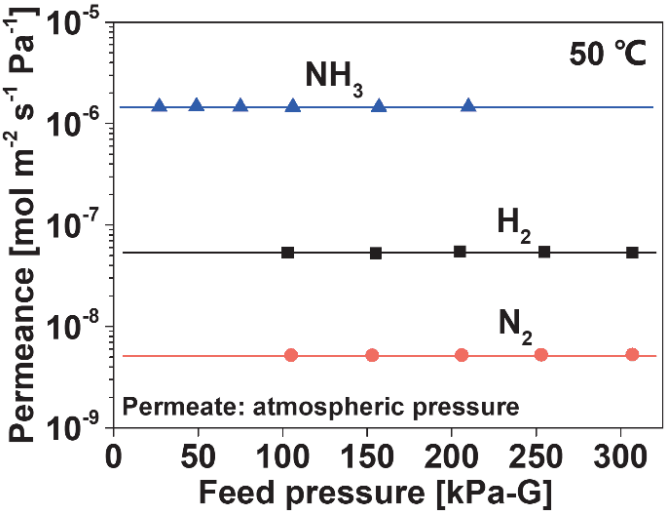

Fig. 3-12. Pressure dependence of H_2, N_2, and NH_3 permeance for 0.50 Ni-BTPA membrane at 50 °C.

Fig. 3-S15 demonstrates the time course for H_2, N_2, and NH_3 permeance during single- and binary-gas permeation. H_2, N_2, and NH_3 permeance was almost constant in both single- and binary-gas permeation at 100 °C, which means a negligible mixing effect in Ni-BTPA membrane.

3.3.5 Trade-offs of various membranes

Fig. 3-13 summarizes various membrane performances for NH_3 permeance, NH_3/N_2, and NH_3/H_2 permselectivity at ≤ 50 and 200 °C. Although most membranes exhibited superior NH_3/H_2 and NH_3/N_2 selectivities and acceptable NH_3 permeance (10^{-7}~10^{-6} mol m^{-2} s^{-1} Pa^{-1}) at 25 °C, the effect of temperature on NH_3/H_2 and NH_3/N_2 selectivities is inevitable. For example, the NH_3/H_2 selectivity was decreased dramatically from 307 at 25 °C, 23.8 at 50 °C to 3.8 at 100 °C, and NH_3/N_2 selectivity was reduced from 2236 at 25 °C, 221 at 50 °C to 20 at 100 °C [21] for MFI membranes as shown in Figs. 3-13 (a) and (b) and Table 3-S2. As the NH_3 permeance increased with raising Ni/*N*-*H* molar ratio in Fig. 3-11, and Figs. 3-13 (c) and (d) clearly shows that 0.50 Ni-BTPA are

excellent in NH_3/N_2 and NH_3/H_2 permselectivity by comparison with the LTA zeolitic imidazolate framework (ZIF-21) [12], 2D-MXene [47], and Prussian Blue membranes [48] that displayed ideal NH_3/H_2 selectivity of 12-50 at 25 °C and Nafion-based membranes that showed ideal NH_3/N_2 and NH_3/H_2 selectivities of 24.8 and 2.6 respectively at 200 °C [49]. This could be attributed mainly to the affinity of nickel to NH_3 and to improvements in the NH_3 permeation resistance caused by an increase in the nickel content. Membranes that could be used over a wide temperature range would also facilitate the development and practical application of membrane reactors for NH_3 synthesis and decomposition. [50,51]

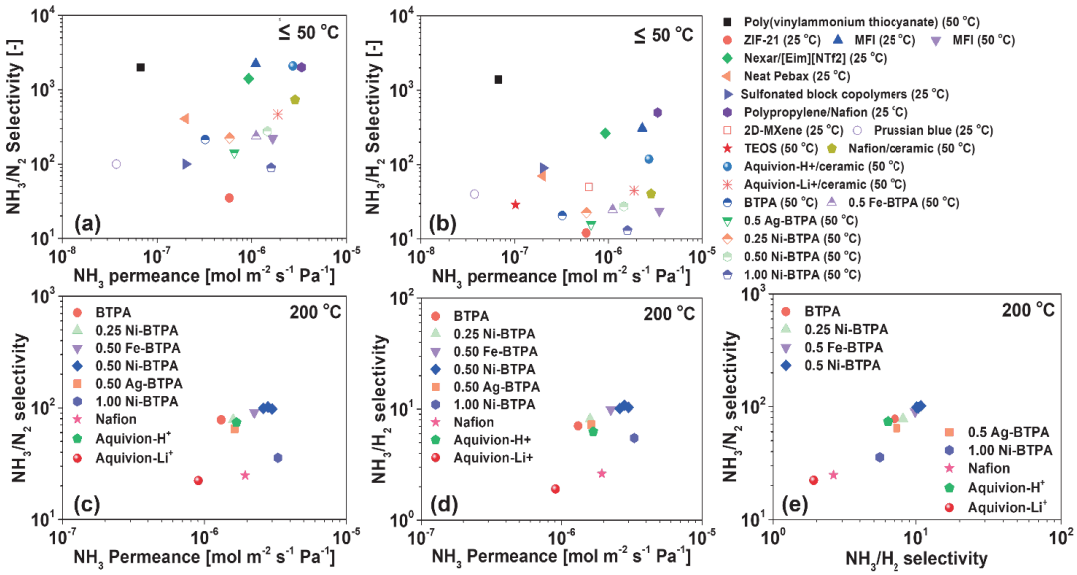

Fig. 3-13. Trade-offs for NH_3 permeance, NH_3/N_2, and NH_3/H_2 selectivity of BTPA-based and other membranes at different temperatures. All data are listed in Table 3-S2.

3.4 Conclusions

With an increase in the amount of nickel doping in BTPA, the coordination between nickel and propylamines is enhanced, particularly for 1.00 Ni-BTPA, as shown by FT-IR and UV-vis analysis, resulting in a weakening of the coordination between *N-H* and *N=O* that originates with an acid-base interactions. For 1.00 Ni-BTPA, the

strengthening coordination between nickel and *N-H* and the interparticle pore caused by the aggregation and/or segregation of nickel nanoparticles not only negatively affects the NH_3 affinity but also weakened the molecular sieving. The results from both NH_3-TPD and simulation prove that 0.50 Ni-BTPA has sufficient coordination sites and considerable interaction intensity with NH_3, which can effectively improve the NH_3 permselectivity by balancing molecular sieving (pore size) and membrane affinity. The optimal performance was obtained with 0.50 Ni-BTPA membrane, showing NH_3 permeance of ~2.8×10^{-6} mol m^{-2} s^{-1} Pa^{-1} with ideal NH_3/H_2 selectivity of 11 and NH_3/N_2 selectivity of 102 at 200 °C.

References

[1] S. Chatterjee, R.K. Parsapur, K.W. Huang, Limitations of ammonia as a hydrogen energy carrier for the transportation sector, *ACS Energy Lett.* 6 (2021) 4390-4394.

[2] Y. Ishimoto, M. Voldsund, P. Neksa, S. Roussanaly, D. Berstad, S.O. Gardarsdottir, Large-scale production and transport of hydrogen from Norway to Europe and Japan: Value chain analysis and comparison of liquid hydrogen and ammonia as energy carriers, *Int. J. Hydrogen Energ.* 45 (2020) 32865-32883.

[3] M.J. Kale, D.K. Ojha, S. Biswas, J.I. Militti, A.V. McCormick, J.H. Schott, P.J. Dauenhauer, E.L. Cussler, Optimizing ammonia separation via reactive absorption for sustainable ammonia synthesis, *ACS Appl. Energy Mater.* 3 (2020) 2576-2584.

[4] C.Y. Liu, K.I. Aika, Modification of active carbon and zeolite as ammonia separation materials for a new de-NOx process with ammonia on-site synthesis, *Res. Chem. Intermed.* 28 (2002) 409-417.

[5] J. Zhang, L. Zheng, Y. Ma, Z. Cai, Y. Cao, K. Huang, L. Jiang, A mini-review on NH_3 separation technologies: Recent advances and future directions, *Energy Fuels* 36 (2022) 14516-14533.

[6] I.I. Cheema, U. Krewer, Operating envelope of Haber-Bosch process design for power-to-ammonia, *RSC Adv.* 8 (2018) 34926-34936.

[7] P. Bernardo, E. Drioli, G. Golemme, Membrane gas separation: A review/state of the art, *Ind. Eng. Chem. Res.* 48 (2009) 4638-4663.

[8] Y. Zhang, J. Xiao, T.C. Zhang, L. Ouyang, S. Yuan, Synthesis of $CuSiO_3$-loaded P-doped porous biochar derived from phytic acid-activated lemon peel for enhanced adsorption of NH_3, *Sep. Purif. Technol.* 283 (2022) 120179.

[9] S. Lian, Q. Zhao, Z. Zhang, R. Li, C. Song, Tailored interfacial microenvironment of mixed matrix membranes based on deep eutectic solvents for efficient CO_2 separation, *Sep. Purif. Technol.* 307 (2023) 122753.

[10] Y. Sun, J. Zhang, H. Li, F. Fan, Q. Zhao, G. He, C. Ma, Ester-crosslinked polymers of intrinsic microporosity membranes with enhanced plasticization resistance for CO_2 separation, *Sep. Purif. Technol.* 314 (2023) 123623.

[11] B. Yang, L. Bai, T. Li, L. Deng, L. Liu, S. Zeng, J. Han, X. Zhang, Super selective ammonia separation through multiple-site interaction with ionic liquid-based hybrid membranes, *J. Membr. Sci.* 628 (2021) 119264.

[12] Q. Wei, J.M. Lucero, J.M. Crawford, J. Douglas Way, C.A. Wolden, M.A. Carreon, Ammonia separation from N_2 and H_2 over LTA zeolitic imidazolate framework membranes, *J. Membr. Sci.* 623 (2021) 119078.

[13] A. Bhown, E.L. Cussler, Mechanism for selective ammonia transport through poly(vinylammonium thiocyanate) membranes, *J. Am. Chem. Soc.* 113 (1991) 742-749.

[14] J. Liu, Z. Chen, R. Wang, S. Alayoglu, T. Islamoglu, S.J. Lee, T.R. Sheridan, H. Chen, R.Q. Snurr, O.K. Farha, J.T. Hupp, Zirconium metal−organic frameworks integrating chloride ions for ammonia capture and/or chemical separation, *ACS Appl. Mater. Interfaces* 13 (2021) 22485-22494.

[15] K. Li, K. Zong, Z. Zhou, D. Deng, Highly efficient absorption and separation of NH3 by simple lithium deep eutectic solvents, *Sep. Purif. Technol.* 279 (2021) 119763.

[16] S. Zeng, Y. Cao, P. Li, X. Liu, X. Zhang, Ionic liquid–based green processes for ammonia separation and recovery, *Curr. Opin. Green. Sust.* 25 (2020) 100354.

[17] O. Camus, S. Perera, B. Crittenden, Y.C. van Delft, D.F. Meyer, Paul P.A.C. Pex, I. Kumakiri, S. Miachon, J.A. Dalmon, S. Tennison, P. Chanaud, E. Groensmit, W. Nobel, Ceramic membranes for ammonia recovery, *AIChE J.* 52 (2006) 2055-2065.

[18] J. Mi, W. Peng, Y. Luo, W. Chen, L. Lin, C. Chen, Q. Zhu, F. Liu, A. Zheng, L. Jiang, A cationic polymerization strategy to design sulfonated micro-mesoporous polymers as efficient adsorbents for ammonia capture and separation, *Macromolecules* 54 (2021) 7010-7020.

[19] B. Yang, L. Bai, S. Zeng, S. Luo, L. Liu, J. Han, Y. Nie, X. Zhang, S. Zhang, NH_3 separation membranes with self-assembled gas highways induced by protic ionic liquids, *Chem. Eng. J.* 421 (2021) 127876.

[20] B. Yang, L. Bai, Z. Wang, H. Jiang, S. Zeng, X. Zhang, X. Zhang, Exploring NH_3 Transport Properties by Tailoring Ionic Liquids in Pebax-Based Hybrid

Membranes, *Ind. Eng. Chem. Res.* 60 (2021) 9570-9577.

[21] X. Duan, D. Kim, K. Narasimharao, S. Al-Thabaitic, M. Tsapatsis, High-performance ammonia-selective MFI nanosheet membranes, *Chem. Commun.* 57 (2021) 580-582.

[22] K. Vikrant, V. Kumar, K.H. Kim, Metal-organic frameworks (MOFs): potential and challenges for capture and abatement of ammonia, *J. Mater. Chem. A* 5 (2017) 22877-22896.

[23] M. Kanezashi, A. Yamamoto, T. Yoshioka, T. Tsuru, Characteristics of ammonia permeation through porous silica membranes, *AIChE J.* 56 (2010) 1204-1212.

[24] L. Yu, M. Kanezashi, H. Nagasawa, M. Guo, N. Moriyama, K. Ito, T. Tsuru, Tailoring ultramicroporosity to maximize CO_2 transport within pyrimidine-bridged organosilica membranes, *ACS Appl. Mater. Interfaces* 11 (2019) 7164-7173.

[25] F.T. Zheng, K. Yamamoto, M. Kanezashi, T. Gunji, T. Tsuru, J. Ohshita, Preparation of hybrid organosilica reverse osmosis membranes by interfacial polymerization of bis[(trialkoxysilyl)propyl]amine, *Chem. Lett.* 47 (2018) 1210-1212.

[26] M. Takenaka, H. Nagasawa, T. Tsuru, M. Kanezashi, Hydrocarbon permeation properties through microporous fluorine-doped organosilica membranes with controlled pore sizes, *J. Membr. Sci.* 619 (2021) 118787.

[27] M. Guo, M. Kanezashi, H. Nagasawa, L. Yu, J. Ohshita, T. Tsuru, Amino-decorated organosilica membranes for highly permeable CO_2 capture, *J. Membr. Sci.* 611 (2020) 118328.

[28] W.W. Yan, U. Anggarini, H.C. Bai, H. Nagasawa, M. Kanezashi, T. Tsuru, Enhanced NH_3 permeation of bis[3-(trimethoxysilyl)propyl] amine membranes via coordination with metals, *J. Membr. Sci.* 678 (2023) 121665.

[29] U. Anggarini, L. Yu, H. Nagasawa, M. Kanezashi, T. Tsuru, Structural transformation of the nickel coordination-induced subnanoporosity of aminosilica membranes for methanol-selective, high-flux pervaporation, *J. Membr. Sci.* 656 (2022) 120613.

[30] T. Tsuru, Nano/subnano-tuning of porous ceramic membranes for molecular separation, *J. Sol. Gel Sci. Technol.* 46 (2008) 349-361.

[31] M.J. Frisch, G.W. Trucks, H.B. Schlegel, G.E. Scuseria, M.A. Robb, J.R. Cheeseman, G. Scalmani, V. Barone, B. Mennucci, G.A. Petersson, H. Nakatsuji, M. Caricato, X. Li, H.P. Hratchian, A.F. Izmaylov, J. Bloino, G. Zheng, J.L. Sonnenberg, M. Hada, M. Ehara, K. Toyota, R. Fukuda, J. Hasegawa, M. Ishida, T. Nakajima, Y. Honda, O. Kitao, H. Nakai, T. Vreven, JA Jr Montgomery, J.E. Peralta, F. Ogliaro, M. Bearpark, J.J. Heyd, E. Brothers, K.N. Kudin, V.N. Staroverov, R. Kobayashi, J. Normand, K. Raghavachari, A. Rendell, J.C. Burant, S.S. Iyengar, J. Tomasi, M. Cossi, N. Rega, J.M. Millam, M. Klene, J.E. Knox, J.B. Cross, V. Bakken, C. Adamo, J. Jaramillo, R. Gomperts, R.E. Stratmann, O. Yazyev, A.J. Austin, R. Cammi, C. Pomelli, J.W. Ochterski, R.L. Martin, K. Morokuma, V.G. Zakrzewski, G.A. Voth, P. Salvador, J.J. Dannenberg, S. Dapprich, A.D. Daniels, Ö. Farkas, J.B. Foresman, J.V. Ortiz, J. Cioslowski, D.J. Fox, Gaussian 09, revision D.01; Gaussian, Inc., Wallingford CT, 2009.

[32] K.P. Jensen, Bioinorganic chemistry modeled with the TPSSh density functional, *Inorg. Chem.* 47 (2008) 10357-10365.

[33] W. Zierkiewicz, D. Michalska, Z. Havlas, P. Hobza, Study of the nature of improper blue-shifting hydrogen bonding and standard hydrogen bonding in the $X_3CH\cdots OH_2$ and $XH\cdots OH_2$ Complexes (X=F, Cl, Br, I): A Correlated Ab Initio Study, *ChemPhysChem* 3 (2002) 511-518.

[34] T. Lu, Sobtop, Version 1.0(dev3), http://sobereva.com/soft/Sobtop (accessed on 2022-Sep-26).

[35] D. Van Der Spoel, E. Lindahl, B. Hess, G. Groenhof, A.E. Mark, H.J.C. Berendsen, GROMACS fast, flexible, and free, *J. Comput. Chem.* 26 (2005) 1701-1718.

[36] J. Wang, R.M. Wolf, J.W. Caldwell, P.A. Kollman, D.A. Case, Development and testing of a general amber force field, *J. Comput. Chem.* 25 (2004) 1157-1174.

[37] L. Martínez, R. Andrade, E.G. Birgin, J.M. Martínez, Software news and update Packmol: a package for building initial configurations for Molecular Dynamics Simulations, *J. Comput. Chem.* 30 (2008) 2157-2164.

[38] W. Humphrey, A. Dalke, K. Schulten, VMD: Visual Molecular Dynamics, *J. Mol. Graph.* 14 (1996) 33-38.

[39] T. Lu, F.W. Chen, Multiwfn: A multifunctional wavefunction analyzer, *J. Comput. Chem.* 33 (2012) 580-592.

[40] C. Lefebvre, H. Khartabil, J.C. Boisson, J. Contreras-García, J. P. Piquemal, E. Hénon, The Independent Gradient Model: A new approach for probing strong and weak interactions in molecules from wave function calculations, *ChemPhysChem* 19 (2018) 724-735.

[41] U. Anggarini, L. Yu, H. Nagasawa, M. Kanezashi, T. Tsuru, Metal-induced microporous aminosilica creates a highly permeable gas-separation membrane, *Mater. Chem. Front.* 5 (2021) 3029-3042.

[42] U. Anggarini, L. Yu, H. Nagasawa, M. Kanezashi, T. Tsuru, Microporous nickel-coordinated aminosilica membranes for improved pervaporation performance of methanol/toluene separation, *ACS Appl. Mater. Interfaces*, 13 (2021) 23247-23259.

[43] J. Breternitz, A. Godula-Jopek, D.H. Gregory, $Ni(NH_3)_2(NO_3)_2$—A 3-D network through bridging nitrate units isolated from the thermal decomposition of nickel hexammine dinitrate, *Inorganics* 6 (2018) 59.

[44] Q.G.J. Malloy, L. Qi, B. Warren, D.R. Cocker III, M.E. Erupe, P.J. Silva, Secondary organic aerosol formation from primary aliphatic amines with NO_3 radical, *Atmos. Chem. Phys.* 9 (2009) 2051-2060.

[45] X. Wu, X. Wang, Y. Hu, H. Chen, X. Liu, X. Dang, Adsorption mechanism study of multinuclear metal coordination cluster Zn_5 for anionic dyes congo red and methyl orange: Experiment and molecular simulation, *Appl. Surf. Sci.* 586 (2022) 152745.

[46] V.A. Basiuk, N. Alzate-Carvajal, L.V. Henao-Holguín, E.V. Rybak-Akimova, E.V. Basiuk, Coordination functionalization of graphene oxide with tetraazamacrocyclic complexes of nickel(II): Generation of paramagnetic centers, *Appl. Surf. Sci.* 371 (2016) 16-27.

[47] D.I. Petukhov, A.S. Kan, A.P. Chumakov, O.V. Konovalov, R.G. Valeev, A.A. Eliseev, MXene-based gas separation membranes with sorption type selectivity, *J. Membr. Sci.* 621 (2021) 118994.

[48] M.A. Komkova, I.S. Sadilov, V.A. Brotsman, D.I. Petukhov, A.A. Eliseev,

Facilitated transport of ammonia in ultra-thin Prussian Blue membranes with potential-tuned selectivity, *J. Membr. Sci.* 639 (2021) 119714.

[49] K. Wakimoto, W.W. Yan, N. Moriyama, H. Nagasawa, M. Kanezashi, T. Tsuru, Ammonia permeation of fluorinated sulfonic acid polymer/ceramic composite membranes, *J. Membr. Sci.* 658 (2022) 120718.

[50] Z.Y. Zhang, J. Douglas Way, C.A. Wolden, Design and operational considerations of catalytic membrane reactors for ammonia synthesis, *AIChE J.*, 67 (2021) e17259.

[51] L. Meng, T. Tsuru, Hydrogen production from energy carriers by silica-based catalytic membrane reactors, *Catal. Today* 268 (2016) 3-11.

Supplementary Material

---------- **SI-1:** The fabrication procedure for sols and membranes ----------

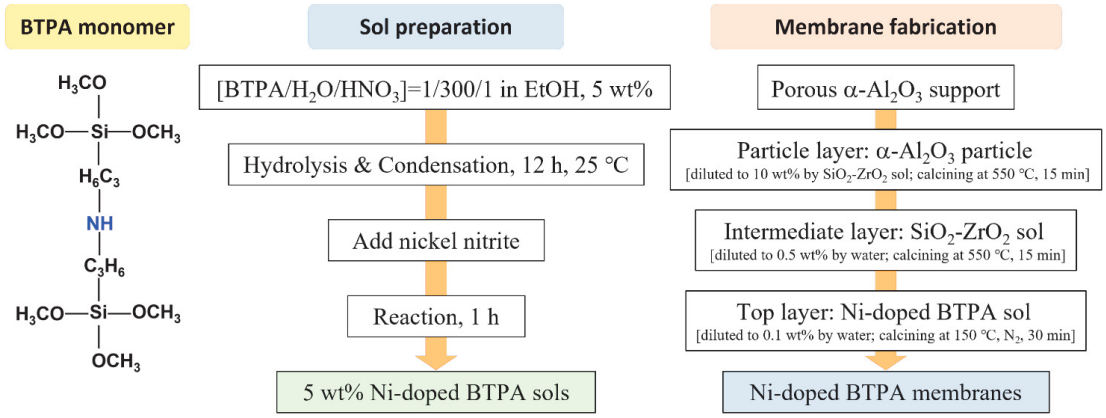

Fig. 3-S1. The fabrication procedure for sols and membranes.

---------- **SI-2:** Dimensionless permeation of N_2 for intermediate layer ----------

Fig. 3-S2 shows the permeation properties of N_2 for different SiO_2-ZrO_2 intermediate layers as a function of the Kelvin diameter, which can be used to estimate the pore sizes of SiO_2-ZrO_2 intermediate layers. These results also confirm the reproducibility of fabricating the SiO_2-ZrO_2 intermediate layer.

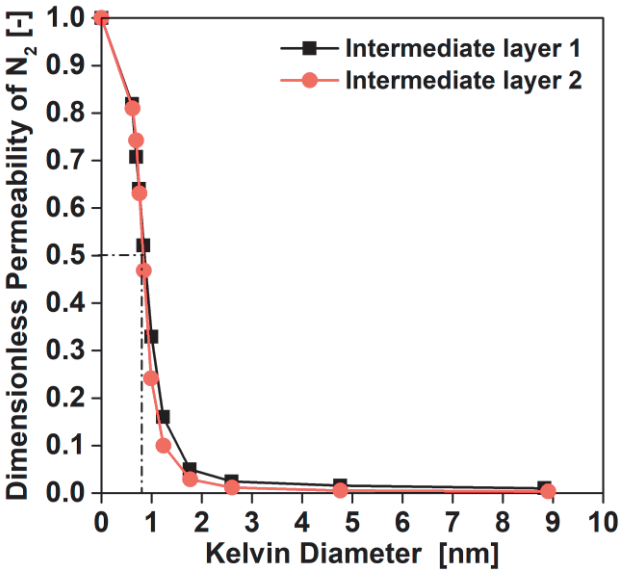

Fig. 3-S2. Dimensionless permeation of N_2 for different SiO_2-ZrO_2 intermediate layers as a function of the Kelvin diameter.

---------- **SI-3:** NH_3 temperature-programmed desorption (NH_3-TPD) ----------

When a 5% NH_3/95% He mixture gas feeding was stopped, NH_3 desorption also occurs at temperatures ranging from room temperature to 40 °C. The sum of the NH_3 desorption amount at room temperature to 40 °C and at 40 to 150 °C is almost equivalent to the NH_3 adsorption amount.

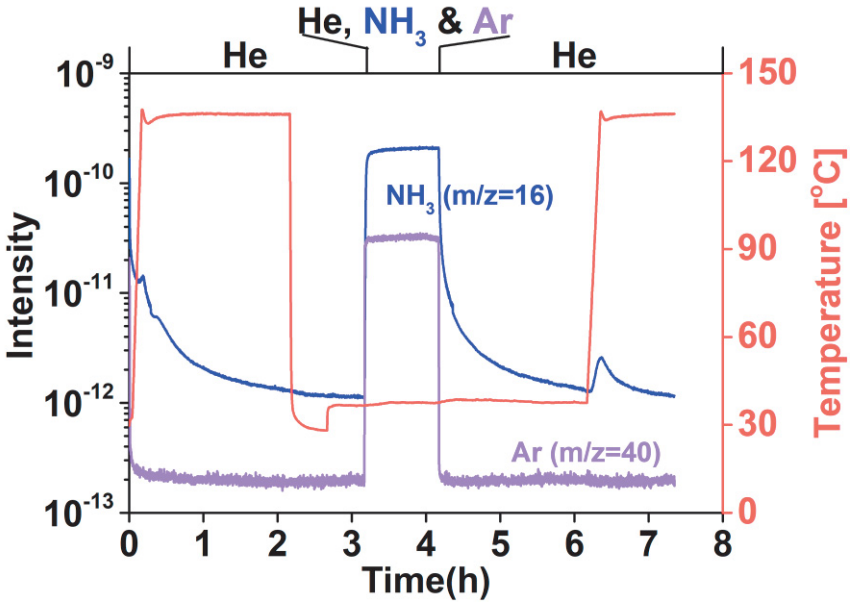

Fig. 3-S3. Time course of mass intensity and temperature during NH_3-TPD measurements for BTPA xerogel powder.

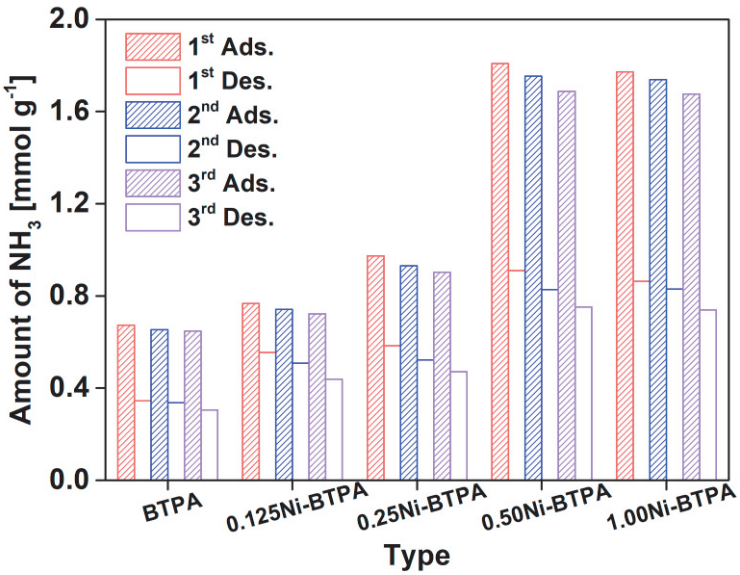

Fig. 3-S4. NH_3 adsorption and desorption results for repeating NH_3-TPD measurements.

---------- **SI-4:** N_2 sorption ----------

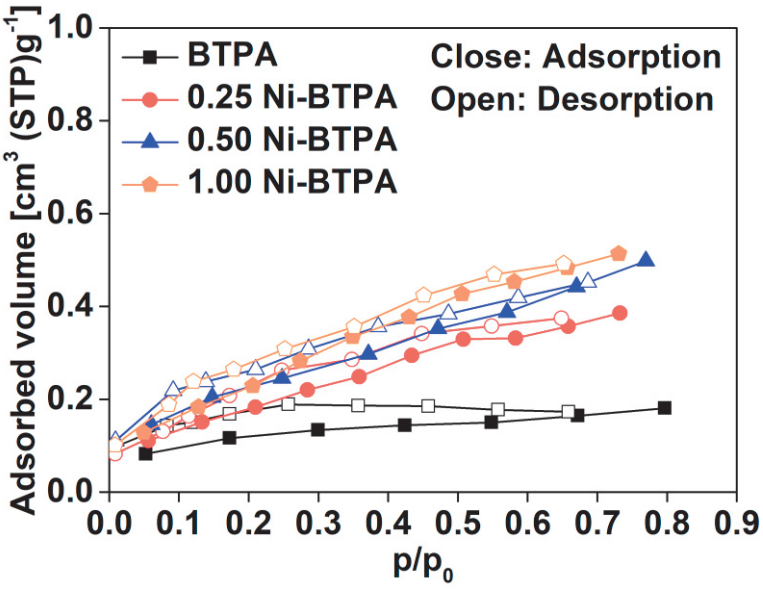

Fig. 3-S5. N_2 adsorption isotherms for BTPA-based xerogel powders at -196 °C, where the powder was obtained at a calcination temperature of 150 °C.

---------- **SI-5:** Simulation process ----------

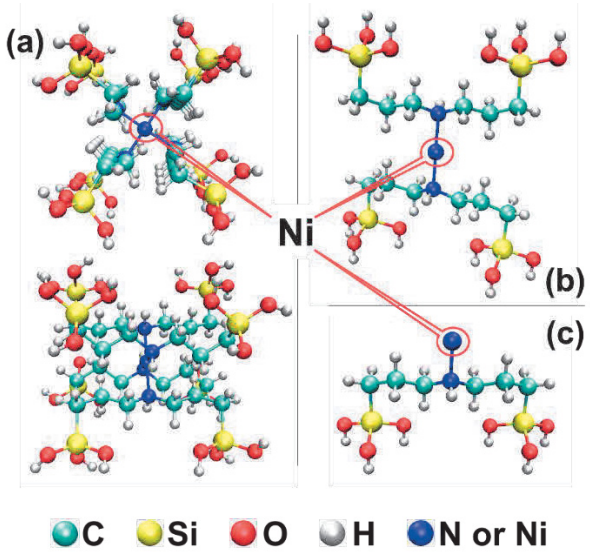

Fig. 3-S6. Theoretical coordination structure of Ni-doped BTPA at different Ni/*N*-*H* molar ratios: (a) Ni/*N*-*H*=0.25, (b) Ni/*N*-*H*=0.50, and (c) Ni/*N*-*H*=1.00.

The Sobtop program was applied to conveniently create a topology file for molecular dynamics simulation based on the *.fchk* file generated from the abovementioned

vibration analysis. All-atoms classic molecular dynamics simulations were performed using Gromacs 2018.4 package with the Amber14sb-OL15 and the generalized AMBER force field. The simulation system was constructed by randomly distributing 600 H_2, 600 N_2, 600 NH_3, and 20 Ni-coordinated BTPA molecules in a box (10 × 10 × 10 nm^3) with periodic boundary conditions using Packmol. Nevertheless, one of each type of the Ni-BTPA molecules was placed in the center of the box (6.0 × 6.0 × 6.0 nm^3), and 600 H_2 or N_2 or NH_3 were randomly placed around the Ni-BTPA molecule to determine the interaction types. After energy minimization and pre-equilibrium, the dynamic trajectory was obtained by running the production phase process at 200 °C for 10 ns. The velocity-rescale method and the parrinello-rahman barostat method were adopted to maintain the temperature constant and the pressure at 1 atm, respectively. The Visual molecular dynamics (VMD) was employed to analyze the dynamic trajectory and to visualize the interaction types between H_2/N_2/NH_3 and Ni-coordinated BTPA combined with Multiwfn by Independent gradient model (IGM) method.

---------- **SI-6:** Analysis of RDF and interaction types ----------

The radial distribution function (RDF) obtained by kinetic trajectory statistics provides the distribution of H_2, N_2, and NH_3 around different Ni-BTPA molecules. As shown in Fig. 3-S7, polar NH_3 can preferentially distribute around all Ni-BTPA molecules compared with H_2 and N_2, which means that Ni-BTPA has the potential to prioritize its adsorption of NH_3 regardless of the nickel doping amount. In particular, NH_3 appears at 0.37 nm with a first g(r) peak of 36.27 for 0.5 Ni-BTPA and with a first peak of 20.92 for 1.0 Ni-BTPA, the affinity of NH_3 for 1.0 Ni-BTPA was slightly inferior to that of 0.5 Ni-BTPA molecule. Besides, the NH_3 affinity greatly decreases for 0.25 Ni-BTPA, which can be ascribed to the binding site (coordination number) of nickel being fully occupied by coordinating with *N-H* in the 0.25 Ni-BTPA molecule.

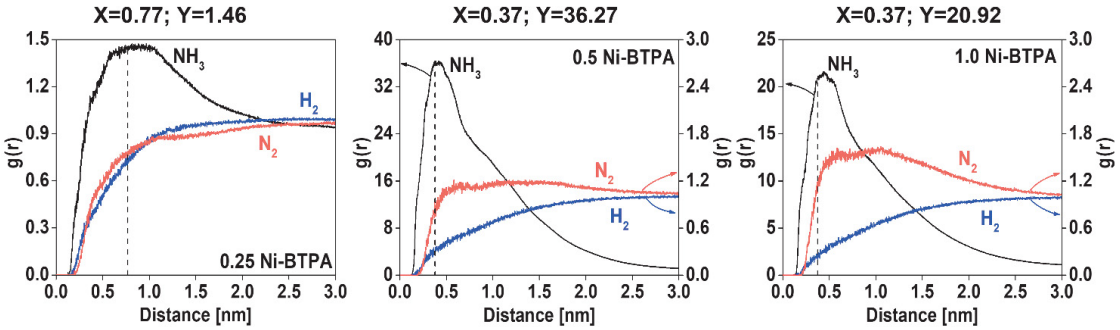

Fig. 3-S7. Radial distribution function of H_2, N_2, and NH_3 around different Ni-BTPA molecules.

Fig. 3-S8 shows the interaction types/intensities (δg_{inter}) between different Ni-BTPA molecules and NH_3 that can be obtained through projecting functions ($sign[\lambda_2(r)\rho(r)]$) onto the IGM isosurface with different colors. All Ni-BTPA molecules can interact with NH_3 by the coordination between nickel and NH_3 and the hydrogen bond and van der Waals force between *Si-OH* and NH_3, between *N-H* and NH_3, and even between alkyl and NH_3. The 0.5 Ni-BTPA has the strongest interaction for NH_3, as shown by the scatter plot in Fig. 3-S8 (b) and the tetra-coordination structure of nickel and *N-H* that adequately occupied the coordination sites of nickel in 0.25 Ni-BTPA, resulting in a decline in the NH_3 affinity. Inversely, although a sufficient number of coordination sites of nickel were exposed in 1.0 Ni-BTPA, its interaction with NH_3 was weaker than that in 0.5 Ni-BTPA. As described by FT-IR, TG-MS, and XPS [1], nickel in 1.0 Ni-BTPA

not only has a stronger coordination with *N-H*, but also can interact with a large amount of *N=O*, which could cause a competitive interaction with NH_3 that certainly would reduce the intensity of the NH_3 affinity/coordination. The experimental and computational results are consistent, which prove that doping excessive nickel into BTPA has a negative effect that improves the NH_3 affinity/adsorption. H_2 and N_2, as non-adsorptive gases, have only weak van der Waals forces with different Ni-BTPA molecules as displayed in Figs. 3-S9 and S10.

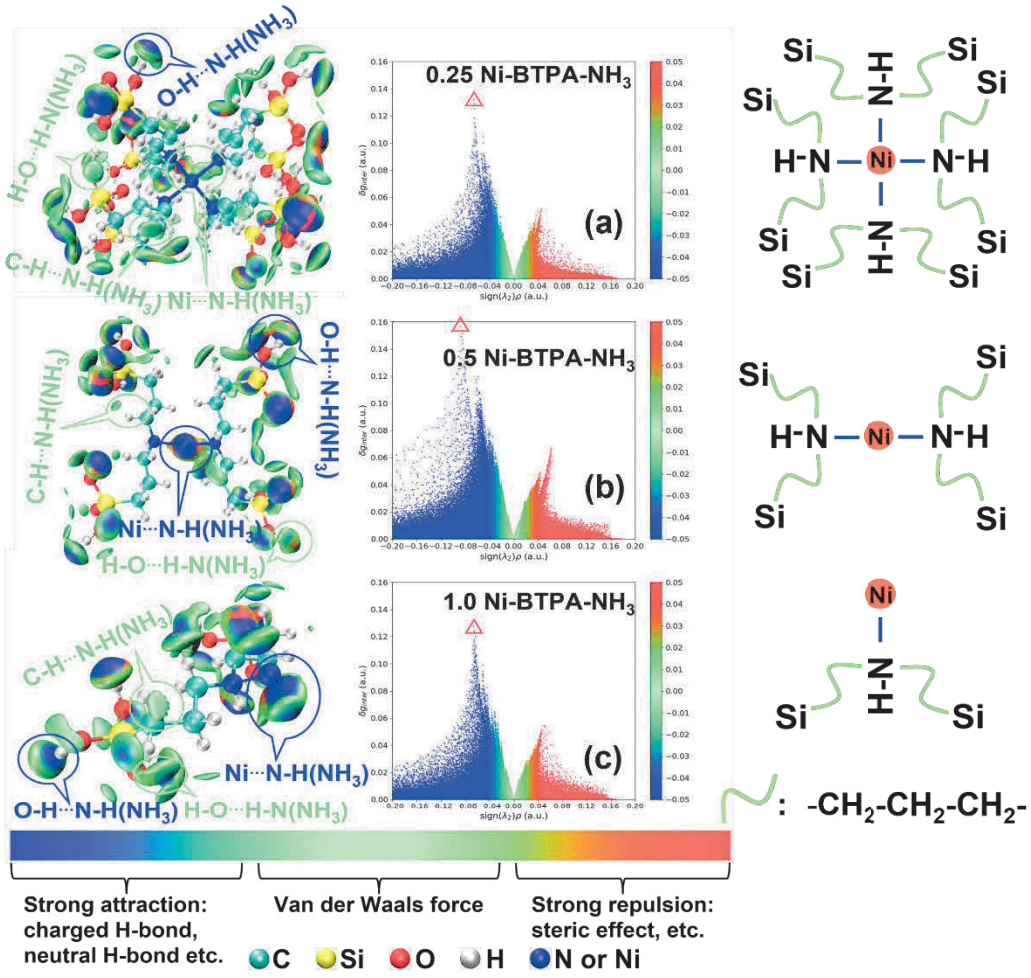

Fig. 3-S8. Color-filled IGM isosurface and scatter plots depicting average noncovalent interaction regions for (a) 0.25 Ni-BTPA, (b) 0.5 Ni-BTPA, and (c) 1.0 Ni-BTPA with NH_3.

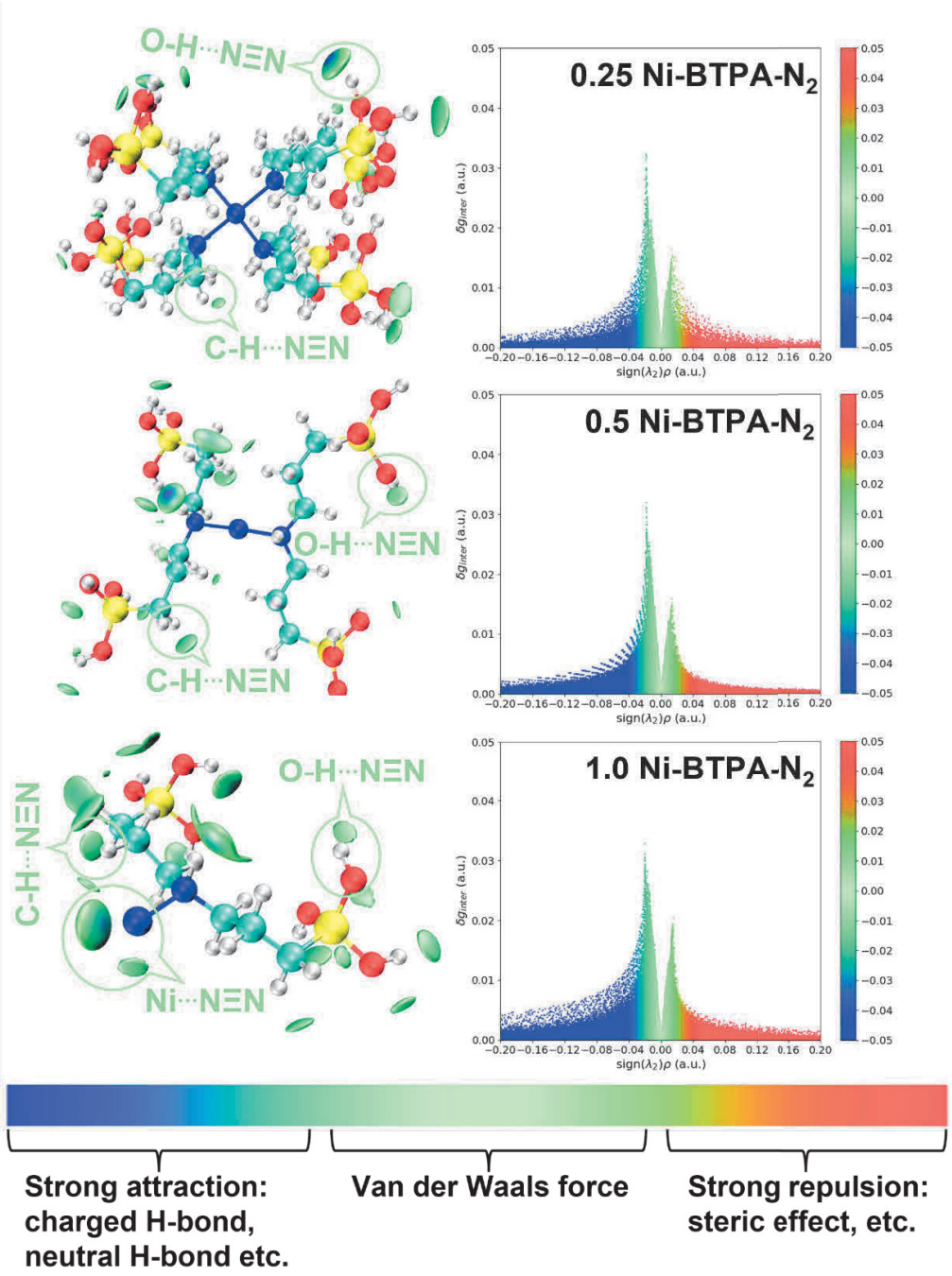

Fig. 3-S9. Color-filled IGM isosurface and scatter plots depicting average noncovalent interaction regions for different Ni-BTPA with N_2.

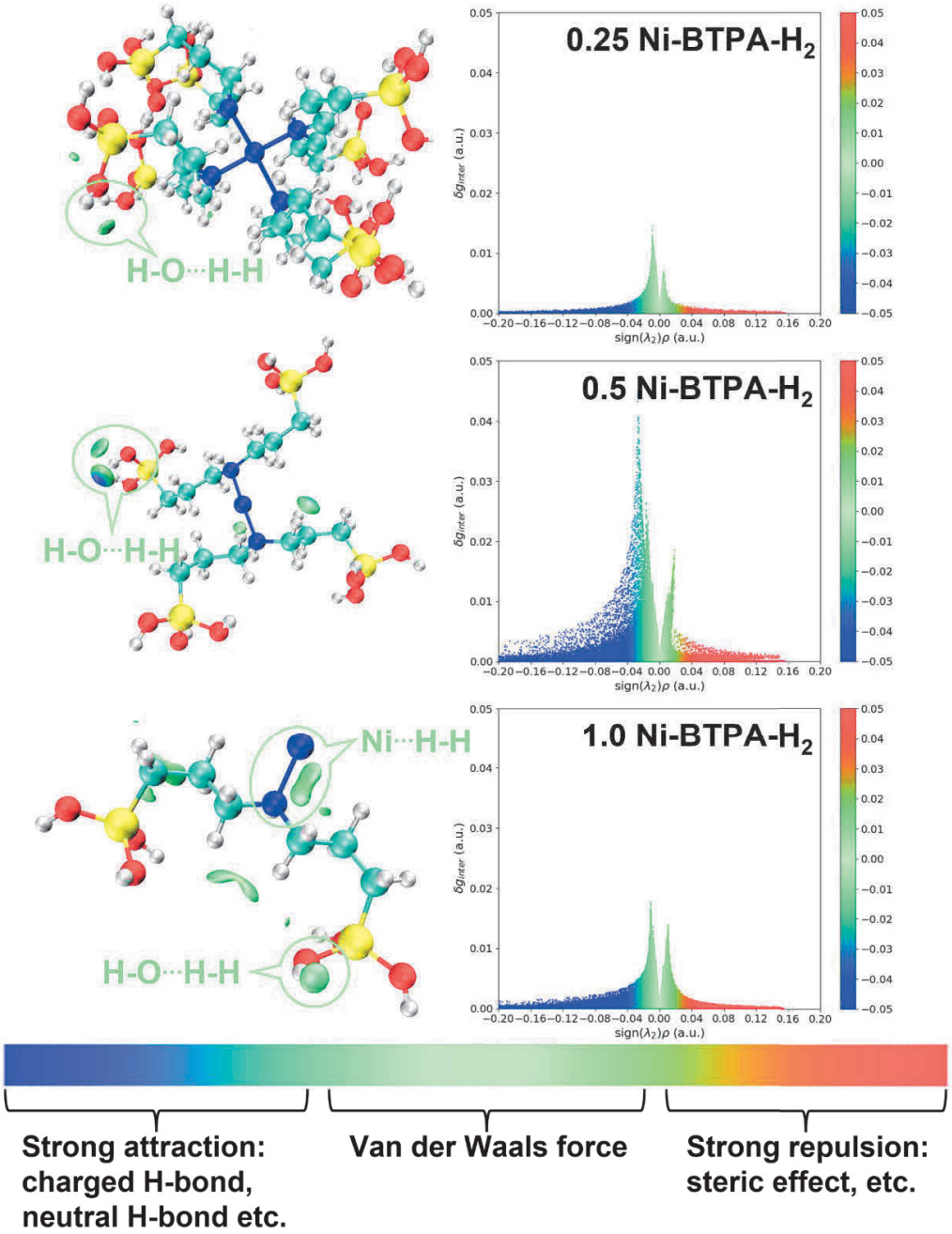

Fig. 3-S10. Color-filled IGM isosurface and scatter plots depicting average noncovalent interaction regions for different Ni-BTPA with H_2.

---------- **SI-7:** Permeation performance of membranes ----------

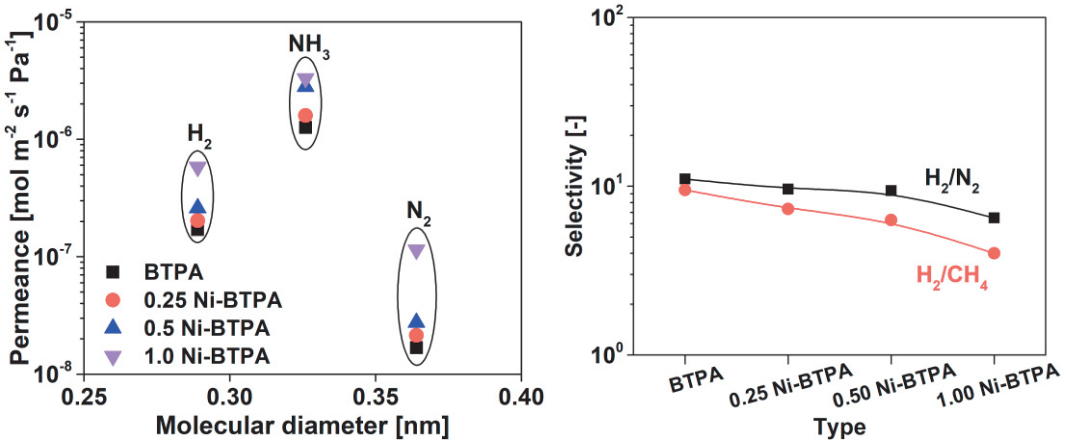

Fig. 3-S11. Kinetic diameter dependence of H_2, N_2, and NH_3 permeance (left), and H_2/N_2 and H_2/CH_4 permselectivity at 200 °C as a function of different nickel doping amounts (right).

---------- **SI-8:** Morphology and photo of membranes ----------

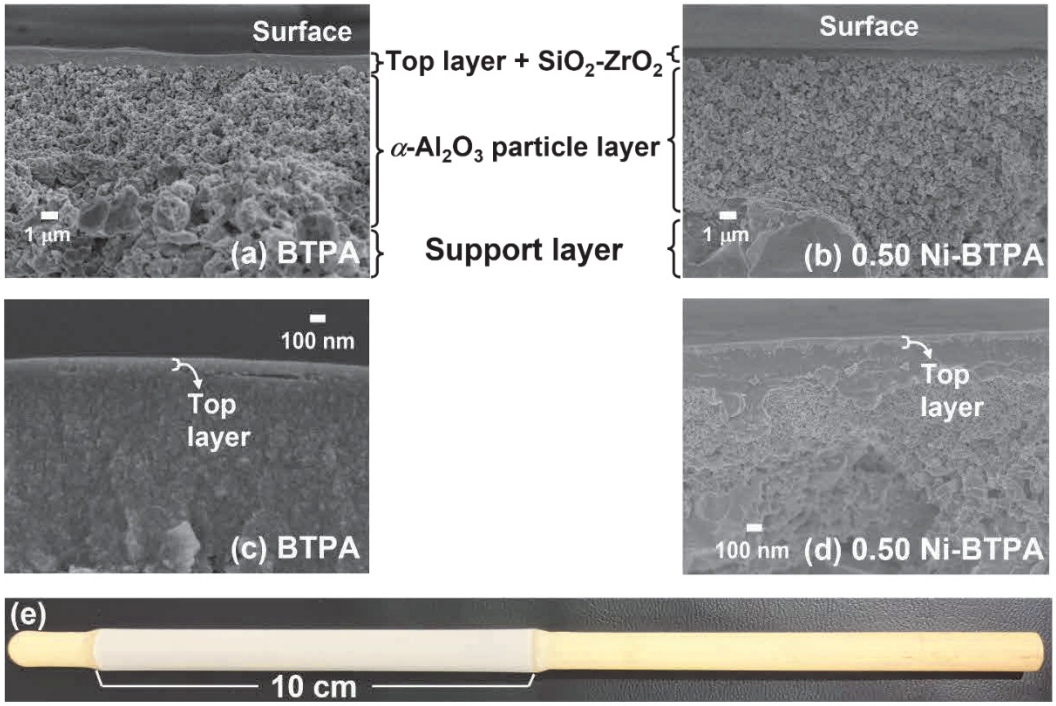

Fig. 3-S12. Morphology of BTPA ((a),(c)) and 0.50 Ni-BTPA ((b),(d)) membranes and photo of 0.50 Ni-BTPA membrane (e).

---------- **SI-9:** Time courses for H_2, N_2, and NH_3 permeance ----------

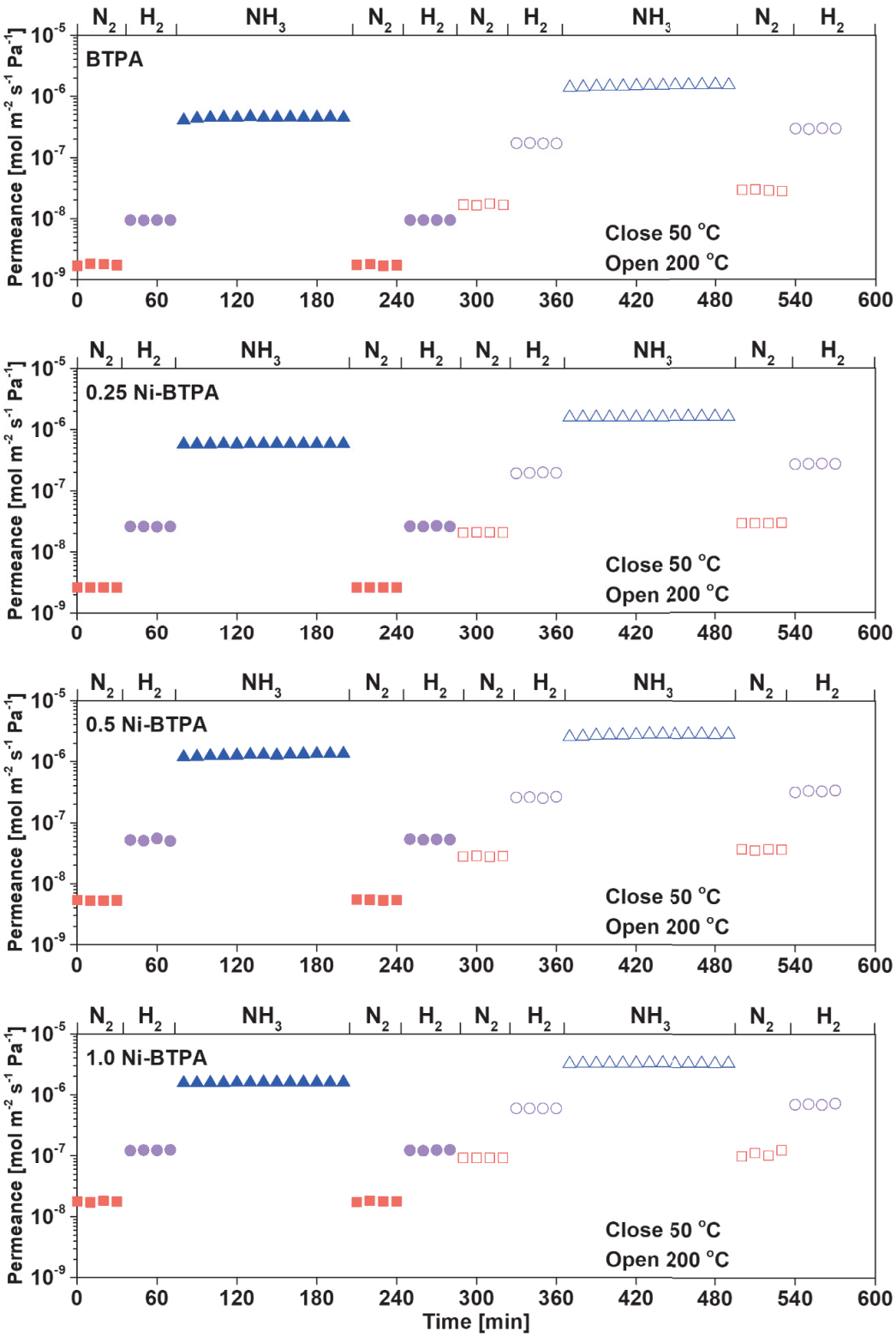

Fig. 3-S13. Time courses for H_2, N_2, and NH_3 permeance of BTPA and different Ni-doped BTPA membranes at 200 and 50 °C.

---------- **SI-10:** Permeance of NH_3, H_2, and N_2 for Nafion and 0.50 Ni-BTPA membranes ----------

Gas permeance of i-th component can expressed by Eq. (1) and (2) based on the modified gas translation (m-GT) model.[2,3] The activation energies ($E_{P,i}$) and permeation constant ($k_{0,i}$) of H_2, N_2, and NH_3 permeation can be determined using Eq. (1) by the regression of permeance, P_i, and temperature, T.

$$P_i = \frac{k_{0,i}}{\sqrt{M_i RT}} exp\left(-\frac{E_{P,i}}{RT}\right) \quad (1)$$

$$k_{0,i} = k_0\left(d_p - d_i\right)^3 \quad (2)$$

P_i: permeance of the i-th component; M_i: molecular weight of the i-th component; R: gas constant; $E_{P,i}$: activation energy of permeation of the i-th component; k_0: structural constant; d_p: pore diameter; d_i: diameter of the i-th component.

Based on the m-GT model, gas selectivity can be expressed as follows.

$$\alpha = \frac{P_i}{P_j} = \frac{k_{0,i}/k_{0,j}}{\sqrt{M_i/M_j}} exp\left(-\frac{E_{P,i} - E_{P,j}}{RT}\right) \quad \text{(i: } NH_3\text{; j: } H_2 \text{ or } N_2\text{;)} \quad (3)$$

It should be noted that $k_{0,i}$ is the configurational factor, which is derived by cosidering the effective diffusivity of the i-th component (molecular size: d_i) though the pores (pore szie: d_p). So this term reflects the effect of diffusion. Based on Eq. (3), the selectivity of NH_3 over H_2 or N_2 is determined by the the ratio of configurational factor (= $k_{0,i}/k_{0,j}$), which can be interpretted as the contribution of difusion to selectivity, and the difference of activation enery ($E_{p,i}$ - $E_{p,j}$).

The difference of activation energy ($E_{p,i}$ - $E_{p,j}$) can be further discussed as follows. Fig. 3-S14 shows the temperature dependence of single-gas permeance (H_2, N_2, and NH_3) for 0.50 Ni-BTPA in Fig. 3-11 and Nafion membranes from Ref. 14. Since H_2 and N_2 are non-adsorptive gases ($\triangle H \approx 0$), the activation energy of permeation ($E_P = \triangle H + E_d$) of H_2 or N_2 is approximately equal to their diffusion energy (E_d), as shown in Table 3-S1. As an adsorbtive gas, NH_3 possesses both the enthalpy of adsorption ($\triangle H$) and diffusion energy (E_d). By assuming E_d of NH_3 is the average of those of H_2

and N_2 due to the simlar moleular sizes, $\triangle H$ of NH_3 is larger for Nafion-based membrane than for 0.50 Ni-BTPA membrane ($\triangle H_{Nafion} > \triangle H_{BTPA}$).

As explained in Eq. (3) for NH_3 selectivity (a), although Nafion-based membrane performed the superior NH_3 permeance and selectivity at low temperature, the superior NH_3 permeance and selectivity of 0.50 Ni-BTPA membrane at 200 °C can be attributed to the additional effect of diffusion ($= k_{0,i}/k_{0,j}$). Hence, the NH_3 permeation in BTPA-based membranes could be ascribed to the synergistic effect of adsorption ($\triangle H$) and diffusion (E_d, $k_{0,i}/k_{0,j}$).

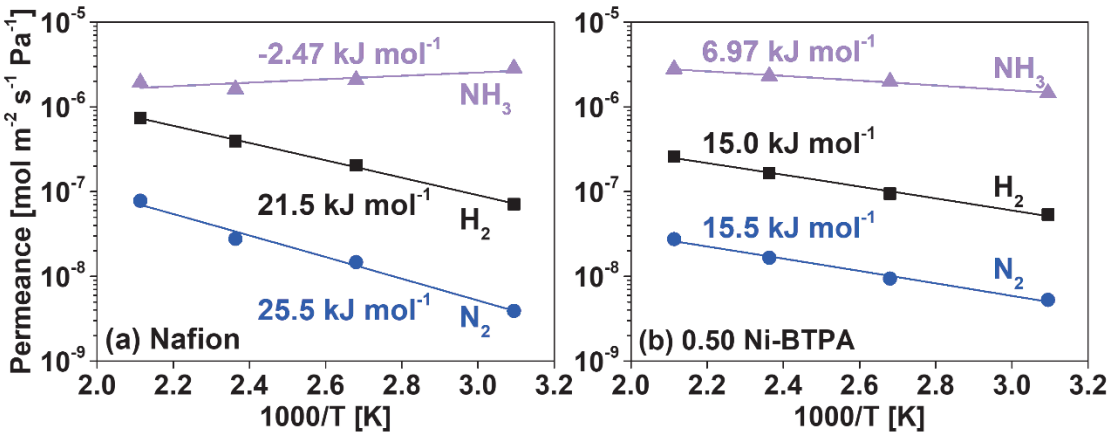

Fig. 3-S14. Permeance of NH_3, H_2, and N_2 for Nafion [14] (a) and 0.50 Ni-BTPA (b) membranes as a function of temperatures.

Table 3-S1. Activation energy (E_P, kJ mol^{-1}) of NH_3, H_2, and N_2 for Nafion [14] and 0.50 Ni-BTPA membranes.

Type	$E_p = \triangle H + E_d$			$E_d \approx$ AVG ($E_{d,H2} + E_{d,N2}$)	$\triangle H = E_p - E_d$
	NH_3	H_2	N_2		NH_3
Nafion	-2.47	21.5	25.5	23.5	-25.97
0.50 Ni-BTPA	6.97	15.0	15.5	15.3	-8.4

---------- **SI-11:** Time courses for single- and binary-gas permeance ----------

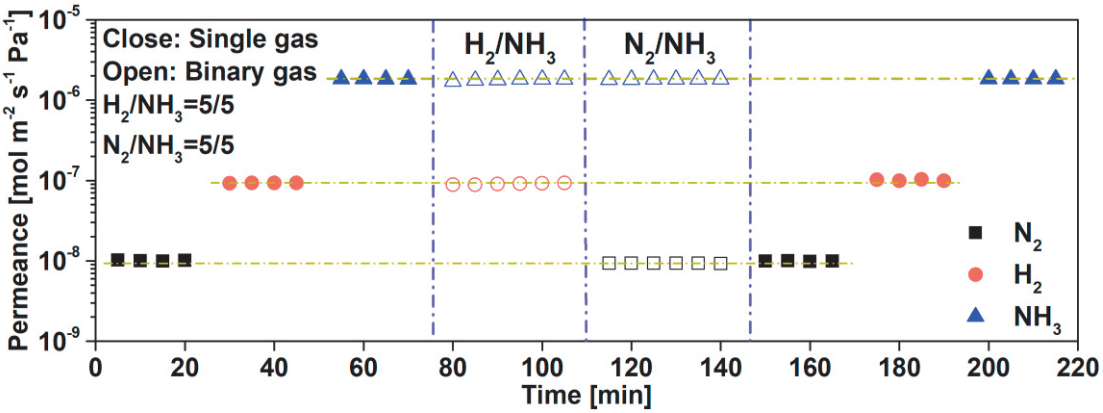

Fig. 3-15. Time courses of selectivity and permeance of NH_3, H_2, and N_2 in single- and binary-gas for 0.50 Ni-BTPA membrane at 100 °C, the binary gases were equimolar NH_3/H_2 and NH_3/N_2, respectively.

Table 3-S2. Data for the selectivity and permeance of various membranes.

Name	Temperature [°C]	NH_3 permeance [mol m^{-2} s^{-1} Pa^{-1}]	NH_3/H_2	NH_3/N_2	Ref
Poly(vinylammonium thio-cyanate)	50.0	6.7000E-08	1390.0	2000.0	4
ZIF-21	25.0	5.7900E-07	12.0	35.0	5
MFI	25.0	2.3000E-06	307.0		6
	25.0	1.1000E-06		2236	
	50.0	3.5000E-06	23.8		
	50.0	1.6600E-06		221	
	100.0	2.7000E-06	3.8		
	100.0	2.5000E-06		20	
Nexar/[Eim][NTf_2]	25.0	9.2829E-07	264.0	1407.0	7
Neat Pebax	25.0	1.9959E-07	70.1	406.7	8
Sulfonated block copolymers	25.0	2.0100E-07	90.0	100.0	9
Polypropylene/Nafion	25.0	3.3500E-06	500.0	2000.0	10
TEOS	50.0	1.0200E-07	28.7		11
2D-MXene	25.0	6.2004E-07	50		12
Prussian Blue	25.0	3.7202E-08	40	100	13
Nafion/ceramic	50.0	2.8544E-06	40.3	730.9	14
	200.0	1.9355E-06	2.6	24.8	
Aquivion-H^+/ceramic	50.0	2.7100E-06	118.6	2085.9	
	200.0	1.6800E-06	6.3	73.9	
Aquivion-Li^+/ceramic	50.0	1.8800E-06	44.7	465.6	
	200.0	9.0500E-07	1.9	22.3	
BTPA	50.0	3.2208E-07	20.6	214.2	15
	200.0	1.3107E-06	7.1	78.1	
0.50 Fe-BTPA	50.0	1.1110E-06	24.6	237.6	
	200.0	2.2437E-06	9.9	90.6	
0.50 Ag-BTPA	50.0	6.5437E-07	15.7	142.6	
	200.0	1.6300E-06	7.3	64.7	
0.25 Ni-BTPA	50.0	5.8244E-07	22.6	223.8	This
	200.0	1.5923E-06	8.1	78.1	work
0.50 Ni-BTPA	50.0	1.4614E-06	27.3	276.7	This
	200.0	2.7995E-06	10.8	101.7	work
1.00 Ni-BTPA	50.0	1.5960E-06	12.9	88.7	This
	200.0	3.2910E-06	5.5	35.6	work

References

[1] U. Anggarini, L. Yu, H. Nagasawa, M. Kanezashi, T. Tsuru, Microporous nickel-coordinated aminosilica membranes for improved pervaporation performance of methanol/toluene separation, *ACS Appl. Mater. Interfaces* 13 (2021) 23247-23259.

[2] T. Yoshioka, M. Kanezashi, T. Tsuru. Micropore size estimation on gas separation membranes: A study in experimental and molecular dynamics. *AIChE J.* 59 (2013) 2179-2194.

[3] H.R. Lee, T. Shibata, M. Kanezashi, T. Mizumo, J. Ohsita, T. Tsuru, Pore-size-controlled silica membranes with disiloxane alkoxides for gas separation. *J. Membr. Sci.* 383 (2011) 152-158.

[4] D.V. Laciak, R. Quinn, G.P. Pez, J.B. Appleby, P.S. Puri, Selective permeation of ammonia and carbon dioxide by novel membranes, *Sep. Sci. Technol.* 25 (1990) 1295-1305.

[5] Q. Wei, J.M. Lucero, J.M. Crawford, J. Douglas Way, C.A. Wolden, M.A. Carreon, Ammonia separation from N_2 and H_2 over LTA zeolitic imidazolate framework membranes, *J. Membr. Sci.* 623 (2021) 119078.

[6] X. Duan, D. Kim, K. Narasimharao, S. Al-Thabaitic, M. Tsapatsis, High-performance ammonia-selective MFI nanosheet membranes, *Chem. Commun.* 57 (2021) 580-582.

[7] B. Yang, L. Bai, S. Zeng, S. Luo, L. Liu, J. Han, Y. Nie, X. Zhang, S. Zhang, NH_3 separation membranes with self-assembled gas highways induced by protic ionic liquids, *Chem. Eng. J.* 421 (2021) 127876.

[8] B. Yang, L. Bai, Z. Wang, H. Jiang, S. Zeng, X. Zhang, X. Zhang, Exploring NH_3 Transport Properties by Tailoring Ionic Liquids in Pebax-Based Hybrid Membranes, *Ind. Eng. Chem. Res.* 60 (2021) 9570-9577.

[9] W.A. Phillip, E. Martono, L. Chen, M.A. Hillmyer, E.L. Cussler, Seeking an ammonia selective membrane based on nanostructured sulfonated block copolymers, *J. Membr. Sci.* 337 (2009) 39-46.

[10] V. Tricoli, E.L. Cussler, Ammonia selective hollow fibers, *J. Membr. Sci.* 104 (1995)

19-26.

[11] M. Kanezashi, A. Yamamoto, T. Yoshioka, T. Tsuru, Characteristics of Ammonia Permeation Through Porous Silica Membranes, *AIChE J.* 56 (2010) 1204-1212.

[12] D.I. Petukhov, A.S. Kan, A.P. Chumakov, O.V. Konovalov, R.G. Valeev, A.A. Eliseev, MXene-based gas separation membranes with sorption type selectivity, *J. Membr. Sci.* 621 (2021) 118994.

[13] M.A. Komkova, I.S. Sadilov, V.A. Brotsman, D.I. Petukhov, A.A. Eliseev, Facilitated transport of ammonia in ultra-thin Prussian Blue membranes with potential-tuned selectivity, *J. Membr. Sci.* 639 (2021) 119714.

[14] K. Wakimoto, W.W. Yan, N. Moriyama, H. Nagasawa, M. Kanezashi, T. Tsuru, Ammonia permeation of fluorinated sulfonic acid polymer/ceramic composite membranes, *J. Membr. Sci.* 658 (2022) 120718

[15] W.W. Yan, U. Anggarini, H.C. Bai, H. Nagasawa, M. Kanezashi, T. Tsuru, Enhanced NH_3 permeation of bis[3-(trimethoxysilyl)propyl] amine membranes via coordination with metals, *J. Membr. Sci.* 678 (2023) 121665.

Chapter 4

Development of sulfonated (3-Mercaptopropyl)trimethoxysilane membranes with thermal stability and excellent NH_3 perm-selectivity at 300 °C

4.1 Introduction

Ammonia (NH_3) synthesized by the Haber-Bosch process has made unparalleled contributions to fertilizer and crop production worldwide, [1,2] and can also be regarded as an increasingly important carbon-free hydrogen energy-carrier because of its high hydrogen-storage capacity (17.6 wt%) and volumetric density (107.7 $kg_{H_2} m^{-3}$). [3,4] The production of green NH_3 using N_2 and H_2 from air separation and water electrolysis, respectively, has attracted increasing attention. Since low temperatures are dynamically favorable for NH_3 conversion, NH_3 synthesis at low temperatures, such as 50 °C, have been groundbreakingly reported using various types of catalysts including Ru/CaFH [5]. However, the NH_3 production rate and the limited conversion are still not ideal below 250 °C similar to that of conventional Fe- and Ru-based catalysts. [6,7] Fig. 4-1 shows catalytic membrane reactors (CMRs) consisting of reaction and concurrently selective membrane separation are proposed to enhance both thermodynamics and kinetics, [8] but membranes with NH_3 perm-selectivity and thermal stability are the key to realize CMRs for NH_3 synthesis.

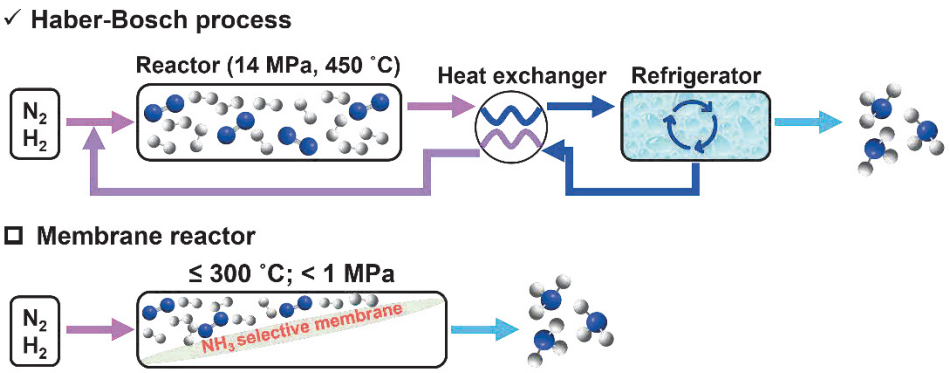

Fig. 4-1. Schematic diagram of the Haber-Bosch and membrane reactor process.

Currently, high temperatures still are required to obtain a practical reaction rate in NH_3 synthesis with high yield, which also propounds a demanding requirement on the use of membrane separation techniques with thermal stability and NH_3 perm-selectivity. Various membranes, such as polymer membranes [9,10], ionic liquid/deep eutectic solvent-based membranes [11,12], zeolite framework membranes [13,14], and silica-based membranes [15,16], have been developed to improve NH_3 affinity, permeance, and perm-selectivity from the mixture of H_2, N_2, and NH_3. According to the NH_3 yields reported at different temperatures, [6-8] it would be feasible to perform NH_3 synthesis with a high yield obtained using a Ru-based catalyst above 250 °C. However, most polymer membranes such as Nafion [17] and polyvinylammonium thiocyanate [18] could be partly corroded/destroyed at high temperatures and/or NH_3 concentrations. Besides, most zeolite and metal framework membranes would exhibit high NH_3 perm-selectivity only at low temperatures [13,14]. Tetraethoxysilane (TEOS) derived membranes performed a favorable NH_3/H_2 selectivity of 28.7 from isometric NH_3/H_2 at 50 °C in binary gas permeation but NH_3/H_2 selectivity of 0.083 at 400 °C. [16]

Recently, perfluorosulfonic acid (PFSA)/ceramic composite membranes [19] and

nickel-doped bis[3-(trimethoxysilyl)propyl] amine (Ni-BTPA) membranes [20] showed a superior NH_3 permeance and selectivity based on Lewis and/or Brønsted acid-base interactions, coordination as well as hydrogen bonds. Although PFSA-based membranes exceeded high NH_3 permeance of 10^{-6} mol m^{-2} s^{-1} Pa^{-1} with comparable NH_3 selectivity based on acid-base interactions at 50 °C, both NH_3 permeance and selectivity were obviously decreased with rising temperatures, especially NH_3/H_2 and NH_3/N_2 selectivity of 2 and 22, respectively, at 200 °C. Even if Ni-BTPA membranes showed a favorable NH_3 permeance and perm-selectivity at 200 °C, the propylamine chains in BTPA would be decomposed greatly at > 200 °C with the increase of $Ni(NO_3)_2$ doping amount, [21] which is hard to accurately control pore sizes and improve NH_3 affinity.

(3-Mercaptopropyl)trimethoxysilane (MPTMS)-modified silica xerogels have been reported to selectively adsorb trace gaseous NH_3 from air by chemical interactions through sulfonated groups and showed a sufficient thermal stability around 300 °C. [22] Furthermore, MPTMS-based silica xerogels exhibited a high NH_3 adsorption capacity of 4.02 mmol g^{-1} at 0.1 bar and 7.00 mmol g^{-1} at 1.0 bar, and can efficiently capture trace NH_3 from the gas mixture with an initial concentration below 2 ppm, indicating a promising and strong NH_3 affinity for MPTMS. Nevertheless, MPTMS derived membranes, which are expected to enable the continuous separation and can be integrated with catalysts to CMRs, have never been reported for NH_3 separation.

In this study, MPTMS sols were prepared via hydrolysis and condensation of MPTMS precursors and mixed with H_2O_2 to oxidize mercaptan (*S-H*) to *S=O* groups in oxidized MPTMS sols as confirmed by X-ray photoelectron spectroscopy (XPS)

analysis, then both sols were dried to obtain xerogels. The thermal stability of propyl chains and sulfonated groups in as-prepared sols and xerogels around 300 °C were verified via Fourier transform infrared spectrometer (FT-IR), thermogravimetric mass spectrometer (TG-MS), and N_2 adsorption measurements. Additionally, NH_3 temperature-programmed desorption (NH_3-TPD) was used to probe the NH_3 affinity and evaluate the NH_3 adsorption amount for MPTMS xerogels with and without H_2O_2 oxidation. The MPTMS membranes were fabricated from unoxidized and oxidized MPTMS sols and used for single and binary gas permeation, showing an excellent NH_3 permeance and selectivity at 50-300 °C.

4.2 Experiments

4.2.1 Sols, xerogels, and membranes preparation

(3-Mercaptopropyl)trimethoxysilane (85%, MPTMS) was purchased from Thermo Fisher Scientific Inc., Japan and used without further purification. MPTMS sols were prepared via the hydrolysis and condensation of MPTMS precursors in ethanol with the hydrochloric acid (HCl) as a catalyst to promote reaction. Briefly, a mixture of HCl and water was added to MPTMS precursors dissolved in ethanol under continuous stirring and reacted for 12 h at room temperature. The concentration of MPTMS precursors in the sol solution is maintained at 5 wt%, whereas the molar ratio of components in the sol was at MPTMS/H_2O/HCl = 1/50/(0.0, 0.1, 0.2, 0.5, and 1.0). Furthermore, hydrogen peroxide (H_2O_2, 30 wt%) was dropped into fresh MPTMS sols with a sol/H_2O_2 mass ratio of 1/0.05, 1/0.1, and 1/0.2 to obtain the oxidized sols under constant stirring for some time. All sols were dried to xerogels at room temperature.

A porous α-alumina tube (length: 100 mm, average pore size: 1 μm, porosity: 50%, kindly supplied by Nikkato Cor. Japan) as the support was coated with two types of α-alumina particles (0.2 and 2 μm) dispersed in 2 wt% SiO_2-ZrO_2 sols and calcined at 550 °C for 15 min to cover all the macropores. This process was repeated 3-4 times. Then, the particle layers were further coated via utilizing 0.5 wt% SiO_2-ZrO_2 sols, followed by calcination at 550 °C for 15 min, resulting in the intermediate layer with pore sizes close to 1 nm. [23] Finally, the top separation layers were fabricated via coating the unoxidized or oxidized MPTMS sols that were diluted to 1.0 wt% with ethanol on the SiO_2-ZrO_2 intermediate layer, and calcining at 300 °C for 20-30 min under a N_2 atmosphere (sol-gel method). More details of the membrane fabrication process can be found elsewhere. [24,25]

4.2.2 Characterization

The size distribution of all sols was analysed via a Malvern Zetasizer (ZEN 3600) equipped with dynamic light scattering (DLS). The chemical structure and thermal stability of each film prepared by coating sols onto KBr plates and then calcined at different temperatures under a N_2 atmosphere were examined via FT-IR-4100, JASCO, Japan. XPS (JEOL RE series JES-RE1X ESR) was used to analyse the chemical states and examine the bonding energy. All samples were prepared by spin-coating (1500 rpm) the unoxidized and oxidized MPTMS sols onto the surface of a silicon wafer. Then, the samples were calcined at 300 °C under a N_2 atmosphere and dried in a vacuum oven overnight before a XPS measurement. The thermal stability of all xerogels were detected via TG-MS, TGA-DTA-PIMS 410/S, Rigaku, Japan. The xerogel powders

calcined at 300 °C under a N_2 atmosphere were evaluated for the pore size via a N_2 adsorption measurement (BELL Inc., Japan) after evacuating at 200 °C under vacuum conditions for 12 h. The membrane morphology was observed via a scanning electron microscope (SEM, HITACHI S-4800, JEOL, Japan). NH_3-TPD (BELCAT-AT equipped with BELMASS-HT, BELL Inc., Japan) was carried out to evaluate NH_3 adsorption and desorption amount of each xerogel powder calcined at 300 °C under a N_2 atmosphere. The details of the measurement program are presented in the Supplementary Material (SI-1).

4.2.3 Single and binary gas permeation measurement

As depicted in Fig. 4-S1, the experimental apparatus was applied to the single and binary gas permeation, including high-purity He, H_2, NH_3, N_2, CH_4, CF_4, and SF_6. After removing the adsorbed water molecules under a He flow at 200 °C at least for 6 h, each gas was fed into the outside of the membrane under upstream pressures at 200-300 kPa and at 50-300 °C, and the permeate stream was kept at atmospheric pressure. The permeate flow-rate of each gas, except for NH_3, was measured by utilizing a film flow meter (Horiba, Co. Ltd., Japan) at a range from 50-300 °C. The NH_3 permeance cannot be measured with a film flow meter because NH_3 is inherently toxic and water-soluble, so the mass flow meter 4 (Fig. 4-S1), that has been calibrated via a gas chromatograph (GC), was used to measure the flow rate of the permeated NH_3 by closing the retentate valve (V-10a in Fig. 4-S1). The errors of the gas flowrates were less than 5% when the permeance exceeds 10^{-10} mol m^{-2} s^{-1} Pa^{-1} and less than 50% while a the permeance is below 10^{-10} mol m^{-2} s^{-1} Pa^{-1}. GC-1 equipped with a Porapack N column was used to

detect the concentration of NH_3/H_2 and NH_3/N_2 mixture, and GC-2 equipped with a Molecular Sieve X column was utilized to analyze the concentration of H_2/N_2 mixture.

Gas permeance P_i (mol m^{-2} s^{-1} Pa^{-1}) for component i in single and binary gas permeation was calculated using equation (Eq-1).

$$P_i = \frac{F_i}{\Delta p_i} \qquad \text{Eq-1}$$

The pressure drop, Δp_i^s and Δp_i^b, *in* single and binary gas permeations were calculated according to the following equations (Eq-2) and (Eq-3), respeatively.

$$\Delta p_i^s = p_{f,i}^s - p_{p,i}^s \qquad \text{Eq-2}$$

$$\Delta p_i^b = \frac{p_{f,i}^b - p_{r,i}^b}{ln\frac{(p_{f,i}^b - p_{p,i}^b)}{(p_{r,i}^b - p_{p,i}^b)}} \qquad \text{Eq-3}$$

The selectivity of component *i* over component *j*, $\alpha_{i,j}$, was calculated via equation (Eq-4):

$$\alpha_{i,j} = \frac{P_i}{P_j} \qquad \text{Eq-4}$$

F_i: permeate flow-rate of component *i*; $p_{f,i}^s$ and $p_{p,i}^s$: pressure of pure component *i* in feed and permeate side, respectively, in single gas permeation. $p_{f,i}^b$, $p_{r,i}^b$, and $p_{p,i}^b$: partial pressure of component *i* in feed, retentate, and permeate side, respectively, in binary gas permeation.

4.3 Results and discussions

4.3.1 Structure of unoxidized MPTMS sols with different HCl molar ratios

Fig. 4-2 (a) shows that the DLS size distribution of fresh MPTMS sols with different HCl molar ratios is almost similar, regardless of the HCl amount. The size distribution of the sol was not clearly increased after storing the sols at 50 °C for several days under

an air atmosphere (Fig. 4-2 (b)), which indicates that MPTMS sols have sufficient stability.

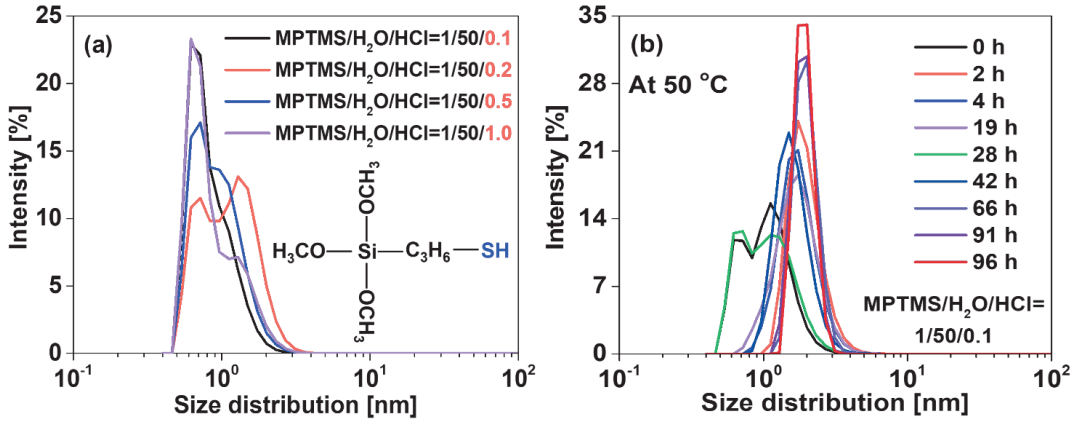

Fig. 4-2. Size distribution of MPTMS sols with different HCl ratios (a); that of MPTMS sols stored at 50 °C (b).

Figs. 4-3 and S2 demonstrate FT-IR spectra for MPTMS films that were prepared from MPTMS sols with different HCl molar ratios (MPTMS/HCl=1/0, 1/0.1, 1/0.2, 1/0.5, and 1/1.0) and calcined at different temperatures (uncalcined, 200, 250, 300, and 350 °C). For the prepared MPTMS sol without using HCl as a catalyst, as shown in Fig. 4-S2 (left), no obvious *Si-O-Si* characteristic peaks were observed around 1000 cm^{-1} compared with the sols using HCl as a catalyst, similar to MPTMS monomers. These results illustrate that HCl as a catalyst was necessary to promote hydrolysis and condensation. Besides, the characteristic peak of adsorbed water (~1630 cm^{-1} [29]) can be clearly observed for MPTMS films prepared from the molar ratio of MPTMS/HCl ≥ 1/0.2, which could be attributed to the Cl^- stabilization of *Si-OH* by ionic interactions [26-28] to increase hydrophilicity [30]. As reported [31-33] and displayed in Fig. 4-3 (right), the deformation band around 2550 cm^{-1} can be assigned to the *S-H* groups.

As for MPTMS monomers and the sol without using HCl, since there is no acidic

catalyst to promote hydrolysis and condensation, the network structure had completely disappeared possibly due to the evaporation of monomers even at 200 °C in Fig. 4-S2. Furthermore, the characteristic peaks of *Si-OH* and adsorbed water gradually decreased with an increase in calcination temperatures, which could be ascribed to the transformation of *Si-OH* groups to *Si-O-Si* groups through condensation at high temperatures owing to the dynamic sol-gel process. [34] As exhibited in Fig. 4-3 (right), the characteristic peaks of *S-H* almost disappeared at 350 °C. However, the characteristic peaks of *C-H* in all MPTMS prepared with HCl were still clear even calcined at 350 °C, which indicates that the propanethiol chains have the excellent stability at 300 °C at least.

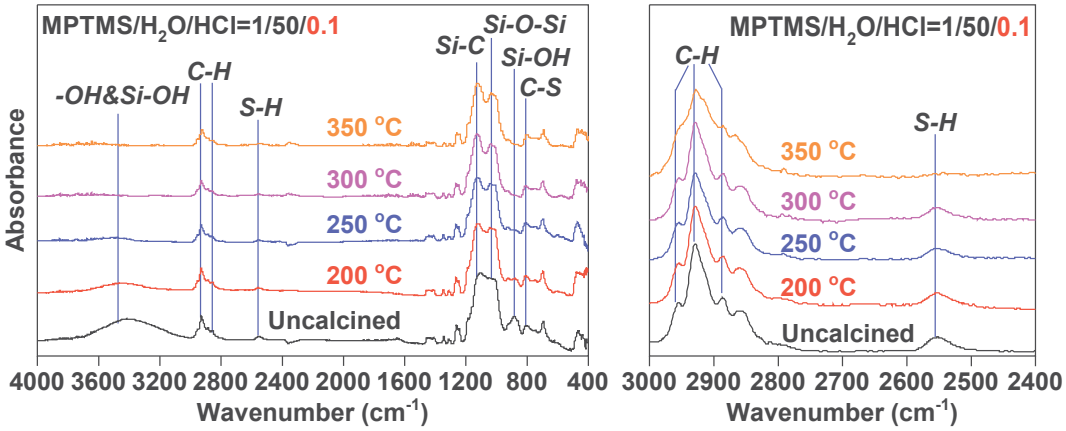

Fig. 4-3. FT-IR spectra for MPTMS films with molar ratio of MPTMS/HCl = 1/0.1 at different calcination temperatures (left); the narrow FT-IR spectra of *C-H* and *S-H* deformation bands ranging from 3000 to 2400 cm^{-1}(right).

Fig. 4-4 shows TG and N_2 adsorption analyses of all MPTMS xerogels with different HCl molar ratios. Clearly, when HCl was not used, the xerogel showed a dramatic decrease in TG, indicating MPTMS was decomposed and/or evaporated about 200 °C. On the other hand, the thermal properties of MPTMS xerogels prepared using HCl were almost the same, irrespectively of acid ratios, which confirms the thermal stability around 300 °C due to no weight-loss. Furthermore, the weight-loss at the first stage was

~21.2 wt% that is consistent with the proportion of *S-H*/total molecular weight (33/154=21.4%). The weight-loss observed from 300-400 °C can be attributed to the decomposition of *S-H*, which was also proven by the signal peaks of m/z = 33 mainly detected at 300-400 °C in Fig. 4-S3. Moreover, as indicated in Fig. 4-4 (b), MPTMS xerogels with different HCl molar ratios always showed a dense structure, independently of the HCl amount, probably because the propyl chains which retain at 300 °C formed non-porous networks due to its flexibility.

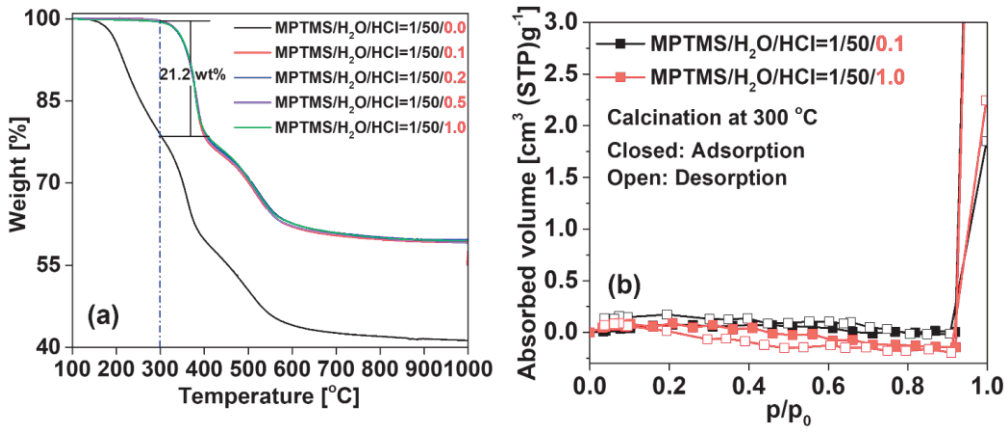

Fig. 4-4. TG measurement (a) and N_2 adsorption (b) of MPTMS xerogel powders with different HCl mole ratios.

4.3.2 Structure of oxidized MPTMS sols with different sol/H_2O_2 mass ratios

Fig. 4-5 exhibits the size distribution of the oxidized MPTMS sols with different mass ratios of sol/H_2O_2 (1/0.05, 1/0.1, and 1/0.2 g/g). When the MPTMS sols with MPTMS/HCl molar ratio=1/1.0 was added with H_2O_2, the sol size was increased rapidly with the increase of oxidation time and H_2O_2 dosage, indicating that H_2O_2 enhanced the condensation of MPTMS sols. This can be attributed to the hydrogen bonds between H_2O_2 and *Si-OH/ Si-O-Si* to form a seven-member ring cluster with less tension, [35,36] probably further improving the condensation of most residual *Si-OH*. On the other hand, the size of MPTMS sols with an MPTMS/HCl molar ratio=1/0.1 was only

increased slightly with an increase in the oxidation time and H_2O_2 dosage. These results indicated that numerous *Si-OH* groups could be further condensed by oxidating with H_2O_2 and transformed to *Si-O-Si* groups to increase the size of MPTMS sols. For MPTMS sols with an MPTMS/HCl molar ratio=1/0.1, the sol size was basically stable around 10 nm even after 15 days, which can be used to fabricate membranes. [20,21]

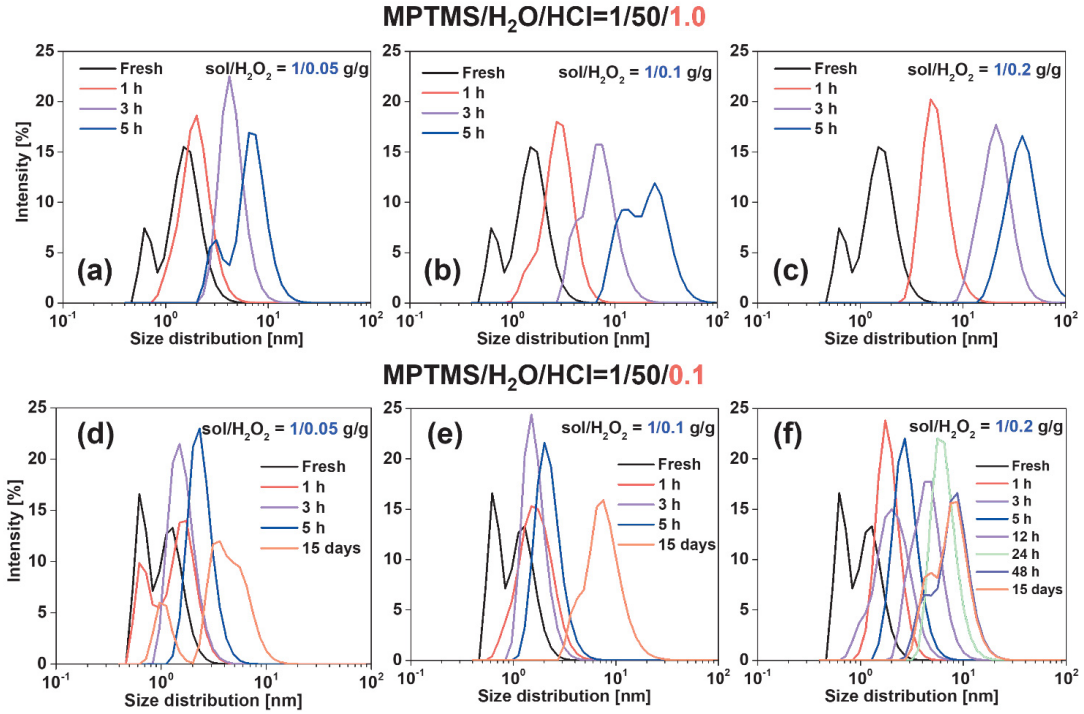

Fig. 4-5. Size distributions of MPTMS sols containing MPTMS/HCl molar ratio=1/1.0 (a, b, and c) and 1/0.1 (d, e, and f) with oxidation using sol/H_2O_2 mass ratio=1/0.05 (a, d), 1/0.1 (b, e), and 1/0.2 (c, f).

Fig. 4-6 demonstrates FT-IR spectra for uncalcined MPTMS films with different MPTMS/HCl molar ratios and sol/H_2O_2 mass ratios. Because the MPTMS sol with MPTMS/HCl molar ratio=1/0.1 has undergone sufficient hydrolysis and condensation without more ionic interactions between Cl^- and *Si-OH*, H_2O_2 oxidation had mildly affected the characteristic peaks of *Si-OH* and *Si-O-Si*. Because the *Si-C*, *C-H*, and *C-S* peaks in both unoxidized and oxidized MPTMS films are similar, regardless of H_2O_2

and HCl amount, H_2O_2 oxidation did not negatively affect the MPTMS network structure obtained after hydrolysis and condensation. According to the published papers [22,37,38], the sulfonated groups are possibly located at 1200-1400 cm^{-1}. As exhibited in Fig. 4-6 (right), the new peaks appeared around 1310 cm^{-1} in the narrow FT-IR spectra of MPTMS films before and after oxidation, which can belong to the sulfonated groups such as *S=O* and SO_3^{-1}.

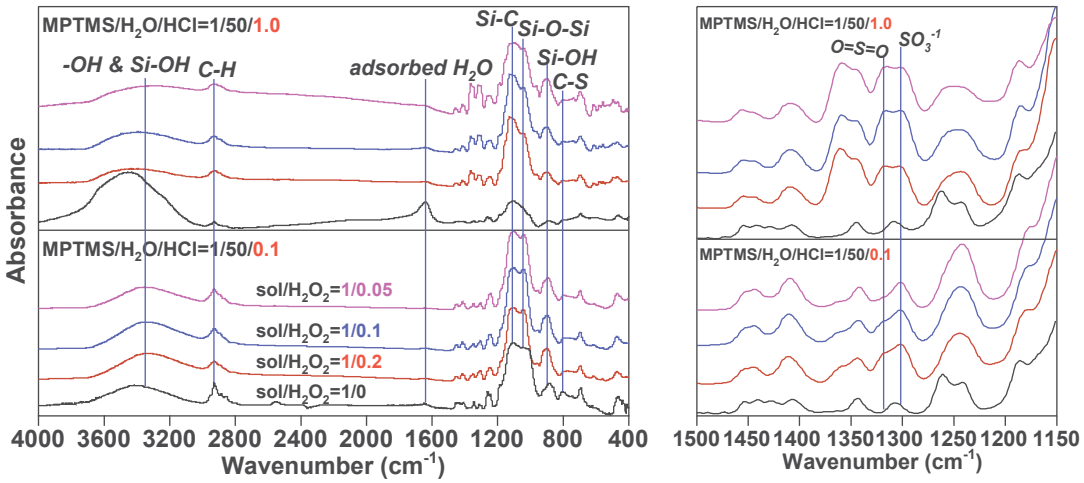

Fig. 4-6. FT-IR spectra for uncalcined MPTMS films with different HCl molar ratios and sol/H_2O_2 mass ratios (left); the narrow FT-IR spectra of sulfonated groups deformation band at different sol/H_2O_2 mass ratios ranging from 1500 to 1150 cm^{-1}(right).

As shown in Fig. 4-S4, the structural changes of MPTMS films coated the sol with different sol/H_2O_2 mass ratios (1/0.05 and 1/0.2 g/g) with oxidation times were characterized by FT-IR. The *C-H* and *Si-C* peaks of these two types of MPTMS films were still clearly observed, regardless of H_2O_2 dosage, even oxidation for 12 h, which indicates that H_2O_2 oxidation did not clearly affect propyl chains. Fig. 4-S5 displays the narrow FT-IR spectra of *C-H* and *S-H* groups as well as sulfonated groups with oxidation time. When less H_2O_2 (sol/H_2O_2=1/0.05) was used, the *S-H* peaks gradually decreased with the extension of oxidation time, and completely disappeared for 12 h.

However, the *S-H* groups have completely disappeared after oxidation for only 0.5 h while using more H_2O_2 (sol/H_2O_2= 1/0.2). As indicated in Fig. 4-S5 (right), the new sulfonated groups (*S=O* and SO_3^{-1}) were obtained within 0.5 h from the beginning of oxidation whether less or more H_2O_2 (sol/H_2O_2=1/0.05 or 1/0.2) was used. To completely oxidize *S-H* into sulfonated groups, it is better to use more H_2O_2 (sol/H_2O_2= 1/0.2) and oxidate for 12 h.

Fig. 4-7 illustrates the XPS analysis of unoxidized and oxidized MPTMS films. Wide scan spectra and atomic ratios show that all elements were observed, and their relative intensities did not change obviously in either oxidized or unoxidized MPTMS films. Additionally, after analyzing a high-resolution spectrum of S_{2p}, the binding energy of S_{2p} in the unoxidized MPTMS films has blue-shifted from 164.4 to 168.8 eV, [22] which further confirms that *S-H* groups were completely oxidized by H_2O_2 to transform sulfonated groups such as *S=O* that were possibly derived from sulfite, sulfone, sulfate, and sulfonic groups, meaning that sulfur oxidization groups may coexist in a variety of forms, as the deconvoluted spectrum of oxidized S_{2p} shows.

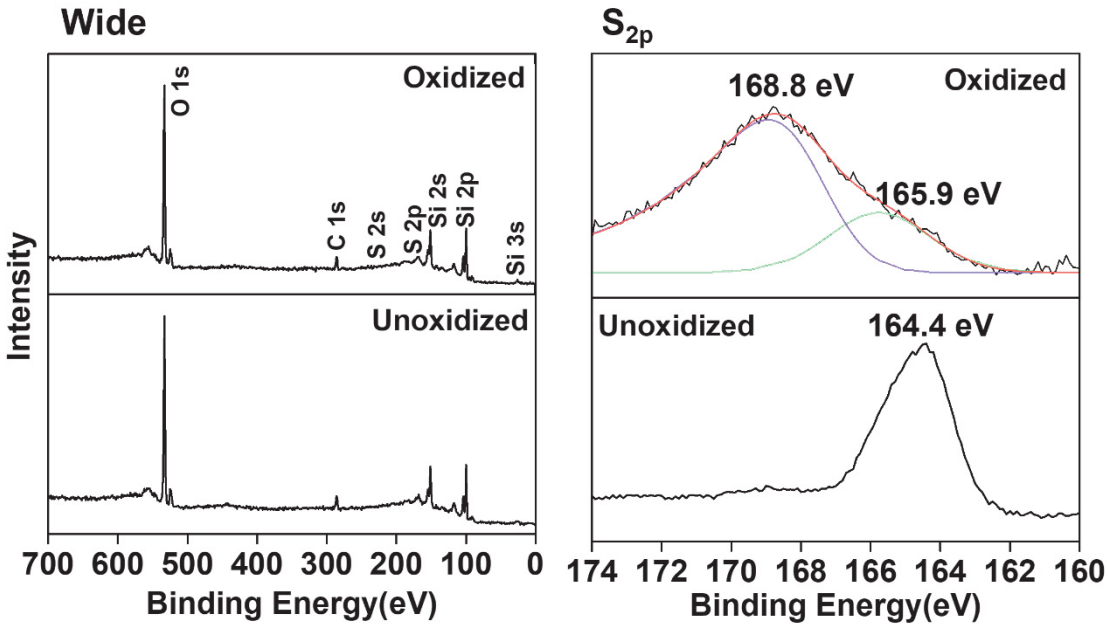

Fig. 4-7. XPS analysis of unoxidized and oxidized MPTMS films (molar ratio of MPTMS/HCl=1/0.1; mass ratio of sol/H_2O_2=1/0.2) calcined at 300 °C: wide scan spectra (left) and high-resolution S_{2p} spectra (right).

Fig. 4-8 displays FT-IR spectra for unoxidized and oxidized MPTMS films at different calcination temperatures. As the calcination temperature rises from 200 to 350 °C, the *Si-OH* peaks gradually disappear in Fig. 4-8 (a) owing to their condensation to *Si-O-Si* in the dynamic sol-gel process. In addition, the peak ratio of *Si-C*/*Si-O-Si* was slightly decreased at 350 °C because either more *Si-O-Si* groups can be obtained from the condensation of *Si-OH* groups, or a part of propyl chains decomposes up to 350 °C. As demonstrated in Figs. 4-8 (b) and (c), the characteristic peaks of *C-H* were deformed and its intensity was reduced after calcination at 350 °C, and the characteristic peaks of the sulfonated groups obtained by oxidizing *S-H* also greatly decreased.

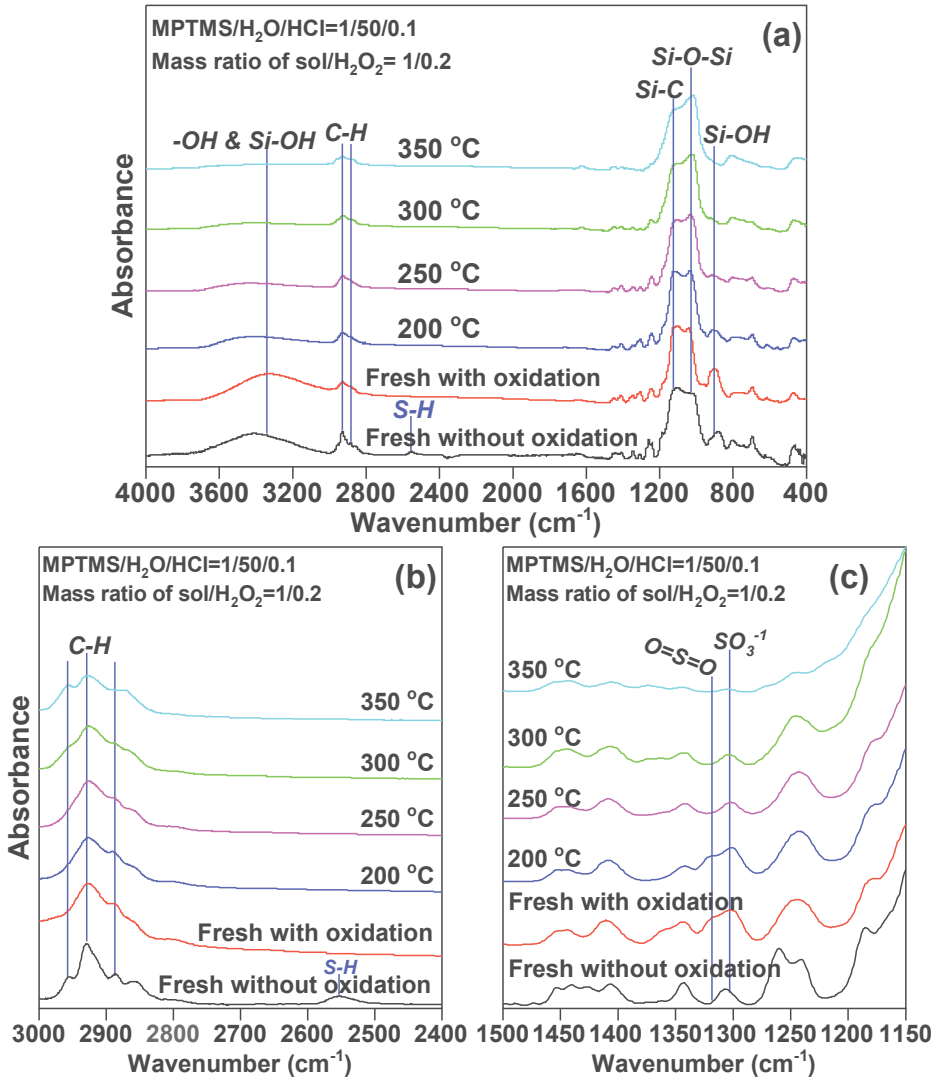

Fig. 4-8. FT-IR spectra for unoxidized and oxidized MPTMS films at different calcination temperatures (a); the narrow FT-IR spectra of *C-H* and *S-H* groups (b) as well as sulfonated groups (c) ranging from 3000 to 2400 and from 1500 to 1150 cm^{-1}, respectively, at different calcination temperatures.

Figs. 4-9 (a) and (b) illustrate TG and N_2 adsorption analyses of unoxidized and oxidized MPTMS xerogels, respectively. Compared to the thermal property of unoxidized MPTMS xerogels, the oxidized MPTMS xerogels underwent the first stage of weight-loss from 100 to 300 °C (~4.77 wt%), which could be ascribed to the desorption of H_2O as explained in detail in SI-6, consistent with the FT-IR results. A further increase in temperature showed a dramatic weight-loss, possibly caused by a serious

decomposition of sulfonated groups. From analyzing the pore structures of unoxidized and oxidized MPTMS xerogels calcined at 300 °C by N_2 adsorption, even the oxidized MPTMS xerogel by H_2O_2 also showed a dense structure in Fig. 4-9 (b) similar to that of unoxidized MPTMS xerogel. Therefore, although the oxidized MPTMS xerogel showed slight weight-loss at 100-300 °C probably due to the desorption of adsorbed H_2O or H_2O derived from the condensation of *Si-OH*, N_2 adsorption also suggested that the main structure containing the propyl chains did barely change, which is consistent with the thermal stability of the propyl chains confirmed via FT-IR and TG analysis.

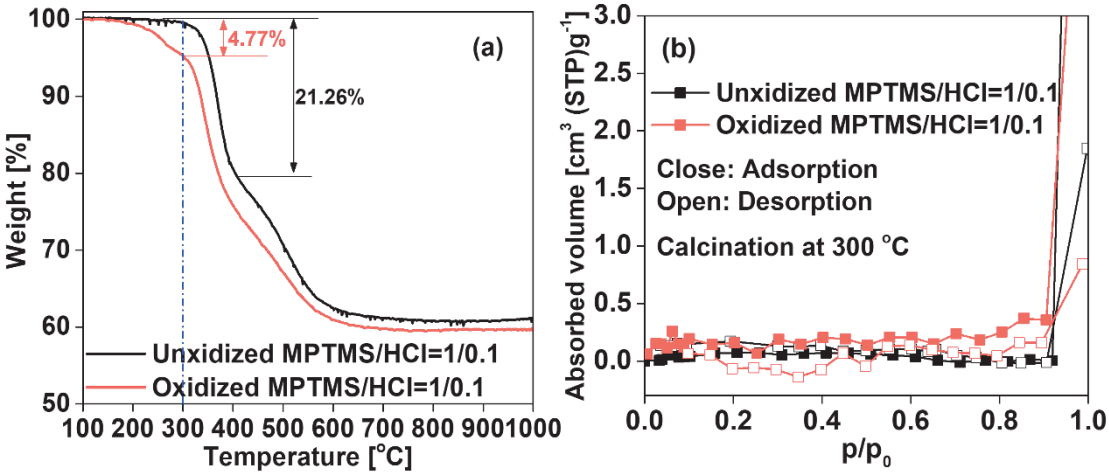

Fig. 4-9. TG measurement (a) and N_2 adsorption (b) of unoxidized and oxidized MPTMS (mass ratio of sol/H_2O_2=1/0.2) xerogel powders.

NH_3-TPD was measured to evaluate the NH_3 affinity and adsorption amounts for unoxidized and oxidized MPTMS xerogels calcined at 300 °C as summarized in Figs. 4-10 and S7. Clearly, the unoxidized MPTMS xerogel has two desorption stage in Fig. 4-S7 (a), indicating that NH_3 partially desorbed around 40 °C before the temperature-programmed started, then completely desorbed as increasing to 300 °C. A medium NH_3 affinity at ~175 °C was attributed to the interactions between *S-H* and NH_3 in Fig. 4-10 (a). [39] However, two NH_3 desorption peaks for oxidized MPTMS xerogels were

displayed around 125 and 230 °C, respectively, which could be assigned to weak and strong NH_3 affinity sites [40,41] caused by *Si-OH/Cl* and sulfonated groups, respectively. As exhibited in Fig. 4-10 (b), the NH_3 adsorption amount for the oxidized MPTMS xerogel is ~1.41 mmol g^{-1}, approximately two times higher than that of unoxidized MPTMS xerogel (~0.75 mmol g^{-1}). It could be attributed to the enhanced acid-base interaction because the sulfonated groups derived from the oxidation of *S-H* have strong acidity and more acidic sites, as a schematic diagram (Fig. 4-10 right) shows. Notably, NH_3 adsorption amount of the oxidized MPTMS was greatly higher than that of per-fluorosulfonic acid, such as Nafion. [20] Besides, the NH_3 desorption amounts at 40 °C for the unoxidized xerogel were almost twice that at 40-300 °C, however, the oxidized xerogel showed a similar NH_3 desorption amounts at both 40 °C and 40-300 °C.

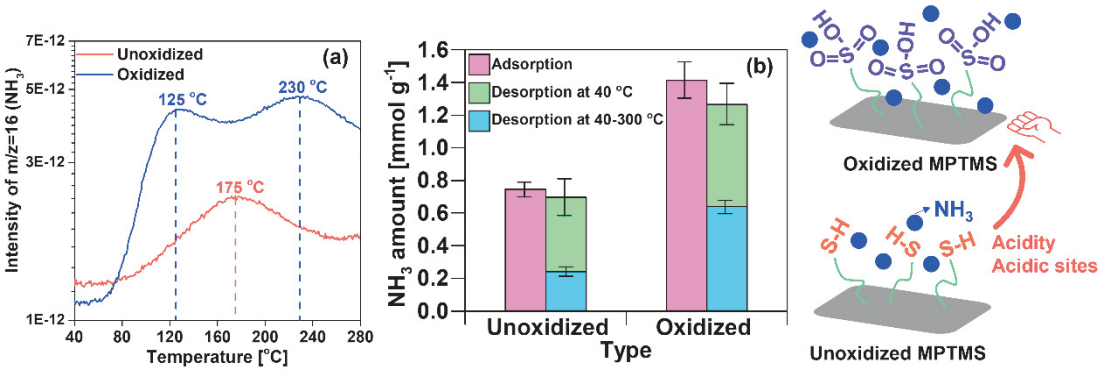

Fig. 4-10. Intensity of NH_3 (m/z=16) during NH_3-TPD measurements for unoxidized and oxidized MPTMS xerogel powders (a); NH_3 adsorption and desorption amounts of unoxidized and oxidized MPTMS xerogels calcined at 300 °C (b).

4.3.3 Performance of unoxidized and oxidized MPTMS membranes

Fig. 4-11 shows the morphology of unoxidized and oxidized MPTMS membranes. The MPTMS membrane prepared with the sol oxidized by H_2O_2 showed a thicker top-separation layer (~900 nm) than the MPTMS membrane without H_2O_2 oxidation, which

could be attributed to the increased size of the oxidized sols and its benign accumulation on the SiO_2-ZrO_2 intermediate layer.

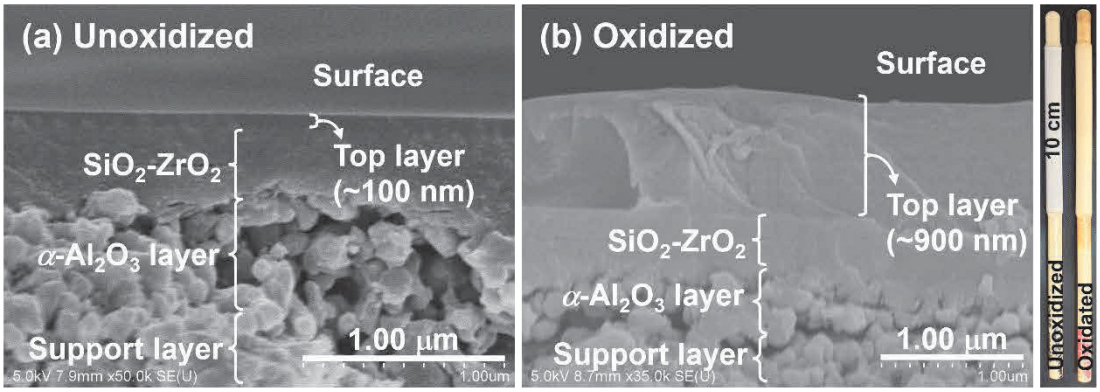

Fig. 4-11. Morphology of unoxidized (a) and oxidized (b) MPTMS membranes.

Fig. 4-12 shows single gas permeance at 200 °C for MPTMS membranes prepared from MPTMS sols with and without oxidation as a function of molecular diameter. As reported in previous paper, [42] because of the molecular sieving effect, the permeance obviously decreased as the molecular diameter of all non-adsorptive gases. Especially, the unoxidized MPTMS membrane showed high gas perm-selectivity such as H_2/N_2 and H_2/SF_6 selectivities of 9 and 1200, respectively, which were considerably higher than Knudsen selectivity. On the other hand, the oxidized MPTMS membrane showed that the gas perm-selectivity of non-adsorptive gases (He, H_2, N_2, CH_4, CF_4, and SF_6) follows Knudsen diffusion, which could be ascribed to the formation of large pores such as pinholes. [43] Although the molecular diameter of NH_3 has been reported to be 0.326 nm [44] similar to that of N_2, its permeance was greatly promoted to be even higher than that of H_2 and He. This enhanced NH_3 permeance can be ascribed to the adsorptive nature through adsorption-diffusion for both unoxidized and oxidized MPTMS membranes. Surprisingly, the oxidized MPTMS membrane showed a high NH_3/H_2

selectivity of > 20 with an NH_3 permeance of ~1.3 × 10^{-7} mol m^{-2} s^{-1} Pa^{-1} at 200 °C.

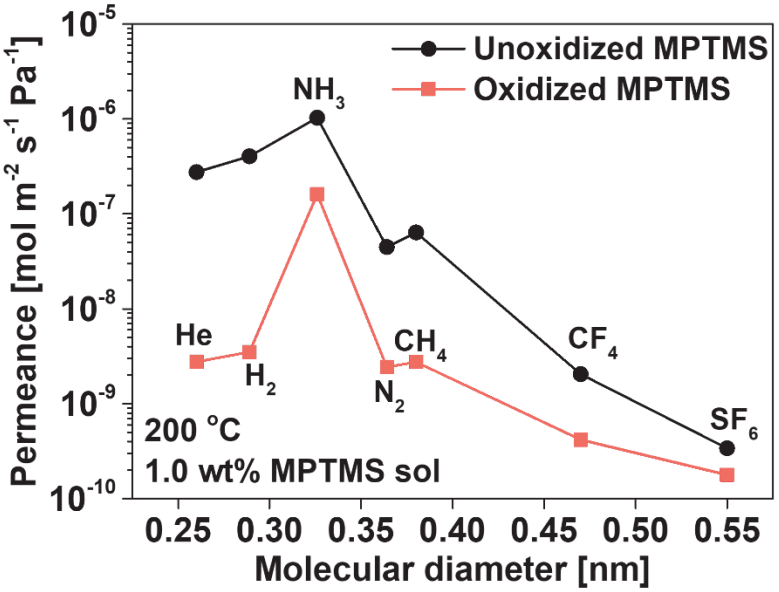

Fig. 4-12. Kinetic diameter dependence of single gas permeance at 200 °C for unoxidized and oxidized MPTMS membranes.

Fig. 4-13 exhibits the temperature dependence of single gas permeance and permselectivity from 50 to 300 °C for MPTMS membranes with and without oxidation. Importantly, NH_3 permeance increased with increasing temperature for oxidized MPTMS membranes at 50-300 °C. Inversely, PFSA-based membranes such as Nafion- and Aquivion-based membranes also contains sulfonic acid functional groups similar to oxidized MPTMS membrane, which showed a decrease in NH_3 permeance with a temperature arise from 50 to 200 °C. [19,45] However, unoxidized MPTMS membranes showed that NH_3 permeance first slightly increased with an increasing temperature at 50-200 °C, and then decreased with further raising to 250 and 300 °C, which can be attributed to its medium NH_3 affinity only around 175 °C. The permeance of H_2 and N_2 as the non-adsorptive gases always increased with an increase in temperatures, regardless of the membrane type.

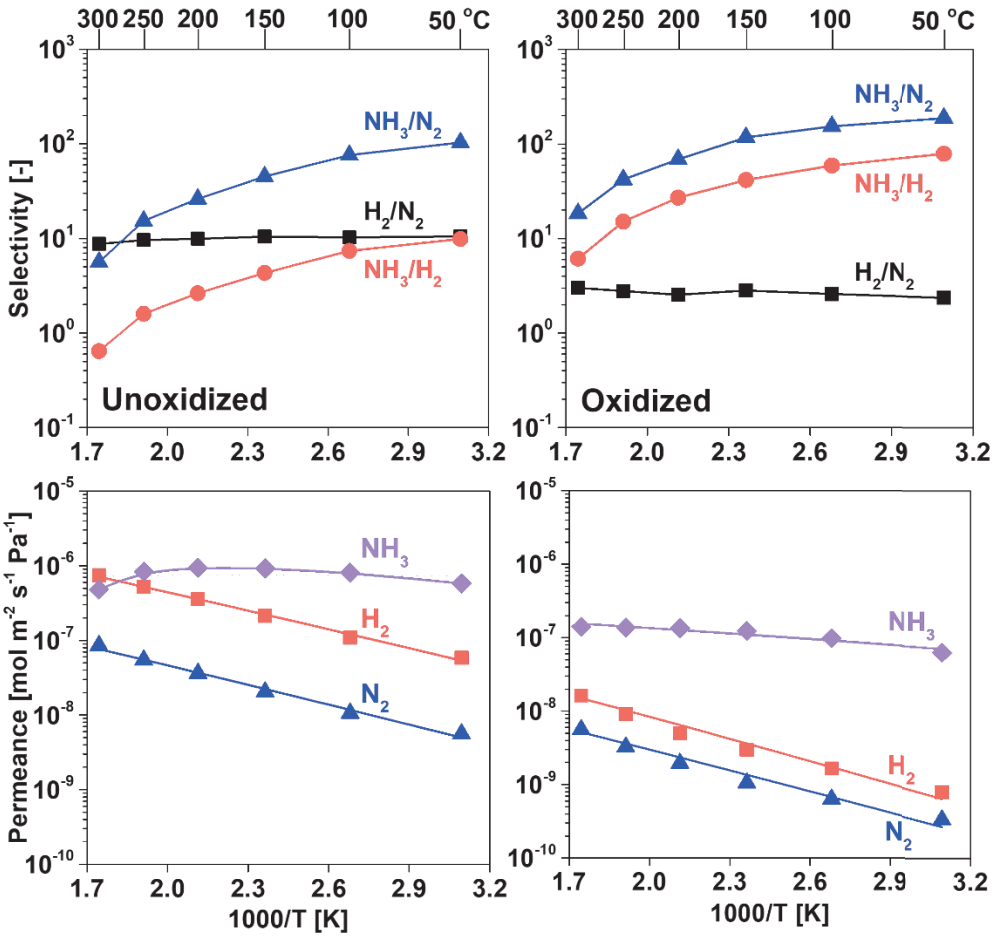

Fig. 4-13. H_2, N_2, and NH_3 permeance and selectivity ranging from 50 to 300 °C for unoxidized (left) and oxidized (right) MPTMS membranes.

Compared to unoxidized MPTMS membranes, the oxidized MPTMS membranes showed that the permeance of both adsorptive NH_3 and non-adsorptive H_2 and N_2 decreased by almost an order of magnitude, which could be attributed to the dense network structure resulting from the facilitated condensation by H_2O_2 oxidation, the filling of the network pores by bulky sulfonated groups such as *S=O* and SO_3^{-1} [22] obtained by *S-H* oxidation, and/or a thicker top-separation layer observed by SEM. As mentioned earlier, although the molecular size of NH_3 is between H_2 and N_2, NH_3 permeance is still higher than N_2 or even H_2 permeance because of the selective adsorption and diffusion through the top-separation layer. At 300 °C, the oxidized MPTMS membranes

showed an excellent NH_3 selectivity of 6 for NH_3/H_2 and 18 for NH_3/N_2 with a NH_3 permeance of ~1.4×10^{-7} mol m^{-2} s^{-1} Pa^{-1}, whereas an NH_3 permeance of ~4.8×10^{-7} mol m^{-2} s^{-1} Pa^{-1} and NH_3/H_2 selectivity of 0.6 and NH_3/N_2 selectivity of 6 for unoxidized MPTMS membranes. Moreover, Fig. 4-14 and Table 4-S1 summarize the trade-off of the NH_3 permeance and NH_3/H_2 selectivity at 200 °C for various membranes. NH_3 permeation at temperatures higher than 100 °C was reported in only several papers and those even 200 °C are quite rare. [19-21,46-48] Although Na^+-gated nanochannel membranes exhibited excellent NH_3 selectivity (NH_3/H_2: > 300; NH_3/N_2: >1000) at 200 °C, its NH_3 permeance was less than satisfactory (2-5 $\times 10^{-8}$ mol m^{-2} s^{-1} Pa^{-1}) [47,48] compared to oxidized MPTMS membrane (1.3×10^{-7} mol m^{-2} s^{-1} Pa^{-1}). Noteworthily, in order to achieve NH_3 production using CMRs, it has been reported that the membrane performance is at least NH_3/H_2 selectivity > 4 and NH_3/N_2 selectivity > 10 with a NH_3 permeance > 3.4×10^{-8} mol m^{-2} s^{-1} Pa^{-1} and a CMR at 300 °C is favorable compared to packed bed reactor at 400 °C for NH_3 production. [49] To realize the great benefits using CMRs for NH_3 synthesis, NH_3 permeance and selectivity of membranes should be balanced or simultaneously promoted, so we believe oxidized MPTMS membranes has the superior NH_3 separation potential and further enhanced the feasibility of membrane reactor for NH_3 synthesis. [50]

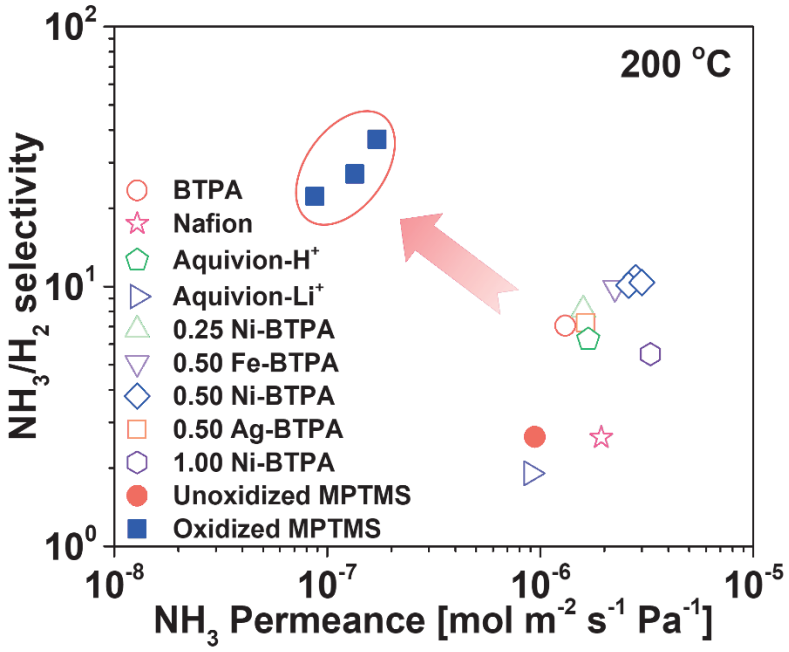

Fig. 4-14. Trade-off of the NH_3 permeance and NH_3/H_2 selectivity at 200 °C for various membranes. Each point indicates the permeance of the different membranes.

Fig. 4-15 indicates the sequence of permeation for H_2, N_2, and NH_3 with a temperature-swing from 50 to 300 °C for MPTMS membranes with and without oxidation. After several temperature-swings, H_2, N_2, and NH_3 permeances were almost the same as those in the initial state whether MPTMS membrane was oxidized or unoxidized. Particularly, the performance of an oxidized MPTMS membrane, even after multiple temperature changes at 50, 200, and 300 °C, did not change significantly, as shown in Fig. 4-15 (c), showing a sufficient thermal stability and NH_3 resistance. Moreover, the similar H_2, N_2, and NH_3 permeances for the three different the oxidized MPTMS membranes are shown in Fig. 4-S8, which has further confirmed the favorable reproducibility for oxidized MPTMS membranes.

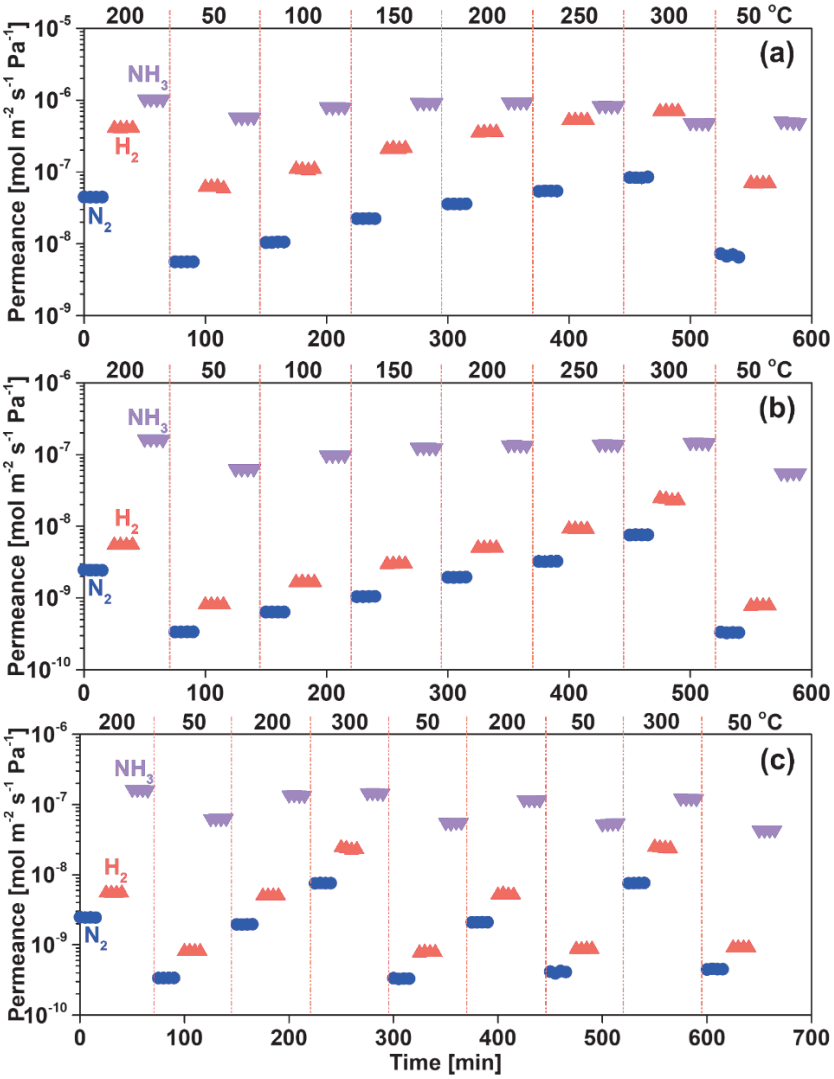

Fig. 4-15. Time course for single H_2, N_2, and NH_3 permeance at temperatures ranging from 50 to 300 °C for unoxidized (a) and oxidized (b) MPTMS membranes, and the measurement again for oxidized (c) MPTMS membranes.

Fig. 4-16 displays the time course of NH_3, H_2, and N_2 permeances as well as NH_3 selectivity during single and binary gas permeation at 300 °C using an oxidized MPTMS membrane. Impressively, TEOS-derived membranes showed that the preferentially adsorbed NH_3 could inhibit H_2 and N_2 permeation at low temperatures to achieve high NH_3 selectivity, [16] meanwhile, the thermodynamically favored sorption for NH_3 in ultra-thin Prussian Blue membranes also resulted in an improved NH_3/H_2 selectivity. [51] This property was limited to low temperatures, and a higher H_2

selectivity than NH_3 was obtained at high temperatures such as 400 °C for TEOS-derived membranes. [16] This trend was explained by surface diffusion of NH_3 induced by selective adsorption. As for oxidized MPTMS membrane, neither NH_3, H_2, and N_2 permeances nor NH_3 selectivity showed any obvious variation in both single and binary gas permeation at 300 °C, which indicates that the inhibition effect of NH_3 permeation on H_2 and N_2 permeances was also eliminated at high temperatures, even though the oxidized MPTMS showed strong NH_3 affinity.

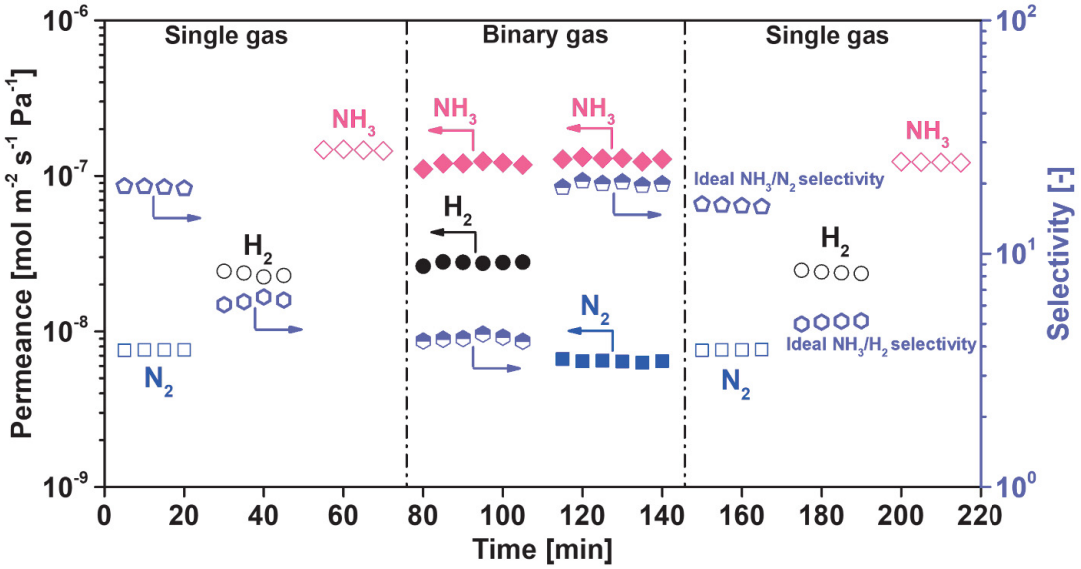

Fig. 4-16. Time courses of selectivity and permeance of NH_3, H_2, and N_2 in single and binary gas permeation for oxidized MPTMS membrane at 300 °C. Feed ratios of NH_3/H_2 and NH_3/N_2 = 1/1.

Combined with the above discussion, therefore, as shown in the schematic diagram in Fig. 4-17, the MPTMS membrane fabricated by the oxidized sols not only exhibits a dense top-separation layer that could inhibit H_2 and N_2 permeance, but also display the Knudsen diffusion properties for non-adsorptive gas molecules, possibly due to the formation of large pores such as pinholes. Nevertheless, as an adsorptive gas, NH_3 can still permeate rapidly even in the dense top layer because of the enhanced acidity and

increased acidic sites, showing an obvious surface adsorption and diffusion mechanism.

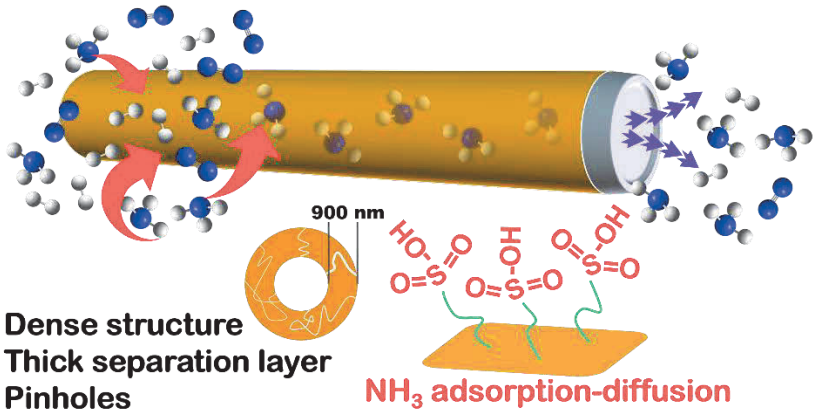

Fig. 4-17. Schematic diagram of MPTMS membrane with H_2O_2 oxidation.

4.4. Conclusions

The unoxidized (3-mercaptopropyl)trimethoxysilane (MPTMS) sols were prepared, and further oxidized by H_2O_2 to improve NH_3 affinity. FT-IR and XPS analyses showed that *S-H* groups can be completely oxidized to sulfonated groups via oxidizing sol solution with H_2O_2. The thermal stability of MPTMS xerogels with and without oxidation was proven around 300 °C via TG-MS analysis. Furthermore, the xerogel powders were always maintained a dense structure using N_2 adsorption due to the flexible and stable propyl chains, independently of H_2O_2 oxidation. Compared with unoxidized MPTMS xerogels, the oxidized xerogels expressed an intense NH_3 affinity and a large NH_3 adsorption amounts because of the improved acidity and increased acidic sites to enhance acid-base interactions from NH_3-TPD results. For single and binary gas permeation, the oxidized MPTMS membranes showed an excellent NH_3/H_2 selectivity of 6 and NH_3/N_2 selectivity of 18 with an NH_3 permeance of ~1.4×10^{-7} mol m^{-2} s^{-1} Pa^{-1} at 300 °C. This can be ascribed to the efficiently selective adsorption on the top-separation layers and the effectual diffusion through membranes.

References

[1] J.W. Erisman, M.A. Sutton, J. Galloway, Z. Klimont, W. Winiwarter, How a century of ammonia synthesis changed the world, *Nat. Geosci.* 1 (2010) 636-639.

[2] S. Ornes, Green ammonia could produce climate-friendly ways to store energy and fertilize farms, *PNAS* 118 (2021) e2119584118.

[3] S. Chatterjee, R.K. Parsapur, K.W. Huang, Limitations of ammonia as a hydrogen energy carrier for the transportation sector, *ACS Energy Lett.* 6 (2021) 4390-4394.

[4] Y. Kojima, M. Yamaguchi, Ammonia as a hydrogen energy carrier, *Int. J Hydrogen Energ.* 47 (2022) 22832-22839.

[5] M. Hattori, S. Iijima, T. Nakao, H. Hosono, M. Hara, Solid solution for catalytic ammonia synthesis from nitrogen and hydrogen gases at 50 °C, *Nat. Commun*. 11 (2020) 2001. DOI: https://doi.org/10.1038/s41467-020-15868-8.

[6] X. Peng, H.X. Liu, Y. Zhang, Z.Q. Huang, L. Yang, Y. Jiang, X. Wang, L. Zheng, C. Chang, C.T. Au, L. Jiang, J. Li, Highly efficient ammonia synthesis at low temperature over a Ru-Co catalyst with dual atomically dispersed active centers, *Chem. Sci.* 12 (2021) 7125-7137.

[7] M. Hattori, N. Okuyama, H. Kurosawa, M. Hara, Low-temperature ammonia synthesis on iron catalyst with an electron donor, *J. Am. Chem. Soc.* 145 (2023) 7888-7897.

[8] X. Feng, R. Long, C. Liu, Y. Lu, X. Liu, Flexible Z-scheme heterojunction membrane reactors for visible-light-driven antibiotic degradation and oil-water separation, *Chem. Eng. J.* 471 (2023) 14444.

[9] W.A. Phillip, E. Martono, L. Chen, M.A. Hillmyer, E.L. Cussler, Seeking an ammonia selective membrane based on nanostructured sulfonated block copolymers, *J. Membrane Sci.* 337 (2009) 39-46.

[10] J. Mi, W. Peng, Y. Luo, W. Chen, L. Lin, C. Chen, Q. Zhu, F. Liu, A. Zheng, L. Jiang, A cationic polymerization strategy to design sulfonated micro-mesoporous polymers as efficient adsorbents for ammonia capture and separation, *Macromolecules* 54 (2021) 7010-7020.

[11] B. Yang, L. Bai, T. Li, L. Deng, L. Liu, S. Zeng, J. Han, X. Zhang, Super selective ammonia separation through multiple-site interaction with ionic liquid-based hybrid membranes, *J. Membrane Sci.* 628 (2021) 119264.

[12] B. Yang, L. Bai, Z. Wang, H. Jiang, S. Zeng, X. Zhang, X. Zhang, Exploring NH_3 transport properties by tailoring ionic liquids in Pebax-based hybrid membranes, *Ind. Eng. Chem. Res.* 60 (2021) 9570-9577.

[13] Q. Wei, J.M. Lucero, J.M. Crawford, J. Douglas Way, C.A. Wolden, M.A. Carreon, Ammonia separation from N_2 and H_2 over LTA zeolitic imidazolate framework membranes, *J. Membrane Sci.* 623 (2021) 119078.

[14] X. Duan, D. Kim, K. Narasimharao, S. Al-Thabaitic, M. Tsapatsis, High-performance ammonia-selective MFI nanosheet membranes, *Chem. Commun.* 57 (2021) 580-582.

[15] O. Camus, S. Perera, B. Crittenden, Y.C. van Delft, D.F. Meyer, P.P.A.C. Pex, I. Kumakiri, S. Miachon, J.A. Dalmon, S. Tennison, P. Chanaud, E. Groensmit, W. Nobel, Ceramic membranes for ammonia recovery, *AIChE J.* 52 (2006) 2055-2065.

[16] M. Kanezashi, A. Yamamoto, T. Yoshioka, T. Tsuru, Characteristics of ammonia permeation through porous silica membranes, *AIChE J.* 56 (2010) 1204-1212.

[17] Y. He, E.L. Cussler, Ammonia permeabilities of perfluorosulfonic membranes in various ionic forms, *J. Membrane Sci.* 68 (1992) 43-52.

[18] A. Bhown, E.L. Cussler, Mechanism for selective ammonia transport through poly(vinylammonium thiocyanate) membranes, *J. Am. Chem. Soc.* 113 (1991) 742-749.

[19] K. Wakimoto, W.W. Yan, N. Moriyama, H. Nagasawa, M. Kanezashi, T. Tsuru, Ammonia permeation of fluorinated sulfonic acid polymer/ceramic composite membranes, *J. Membrane Sci.* 658 (2022) 120718.

[20] W.W. Yan, U. Anggarini, H.C. Bai, H. Nagasawa, M. Kanezashi, T. Tsuru, Enhanced NH_3 permeation of bis[3-(trimethoxysilyl)propyl] amine membranes via coordination with metals, *J. Membrane Sci.* 678 (2023) 121665.

[21] W.W. Yan, U. Anggarini, K. Wakimoto, H.C. Bai, H. Nagasawa, M. Kanezashi, T. Tsuru, Optimization of Ni-amine coordination for improving NH_3 permeation

through nickel-doped bis[3-(trimethoxysilyl)propyl] amine membranes, *Sep. Purif. Technol.* 326 (2023) 124809.

[22] T.T. Hu, F. Liu, S. Dou, L.B. Zhong, X. Cheng, Z.D. Shao, Y.M. Zheng, Selective adsorption of trace gaseous ammonia from air by a sulfonic acid-modified silica xerogel: preparation, characterization and performance, *Chem. Eng. J.* 443 (2022) 136357.

[23] T. Tsuru, Nano/subnano-tuning of porous ceramic membranes for molecular separation, *J. Sol-Gel Sci. Technol.* 46 (2008) 349-361.

[24] X. Yu, H. Nagasawa, M. Kanezashi, T. Tsuru, Improved thermal and oxidation stability of bis(triethoxysilyl)ethane (BTESE)-derived membranes, and their gas-permeation properties, *J. Mater. Chem. A* 6 (2018) 23378.

[25] L. Yu, M. Kanezashi, H. Nagasawa, J. Oshita, A. Naka, T. Tsuru, Pyrimidine-bridged organoalkoxysilane membrane for high-efficiency CO_2 transport via mild affinity, *Sep. Purif. Technol.* 178 (2017) 232-241.

[26] D. Singappuli-Arachchige, I.I. Slowing, Control of interfacial pH in mesoporous silica nanoparticles via surface functionalization, *J. Chem. Phys.* 152 (2020) 034703.

[27] C. Pirez, A.F. Lee, J.C. Manayil, C.M.A. Parlettb, K. Wilson, Hydrothermal saline promoted grafting: a route to sulfonic acid SBA-15 silica with ultra-high acid site loading for biodiesel synthesis, *Green Chem.* 16 (2014) 4506.

[28] C. Pireza, J.C. Morina, J.C. Manayilb, A.F. Leec, K. Wilson, Sol-gel synthesis of SBA-15: Impact of HCl on surface chemistry, *Micropor. Mesopor. Mat.* 271 (2018) 196-202.

[29] A. da Cruz Schneid, L. Jose Calumby Albuquerque, G. Borba Mondo, M. Ceolin, A. Silvio Picco, M. Borba Cardoso, Colloidal stability and degradability of silica nanoparticles in biological fluids: a review, *J. Sol-Gel Sci. Technol.* 102 (2022) 41-62.

[30] J. Fujiki, K. Yogo, E. Furuya, Role of silanol groups on silica gel on adsorption of benzothiophene and naphthalene, *Fuel* 215 (2018) 463-467.

[31] R. Babhu Vignesh, T. Nesakumar Jebakumar Immanuel Edison, M.

Gopalakrishnan Sethuraman, Sol-gel coating with 3-mercaptopropyltrimethoxysilane as precursor for corrosion protection of aluminium metal, *J. Mater. Sci. Technol.* 30(2014) 814-820.

[32] S. Ito, M. Nishi, K. Kanamori, K. Nakanishi, T. Kurahashi, S. Matsubara, Y. Shimotsuma, K. Miura, K. Hirao, (3-Mercaptopropyl)trimethoxysilane-derived porous gel monolith via thioacetal reaction-assisted sol-gel route, *IOP Conf. Ser.: Mater. Sci. Eng.* 18 (2011) 032003. DOI: 10.1088/1757-899X/18/3/032003.

[33] J.J. Senkevich, C.J. Mitchell, G.R. Yang, T.M. Lu, Surface chemistry of mercaptan and growth of pyridine short-chain alkoxy silane molecular layers, *Langmuir* 18 (2002) 1587-1594.

[34] A. Ghoussoub, J.M. Lehn, Dynamic sol-gel interconversion by reversible cation binding and release in G-quartet-based supramolecular polymers, *Chem. Commun.* 2005 5763-5765.

[35] D. Lewandowski, D. Bajerlein, G. Schroeder, Adsorption of hydrogen peroxide on functionalized mesoporous silica surfaces, *Struct. Chem.* 25 (2014) 1505-1512.

[36] J. Ĵegliński, G.P. Piotrowski, R. Piękoś, A study of interaction between hydrogen peroxide and silica gel by FTIR spectroscopy and quantum chemistry, *J. Mol. Struct.* 794 (2006) 83-91.

[37] A. Enotiadis, L.G. Boutsika, K. Spyrou, C. Simaric, I. Nicotera, A facile approach to fabricating organosilica layered material with sulfonic groups as an efficient filler for polymer electrolyte nanocomposites, *New J. Chem.* 41 (2017) 9489-9496.

[38] W. Zhang, B. Zhang, G. He, B. Liu, Z. Jiang, X. Yang, C. Li, Enhanced water retention and proton conductivity of proton exchange membranes by incorporating hollow polymer microspheres grafted with sulfonated polystyrene brushes, *RSC Adv.* 5 (2015) 5343-5356.

[39] S.A. Ali, F.M. Almulla, B. Rabindran Jermy, A.M. Aitani, R.H. Abudawoud, M. AlAmer, Z.S.Qureshi, T.Mohammad, H.S. Alasiri, Hierarchical composite catalysts of MCM-41 on zeolite Beta for conversion of heavy reformate to xylenes, *J. Ind. Eng. Chem.* 98 (2021) 189-199.

[40] C. Rajendran, G. Satishkumar, C. Lang, E.M. Gaigneaux, Alumina grafted SBA-

15 sustainable bifunctional catalysts for direct cross-coupling of benzylic alcohols to diarylmethanes, *Catal. Sci. Technol.* 10 (2020) 2583-2592.

[41] C. Auepattana-aumrung, V. Márquez, S. Wannakao, B. Jongsomjit, J. Panpranot, P. Praserthdam, Role of Al in Na-ZSM-5 zeolite structure on catalyst stability in butene cracking reaction, *Scientific Reports* 10 (2020) 13643.

[42] M. Kanezashi, T. Matsutani, H. Nagasawa, T. Tsuru, Fluorine-induced microporous silica membranes: Dramatic improvement in hydrothermal stability and pore size controllability for highly permeable propylene/propane separation, *J. Membrane Sci.* 549 (2018) 111-119.

[43] U. Anggarini, L. Yu, H. Nagasawa, M. Kanezashi, T. Tsuru, Structural transformation of the nickel coordination-induced subnanoporosity of aminosilica membranes for methanol-selective, high-flux pervaporation, *J. Membrane Sci.* 656 (2022) 120613.

[44] M. Kanezashi, A. Yamamoto, T. Yoshioka, T. Tsuru, Characteristics of ammonia permeation through porous silica membranes, *AIChE J.*, 56 (2010) 1204-1212.

[45] Y.K. He, E.L. Cussler, Ammonia permeabilities of perfluorosulfonic membranes in various ionic forms, *J. Membrane Sci.* 68 (1992) 43-52.

[46] X. Duan, D. Kim, K. Narasimharao, S. Al-Thabaitic, M. Tsapatsis, High-performance ammonia-selective MFI nanosheet membranes, *Chem. Commun.*, 57 (2021) 580-582.

[47] S. Padinjarekutt, B. Sengupta, H. Li, K. Friedman, D. Behera, R. Lecaros, M. Yu, Synthesis of Na^+-gated nanochannel membranes for the ammonia (NH_3) separation, *J. Membrane Sci.* 674 (2023) 121512

[48] S. Padinjarekutt, H. Li, S. Ren, P. Ramesh, F. Zhou, S. Li, G. Belfort, M. Yu, Na^+-gated nanochannel membrane for highly selective ammonia (NH_3) separation in the Haber-Bosch process, *Chem. Eng. J.* 454 (2023) 139998.

[49] Z. Zhang, J. Douglas Way, C.A. Wolden, Design and operational considerations of catalytic membrane reactors for ammonia synthesis, *AIChE J.* (2021) e17259.

[50] A.T. Larson, R.L. Dodge, The ammonia equilibrium, *J. Am. Chem. Soc.* 45 (1923) 2918-2930.

[51] M.A. Komkova, I.S. Sadilov, V.A. Brotsman, D.I. Petukhov, A.A. Eliseev, Facilitated transport of ammonia in ultra-thin Prussian Blue membranes with potential-tuned selectivity, *J. Membrane Sci.* 639 (2021) 119714.

Supplementary Material

---------- **SI-1**: NH_3 temperature-programmed desorption (NH_3-TPD) ----------

The NH_3 affinity and amount of the xerogel powders was probed using NH_3 temperature-programmed desorption (NH_3-TPD). All xerogel powders were pre-calcined under a N_2 atmosphere at 300 °C. The measurement program is detailed below. Firstly, the pre-treated xerogel powders were further degassed to remove adsorbed water via utilizing dry helium at 30 mL min^{-1} for 120 min at 150 ℃. After cooling and held at 28 ℃ for 60 min, 5% NH_3/95% He mixture gases at 30 mL min^{-1} and Ar gas at 1 mL min^{-1} were put into the sample cell for 90 min to reach adsorption saturation. When the NH_3 adsorption was finished, the dry helium at 30 mL min^{-1} continued to flow into the system at room temperature for 120 min. Finally, the NH_3 desorption program was implemented as the temperature increased from 40 to 300 ℃ at 10 ℃ min^{-1} and maintained at 300 ℃ for 15 min. The followed Eq-1 and Eq-2 were used to calculate the NH_3 adsorption and desortion amount, respectively. Each sample was measured 3 times to obtain the average amount of NH_3 adsorption and desorption.

$$NH_3 \text{ adsorption amount} = \frac{1}{m}\int_{t1}^{t2}\left(\frac{I_{Ar,t}\frac{I_{NH_3,\,in}}{I_{Ar,in}} - I_{NH_3,t}}{I_{NH_3,\,in}}\right)Q_{NH_3}\,dt \quad \text{Eq-1}$$

$$NH_3 \text{ desorption amount (40→300 °C)} = \frac{1}{m}\int_{t3}^{t4}\left(\frac{I_{NH_3,t}}{I_{NH_3,\,in}}\right)Q_{NH_3}\,dt \quad \text{Eq-2}$$

m: weight of sample; $I_{i,in}$: intensity of the feed i-th component; $I_{i,t}$: intensity of the feed i-th component at each moment; Q_{NH_3}: flow rate of NH_3.

---------- **SI-2**: Experimental apparatus ----------

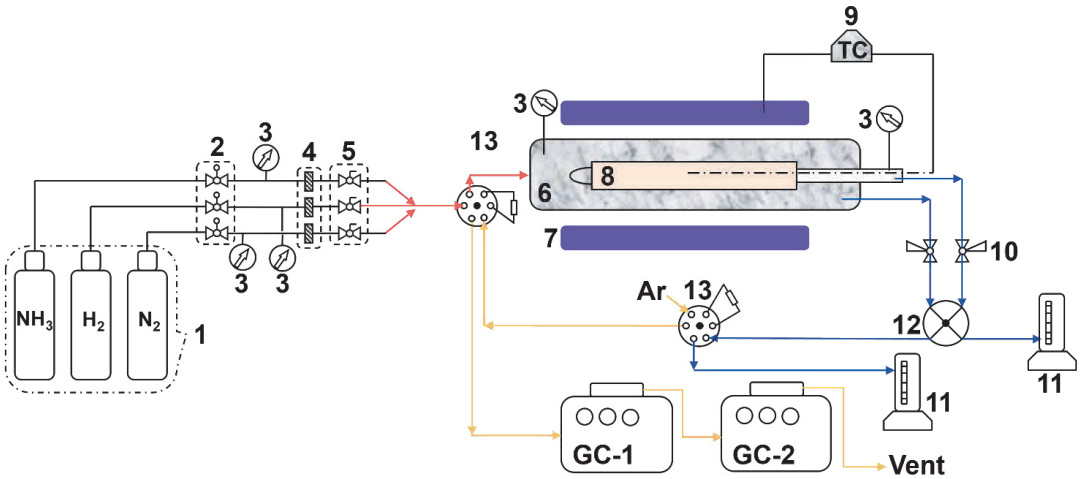

1. Gas cylinder 2. Pressure controller 3. Pressure gauge 4. Mass flow controller
5. Stop valve 6. Membrane module 7. Furnace 8. Membrane
9. Temperature controller (TC) 10. Back pressure valve
11. Bubble film meter 12. 4-way valve 13. 6-way valve

Fig. 4-S1. Schematic diagram of the single-gas permeation measurement.

---------- **SI-3**: FT-IR spectra of MPTMS films with different HCl molar ratios ---------

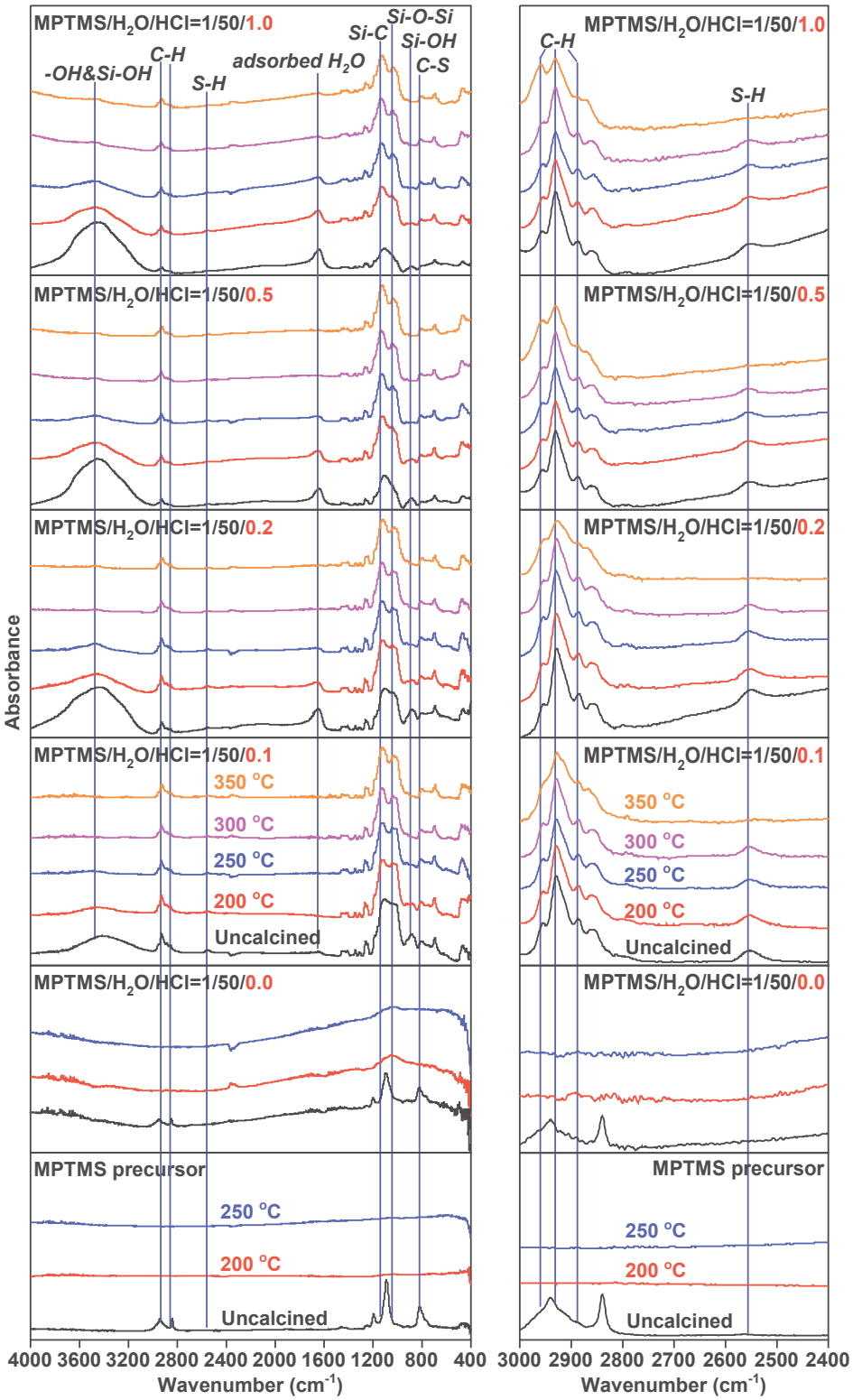

Fig. 4-S2. FT-IR spectra for MPTMS films with different HCl molar ratios at different calcination temperatures (left); the narrow FT-IR spectra of *C-H* and *S-H* deformation bands ranging from 3000 to 2400 cm^{-1}(right).

---------- **SI-4**: Mass signal of m/z = 33 of MPTMS xerogel powders ----------

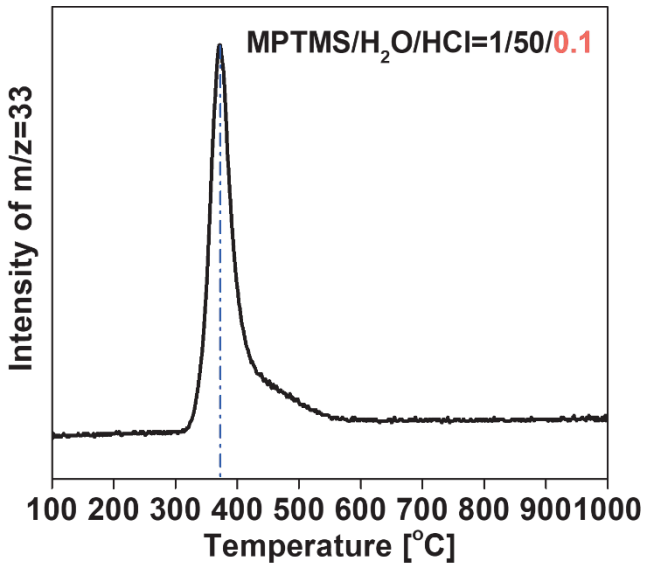

Fig. 4-S3. Mass signal of m/z = 33 of MPTMS xerogel powders with molar ratio of MPTMS/HCl = 1/0.1 by TG-MS.

---------- **SI-5**: FT-IR spectra of oxidized MPTMS films with oxidation time ----------

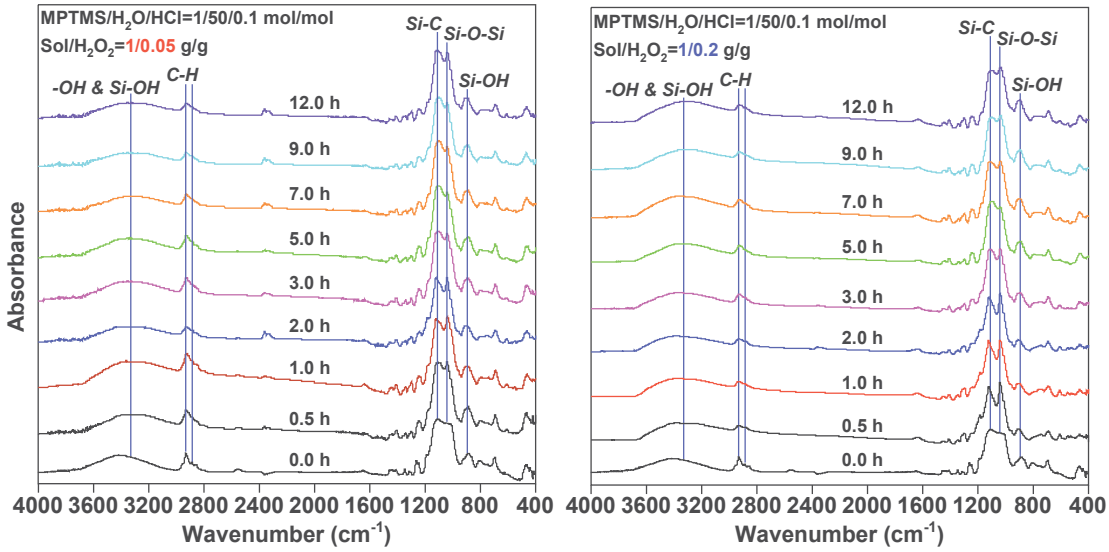

Fig. 4-S4. Time course of FT-IR spectra of MPTMS films prepared from sol/H_2O_2 mass ratios of 1/0.05 (left) and 1/0.2 (right).

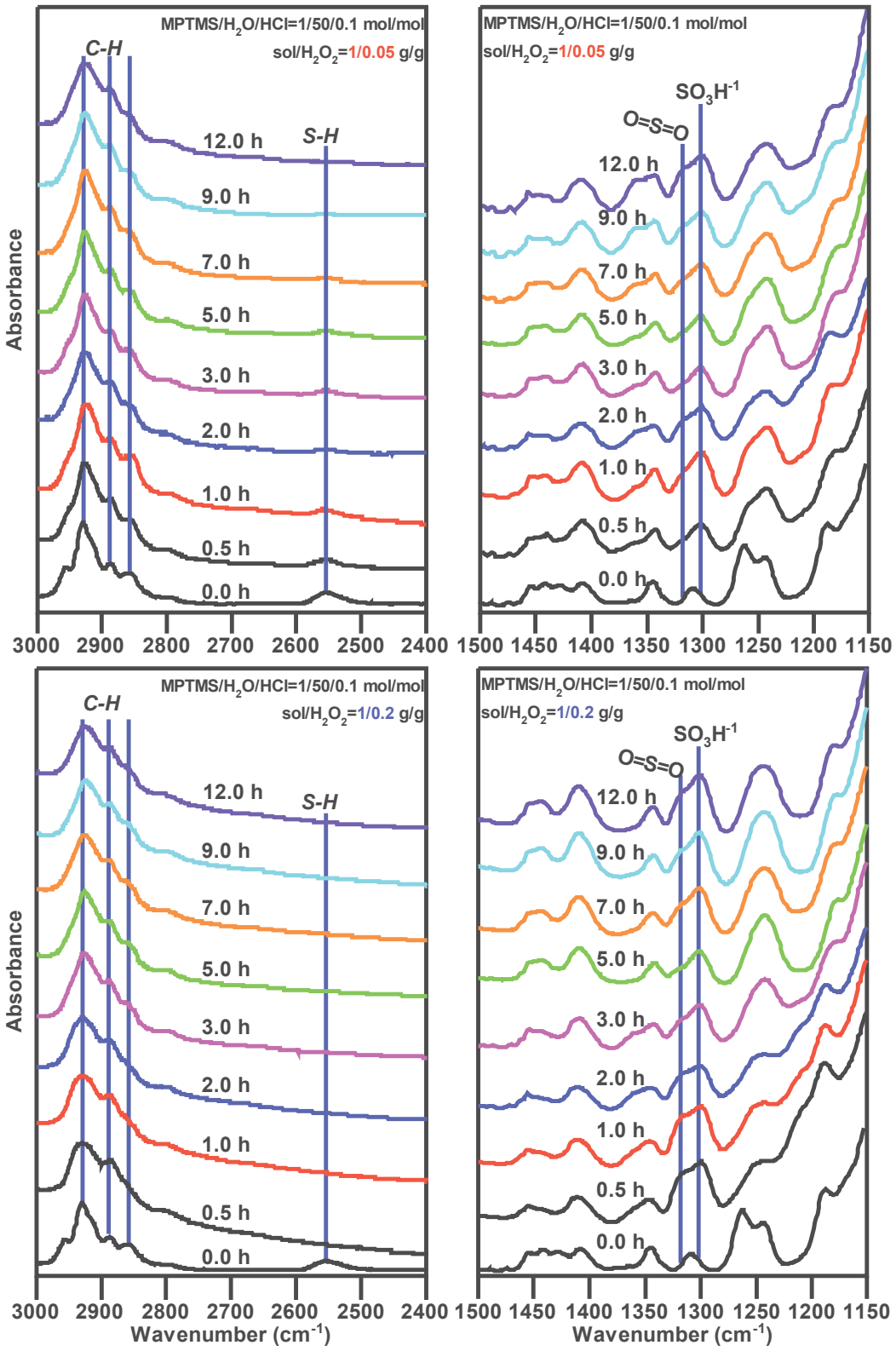

Fig. 4-S5. The narrow FT-IR spectra of *C-H* and *S-H* (left) as well as *S=O* and SO_3^{-1} (right) deformation bands with oxidation time ranging from 3000 to 2400 and from 1500 to 1150 cm^{-1}, respectively, at sol/H_2O_2 mass ratios of 1/0.05 (top) and 1/0.2 (bottom).

---------- **SI-6**: Mass signal of m/z = 18, 33, 44, and 48 in unoxidized and oxidized MPTMS ----------

Although it is difficult to categorically assign m/z to a specific functional group, the m/z = 18, 33, 44, and 48 possibly be attributed to the ion fragment of H_2O, *S-H*, CO_2, and *S=O*, respectively, according to their atomic mass. The mass signal of m/z = 18 only displays a peak around 350 °C possibly due to the desorption of H_2O originated from the condensation of *Si-OH*, but its intensity increased with temperature. Therefore, the weight-loss within 100-300 °C for MPTMS xerogels with oxidation in Fig. 9 in the main text could be attributed to the decomposition and/or evaporation of adsorbed water and free sulfate as shown in Figs. 4-S6 (a) and (c). Fig. 4-S6 (b) shows that the elemental *C* from the propyl chains probably be decomposed in the form of CO_2 over 400 °C, consistent with the second weight-loss stage in Fig. 9. Moreover, the signal peaks of m/z = 48 (*S=O*) and m/z = 33 (*S-H*) are mainly and approximatively distributed in the 300-400 °C in Figs. 4-S6 (c) and (d), which can confirm the thermal stability of *S-H* and sulfonated groups.

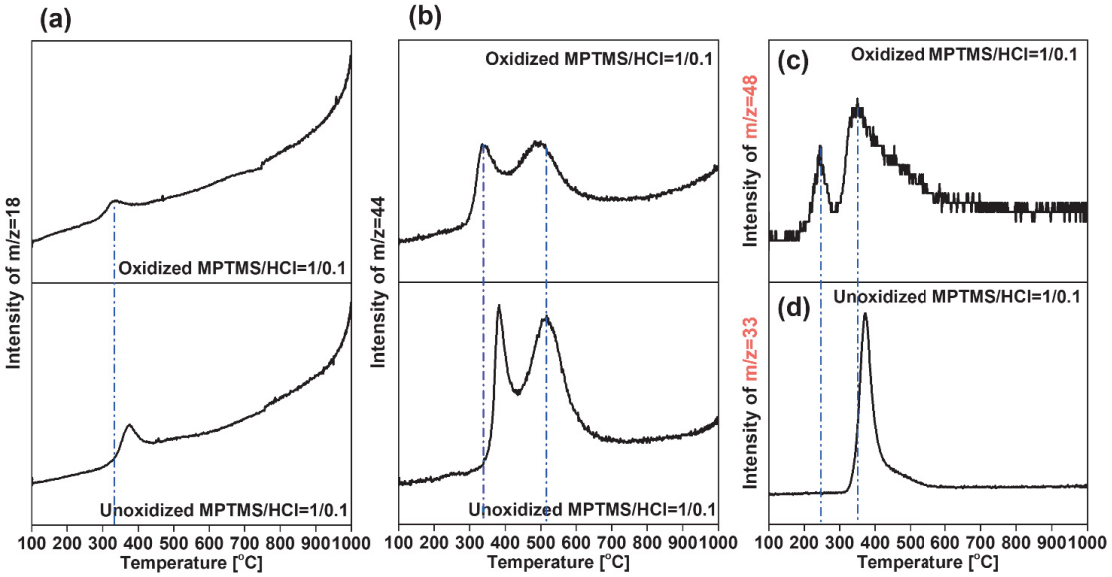

Fig. 4-S6. The mass signal of m/z = 18, 33, 44, and 48 in unoxidized and oxidized MPTMS as a function of thermal treatment from TG-MS.

---------- **SI-7**: Time course for NH_3-TPD measurements ----------

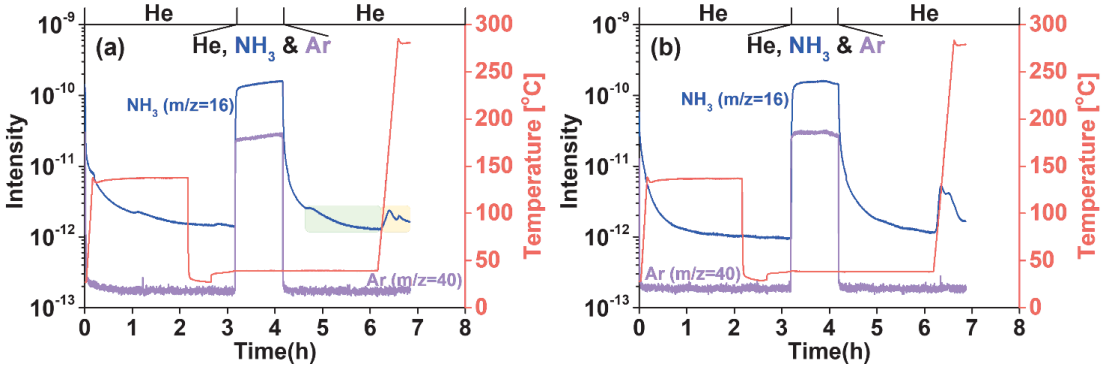

Fig. 4-S7. Time course of mass intensity and temperature during NH_3-TPD measurements for unoxidized (a) and oxidized MPTMS xerogel powders (b).

-------- **SI-8**: Trade-off of the NH_3 permeance and NH_3/H_2 selectivity at 200 °C --------

Table 4-S1. Data for the selectivity and permeance of various membranes at 200 °C.

Membrane	NH_3 permeance [mol m^{-2} s^{-1} Pa^{-1}]	NH_3/H_2	Ref
Nafion/ceramic	1.9355E-06	2.6	
Aquivion-H^+/ceramic	1.6800E-06	6.3	1
Aquivion-Li^+/ceramic	9.0500E-07	1.9	
BTPA	1.3107E-06	7.1	
0.50 Fe-BTPA	2.2437E-06	9.9	2
0.50 Ag-BTPA	1.6300E-06	7.3	
0.25 Ni-BTPA	1.5923E-06	8.1	
0.50 Ni-BTPA	2.7995E-06	10.8	3
1.00 Ni-BTPA	3.2910E-06	5.5	
Unoxidized MPTMS	9.4379E-07	2.6	This work
Oxidized MPTMS	1.3488E-07	27.1	

---------- **SI-9**: Reproducibility of oxidized MPTMS membranes fabrication ----------

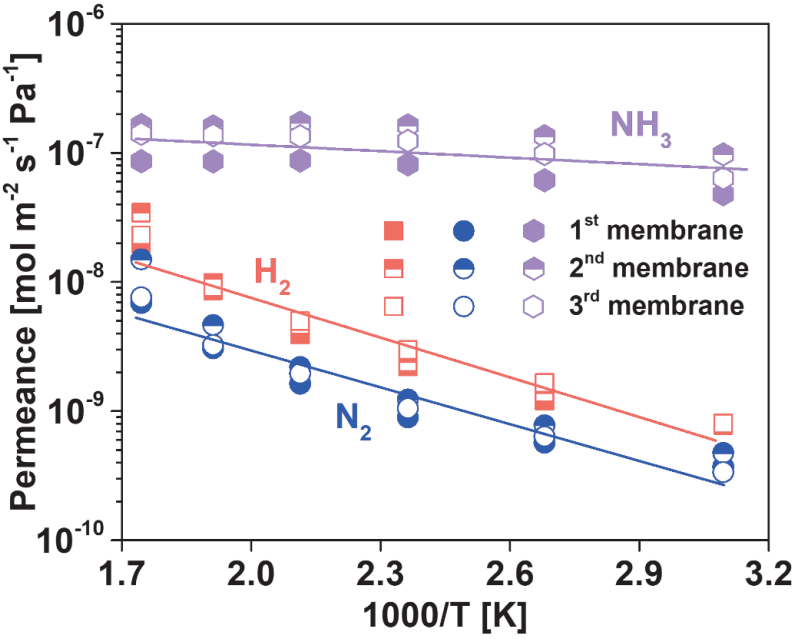

Fig. 4-S8. Reproducibility of membrane fabrication for oxidized MPTMS membranes by comparing H_2, N_2, and NH_3 permeance ranging from 50 to 300 °C.

References

[1] K. Wakimoto, W.W. Yan, N. Moriyama, H. Nagasawa, M. Kanezashi, T. Tsuru, Ammonia permeation of fluorinated sulfonic acid polymer/ceramic composite membranes, *J. Membr. Sci.*, 658 (2022) 120718

[2] W.W. Yan, U. Anggarini, H.C. Bai, H. Nagasawa, M. Kanezashi, T. Tsuru, Enhanced NH_3 permeation of bis[3-(trimethoxysilyl)propyl] amine membranes via coordination with metals, *J. Membr. Sci.*, 678 (2023) 121665.

[3] W.W. Yan, U. Anggarini, K. Wakimoto, H.C. Bai, H. Nagasawa, M. Kanezashi, T. Tsuru, Optimization of Ni-amine coordination for improving NH_3 permeation through nickel-doped bis[3-(trimethoxysilyl)propyl] amine membranes, *Sep. Purif. Technol.* 326 (2023) 124809.

Chapter 5

Fabrication of 3-(trihydroxysilyl)-1-propanesulfonic acid membranes with superior affinity and selectivity for NH_3 permeation over H_2 and N_2 at 50-300 °C

5.1 Introduction

Since the advent of the Haber-Bosch process for ammonia (NH_3) synthesis at 400-500 °C and 30-50 MPa using Fe-based catalysts, [1,2] NH_3 has been not only devoted to fertilizer and crop production but is increasingly regarded as an important carbon-free hydrogen energy-carrier and value-added chemical due to its high hydrogen density (107.7 $kg_{H_2} m^{-3}$) and capacity (17.6 wt%). [3,4] However, the harsh conditions not only caused excessive energy consumption but also failed to acquire a high NH_3 conversion due to the limitation of thermodynamic equilibrium. Catalytic membrane reactor (CMR) technology, that consists of reaction and concurrent membrane separation to improve thermodynamics and kinetics, [5-7] would be highly expected for producing green NH_3 [8] that can be synthesized utilizing N_2 and H_2 from air separation and water electrolysis, respectively. Particularly, NH_3 conversion can be increased or exceed the equilibrium conversion even under mild conditions (250-350 °C and 1-10 bar) via selective removal of NH_3 from the reaction side to the permeate side through a CMR. Although low temperature can thermodynamically promote the synthetic NH_3 conversion because of the exothermic NH_3 synthesis reaction and the activity of low-temperature catalysts have been reported to be developed, high temperatures such as ≥ 250 °C would be still needed at present owing to the low efficiency of the catalyst and the low NH_3 yield.

Therefore, membranes with highly tolerable temperature and excellent NH_3 perm-selectivity, as the core of CMRs, are urgently desired because high temperature promotes the NH_3 production rate of the existing catalyst but easily cause membrane decomposition and/or decreased separation factor. [9,10]

Recently, the theoretical design of a CMR model for NH_3 synthesis was reported by mathematical simulation. Special attention was paid to the performance of the membrane, which should at least be required NH_3/H_2 selectivity of > 4, NH_3/N_2 selectivity of > 10, and high NH_3 permeance of ~3.4×10^{-7} mol m^{-2} s^{-1} Pa^{-1} (1000 GPU) can further increase gains. [11] However, because of the limited performance of existing catalysts including Ru- and Fe-based as well as heterogeneous catalysts [12-14], especially for reaction rate, reaction temperatures above 250 °C still seem essential for NH_3 synthesis, [15,16] which can also extend the advantages of a CMR. Consequently, this further increases the demand for membrane properties, especially temperature tolerance of the membrane.

Retrospectively, polymer membranes, such as poly(vinylammonium thiocyanate) [17], perfluorosulfonic acid (PFSA) [18,19], cellulose acetate [20,21], have long been reported an NH_3 permeance of ~10^{-8} mol m^{-2} s^{-1} Pa^{-1} with NH_3 selectivity of 100-1000 around room temperature based on diffusion-solubility mechanism. After contacting with NH_3 at high temperatures, the plasticization and/or corrosion of the membrane [19] would inevitably reduce the separation factors. Moreover, ionic liquid (IL)/deep eutectic solvent (DES)-based membranes can be flexibly designed by selecting various cations and anions, which expressed a favorable NH_3 permeance (~10^{-7} mol m^{-2} s^{-1} Pa^{-1}) and

selectivity (~100) on account of high NH_3 affinity. [22,23] Nevertheless, the performance of IL/DES-based membranes and zeolite/metal framework membranes [24-26] at high temperatures was rarely reported, which undoubtedly limits the application of the membrane such as CMR, because the temperature needed to synthesize NH_3 is at least 50 °C [27]. Although tetraethoxysilane (TEOS) derived membranes exhibited a comparable NH_3/H_2 selectivity of 28.7 from isometric NH_3/H_2 mixture at 50 °C due to the blocked H_2 permeation by the preferentially adsorbed NH_3, NH_3/H_2 selectivity was inversely 0.083 at 400 °C. [28]

Recent advances in NH_3 separation membranes are PFSA/ceramic composite membranes [29], metal-doped bis[3-(trimethoxysilyl)propyl] amine (BTPA) membranes [30], and Na^+-gated nanochannel membranes [31], which showed an outstanding NH_3 permeance and selectivity as well as stability from 50 to 200 °C. Although the membrane performance was evaluated over a wide temperature range, the key factors for NH_3 separation, including NH_3 permeance and selectivity, were less satisfactory. The NH_3 permeance and selectivity with raising temperatures were decreased dramatically for PFSA-derived membranes such as Nafion/ceramic composite membrane. For example, NH_3 permeance slightly decreased from ~2.8×10^{-6} to ~1.9×10^{-6} mol m^{-2} s^{-1} Pa^{-1} as the temperature rose from 50 to 200 °C, while the selectivity of NH_3/H_2 > 40 and NH_3/N_2 >730 greatly decreased to ~2 and ~25, respectively. Additionally, the propylamine chains in metal-doped BTPA membrane could tend to decompose around 200 °C as the amount of metal doping increases, [32] which makes it difficult to control the pore size and weaken the coordination between propylamine and metal (for example, nickel).

Compared to PFSA- and BTPA-derived membranes, Na^+-gated nanochannel membrane expressed a surprising NH_3/H_2 selectivity of > 300 and NH_3/N_2 selectivity of >1000 even at 200 °C, but NH_3 permeance ($2\text{-}5\times10^{-8}$ mol m^{-2} s^{-1} Pa^{-1}) needs to be further improved. [31] Generally, high temperature is unfavorable to NH_3 selective permeation. This could be attributed to the high temperature promoting the degradation of these materials as well as weakening their NH_3 affinity. Another reason is possibly due to the activated diffusion of the H_2 and N_2 permeation, resulting in H_2 and N_2 permeance promoting at high temperatures more than NH_3 permeance.

For further improvement in NH_3 permselectivity at high temperatures, we reported (3-mercaptopropyl)trimethoxysilane (MPTMS) derived membranes. The mercaptan groups (-*SH*) can be oxidized to sulfonated groups by H_2O_2 as shown in Fig. 5-1, which significantly improved the NH_3 affinity based on acid-base interactions between NH_3 and sulfonated groups. This was originally proven by selectively capturing trace NH_3 from air with an initial NH_3 concentration < 2 ppm. [33] Afterwards, oxidized MPTMS membranes was successfully fabricated for separating NH_3 from H_2 and N_2 at 50-300 °C in our research group, which showed a moderate NH_3 selectivity (NH_3/H_2 = 6 and NH_3/N_2 = 18) with an NH_3 permeance of ~1.4×10^{-7} mol m^{-2} s^{-1} Pa^{-1} at 300 °C. [34] However, because the MPTMS sol size was difficult to control after H_2O_2 oxidation, oxidized MPTMS membranes showed a poor molecular sieving, which can be verified by non-adsorptive gas permeation (He, H_2, N_2, CH_4, CF_4, and SF_6) similar to Knudsen diffusion. Additionally, mercaptan groups (*S-H*) were also difficult to be completely oxidized to -SO_3H by XPS analysis.[34] Therefore, 3-(trihydroxysilyl)-1-

propanesulfonic acid (TPS) which contains -SO_3H groups in the chemical structure without any oxidation are greatly attractive to prepare TPS derived membranes with high NH_3 permeance and selectivity.

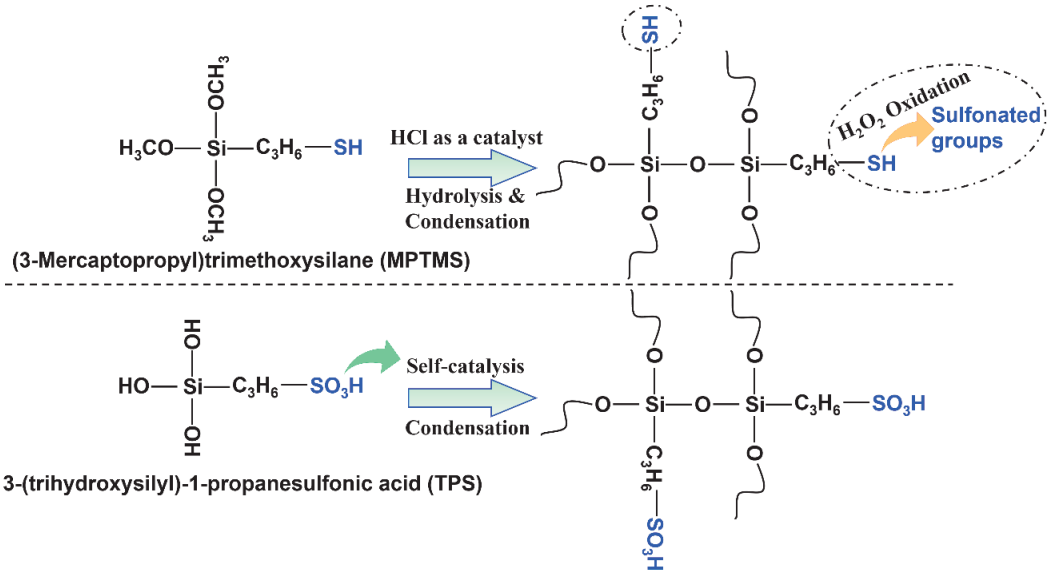

Fig. 5-1. Structure of MPTMS and TPS precursors and their derived siloxane structure.

Herein, we propose the use of TPS, the molecular structure of which can be found in Fig. 5-1, for fabricating NH_3-selective membranes. Since TPS consists of sulfonic acid groups (-SO_3H), direct coating of TPS solutions enables the formation of -SO_3H groups, which requires no oxidation process such as MPTMS and would offer a simple fabrication process. TPS was diluted to 0.1 wt% with ethanol (EtOH), and its solutions were directly coated on intermediate layer for fabricating TPS membranes with superior molecular sieving and NH_3 affinity. The properties of TPS solution and its derived films and xerogels were examined by various characterizations. Importantly, NH_3 adsorption and temperature-programmed desorption (NH_3-TPD) uncovered an intensive NH_3 affinity for TPS (an NH_3 adsorption amount of ~3.0 mmol g^{-1}) due to the inherently proton-acidic -SO_3H groups in TPS. The NH_3 permeance and selectivity of TPS

membranes were evaluated by single and binary gas permeation over a wide range of temperatures from 50 to 300 °C, which have confirmed the superior NH_3 permselectivity at high temperatures.

5.2 Experiments

5.2.1 TPS solution and membrane preparation

3-(trihydroxysilyl)-1-propanesulfonic acid in water (35%) was purchased from Oakwood Chemical, Inc., Japan and used without further purification. Fig. 5-2 shows the membrane preparation procedure. Firstly, two types of *α*-alumina particles of 0.2 and 2 μm were dispersed at the concentration of 10 wt% in 2 wt% SiO_2-ZrO_2 sols. They were coated on the surface of porous *α*-alumina tube (length: 100 mm, average pore size: 1 μm, porosity: 50%, kindly supplied by Nikkato Cor. Japan) and calcined at 550 °C for 15 min to cover all macropores. This process was repeated 3-4 times to obtain the particle layers. Secondly, 0.5 wt% SiO_2-ZrO_2 sols obtained by diluting 2 wt% SiO_2-ZrO_2 sols with water was coated on the particle layer, followed by calcination at 550 °C for 15 min, which can form the intermediate layer with pore size close to 1 nm. [35] Finally, 0.1 wt% TPS solution diluted with EtOH and water, name for TPS-EtOH and TPS-H_2O, respectively, was directly coated on the SiO_2-ZrO_2 intermediate layer, followed by calcination at 300 °C for 20-30 min under a N_2 atmosphere.

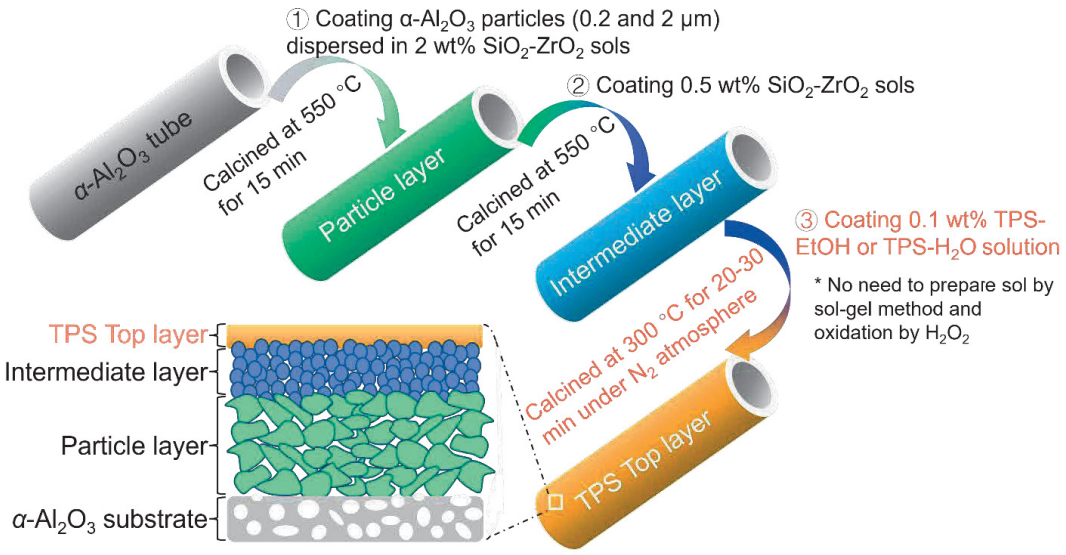

Fig. 5-2. Procedure of membrane preparation and schematic the layered structures of membrane.

5.2.2 Characterization and gas permeation measurement

Malvern Zetasizer (ZEN 3600) equipped with dynamic light scattering (DLS) was used to analyse the size distribution of 5 wt% TPS-EtOH and TPS-H_2O solutions. Fourier transform infrared spectrometer (FT-IR-4100, JASCO, Japan) was utilized to examine the chemical structure and stability of TPS films that were prepared by drip-coating 5 wt% TPS-EtOH or TPS-H_2O solution onto KBr plates and calcined at different temperatures under a N_2 atmosphere. Besides, 5 wt% TPS-EtOH and TPS-H_2O solutions were spin-coated onto silicon wafer and calcined at 300 °C under a N_2 atmosphere, followed by drying in a vacuum oven overnight and analysis via an X-ray photoelectron spectrometer (XPS, JEOL RE series JES-RE1X ESR spectrometer). TPS xerogel powders were prepared by drying both TPS solutions at 50 °C and their thermal stability were detected via a thermogravimetric mass spectrometer (TG-MS, TGA-DTA-PIMS 410/S, Rigaku, Japan). TPS-EtOH and TPS-H_2O xerogel powders uncalcined and calcined at 300 °C under a N_2 atmosphere were characterized by an X-Ray

diffractometer (XRD) D2 PHASER (Bruker, Germany) equipped with Cu-Kα radiation in a 2θ range of from 5 to 80º. The pore structure of calcined TPS-EtOH and TPS-H_2O xerogel powders that were further evacuated at 200 °C under vacuum conditions for 12 h, was evaluated via a N_2 adsorption-desorption apparatus (BELL Inc., Japan). NH_3 adsorption and desorption amounts of calcined TPS-EtOH and TPS-H_2O xerogel powders were measured via an NH_3-TPD (BELCAT-AT and BELMASS-HT, BELL Inc., Japan). The details of NH_3-TPD measurement program are shown in the Supplementary Material (SI-1). Scanning electron microscope (SEM, HITACHI S-4800, JEOL, Japan) was used to observe the morphology of TPS membrane.

The permeances of high purity He, H_2, NH_3, N_2, CH_4, CF_4, and SF_6 were measured at 50-300 °C by pressuring the outside of the membrane at 200-300 kPa while the permeate stream was maintained at atmospheric pressure via the single gas permeation. In addition, the binary gas permeation at 300 °C was performed to verify the permeation properties of the NH_3 mixtures (NH_3/H_2 and NH_3/N_2). Upstream and permeate pressures were kept at 300 kPa and atmospheric pressure, respectively. The detailed measurement procedure of single and binary gas permeation and experimental apparatus can be found in SI-2.

5.3 Results and discussions

5.3.1 Chemical structure and thermal properties of TPS sol, film, and xerogel

Fig. 5-3 shows the DLS size distribution of TPS-EtOH and TPS-H_2O solutions. Obviously, the DLS size of TPS-EtOH and TPS-H_2O solutions was mainly distributed in 2-3 and 1-2 nm, respectively. Large size in EtOH could be attributed to the promoting

effect of EtOH as a cosolvent on condensation, which could be supported by the fact that increasing the EtOH concentration decreases the hydrolysis reaction and promotes the condensation of hydrophilic silanol, resulting in the growth of particles and obtaining larger silica nanoparticles. [36] Since the pore size of the intermediate layer was around 1 nm, the size of the TPS-H_2O solution may not be sufficient to cover all micropores of intermediate layers so that a membrane with benign molecular sieving was difficult to be fabricated. Moreover, TPS-EtOH and TPS-H_2O solutions showed a stable size distribution after stirring the sols at 50 °C for several to 22 h under an air atmosphere, indicating the sufficient stability.

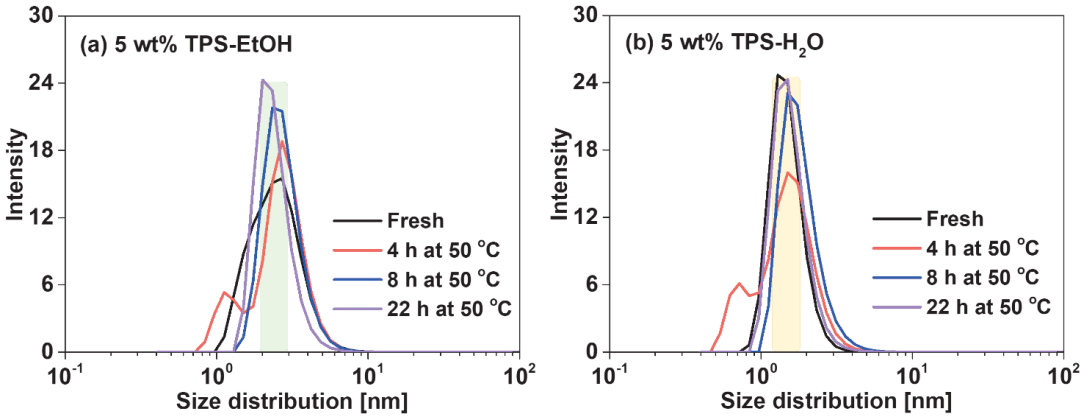

Fig. 5-3. Size distribution of TPS-EtOH (a) and TPS-H_2O (b) solutions and then stirred at 50 °C for several to 22 h.

Figs. 5-4 and 5-S3 exhibit FT-IR spectra of a narrow and wide range, respectively, for TPS films coated on KBr plate with TPS-EtOH and TPS-H_2O solutions and calcined at different temperatures (uncalcined and 100-350 °C). Both of fresh TPS films displayed the approximately similar spectra, indicating a similar chemical structure, independently of solvent type. Moreover, the characteristic peaks of *-OH* groups around 3100-3600 cm^{-1} and *Si-O-Si* groups around 1040-1100 cm^{-1} [37,38] were always clear and

showed approximately the same absorption intensity for both uncalcined and calcined at 350 °C. This can be explained as TPS monomers were possibly condensed to form a siloxane network structure owing to sulfonic acid (-SO_3H) as a self-catalyst for the promotion of condensation, [38,39] and the condensed TPS polymers still contain quite a few silanol groups even at 350 °C. Furthermore, as shown in Fig. 5-4 (left), the characteristic peak of *Si-OH* groups around 900 cm^{-1} was mildly shifted to high wavenumber (blue-shift) as the temperature goes from 150 to 200 °C, which could be attributed to the enhanced interactions between *Si-OH* groups and/or between *Si-OH* and -SO_3H groups due to the promotion of high temperature on the dynamic condensation. [30,32]

As shown in Figs. 5-4 and 5-S3 (right), both TPS films showed particularly prominent deformation band of -SO_3H groups around 1195 cm^{-1} [39] and common *S=O* groups around 1300-1410 cm^{-1} [33,34,37,38]. However, oxidized MPTMS film only indicated *S=O* and -SO_3^- groups that originated from the oxidization of -*SH* of MPTMS by H_2O_2. [33,34] No -SO_3H groups were observed possibly because -*SH* is difficult to completely oxidize to proton-acidic -SO_3H groups, but instead coexists in a variety of oxidized sulfur groups, such as such as sulfite, sulfone, sulfate, and/or sulfonic groups. [34] Furthermore, as the calcination temperature rises from 200 to 250 °C, the peaks of *Si-O-Si* groups around 1100 cm^{-1} increases significantly compared with that of -SO_3H groups and were almost unchanged from 250 to 350 °C, meaning that an increase in calcination temperature to 250 °C was sufficient to induce the condensation of *Si-OH* to form a dense siloxane network structure. Additionally, the thermal stability of propyl chains and sulfonic acid groups at 300 or 350 °C was also confirmed by the characteristic peaks of *C-*

H and -*SO₃H* groups in Figs. 5-4 and 5-S3.

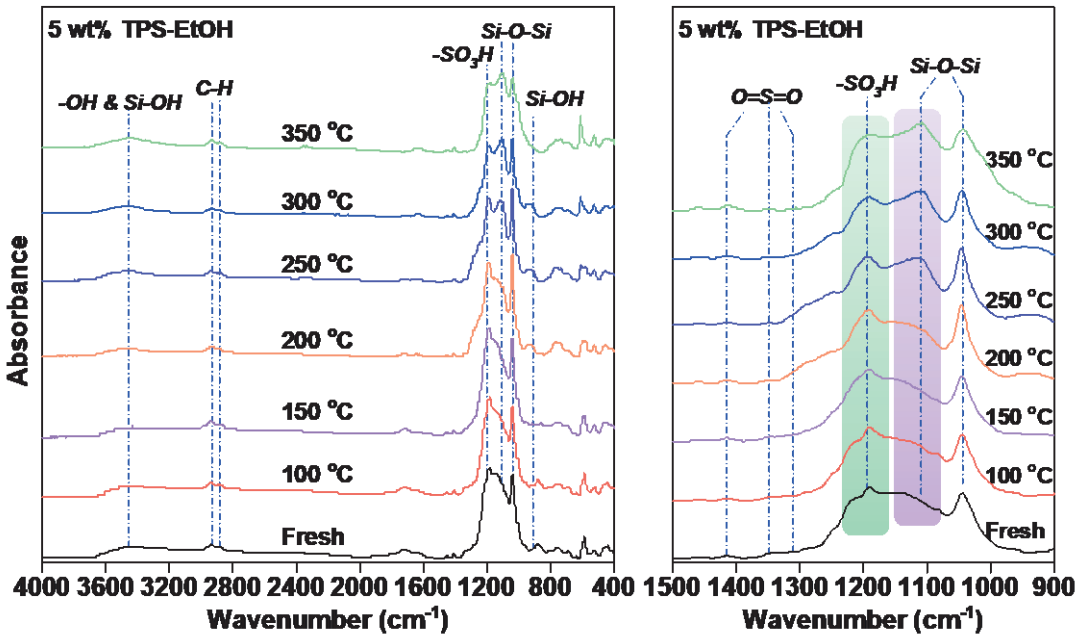

Fig. 5-4. Wide FT-IR spectra (left) and narrow FT-IR spectra ranging from 1500 to 900 cm^{-1} (right) of TPS-EtOH films at different calcination temperatures.

Fig. 5-5 shows the XRD patterns of uncalcined and calcined TPS xerogel powders dried from TPS-EtOH and TPS-H_2O solutions. Both TPS-EtOH and TPS-H_2O xerogel powders showed an amorphous phase with a broad peak around 21°, which can be ascribed to amorphous *Si-O-Si* networks, even for uncalcined xerogel powders. This further proves that TPS can rapidly condense or has already condensed during the preparation of the xerogel to form an amorphous siloxane-derived network structure because of -*SO₃H* groups inherently active as a self-catalyst, consistent with FTIR results.

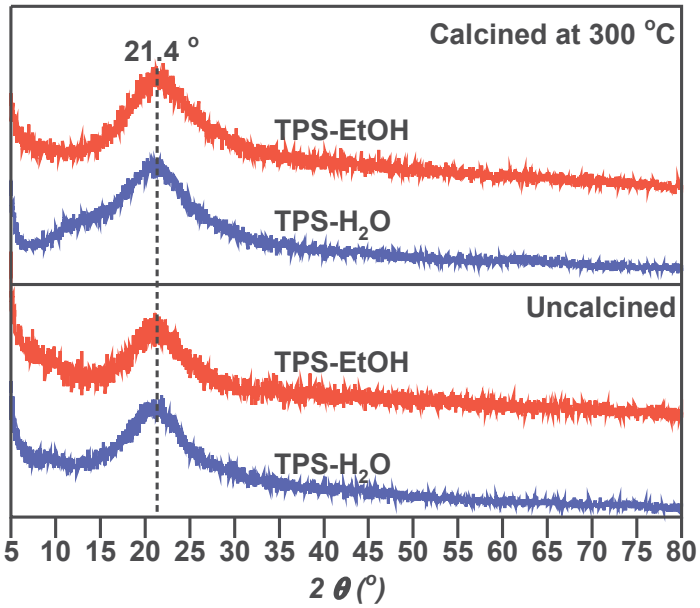

Fig. 5-5. Wide angle XRD patterns for uncalcined and calcined TPS-EtOH and TPS-H_2O xerogel powders.

Fig. 5-6 shows TG-MS measurement of TPS-EtOH and TPS-H_2O xerogel powders. Firstly, the xerogel powders underwent a weight-loss of ~21 wt% at 100-300 °C. To explain this phenomenon in more detail, the mass signal of m/z = 18, 44, and 48 was analyzed and assigned to H_2O, CO_2, and *S*=*O*, respectively, during TG-MS measurement in Fig. 5-S4. The minor signal peaks of CO_2 and *S*=*O* were detected at ~240 °C and the major signal peaks caused by the decomposition of propane chains and sulfonic acid groups were observed over 400 °C, implying that the propyl chains and sulfonic acid groups have only partially decomposed up to 300 °C, which is consistent with that no significant changes in -*CH*- and -*SO₃H* functional groups were observed from FTIR spectra from 100 to 250 °C, even to 350 °C. These can possibly be explained by the desorption of a large amount of the adsorbed H_2O on sulfonic groups, which was originally contained in TPS monomers and/or adsorbed during the sample handling, and/or the formed H_2O from *Si*-*OH* condensation as well as the decomposition of some poorly

condensed TPS polymers at 100-300 °C. Because the main structure only slightly decomposed even when the temperature rose above 350 °C by combining the analysis results of FT-IR and mass signals as a function of temperature. Although the xerogel powder has been maintained at 100 °C for 2 h to remove the adsorbed H_2O as much as possible, the signal peak of H_2O molecules (m/z = 18) still appears as the temperature continues to rise above 400 °C. This could be ascribed to the desorption of strongly adsorbed H_2O on sulfonic groups and/or the formed H_2O molecules when *Si-OH* groups were dynamically condensed to transform to siloxane structures at high temperatures. This can further improve the thermal stability of TPS xerogel powders, irrespectively of the solvent type.

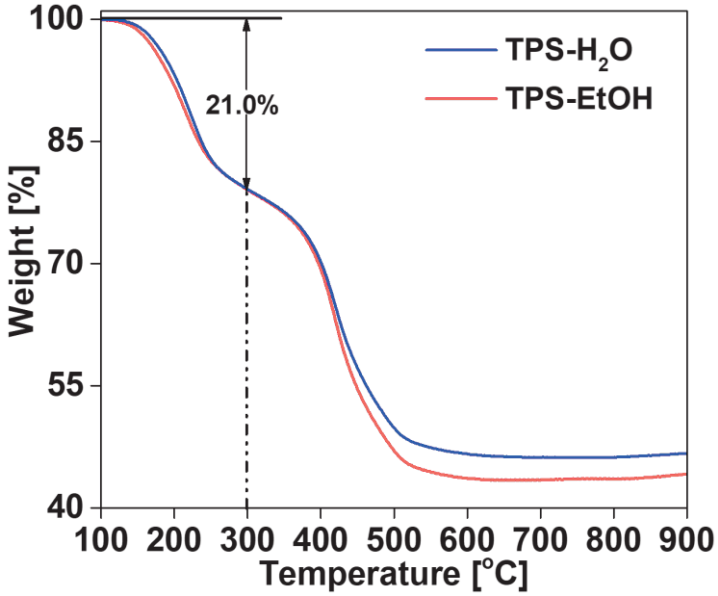

Fig. 5-6. TG-MS measurement of TPS-EtOH and TPS-H_2O xerogel powders.

5.3.2 Elemental analysis, N_2 adsorption, and NH_3 affinity of TPS samples

Fig. 5-7 demonstrates the results of XPS analysis for TPS-EtOH and TPS-H_2O films calcined at 300 °C. Nearly identical wide scan spectra was collected in both TPS-EtOH and TPS-H_2O samples, and the binding energy of S_{2p} in both TPS samples was almost

the same at 168.7 eV, as shown in Fig. 5-7 (b), consistent with the results in oxidized MPTMS samples [33,34]. The protonic sulfonic acid groups inherent in TPS can be determined exactly by XPS analysis, while the oxidized sulfur groups obtained by oxidizing *S-H* of MPTMS with H_2O_2 probably existed simultaneously in various chemical states from the deconvoluted spectrum of oxidized S_{2p} region, [34] which could partly weaken NH_3 affinity with oxidized MPTMS.

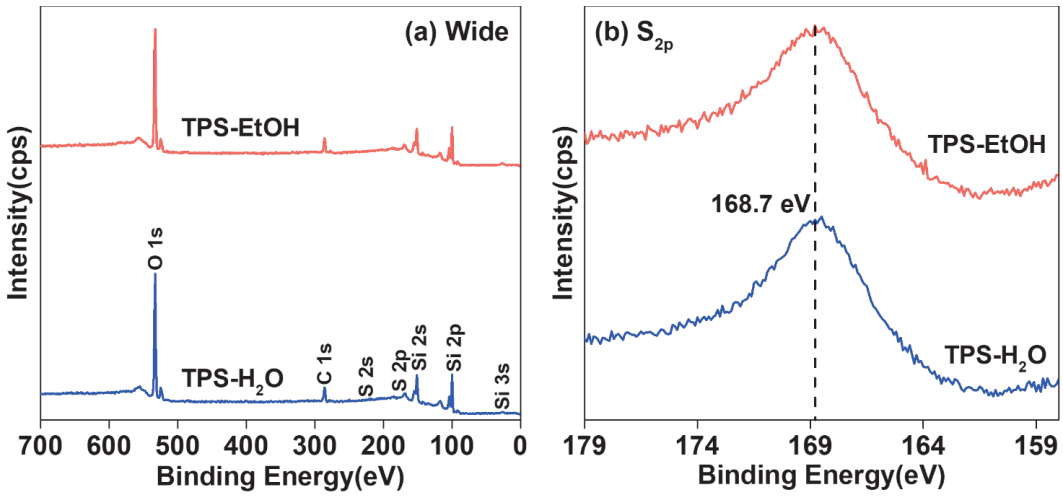

Fig. 5-7. XPS analysis of TPS-EtOH and TPS-H_2O films calcined at 300 °C: wide scan spectra (a) and high-resolution S_{2p} spectra (b).

Fig. 5-8 displays N_2 adsorption for TPS-EtOH and TPS-H_2O xerogel powders calcined at 300 °C. Although both TPS xerogel powders exhibit dense structure due to the flexibility of propyl chains and/or the filling of pores by bulky -SO_3H groups, specific surface area (S_{BET}) of TPS-EtOH xerogel powders slightly higher than that of TPS-H_2O xerogel powders, which can be supported by the fact that specific surface area of synthetic silica nanoparticles increased by increasing the ethanol content to obtain high quality and uniform spherical particles [40]. The dense structure in TPS xerogel powders calcined at 300 °C also further confirmed the thermal stability of the TPS-derived siloxane network.

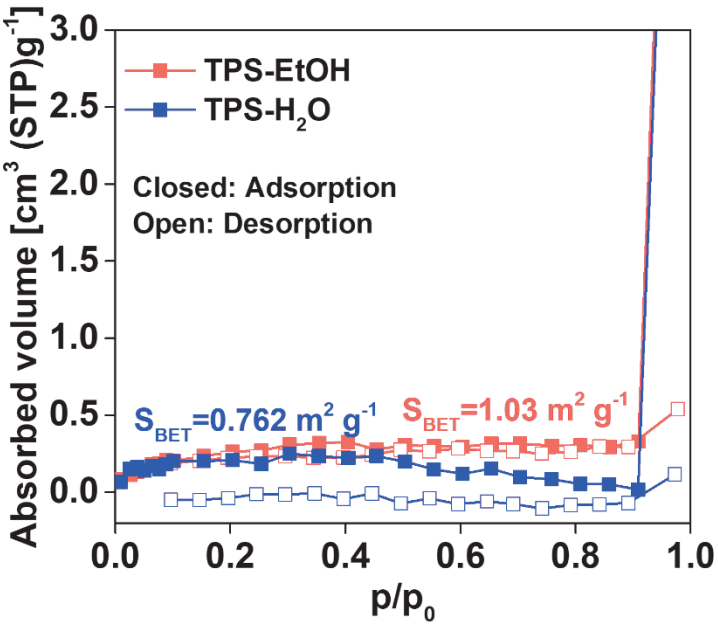

Fig. 5-8. N_2 adsorption of TPS-EtOH and TPS-H_2O xerogel powders calcined at 300 °C.

Fig. 5-9 (a) shows the summary of NH_3 adsorption and desorption amounts, while Fig. 5-9 (b) shows the intensity of NH_3 (m/z=16) as a function of temperatures for TPS-EtOH, TPS-H_2O, and oxidized MPTMS [34] xerogel powders, all of which were calcined at 300 °C. Adsorption amount of NH_3 at 40 °C for all samples are well matched to their sum of desorption amounts at 40 °C, which corresponds to NH_3 adsorbed weakly, and the following desorption at 40-300 °C, which corresponds to NH_3 strongly adsorbed. In addition, a clear peak of NH_3 desorption was observed at 142-145 °C, which again indicates strong adsorption of NH_3. Obviously, NH_3 adsorption amounts of both TPS xerogel powders prepared from EtOH (3.08 mmol g^{-1}) and H_2O (2.86 mmol g^{-1}) were twice as that of oxidized MPTMS xerogel powders (1.41 mmol g^{-1}). Especially NH_3 desorption amounts of TPS from 40-300 °C were four times as much as that of oxidized MPTMS. Comparison of FT-IR spectra reveals, the characteristic peaks of -*SO_3H* groups (1195 cm^{-1}) were significant in TPS films (Fig. 5-4) compared with that in

MPTMS after oxidation by H_2O_2. [34] Through a comprehensive analysis of FT-IR, XPS, and NH_3-TPD, high NH_3 adsorption amounts of TPS can be attributed to the fact that NH_3 affinity of the inherently proton-acidic -*SO_3H* groups in TPS was stronger than that of oxidized sulfur group consisting of various forms of *S=O* in oxidized MPTMS as explained in XPS analyses. [34] Moreover, TPS-EtOH xerogel powders showed a slightly improved NH_3 affinity compared to that in TPS-H_2O xerogel powders, which can be confirmed from NH_3 adsorption amounts (Fig. 5-9 (a)) and from the distribution of signal peaks of m/z=16 with temperature (Fig. 5-9 (b)). It is possibly because TPS-EtOH xerogel powders have a more uniform pore distribution and a larger specific surface area from N_2 adsorption results. [40]

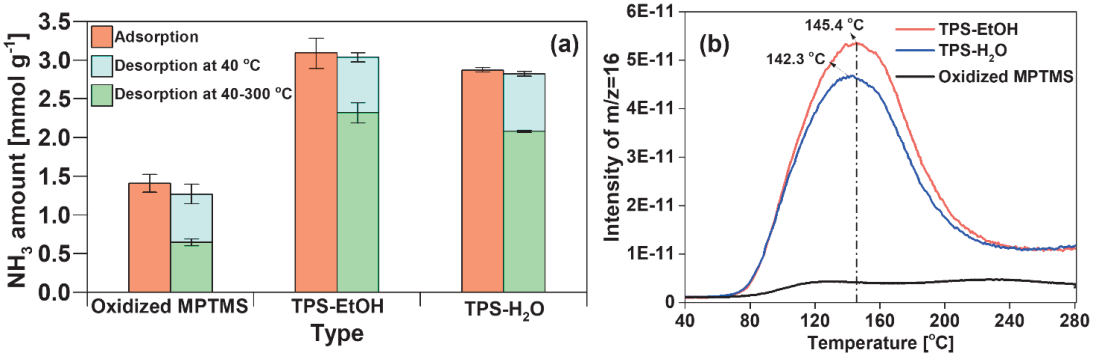

Fig. 5-9. NH_3 adsorption and desorption amounts of oxidized MPTMS [34] and TPS-EtOH and TPS-H_2O xerogel powders calcined at 300 °C (a); their intensity of NH_3 (m/z=16) during NH_3-TPD measurements (b).

5.3.3 Performance of TPS membranes

Fig. 5-10 shows single gas permeance and dimensionless permeance normalized with He permeance at 200 °C, that can minimize the effect of adsorption, as a function of the molecular size of permeating gases for TPS and oxidized MPTMS [34] membranes. It should be noted that Fig. 5-10 (a) shows single gas permeance including NH_3, while Fig. 5-10 (b) shows dimensionless permeance normalized with He permeance, which

excludes NH_3 to clarify the effect of molecular sieving. Since the DLS size of TPS solutions diluted with H_2O was mainly distributed in the range of 1-2 nm, which was probably difficult to effectively cover micropores (~1 nm) on the intermediate layer, the membranes prepared by H_2O-diluted TPS solutions showed high gas permeance similar to that of only intermediate layer in Fig. 5-10 (a), [41,42] and the permeation properties of non-adsorptive gases were almost identical to Knudsen diffusion in Fig. 5-10 (b). Therefore, TPS-H_2O solutions are not recommended for membrane fabrication.

According to the reported permeation properties of oxidized MPTMS membrane, [34] oxidized MPTMS membranes exhibited higher NH_3 permeance and selectivity than non-adsorptive gases, especially He and H_2, due to a superior NH_3 adsorption and diffusion. Nonetheless, oxidized MPTMS membranes contained large pores such as pinholes and expressed the selectivity of Knudsen diffusion for non-adsorptive gases, because it was difficult to control the size of MPTMS sol after H_2O_2 oxidation and the effect of H_2O_2 on the top-separation layer. [34] Inversely, TPS solution diluted with EtOH not only has a suitable size but also avoids the use of H_2O_2, so the fabricated membrane presented not only an excellent NH_3 permeance but also high selectivity, which was beyond the selectivity of Knudsen diffusion for non-adsorptive gases, indicating an outstanding molecular sieving and adsorption-diffusion.

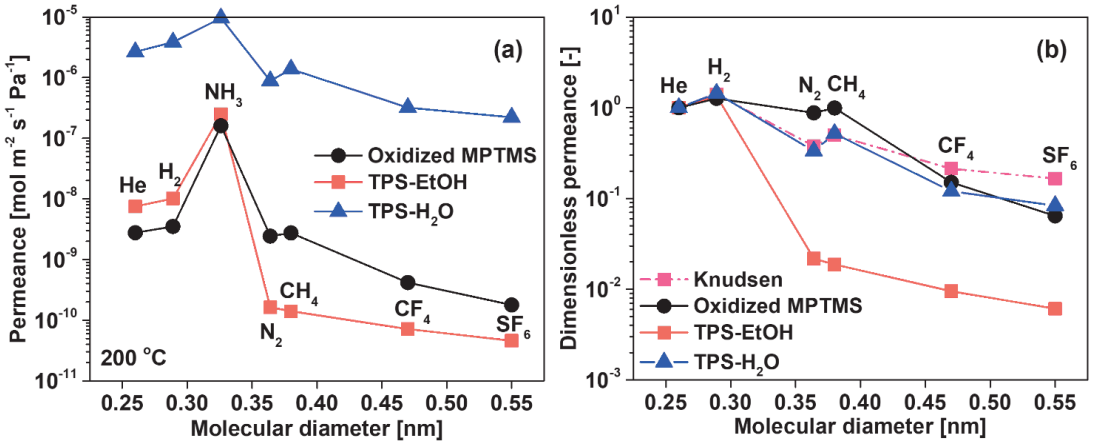

Fig. 5-10. Kinetic diameter dependence of single gas permeance (a) and dimensionless permeance (b) at 200 °C for TPS-derived membranes and oxidized MPTMS-derived membranes.

Fig. 5-11 shows the morphology of TPS-EtOH membranes. The fabricated TPS-EtOH membrane has the multilayer structures, and the boundary of each layer, including support, α-Al_2O_3 particle, intermediate SiO_2-ZrO_2, and top-separation layers, is not clearly observed as shown in Fig. 5-11 (a). Nevertheless, the interlocked structure showed no cracks and would increase the mechanical strength. Based on the cross-sectional SEM of high-resolution shown in Fig. 5-11 (b), the thickness of top-separation layer is about 150 nm and without any defect.

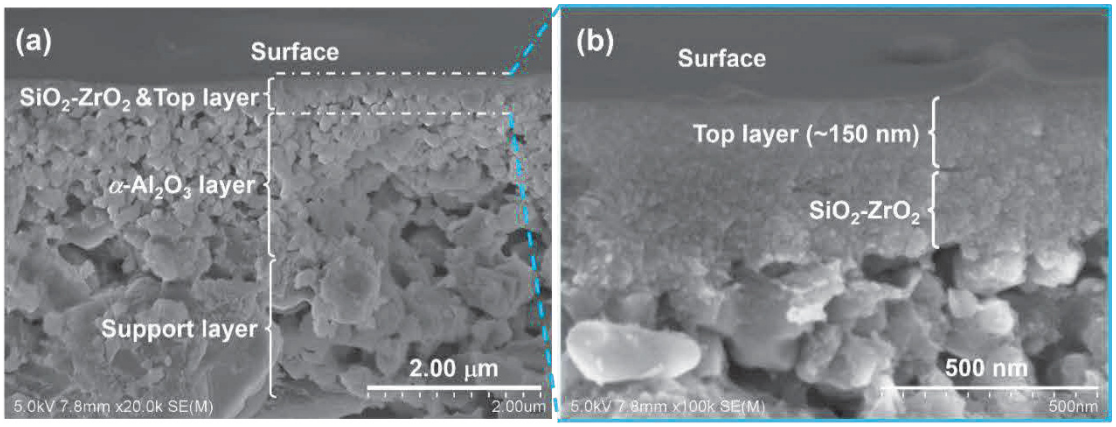

Fig. 5-11. Morphology of TPS-EtOH membranes: (a) low magnification (×20k) and (b) high magnification (×100k).

Fig. 5-12 demonstrates temperature dependence of single gas permeance and perm-

selectivity at temperatures from 50 to 300 °C for TPS-EtOH membranes. Although the kinetic diameter of NH_3 was reported 0.326 nm [28] that is between the kinetic diameters of H_2 (0.289 nm) and N_2 (0.364 nm), NH_3 permeance was much higher than H_2 and N_2 because NH_3 as an adsorptive gas can permeate through the membrane in adsorption-diffusion mechanism. Compared to oxidized MPTMS membranes, N_2 permeance of TPS-EtOH membrane significantly decreased due to a sufficient molecular sieving, which can be proven by high H_2/N_2 selectivity of 113 at 50 °C, 71 at 200 °C, and 39 at 300 °C. Furthermore, NH_3 permeance slightly increased from 1.8×10^{-7} to 2.6×10^{-7} mol m^{-2} s^{-1} Pa^{-1} with increasing temperature from 50 to 300 °C in Fig. 5-12 (b), which is similar to oxidized MPTMS membrane but opposite to PFSA-derived membranes [19,29].

The activation energy ($E_{P,i}$) of H_2, N_2, and NH_3 permeation was calculated using Eq-1 and Eq-2 by the regression of permeance (P_i) as a function of temperature (T) based on the modified gas translation (m-GT) model [43-45].

$$P_i = \frac{k_{0,i}}{\sqrt{M_i RT}} \exp\left(-\frac{E_{P,i}}{RT}\right) \quad \text{Eq-1}$$

$$k_{0,i} = k_0\left(d_p - d_i\right)^3 \quad \text{Eq-2}$$

P_i: permeance of the i-th component; M_i: molecular weight of the i-th component; R: gas constant; $E_{P,i}$: activation energy of permeation of the i-th component; k_0: structural constant; d_p: pore diameter; d_i: diameter of the i-th component.

$E_{P,i}$ can be defined as the sum of the adsorption enthalpy ($\triangle H_i < 0$) that can be ascribed to the affinity between membrane and the permeated gas, and the activation energy for diffusion ($E_{d,i} > 0$) that can be dominated by molecular sieving, i.e., $E_{P,i}$ =

$\triangle H_i + E_{d,i}$. Since H_2 and N_2 are non-adsorptive gases, i.e., $\triangle H \approx 0$, so $E_P = E_d$, as listed in Table 5-1 and Fig. 5-S5. Therefore, E_d of NH_3, contributed by the molecular sieving effect, can be assumed the average of those of H_2 and N_2 due to its kinetic diameter between H_2 and N_2. Consequently, TPS-EtOH membrane has higher E_d than oxidized MPTMS membrane owing to its tighter structure and favorable molecular sieving. Additionally, $-\triangle H$ of NH_3 is larger for TPS-EtOH membrane than for oxidized MPTMS membrane ($-\triangle H_{MPTMS}$ (14 kJ/mol)< $-\triangle H_{TPS}$ (22 kJ/mol) ≈ $-\triangle H_{Nafion}$ (26.5 kJ/mol)) because of its intensive NH_3 affinity and multifold NH_3 adsorption amounts caused by the strongly protonically acidic -SO_3H groups inherent in TPS or Nafion, as explained in the XPS analyses in Fig. 5-7. $E_{P,NH_3} - E_{d,NH_3} = \triangle H_{NH_3}$ is also summarized in Table 5-1, showing a strong NH_3 affinity from higher $\triangle H_{NH_3}$ for TPS-EtOH membranes than oxidized MPTMS membranes.

As shown in Fig. 5-13 that summarizes the properties of recently studied membranes, we have found that NH_3 diffusion based on pore size and NH_3 affinity based on acidic -SO_3H groups generally show an inverse relationship, i.e., low permeation potential vs. high separation potential. Although Nafion/ceramic membranes showed better potential than TPS-EtOH membranes, NH_3 permeation in Nafion/ceramic membranes always decreases with the increase of temperature, which is not beneficial to the use of CMRs for NH_3 synthesis at high temperatures. Furthermore, the permeation properties of CO_2 through the membranes with different types of aimine (different basicity) including primary amine (-NH_2) and pyrimidines reasonably showed that high CO_2 affinity (-NH_2) might have possibly hindered CO_2 permeation. [46] This conclusion can also be probably

applied to explain the NH_3 permeation properties of TPS membranes. In addition to high NH_3 affinity, TPS membranes also exhibit high diffusion barriers, which can be ascribed to small size pores. Therefore, the artistic strategy of balancing NH_3 affinity and diffusion is worthy of further study.

Importantly, TPS-EtOH membranes showed an superior NH_3 permeance of ~2.6×10^{-7} mol m^{-2} s^{-1} Pa^{-1} with an excellent NH_3/H_2 selectivity of 7 and NH_3/N_2 selectivity of 266 at 300 °C, and NH_3 permeance of ~1.8×10^{-7} mol m^{-2} s^{-1} Pa^{-1} with an NH_3/H_2 selectivity of 165 and NH_3/N_2 selectivity of 18700 at 50 °C. These performances nearly reach the ideal requirements for a catalytic membrane reactor of NH_3 synthesis from mathematical simulation, including NH_3 permeance of 3.4×10^{-8}-10^{-7} mol m^{-2} s^{-1} Pa^{-1} (100-1000 GPU) with NH_3/N_2 selectivity of > 10. [11] Although NH_3/H_2 selectivity did not achieve the ideal requirement, i.e. >10, it meets the minimum requirement, i.e. >4.

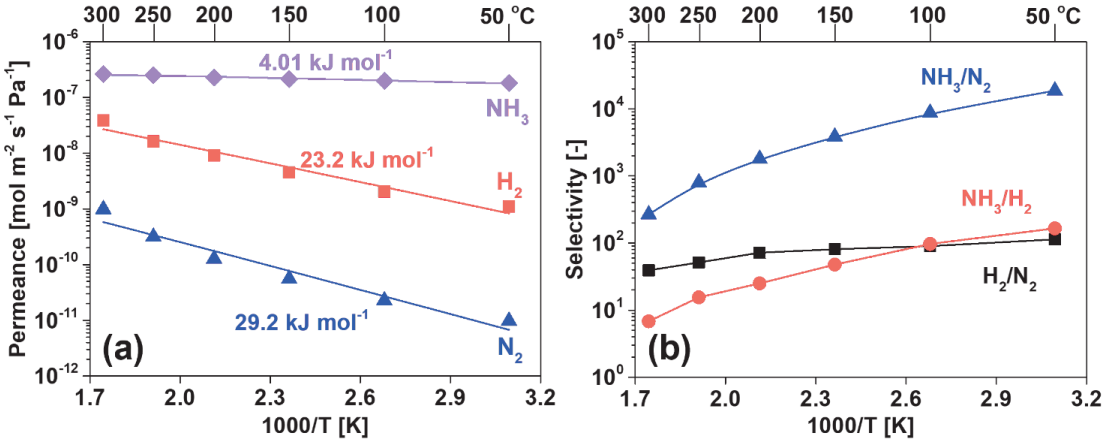

Fig. 5-12. H_2, N_2, and NH_3 permeance (a) and selectivity (b) ranging from 50 to 300 °C for TPS-EtOH membranes.

Table 5-1. Activation energy (E_p, *kJ/mol*) of NH_3, H_2, and N_2, and estimated NH_3 diffusion energy (E_{d,NH_3}) and adsorption enthalpy ($\triangle H_{NH_3}$) for various membranes.

Type	$E_p = \triangle H + E_d$			$E_{d,NH_3} \approx$ AVG ($E_{p,H_2}+E_{p,N_2}$)	$\triangle H = E_p - E_d$	Ref.
	NH_3	H_2	N_2		NH_3	
Nafion/ceramic §	-2.47	22.5	25.5	24.0	-26.5	29
Na^+-gated nanochannel #	~10.5	~14.5		14.5	-3.0	31

Unoxidized MPTMS §	5.84	17.0	17.4	17.2	-11.4	34
Oxidized MPTMS §	6.57	21.1	20.0	20.6	-14.0	
TPS-EtOH §	4.01	23.2	29.2	26.2	-22.2	

§: single gas permeation; #: binary gas permeation.

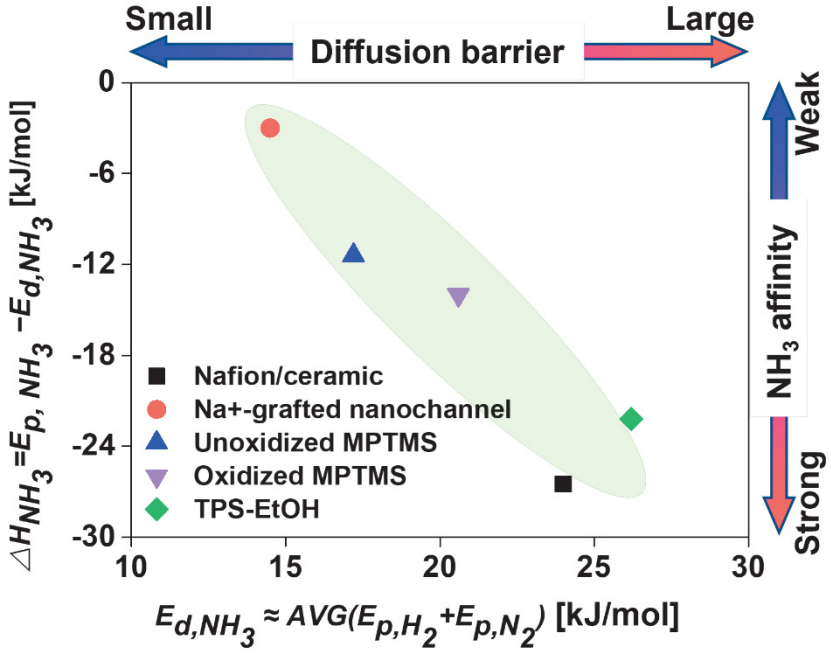

Fig. 5-13. Relationships between the activation energy of NH_3 diffusion (E_{d,NH_3}) and NH_3 adsorption enthalpy ($\triangle H_{NH_3}$) of different membranes.

Fig. 5-14 shows pressure dependence of single H_2, N_2, and NH_3 permeance at 300 °C for TPS-EtOH membranes. Although the feed pressure of NH_3 and H_2 as well as N_2 changed in the range of ~50-200 and ~150-300 kPa, respectively, their permeance and selectivity were almost constant, independently of their respective feed pressure, indicating a negligible surface diffusion effect.

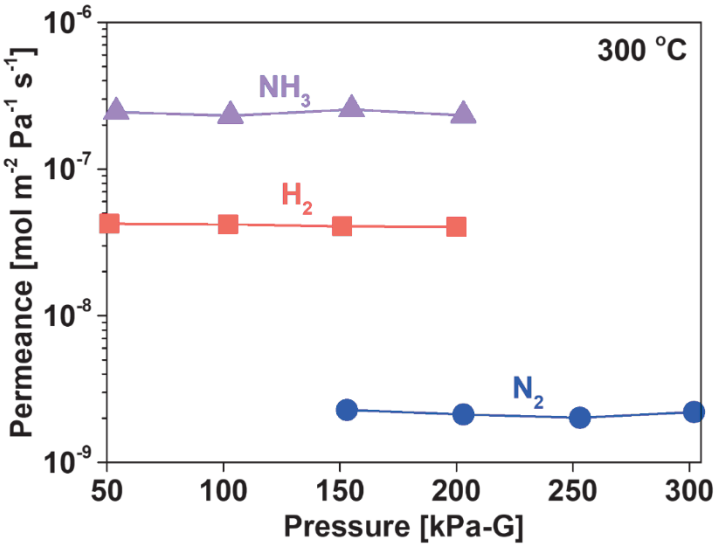

Fig. 5-14. Feed pressure dependence of single H_2, N_2, and NH_3 permeance at 300 °C for a TPS-EtOH membrane (permeate side: atmosphere pressure).

Fig. 5-S6 indicates the sequence of H_2, N_2, and NH_3 permeation measurement with a temperature-swing from 50 to 300 °C for a TPS-EtOH membrane. Obviously, all H_2, N_2, and NH_3 permeances of the second measurement at 200 and 50 °C were approximate to their-respective initial permeance, meaning that TPS-EtOH membrane has a sufficient thermal stability and NH_3 resistance even at 300 °C. Moreover, three TPS-EtOH membranes fabricated in this study showed approximately similar H_2, N_2, and NH_3 permeances ranging from 50 to 300 °C, as summarized in Fig. 5-S7, implying a favorable reproducibility for TPS-EtOH membranes. Additionally, Fig. 5-15 shows NH_3, H_2, and N_2 permeances as well as their selectivities during single and binary gas permeation at 300 °C using a TPS-EtOH membrane. Each permeance in single gas permeation was approximately the same as in binary gas permeation. Because of the weakened adsorption between NH_3 molecules and membrane surface and the strengthened NH_3 diffusion at high temperature such as 300 °C, the inhibition effect that was found in TEOS-derived membranes [28] at low temperatures because the preferentially

adsorbed NH_3 blocks H_2 and N_2 permeances. In addition, the thermodynamically-favored sorption that was found Prussian Blue-derived membranes owing to the promoted NH_3 transport in the form of ammonium. [47] These mixing-effects were not observed for TPS-EtOH membranes. NH_3, H_2, and N_2 permeances as well as their selectivities still exhibited a superior performance in binary gas permeation, consistent with single gas permeation. Additionally, single gas permeances measured before and after binary gas permeation confirmed the stability of the TPS membrane and the reproducibility of the measurement. Based on the above conclusion. it is further speculated that even the permeance of a ternary gas with more complex probably be similar to that of a single gas.

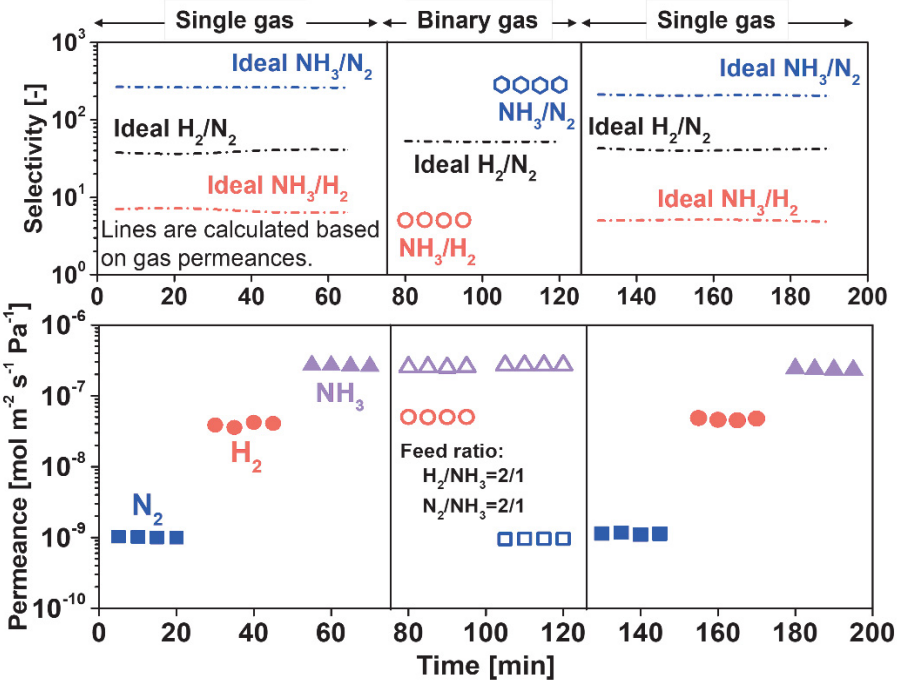

Fig. 5-15. Time courses of selectivity and permeance of NH_3, H_2, and N_2 in single and binary gas permeation at 300 °C for a TPS-EtOH membrane. Feed ratios of H_2/NH_3 and N_2/NH_3 = 2/1.

5.3.4 Trade-off of various membranes

Fig. 5-16 summarizes and compares the performance of various membranes at 50

and 200 °C including NH_3 permeance and NH_3/H_2 and NH_3/N_2 selectivities. At temperatures below 50 °C in Fig. 5-16 (above), TPS-EtOH membranes with a dense structure due to the flexibility of propyl chains and the filling of -*SO_3H* groups expressed a lower NH_3 permeance than PFSA-derived membranes with flexible structures [29] and BTPA-based membranes with enlarged pore size and improved NH_3 affinity through metal coordination [30,48]. But TPS-EtOH membranes showed a remarkable NH_3 selectivity, especially NH_3/N_2 selectivity, because of a comparable NH_3 adsorption-diffusion and molecular sieving. According to the results of FT-IR and NH_3-TPD, TPS-EtOH membranes have intrinsic protonic -*SO_3H* groups that showed the increased NH_3 affinity and permeance, while H_2O_2-oxidized MPTMS membranes showed the lower NH_3 selectivity for oxidized MPTMS membrane because of large pore such as pinholes probably induced by the effects of H_2O_2.

Until now, NH_3 permeation at temperatures higher than 200 °C were rarely reported. Fig. 5-16 (below) summarizes the membranes that were used for NH_3 separation at 200 °C. Generally, NH_3 permeance and selectivity always show a negative correlation, so-called trade-off, especially NH_3 permeance vs. NH_3/H_2 selectivity in Fig. 5-16 (below). NH_3 permeance in both PFSA- and BTPA-derived membranes was close to ~10^{-6} mol m^{-2} s^{-1} Pa^{-1}, but NH_3 selectivity in PFSA-derived membrane was lower than that in BTPA-derived membrane due to the weakening of acid-base interaction at high temperature, which can further be confirmed by the decreasing NH_3 permeance with increasing temperature. [29] Furthermore, TPS-EtOH and oxidized MPTMS membranes showed the separation performance approximately on the upper bound with an order of

magnitude higher NH_3 permeance of ~10^{-7} mol m^{-2} s^{-1} Pa^{-1} than Na^+-grafted nanochannel membrane [49]. The surprising NH_3/N_2 selectivity of ~1700 was also achieved in TPS-EtOH membrane at 200 °C, similar to Na^+-grafted nanochannel membrane, which can be ascribed to the synergistic effects of superior molecular sieving and adsorption-diffusion. Compared to oxidized MPTMS membranes, the approximate NH_3/H_2 and remarkable NH_3/N_2 selectivities were obtained in TPS-EtOH membranes, which means that the pore size of TPS-EtOH membrane should be between the kinetic diameters of H_2 and N_2, i.e., 0.30-0.35 nm. This is consistent with the reported effective pore size of ~0.35 nm for NH_3 separation membranes [28], confirming that TPS-EtOH membranes are promising for NH_3-selective membranes at high temperatures.

Moreover, a $ZnCl_2$ immobilized molten salt (IMS) membrane was reported in 1992 at 250-300 °C [50] and quite recently for NH_3 separation at 290-325 °C and 1 atm, [51] showing excellent NH_3 permeance of 6.1×10^{-7} mol m^{-2} s^{-1} Pa^{-1} with NH_3/N_2 and NH_3/H_2 ideal selectivities of 11375 and > 10^7, respectively, at 300 °C. Since the stability of liquid membrane is concerned due to the possible evaporation of the liquid and/or leak-out via pressure-drop, the performance of the liquid membranes including molten salt will have to be examined under wide temperature range (25-350 °C) and different pressure-swing. Furthermore, a two-dimensional mathematical model of a micro-structured membrane reactor with $ZnCl_2$ IMS membrane was used to simulate catalysis membrane reactors. [52]

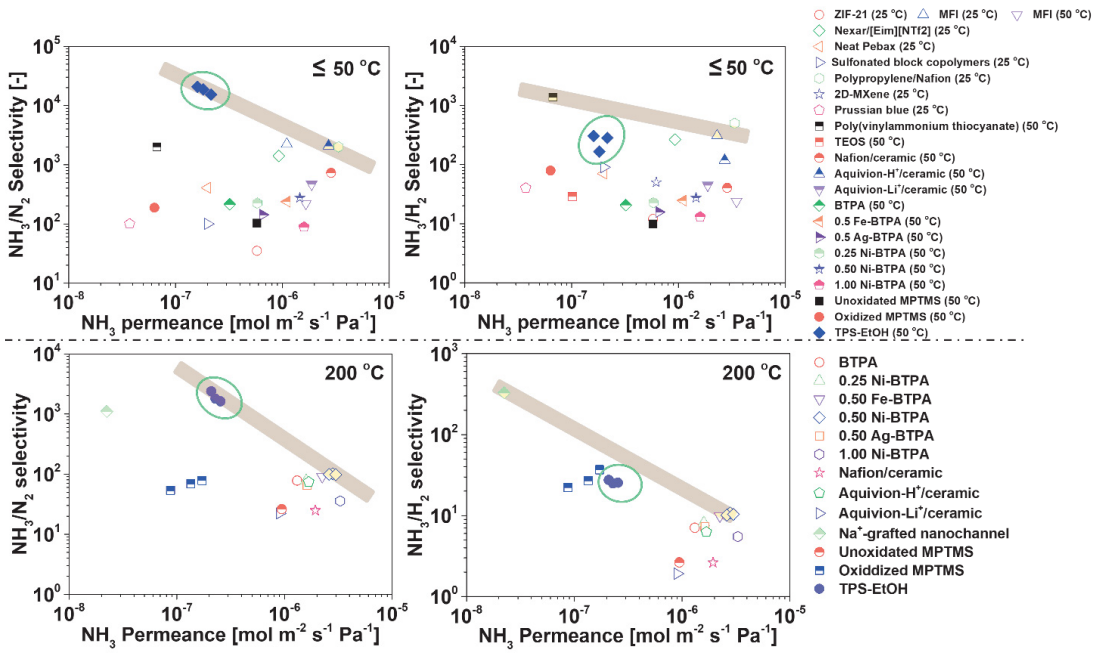

Fig. 5-16. Trade-off of NH_3 permeance, NH_3/H_2 and NH_3/N_2 selectivity at 50 (above) and 200 °C (below) for various membranes. Each point indicates the permeance of the different membranes. All plotted data are summarized in Table 5-S1.

5.4 Conclusions

3-(trihydroxysilyl)-1-propanesulfonic acid (TPS) was diluted to 0.1 wt% with ethanol to fabricate sulfonic silica-based membranes. The thermal stability of -*SO₃H* groups and propyl chains was proven by FT-IR analysis of TPS films calcined from 100 to 350 °C, and the siloxane network structure was formed by the self-catalyzed condensation of silanol (*Si-OH*) with the intrinsically acidic -*SO₃H* groups, as the amorphous structure shown by XRD patterns. Because of the flexibility of propyl chains and/or the filling of pores by bulky sulfonic acid groups, TPS xerogel powders calcined at 300 °C still showed a dense structure via N_2 adsorption, which further confirmed the thermal properties combined with XPS measurement. Owing to the inherently stronger proton-acidic -*SO₃H* groups in TPS, an intensive NH_3 affinity for TPS (an NH_3 adsorption amount of ~3.0 mmol g^{-1}) was observed twice higher than oxidized MPTMS by NH_3-

TPD. For single and binary gas permeation, TPS-EtOH membranes showed a superior NH_3 permeance of ~2.6 and ~1.8×10^{-7} mol m^{-2} s^{-1} Pa^{-1} with an excellent NH_3/H_2 selectivity of 7 and 165, and NH_3/N_2 selectivity of 266 and 18700 at 300 and 50 °C, respectively.

References

[1] J.W. Erisman, M.A. Sutton, J. Galloway, Z. Klimont, W. Winiwarter, How a century of ammonia synthesis changed the world, *Nat. Geosci.* 1 (2010) 636-639.

[2] J. Humphreys, R. Lan, S. Tao, Development and recent progress on ammonia synthesis catalysts for Haber-Bosch process, *Adv. Energy Sustainability Res.* 2 (2021) 2000043.

[3] S. Chatterjee, R.K. Parsapur, K.W. Huang, Limitations of ammonia as a hydrogen energy carrier for the transportation sector, *ACS Energy Letters* 6 (2021) 4390-4394.

[4] Y. Kojima, M. Yamaguchi, Ammonia as a hydrogen energy carrier, *Int. J Hydrogen Energ.* 47 (2022) 22832-22839.

[5] L. Meng, M. Kanezashi, X. Yu, T. Tsuru, Enhanced decomposition of sulfur trioxide in the water-splitting iodine-sulfur process via a catalytic membrane reactor, *J. Mater. Chem. A* 4 (2016) 15316-15319.

[6] T. Sato, H. Nagasawa, M. Kanezashi, T. Tsuru, Transesterification membrane reactor with organosilica membrane in batch and continuous flow modes, *Chem. Eng. J.* 450 (2022) 137862.

[7] T. Sato, H. Nagasawa, M. Kanezashi, T. Tsuru, Enhanced production of butyl acetate via methanol-extracting transesterification membrane reactors using organosilica membrane: Experiment and modeling, *Chem. Eng. J.* 429 (2022) 132188.

[8] A.G. Olabi, M. Ali Abdelkareem, M. Al-Murisi, N. Shehata, A. Hai Alami, A. Radwan, T. Wilberforce, K.J. Chae, E. Taha Sayed, Recent progress in green ammonia: Production, applications, assessment; barriers, and its role in achieving the sustainable development goals, *Energ. Convers. Manage.* 277 (2023) 116594.

[9] Z. Rizki, E. Suryawirawan, A.E.M. Janssen, A. van der Padt, R.M. Boom, Modelling temperature effects in a membrane cascade system for oligosaccharides, *J. Membrane Sci.* 610 (2020) 118292.

[10] S.J. Kim, S. Yang, G.K. Reddy, P. Smirniotis, J. Dong, Zeolite Membrane reactor for high-temperature water-gas shift reaction: effects of membrane properties and operating conditions, *Energy Fuels* 27 (2013) 4471-4480.

[11] Z. Zhang, J. Douglas Way, C.A. Wolden, Design and operational considerations of catalytic membrane reactors for ammonia synthesis, *AIChE J.* (2021) e17259.

[12] Y. Kobayashi, Y. Tang, T. Kageyama, H. Yamashita, N. Masuda, S. Hosokawa, H. Kageyama, Titanium-based hydrides as heterogeneous catalysts for ammonia synthesis, *J. Am. Chem. Soc.* 139 (2017) 18240-18246.

[13] X. Peng, H.X. Liu, Y. Zhang, Z.Q. Huang, L. Yang, Y. Jiang, X. Wang, L. Zheng, C. Chang, C.T. Au, L. Jiang, J. Li, Highly efficient ammonia synthesis at low temperature over a Ru-Co catalyst with dual atomically dispersed active centers, *Chem. Sci.* 12 (2021) 7125-7137.

[14] M. Hattori, N. Okuyama, H. Kurosawa, M. Hara, Low-temperature ammonia synthesis on iron catalyst with an electron donor, *J. Am. Chem. Soc.* 145 (2023) 7888-7897.

[15] Z. Zhang, C. Karakaya, Robert J. Kee, J. Douglas Way, C.A. Wolden, Barium-promoted ruthenium catalysts on yittria-stabilized zirconia supports for ammonia synthesis, *ACS Sustainable Chem. Eng.* 7 (2019) 18038-18047.

[16] J. Humphreys, R. Lan, S. Chen, S. Tao, Improved stability and activity of Fe-based catalysts through strong metal support interactions due to extrinsic oxygen vacancies in $Ce_{0.8}Sm_{0.2}O_{2-\delta}$ for the efficient synthesis of ammonia, *J. Mater. Chem. A* 8 (2020) 16676-16689.

[17] A. Bhown, E.L. Cussler, Mechanism for selective ammonia transport through poly(vinylammonium thiocyanate) membranes, *J. Am. Chem. Soc.* 113 (1991) 742-749.

[18] V. Tricoli, E.L. Cussler, Ammonia selective hollow fibers, *J. Membrane Sci.* 104 (1995) 19-26.

[19] Y. He, E.L. Cussler, Ammonia permeabilities of perfluorosulfonic membranes in various ionic forms, *J. Membrane Sci.* 68 (1992) 43-52.

[20] I.V. Vorotyntsev, P.N. Drozdov, N.V. Karyakin, Ammonia permeability of a cellulose acetate membrane, *Inorg. Mater.* 42 (2006) 231-235.

[21] A. Raza, S. Farrukh, A. Hussain, Synthesis, characterization and NH_3/N_2 gas permeation study of nanocomposite membranes, *J. Polym. Environ.* 25 (2017) 46-55.

[22] B. Yang, L. Bai, T. Li, L. Deng, L. Liu, S. Zeng, J. Han, X. Zhang, Super selective ammonia separation through multiple-site interaction with ionic liquid-based hybrid membranes, *J. Membrane Sci.* 628 (2021) 119264.

[23] B. Yang, L. Bai, Z. Wang, H. Jiang, S. Zeng, X. Zhang, X. Zhang, Exploring NH_3 transport properties by tailoring ionic liquids in Pebax-based hybrid membranes, *Ind. Eng. Chem. Res.* 60 (2021) 9570-9577.

[24] K. Vikrant, V. Kumar, K.H. Kim, D. Kukkar, Metal-organic frameworks (MOFs): potential and challenges for capture and abatement of ammonia, *J. Mater. Chem. A* 5 (2017) 22877-22896.

[25] Q. Wei, J.M. Lucero, J.M. Crawford, J. Douglas Way, C.A. Wolden, M.A. Carreon, Ammonia separation from N_2 and H_2 over LTA zeolitic imidazolate framework membranes, *J. Membrane Sci.* 623 (2021) 119078.

[26] X. Duan, D. Kim, K. Narasimharao, S. Al-Thabaitic, M. Tsapatsis, High-performance ammonia-selective MFI nanosheet membranes, *Chem. Commun.* 57 (2021) 580-582.

[27] M. Hattori, S. Iijima, T. Nakao, H. Hosono, M. Hara, Solid solution for catalytic ammonia synthesis from nitrogen and hydrogen gases at 50 °C, *Nat. Commun*. 11 (2020) 2001.

[28] M. Kanezashi, A. Yamamoto, T. Yoshioka, T. Tsuru, Characteristics of ammonia permeation through porous silica membranes, *AIChE J.* 56 (2010) 1204-1212.

[29] K. Wakimoto, W.W. Yan, N. Moriyama, H. Nagasawa, M. Kanezashi, T. Tsuru, Ammonia permeation of fluorinated sulfonic acid polymer/ceramic composite membranes, *J. Membrane Sci.* 658 (2022) 120718.

[30] W.W. Yan, U. Anggarini, H.C. Bai, H. Nagasawa, M. Kanezashi, T. Tsuru, Enhanced NH_3 permeation of bis[3-(trimethoxysilyl)propyl] amine membranes via coordination with metals, *J. Membrane Sci.* 678 (2023) 121665.

[31] S. Padinjarekutt, B. Sengupta, H. Li, K. Friedman, D. Behera, R. Lecaros, M. Yu, Synthesis of Na^+-gated nanochannel membranes for the ammonia (NH_3) separation, *J. Membrane Sci.* 674 (2023) 121512.

[32] W.W. Yan, U. Anggarini, K. Wakimoto, H.C. Bai, H. Nagasawa, M. Kanezashi, T.

Tsuru, Optimization of Ni-amine coordination for improving NH_3 permeation through nickel-doped bis[3-(trimethoxysilyl)propyl] amine membranes, *Sep. Purif. Technol.* 326 (2023) 124809.

[33] T.T. Hu, F. Liu, S. Dou, L.B. Zhong, X. Cheng, Z.D. Shao, Y.M. Zheng, Selective adsorption of trace gaseous ammonia from air by a sulfonic acid-modified silica xerogel: Preparation, characterization and performance, *Chem. Eng. J.* 443 (2022) 136357.

[34] W.W. Yan, K. Wakimoto, N. Moriyama, H. Nagasawa, M. Kanezashi, T. Tsuru, Development of sulfonated (3-Mercaptopropyl)trimethoxysilane membranes with thermal stability and excellent NH_3 perm-selectivity at 300 °C, *J. Membrane Sci.* 696 (2024) 122535.

[35] T. Tsuru, Nano/subnano-tuning of porous ceramic membranes for molecular separation, *J. Sol-Gel Sci. Technol.* 46 (2008) 349-361.

[36] F. Ebrahimi, R. Farazi, E.Z. Karimi, H. Beygi, Dichlorodimethylsilane mediated one-step synthesis of hydrophilic and hydrophobic silica nanoparticles, *Adv. Powder Technol.* 28 (2017) 932-937.

[37] L. Peña, F. Xu, K.L. Hohn, J. Li, D. Wang, Propyl-sulfonic acid functionalized nanoparticles as catalyst for pretreatment of corn stover, *Journal of Biomaterials and Nanobiotechnology* 5 (2014) 8-16. DOI: 10.4236/jbnb.2014.51002.

[38] A. Enotiadis, L.G. Boutsika, K. Spyrou, C. Simaric, I. Nicotera, A facile approach to fabricating organosilica layered material with sulfonic groups as an efficient filler for polymer electrolyte nanocomposites, *New J. Chem.* 41 (2017) 9489-9496.

[39] Y. Kaneko, H. Toyodome, T. Mizumo, K. Shikinaka, N. Iyi, Preparation of a sulfo-group-containing rod-like polysilsesquioxane with a hexagonally stacked structure and its proton conductivity, *Chem. Eur. J.* 20 (2014) 9394-9399.

[40] P. Khodaee, N. Najmoddin, S. Shahrad, The effect of ethanol and temperature on the structural properties of mesoporous silica synthesized by sol-gel method, 25th National and 3rd International Iranian Conference on Biomedical Engineering (ICBME) (2018). DOI: 10.1109/ICBME.2018.8703594.

[41] S. Lawal, M. Kanezashi, H. Nagasawa, T. Tsuru, Development of an

acetylacetonate-modified silica-zirconia composite membrane applicable to gas separation, *J. Membrane Sci.* 599 (2020) 117844.

[42] U. Anggarini, L. Yu, H. Nagasawa, M. Kanezashi, T. Tsuru, Microporous nickel-coordinated aminosilica membranes for improved pervaporation performance of methanol/toluene separation, *ACS Appl. Mater. Interfaces* 13 (2021) 23247-23259.

[43] T. Yoshioka, M. Kanezashi, T. Tsuru. Micropore size estimation on gas separation membranes: A study in experimental and molecular dynamics. *AIChE J.*, 59 (2013) 2179-2194.

[44] M. Kanezashi, T. Sasaki, H. Tawarayama, H. Nagasawa, T. Yoshioka, K. Ito, T. Tsuru, Experimental and theoretical study on small gas permeation properties through amorphous silica membranes fabricated at different temperatures. *J. Phys. Chem. C* 118 (2014) 20323-20331.

[45] H.R. Lee, M. Kanezashi, Y. Shimomura, T. Yoshioka, T. Tsuru, Evaluation and fabrication of pore-size-tuned silica membranes with tetraethoxydimethyl disiloxane for gas separation, *AIChE J.* 57 (2011) 2755-2765.

[46] L. Yu, M. Kanezashi, H. Nagasawa, J. Oshita, A. Naka, T. Tsuru, Pyrimidine-bridged organoalkoxysilane membrane for high-efficiency CO_2 transport via mild affinity, *Sep. Purif. Techol.* 178 (2017) 232-241.

[47] M.A. Komkova, I.S. Sadilov, V.A. Brotsman, D.I. Petukhov, A.A. Eliseev, Facilitated transport of ammonia in ultra-thin Prussian Blue membranes with potential-tuned selectivity, *J. Membrane Sci.* 639 (2021) 119714.

[48] U. Anggarini, L. Yu, H. Nagasawa, M. Kanezashi, T. Tsuru, Metal-induced microporous aminosilica creates a highly permeable gas-separation membrane, *Mater. Chem. Front.* 5 (2021) 3029-3042.

[49] S. Padinjarekutt, H. Li, S. Ren, P. Ramesh, F. Zhou, S. Li, G. Belfort, M. Yu, Na^+-gated nanochannel membrane for highly selective ammonia (NH_3) separation in the Haber-Bosch process, *Chem. Eng. J.* 454 (2023) 139998.

[50] D.V. Laciak, G.P. Pez, P.M. Burban, Molten salt facilitated transport membranes. Part 2. Separation of ammonia from nitrogen ana hydrogen at high temperatures, *J. Membrane Sci.* 65 (1992) 31-38.

[51] M. Adejumo, L. Oleksy, S. Liguori, Innovative NH_3 separation over immobilized molten salt membrane at high temperatures, *Chem. Eng. J.* 479 (2024) 147434,

[52] E. Kucuk, H. Hasan Koybasi, A.K. Avci, Beyond equilibrium ammonia synthesis in a membrane and heat exchange integrated microreactor: A modeling study, *Fuel* 357 (2024) 129858.

Supplementary Material

---------- **SI-1**: NH_3 temperature-programmed desorption (NH_3-TPD) [1] ----------

The NH_3 affinity and amount of the xerogel powders was probed using NH_3 temperature-programmed desorption (NH_3-TPD). All xerogel powders were pre-calcined under a N_2 atmosphere at 300 °C. The measurement program is detailed below. Firstly, the pre-treated xerogel powders were further degassed to remove adsorbed water via utilizing dry helium at 30 mL min^{-1} for 120 min at 150 ℃. After cooling and holding at 28 ℃ for 60 min, 5% NH_3/95% He mixture gases at 30 mL min^{-1} and Ar gas at 1 mL min^{-1} were introduced into the sample cell for 90 min to reach adsorption saturation. When the NH_3 adsorption was finished, the dry helium at 30 mL min^{-1} continued to flow into the system at room temperature for 120 min. Finally, the NH_3 desorption program was implemented as the temperature increased from 40 to 300 ℃ at 10 ℃ min^{-1} and maintained at 300 ℃ for 15 min. The following Eq-1 and Eq-2 were used to calculate the NH_3 adsorption and desorption amount, respectively. Each sample was measured 3 times to obtain the average amount of NH_3 adsorption and desorption.

$$NH_3 \text{ adsorption amount} = \frac{1}{m}\int_{t1}^{t2}\left(\frac{I_{Ar,t}\frac{I_{NH_3,in}}{I_{Ar,in}} - I_{NH_3,t}}{I_{NH_3,in}}\right)Q_{NH_3}\,dt \qquad \text{Eq-1}$$

$$NH_3 \text{ desorption amount (40}\rightarrow\text{300 °C)} = \frac{1}{m}\int_{t3}^{t4}\left(\frac{I_{NH_3,t}}{I_{NH_3,in}}\right)Q_{NH_3}\,dt \qquad \text{Eq-2}$$

m: weight of sample; $I_{i,in}$: intensity of the feed i-th component; $I_{i,t}$: intensity of the feed i-th component at each moment; Q_{NH_3}: flow rate of NH_3.

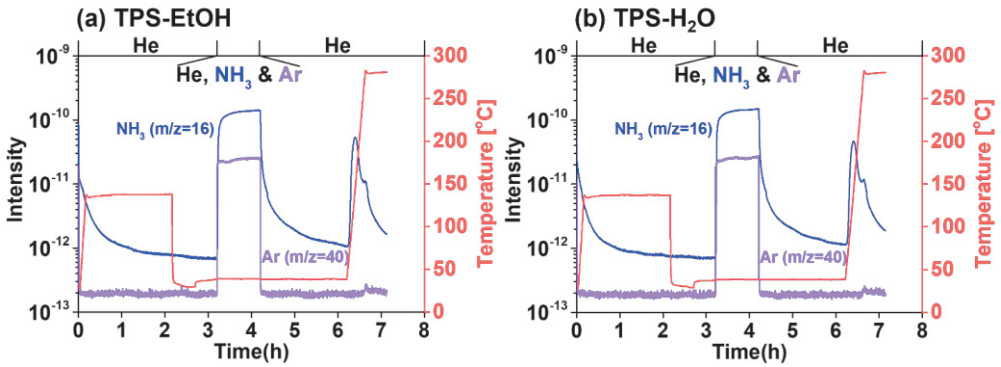

Fig. 5-S1. Time course of mass intensity and temperature during NH_3-TPD measurements for TPS-EtOH (a) and TPS-H_2O (b) xerogel powders calcined at 300 °C.

---------- **SI-2**: Permeation measurement and experimental apparatus [1] ----------

As depicted in Fig. 5-S2, the experimental apparatus was applied to the single and binary gas permeation, including high-purity He, H_2, NH_3, N_2, CH_4, CF_4, and SF_6. After removing the adsorbed water molecules under a He flow at 200 °C at least for 6 h, each gas was fed into the outside of the membrane under upstream pressures at 200-300 kPa and at 50-300 °C, and the permeate stream was kept at atmospheric pressure. The permeate flow-rate of each gas, except for NH_3, was measured by utilizing a film flow meter (Horiba, Co. Ltd., Japan) at a range from 50-300 °C. The NH_3 permeance cannot be measured with a film flow meter because NH_3 is inherently toxic and water-soluble, so the mass flow meter 4 (Fig. 5-S2), that has been calibrated via a gas chromatograph (GC), was used to measure the flow rate of the permeated NH_3 by closing the retentate valve (V-10 (left) in Fig. 5-S2). The errors of the gas flowrates were less than 5% when the permeance exceeds 10^{-10} mol m^{-2} s^{-1} Pa^{-1} and less than 50% while a the permeance is below 10^{-10} mol m^{-2} s^{-1} Pa^{-1}. GC-1 equipped with a Porapack N column was used to detect the concentration of NH_3, and GC-2 equipped with a Molecular Sieve X column was utilized to analyze the concentration of H_2 and N_2. Argon (Ar) gas was used as a carrier gas.

Gas permeance P_i (mol m^{-2} s^{-1} Pa^{-1}) for component i in single and binary gas permeation was calculated using equation (Eq-1).

$$P_i = \frac{F_i}{\Delta p_i} \qquad \text{Eq-1}$$

The pressure drop, Δp_i^s and Δp_i^b, *in* single and binary gas permeations were calculated according to the following equations (Eq-2) and (Eq-3), respeatively.

$$\Delta p_i^s = p_{f,i}^s - p_{p,i}^s \qquad \text{Eq-2}$$

$$\Delta p_i^b = \frac{p_{f,i}^b - p_{r,i}^b}{ln\frac{(p_{f,i}^b - p_{p,i}^b)}{(p_{r,i}^b - p_{p,i}^b)}} \qquad \text{Eq-3}$$

The selectivity of component *i* over component *j*, $\alpha_{i,j}$, was calculated via equation (Eq-4):

$$\alpha_{i,j} = \frac{P_i}{P_j} \qquad \text{Eq-4}$$

F_i: permeate flow-rate of component i; $p^s_{f,i}$ and $p^s_{p,i}$: pressure of pure component i in feed and permeate side, respectively, in single gas permeation. $p^b_{f,i}$, $p^b_{r,i}$, and $p^b_{p,i}$: partial pressure of component i in feed, retentate, and permeate side, respectively, in binary gas permeation.

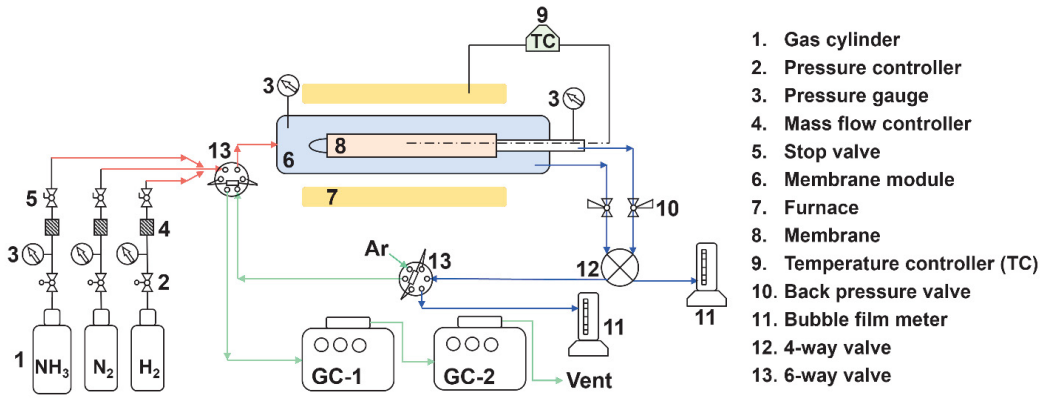

Fig. 5-S2. Schematic diagram of the single and binary gas permeation measurement.

------ **SI-3**: FT-IR spectra of TPS-H_2O films at different calcination temperatures-------

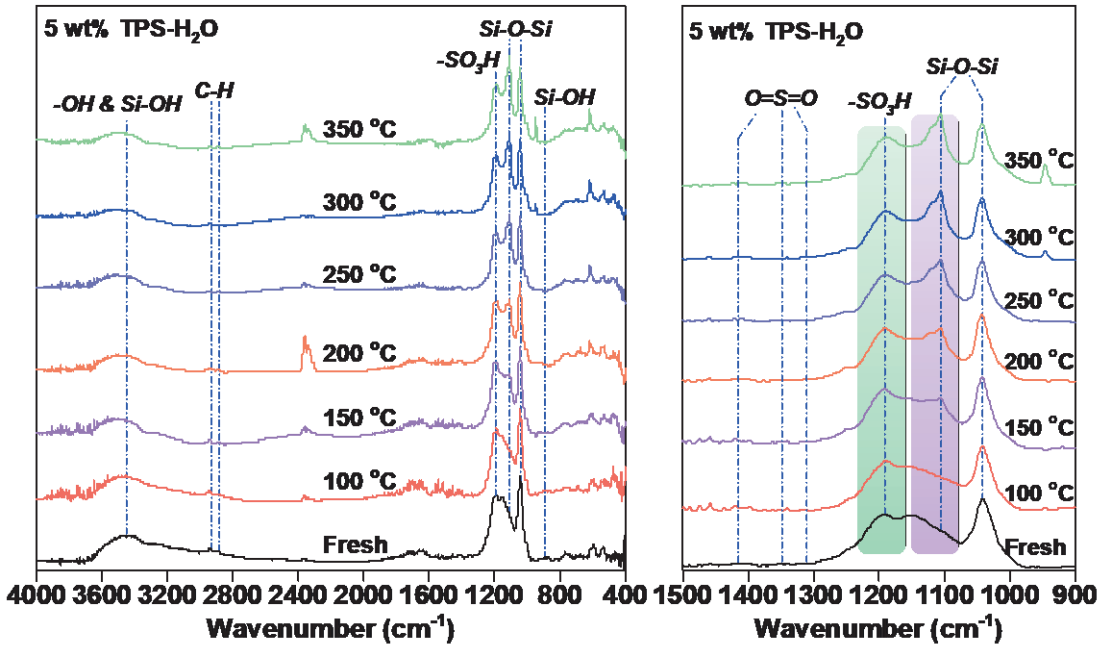

Fig. 5-S3. Wide FT-IR spectra (left) and narrow FT-IR spectra ranging from 1500 to 900 cm^{-1} (right) of TPS-H_2O films at different calcination temperatures.

---------- **SI-4**: Mass signal of m/z = 18, 44, and 48 in TPS xerogel powders ----------

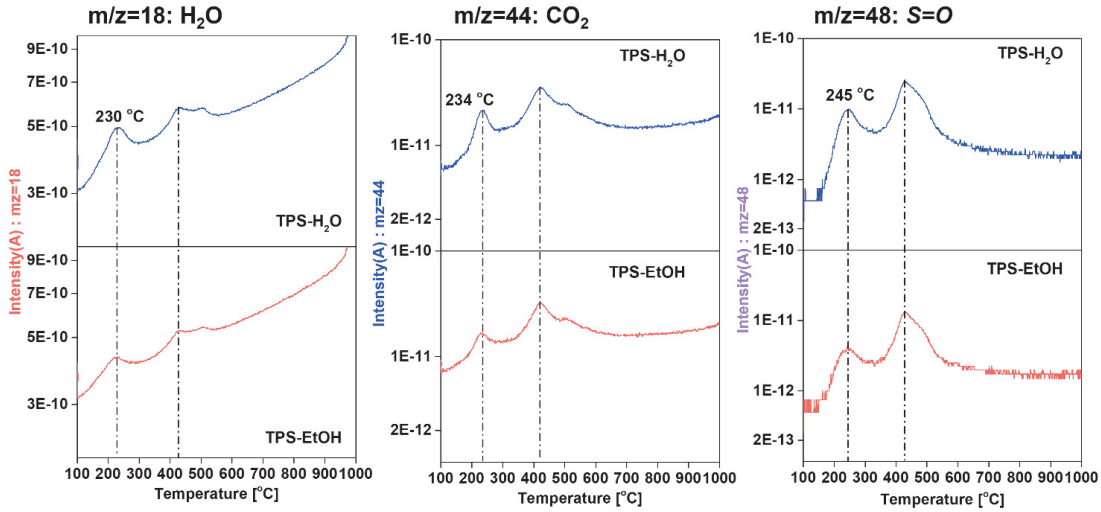

Fig. 5-S4. The mass signal of m/z = 18, 44, and 48 in TPS-EtOH and TPS-H_2O xerogel powders as a function of temperatures by TG-MS.

------ **SI-5**: H_2, N_2, and NH_3 permeance at 50-300 °C for MPTMS membranes [1]-------

Because the unoxidized MPTMS showed a weak NH_3 affinity, NH_3 permeance in unoxidized MPTMS membrane first increased with the increase of the temperature (50-200 °C), and then decreased with the temperature above 200 °C. Therefore, the permeances at 50-200 °C are used to calculate the permeation activation energy of each gas.

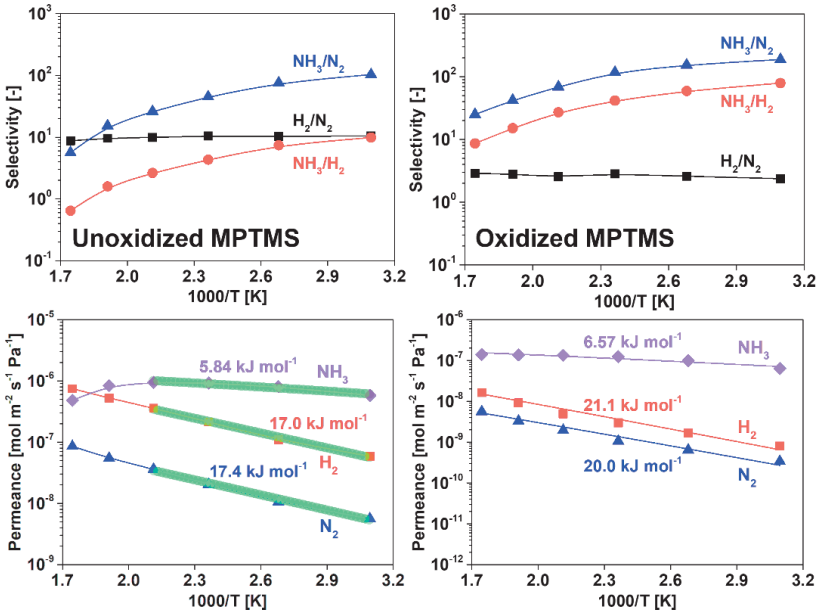

Fig. 5-S5. H_2, N_2, and NH_3 permeance and selectivity ranging from 50 to 300 °C for unoxidized (left) and oxidized MPTMS (right) membranes. [1]

---- **SI-6**: Time course for single H_2, N_2, and NH_3 permeance at temperature-swing ----

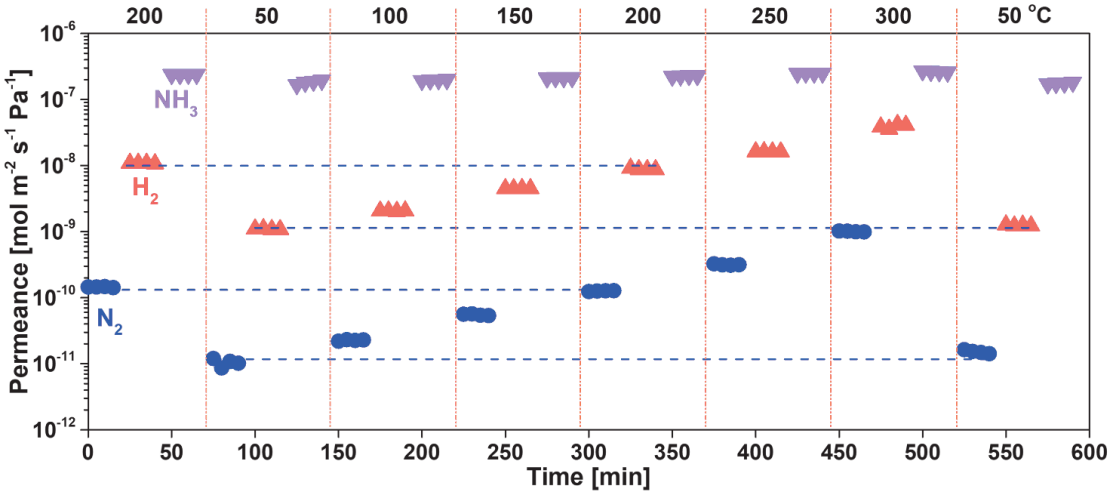

Fig. 5-S6. Time course for single H_2, N_2, and NH_3 permeance at temperatures ranging from 50 to 300 °C for a TPS-EtOH membrane.

------- **SI-7**: Reproducibility of membrane fabrication for TPS-EtOH membranes ------

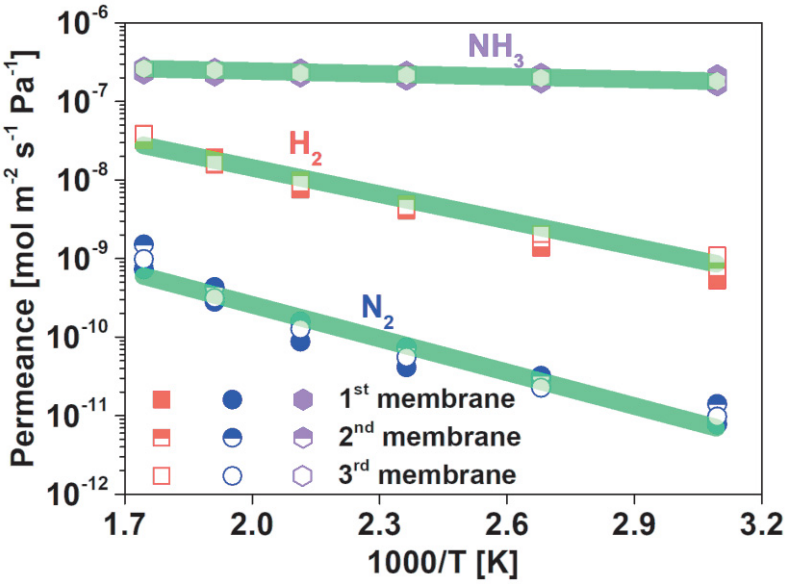

Fig. 5-S7. H_2, N_2, and NH_3 permeances of three different TPS-EtOH membranes at temperatures ranging from 50 to 300 °C.

Table 5-S1. Data for the selectivity and permeance of various membranes.

Name	Temperature [°C]	NH_3 permeance [mol m^{-2} s^{-1} Pa^{-1}]	NH_3/H_2	NH_3/N_2	Ref
Poly(vinylammonium thiocyanate)	24.0	1.6750E-08	6000.0	3600.0	2
	50.0	6.7000E-08	1390.0	2000.0	
ZIF-21	25.0	5.7900E-07	12.0	35.0	3
MFI	25.0	2.3000E-06	307.0	2236.0	4
Nexar/[Eim][NTf_2]	25.0	9.2829E-07	264.0	1407.0	5
Neat Pebax	25.0	1.9959E-07	70.1	406.7	6
Sulfonated block copolymers	25.0	2.0100E-07	90.0	100.0	7
Polypropylene/Nafion	25.0	3.3500E-06	500.0	2000.0	8
Prussian Blue	25.0	3.7202E-08	40.0	100.0	9
2D-MXene	25.0	6.2004E-07	50.0		10
TEOS	50.0	1.0200E-07	28.7		11
	50.0	1.0400E-07	0.1		
Nafion/ceramic	50.0	2.8544E-06	40.3	730.9	
	200.0	1.9355E-06	2.6	24.8	
Aquivion-H^+/ceramic	50.0	2.7100E-06	118.6	2085.9	12
	200.0	1.6800E-06	6.3	73.9	
Aquivion-Li^+/ceramic	50.0	1.8800E-06	44.7	465.6	
	200.0	9.0500E-07	1.9	22.3	
Immobilized molten salt	250.0	3.3500E-06	3000.0	1000.0	13
H^+-Nafion	21.0	2.5735E-07		3000.0	
	200.0	3.4743E-08		3000.0	14
Ag^+-Nafion	21.0	1.5441E-07		600.0	
	200.0	3.1434E-08		300.0	
BTPA	50.0	3.2208E-07	20.6	214.2	
	200.0	1.3107E-06	7.1	78.1	
0.50 Fe-BTPA	50.0	1.1110E-06	24.6	237.6	15
	200.0	2.2437E-06	9.9	90.6	
0.50 Ag-BTPA	50.0	6.5437E-07	15.7	142.6	
	200.0	1.6300E-06	7.3	64.7	
0.25 Ni-BTPA	50.0	5.8244E-07	22.6	223.8	
	200.0	1.5923E-06	8.1	78.1	
0.50 Ni-BTPA	50.0	1.4614E-06	27.3	276.7	16
	200.0	2.7995E-06	10.8	101.7	
1.00 Ni-BTPA	50.0	1.5960E-06	13.0	88.7	
	200.0	3.2910E-06	5.5	35.6	
Unoxidized MPTMS	50.0	5.7928E-07	10.0	103.3	
	200.0	9.4378E-07	2.6	26.2	1
Oxidated MPTMS	50.0	6.3506E-08	79.1	188.0	
	200.0	8.7382E-08	22.2	68.9	
Na^+-grafted nanochannels	200.0	2.2411E-08	328.0	1106	17
TPS-EtOH	50.0	1.6079E-07	306.2	20707.7	This work
	200.0	2.0861E-07	27.5	2377.5	
	50.0	2.1562E-07	282.0	15274.9	
	200.0	2.5434E-07	25.5	1618.9	
	50.0	1.8221E-07	165.3	18711.4	
	200.0	2.2811E-07	25.0	1795.5	

References

[1] W.W. Yan, K. Wakimoto, N. Moriyama, H. Nagasawa, M. Kanezashi, T. Tsuru, Development of sulfonated (3-Mercaptopropyl)trimethoxysilane membranes with thermal stability and excellent NH_3 perm-selectivity at 300 °C, *J. Membrane Sci.* 696 (2024) 122535.

[2] D.V. Laciak, R. Quinn, G.P. Pez, J.B. Appleby, P.S. Puri, Selective permeation of ammonia and carbon dioxide by novel membranes, *Sep. Sci. Technol.* 25 (1990) 1295-1305.

[3] Q. Wei, J.M. Lucero, J.M. Crawford, J. Douglas Way, C.A. Wolden, M.A. Carreon, Ammonia separation from N_2 and H_2 over LTA zeolitic imidazolate framework membranes, *J. Membrane Sci.* 623 (2021) 119078.

[4] X. Duan, D. Kim, K. Narasimharao, S. Al-Thabaitic, M. Tsapatsis, High-performance ammonia-selective MFI nanosheet membranes, *Chem. Commun.* 57 (2021) 580-582.

[5] B. Yang, L. Bai, S. Zeng, S. Luo, L. Liu, J. Han, Y. Nie, X. Zhang, S. Zhang, NH_3 separation membranes with self-assembled gas highways induced by protic ionic liquids, *Chem. Eng. J.* 421 (2021) 127876.

[6] B. Yang, L. Bai, Z. Wang, H. Jiang, S. Zeng, X. Zhang, X. Zhang, Exploring NH_3 Transport Properties by Tailoring Ionic Liquids in Pebax-Based Hybrid Membranes, *Ind. Eng. Chem. Res.* 60 (2021) 9570-9577.

[7] W.A. Phillip, E. Martono, L. Chen, M.A. Hillmyer, E.L. Cussler, Seeking an ammonia selective membrane based on nanostructured sulfonated block copolymers, *J. Membrane Sci.* 337 (2009) 39-46.

[8] V. Tricoli, E.L. Cussler, Ammonia selective hollow fibers, *J. Membrane Sci.* 104 (1995) 19-26.

[9] M.A. Komkova, I.S. Sadilov, V.A. Brotsman, D.I. Petukhov, A.A. Eliseev, Facilitated transport of ammonia in ultra-thin Prussian Blue membranes with potential-tuned selectivity, *J. Membrane Sci.* 639 (2021) 119714.

[10] D.I. Petukhov, A.S. Kan, A.P. Chumakov, O.V. Konovalov, R.G. Valeev, A.A.

Eliseev, MXene-based gas separation membranes with sorption type selectivity, *J. Membrane Sci.* 621 (2021) 118994.

[11] M. Kanezashi, A. Yamamoto, T. Yoshioka, T. Tsuru, Characteristics of Ammonia Permeation Through Porous Silica Membranes. *AIChE J.* 56 (2010) 1204-1212.

[12] K. Wakimoto, W.W. Yan, N. Moriyama, H. Nagasawa, M. Kanezashi, T. Tsuru, Ammonia permeation of fluorinated sulfonic acid polymer/ceramic composite membranes, *J. Membrane Sci.* 658 (2022) 120718.

[13] D.V. Laciak, G.P. Pez, P.M. Burban, Molten salt facilitated transport membranes. Part 2. Separation of ammonia from nitrogen ana hydrogen at high temperatures, *J. Membrane Sci.* 65 (1992) 31-38.

[14] Y. He, E.L. Cussler, Ammonia permeabilities of perfluorosulfonic membranes in various ionic forms, *J. Membrane Sci.* 68 (1992) 43-52.

[15] W.W. Yan, U. Anggarini, H.C. Bai, H. Nagasawa, M. Kanezashi, T. Tsuru, Enhanced NH_3 permeation of bis[3-(trimethoxysilyl)propyl] amine membranes via coordination with metals, *J. Membrane Sci.* 678 (2023) 121665.

[16] W.W. Yan, U. Anggarini, K. Wakimoto, H.C. Bai, H. Nagasawa, M. Kanezashi, T. Tsuru, Optimization of Ni-amine coordination for improving NH_3 permeation through nickel-doped bis[3-(trimethoxysilyl)propyl] amine membranes, *Sep. Purif. Technol.* 326 (2023) 124809.

[17] S. Padinjarekutt, B. Sengupta, H. Li, K. Friedman, D. Behera, R. Lecaros, M. Yu, Synthesis of Na^+-gated nanochannel membranes for the ammonia (NH_3) separation, *J. Membrane Sci.* 674 (2023) 121512.

Chapter 6

Green ammonia production via recycle membrane reactor: Experiment and process simulation

6.1 Introduction

Synthetic ammonia (NH_3), as a world-renowned achievement, has promoted agricultural development and population growth for more one century, thanks to artificial nitrogen fixation processes, i.e. Haber-Bosch (HB) process. [1-3] Moreover, NH_3 can also be regarded as the global second-most produced chemical and has already produced over 230 million metric tons annually, [4] because of its massive demand from fertilizer production as well as the production of pharmaceutical intermediates, plastics, nitric acid, and so on. [5] Recently, NH_3 has greatly attracted much attention as a carbon-free hydrogen-carrier owing to its high hydrogen density (107.7 $kg_{H_2}\ m^{-3}$) and capacity (17.6 wt%) [6,7] as well as superior energy density (12.8 GJ m^{-3}) [8] and can be further considered as a potential fuel-carrier due to its easy liquefaction and comparatively inexpensive storage. [9,10]

Until now, NH_3 has been produced on a large scale through the HB process under extremely harsh conditions including high temperature (425-600 °C) for fast kinetics and intense pressure (20-30 MPa) for high NH_3 conversion. The energy consumption required to produce one ton of NH_3 is about 9-15 MWh. [11] However, only ~15% of NH_3 conversion was obtained by using iron-based catalysts, which could be attributed to the kinetic and thermodynamic limitations. This is ascribed to the fact that the activation of N≡N bonds [12] or the formation of N-H bonds [13] would require a large

amount of energy. Some efficient catalysts such as Ru-based catalysts have been developed to achieve high NH_3 conversion even under relatively low temperature (~350 °C). [14,15] Among them, Ru/Cs/MgO catalyst [16] has been well-recognized and expressed the excellent activity and stability for NH_3 synthesis. [17,18] Reportedly, the super-basic MgO support and the more electronegative Cs promoter synergistically increased the electron donation ability of the Ru catalyst, which can weaken N≡N bonds and accelerate their dissociation. [19,20]

For further eco-friendly NH_3 production, renewable technology was highly expected for green NH_3 production [21] via utilizing H_2 from H_2O electrolysis and N_2 from pressure-swing air adsorption. [22,23] With the expectation of high NH_3 conversion, catalytic membrane reactor (CMR) technology where catalysts are packed/dipped with a membrane in one unit [24] has the immeasurably potential to be used to improve the HB process through the shift of the reaction equilibrium towards the product side. CMR has been applied to various reactions including methane steam reforming [25], water gas shift reaction [26], and methylcyclohexane dehydrogenation [27] as well as the production of methanol and dimethyl ether (DME) via CO_2 hydrogenation membrane reactors [28,29]. Importantly, DME yield of 11% and CO_2 conversion of 12% were obtained even at low temperature, i.e. 275 °C, by removing H_2O to promote the reaction, which is quite attractive. [29]

Importantly, NH_3 separation membranes with a superior NH_3 permselectivity over H_2 and N_2 have been rapidly developed, such as perfluorosulfonic acid (PFSA)/ceramic composite membranes [30] and sulfonated mercaptopropyl)trimethoxysilane (MPTMS)-

derived membranes [31] that we have reported. As for PFSA/ceramic composite membranes, Aquivion/ceramic composite membrane showed a high NH_3 permeance of 2.7×10^{-6} mol m^{-2} s^{-1} Pa^{-1} with excellent NH_3/H_2 selectivity of 120 and NH_3/N_2 selectivity of 2090 at low temperature, i.e., 50 °C and a thermal stability even at 200 °C. [30] Additionally, sulfonated MPTMS membrane can be successfully fabricated for selective NH_3 permeation via the sol-gel method and H_2O_2 oxidization, [31] that can oxidize mercaptan groups (-*SH*) of MPTMS to *S=O* groups, showing an comparable NH_3 permeance of $\sim1.4\times10^{-7}$ mol m^{-2} s^{-1} Pa^{-1} with a moderate NH_3 selectivity ($NH_3/H_2 = 6$ and $NH_3/N_2 = 18$) at 300 °C. As for the reported conclusions, [30,31] sulfonated MPTMS membrane can withstand at 300 °C for about 200 min at least in binary gas permeation. Both membranes benefit from the molecular sieving (kinetic diameter: 0.364 nm (N_2) > 0.326 nm (NH_3) [32] > 0.289 nm (H_2)) and the NH_3 adsorption-diffusion on the membrane surface. In addition to the above-mentioned PFSA- and MPTMS-derived membranes, metal-doped aminosilica [33,34] and zeolite-based membranes [35] also showed superior NH_3 permselectivity, but NH_3-permselectivity decreased dramatically with increasing temperatures due to the reduced adsorptive selectivity.

It is significantly difficult for membranes to be used directly to develop CMR for NH_3 production. Because high temperatures (≥350 °C) are necessary to synthesize NH_3 but NH_3 selective membranes reported so far decomposed partly and/or NH_3 selectivity decreased greatly with increasing temperatures. Hence, as shown in Fig. 6-1, compared with traditional HB process using condenser to recover the synthesized NH_3, it is logically reasonable to propose the use of membrane separators instead of condensers for

separating and recovering NH_3 would lower energy consumption and production cost. CMR process can be used to produce NH_3 on a small scale and efficiently with the low capacities (~< 2-4 t-NH_3/day), [36] which will reduce the intensive capital and high production costs of the HB method. Nevertheless, no paper has reported such recycle membrane reactors (RMRs) probably due to the lack in the availability of NH_3-selective membranes even at moderate temperatures.

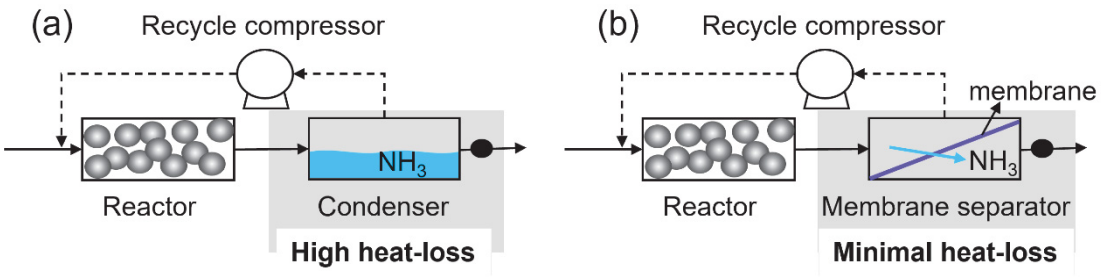

Fig. 6-1. Schematic diagrams of traditional HB process (a) and its improved process using membrane, i.e. RMR (b).

In this study, we proposed a green NH_3 production system, namely RMR where a reactor is combined with membrane separator with recycle flow, as shown in Fig. 6-1 (b). In this system, temperatures of a reactor packed with a Ru (10 wt%)/Cs/MgO catalyst and a membrane separator can be controlled independently. Aquivion/ceramic composite membrane and sulfonated MPTMS membrane were used to selectively extract NH_3 from feed side to permeate side of membranes. NH_3 composition in the reactor outlet and permeate side was analyzed, confirming that the efficient increase in NH_3 mole fraction exceeded that of equilibrium reaction at 350 °C. Moreover, a one-dimensional, isothermal, and plug-flow model was proposed for a mathematical simulation of a RMR to understand the RMR system. Finally, a green NH_3 production system without any H_2 and N_2 loss was designed and simulated via the mathematical model,

which give rationalized suggestions for the NH_3 synthesis under mild conditions via an RMR.

6.2 Theory

6.2.1 Mathematical model of plug flow reactor

A mathematical model with the assumption of steady state operation, plug flow, isothermal reaction, and negligible pressure drop along axial direction was applied to simulate recycle membrane reactor, and the office software, Excel, was used to realize and calculate the mathematical model.

Fig. 6-2 shows a schematic theoretical diagram of recycle membrane reactor that can simulate NH_3 production combined with a packed bed reactor and a membrane separator. In addition, as an ideal model, we assume NH_3 recovery unit which only recovers NH_3, and unreacted H_2 and N_2 are recycled to the reactor. The typical NH_3 synthesis reaction equation ($N_2+3H_2 \rightleftarrows 2NH_3$) was used in this study. Moreover, the kinetic equations of NH_3 synthesis reaction were referred to those proposed by Zhang et al. [37]. The number of active-sate for reaction has been corrected based on the measured reaction performance of Ru(10 wt%)/Cs/MgO catalysts used in this study by considering heat balance under different temperatures, pressures, and feed flow rates via a packed bed reactor, that are summarized in Supporting Information (SI). The reaction rate equation, Eq. (1), is shown below.

$$r_{NH_3} = 2N_s K_1 k_2 \theta^2 \left(P_{N_2} - \frac{P_{NH_3}^2}{P_{H_2}^3 K_{eq}} \right) \quad \text{Eq. (1)}$$

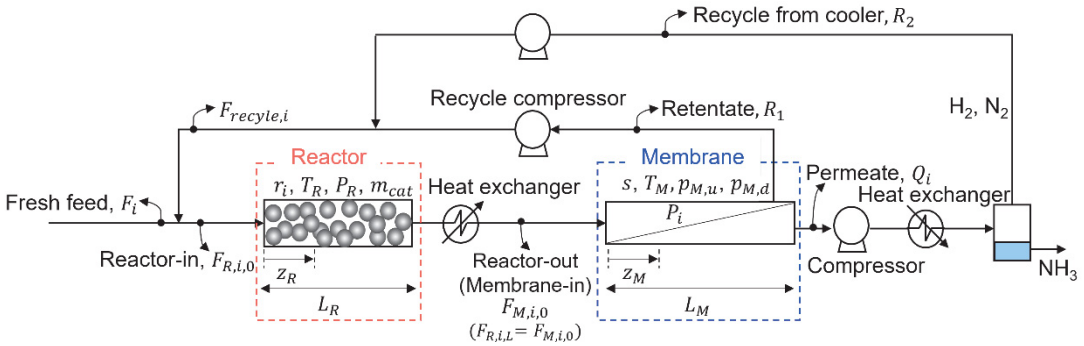

Fig. 6-2. Schematic diagrams of recycle membrane reactor.

The designed reactor model was a tube-type reactor, namely plug flow reactor (PFR), for continuous operation. Assuming steady state conditions including the plug flow and negligible pressure drop and reaction-heat along axial and radial direction, therefore, the i-th component flow rate along the length of the reactor can be expressed from the material balance in the following Eq. (2).

$$\frac{dF_{R,i}}{dz_R} = v_i m'_{cat} r_{NH_3} \quad \text{Eq. (2)}$$

In the system, the reaction starts from the inlet of the reactor, and the concentration and temperature are uniform in the radial direction in reactor. $F_{R,i}$ is the flow rate in reactor of i-th component, z_R is the axial position for the length of the reactor, m'_{cat} is the catalyst weight per reactor unit length, v_i is the stoichiometric number, and r_{NH_3} is the reaction rate.

For membrane permeation, the i-th component flow rate along the membrane is expressed by the following equation (Eq. (3)) based on the mass balance equation:

$$\frac{dF_{M,i}}{dz_M} = -P_i s(p_{M,u,i} - p_{M,d,i}) \quad \text{Eq. (3)}$$

$F_{M,i}$ is the feed flow rate in membrane for i-th component, z_M is the axial position in the membrane, s is the membrane area per membrane unit length, $p_{M,u,i}$ and $p_{M,d,i}$ are the partial pressure of the i-th component on the feed and permeate streams,

respectively.

The retentate stream was recycled to the reactor by a recycle compressor, while the permeate stream is assumed to be recompressed to remove 100% NH_3 (assumed) by compressing and liquefying NH_3 around room temperature and the unreacted H_2 and N_2 are recycled to the inlet of reactor. Because the mole fraction of NH_3 can be greatly improved by using membrane, high NH_3 concentration can be easily liquified based on the saturated vapor pressure of NH_3 (~10 bar at 25 °C; ~4 bar at 0 °C). As shown in Fig, 2, only NH_3 can be removed from the total system, fresh feed ratio of H_2 and N_2 (F_{H_2} and F_{N_2}) should be maintained at 3/1. On the other hand, the inlet flow rate of H_2 and N_2 to the reactor, $F_{R,i,0}$, can be controlled at the arbitrary H_2/N_2 composition in the system. Therefore, considering that the same amount of H_2 and N_2 which permeate through the membrane is supplied to the recycle flow rate (Eqs. (4) and (5)), all fresh feed is converted to Q_{NH_3} and therefore $F_{N_2} = F_{H_2}/3 = Q_{NH_3}/2$ is valid.

$$F_{recycyle,N_2}=R_{N_2}+Q_{N_2} \quad \text{Eq. (4)}$$

$$F_{recycyle,H_2}=R_{H_2}+Q_{H_2} \quad \text{Eq. (5)}$$

6.2.2 Dimensionless equation

The basic equations for reaction and membrane separation can be expressed in dimensionless forms in order to be generalized. The normalized equations (in SI-1) can be obtained using the dimensionless numbers listed Table 6-1.

Table 6-1. Dimensionless numbers used in this study.

Dimensionless number	Symbol	Definition
Damköhler number	Da	$Da=\frac{m_{cat}' L_R}{F_{N_2}} r_{NH_3,0}$
Permeation number	θ	$\theta=\frac{P_{NH_3} s L_M p_{M,u}}{F_{N_2}}$

Permeance ratio	α_i	$\alpha_i=\frac{P_{NH_3}}{P_i}$
Pressure ratio	β	$\beta=\frac{p_{M,d}}{p_{M,u}}$
Axial position	ξ	$\xi=\frac{z}{L}$
Flow ratio in reactor and membrane module	$\overline{f_i}$	$\overline{f_i}=\frac{f_{i,z}}{F_{N_2}}$
Reaction ratio	$R^*_{NH_3}$	$R^*_{NH_3}=\frac{r_{NH_3}}{r_{NH_3,0}}$
Recycle ratio	$\overline{R}$	$\overline{R}=\frac{\sum R_i}{F_{H_2}+F_{N_2}}$
Recovery	$\overline{Q}$	$\overline{Q}=\frac{\sum F_{M,i,l}}{\sum F_{M,i,0}}$

Eq. 2 can be normalized to a dimensionless form and expressed in Eq. (6), the Damköhler number (*Da*), that can be expressed as reaction rate, $m'_{cat}L_R r_{NH_3,0}$ ($r_{i,0}$ is the reaction rate at the inlet), that can be normalized with fresh feed flow (F_{N_2}).

$$\frac{d\overline{f_{R,i}}}{d\xi_R}=\nu_i Da R^*_{NH_3} \quad \text{Eq. (6)}$$

$\overline{f_{R,i}}$(=$F_{R,i}/F_{N_2}$) is the flow rate of i-th component normalized with F_{N_2}, ξ_R is the position normalized with the reactor length.

Eq. 3 is expressed as in Eq. (7) in dimensionless using Permeation number, θ,.

$$\frac{d\overline{f_{M,i}}}{d\xi_M}=-\frac{\theta}{\alpha_i}(x_i-\beta y_i) \quad \text{Eq. (7)}$$

$\overline{f_{M,i}}$ is the flow rate of i-th component in the membrane module normalized with the fresh N_2 flow rate, F_{N_2}, ξ_M is the ratio position to the membrane length. α_i is NH_3 selectivity (NH_3/H_2 and NH_3/N_2), β is the ratio of the total pressure in permeate streams to that of feed stream. x_i and y_i are the mole fractions of the *i*-th component in the feed and permeate streams, respectively.

From the simulations, the flow rates and compositions before and after the reactor as well as those of the retentate and permeate streams of the membrane are calculated. The

flow rates at each location were made dimensionless and summarized as $\overline{R}$ (the recycle flow rate to the fresh feed flow rate) and $\overline{Q}$ (the permeate flow rate to the membrane feed rate) to clarify the effect of the reactor and membrane conditions. The NH_3 permeance and selectivity of each membrane including Aquivion and sulfonated MPTMS membranes were obtained from the single-component permeation data.

The simulations were carried out under a wide range of variables including the membrane performance (permeance and permeance ratio), membrane area, pressure in feed/permeate sides, and H_2/N_2 ratio in recycling flow. Finally, we evaluated the membrane performance which enables green ammonia production under low pressure (≤10 bar-a) and compared it with the actual Haber-Bosch process.

6.3 Experimental

6.3.1 Sols preparation and membranes fabrication

6.3.1.1 Aquivion sol and membrane

Aquivion, as one of perfluorosulfonic acid (PFSA) as shown in Fig. 6-3 (a), was used to prepare sol by mixing the original Aquivion (24 wt%, Aldrich) solution with alcohol aqueous solution, the mass ratio of which was controlled at Aquivion/1-propanol/water/ethanol = 3/56.5/40/0.5 and stirring at room temperature for 1 h.

A α-alumina tube (outer diameter: 10 mm, inner diameter: 8 mm, average pore size: ~1 μm, porosity: 50 %, kindly supplied by Nikkato Inc. Japan.) was used as the membrane support. The α-Al_2O_3 particle layer containing 0.2 μm α-Al_2O_3 particle was firstly formed on the α-alumina tube by firing at 300°C under air atmosphere. A 1,2-bis(triethoxysilyl)ethane (BTESE) colloid sol was then coated and calcined at 300 °C under N_2

atmosphere to form a BTESE intermediate layer with a pore size of about 1 nm. [38] Aquivion/ceramic composite membrane was fabricated by coating the prepared Aquivion sol on the BTESE intermediate layer at room temperature, drying it for 1 h under N_2 atmosphere, and then annealing it at 200 °C. This was repeated three times. More details of fabrication process of PFSA/ceramic composite membrane can be found elsewhere. [30]

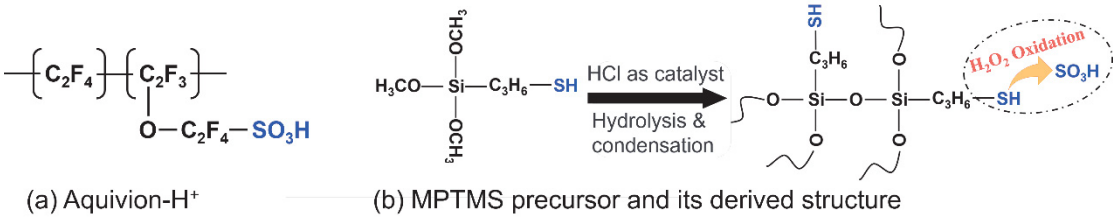

Fig. 6-3. Chemical structure of Aquivion (a) and MPTMS (b).

6.3.1.2 Sulfonated MPTMS sol and membrane

As shown in Fig. 6-3 (b), (3-Mercaptopropyl)trimethoxysilane (MPTMS, 85 wt%, Thermo Fisher Scientific Inc.) sol with the molar ratio of MPTMS/H_2O/HCl = 1/50/0.1 were prepared via the hydrolysis and condensation. Firstly, a mixture of HCl and water was added to MPTMS precursors dissolved in ethanol under continuous stirring and reacted for 12 h at room temperature. Furthermore, hydrogen peroxide (H_2O_2, 30 wt%), by which mercaptan groups can be converted to sulfonic groups, was dropped into fresh MPTMS sols with a sol/H_2O_2 mass ratio of 1/0.2 to obtain the oxidized sols under constant stirring for overnight. All chemicals were used without further purification.

According to the reported fabrication process of sulfonated MPTMS membrane, [31] two types of α-alumina particles (0.2 and 2 μm) dispersed in 2 wt% SiO_2-ZrO_2 sols were coated on the above-mentioned α-alumina tube, which was calcined at 550 °C for

15 min under air atmosphere to form the particle layer. Then, the particle layer was coated with 0.5 wt% SiO_2-ZrO_2 sols, followed by calcination at 550 °C for 15 min under air atmosphere, resulting in the intermediate layer with pore sizes close to 1 nm. Finally, the top separation layers were fabricated via coating oxidized MPTMS sols that were diluted to 1.0 wt% with ethanol on the SiO_2-ZrO_2 intermediate layer, and calcining at 300 °C for 20-30 min under a N_2 atmosphere.

6.3.2 Catalyst preparation

High-purity ultrafine magnesium powder (Ube materials), triruthenium dodecacarbonyl (Aldrich, 99%), tetrahydrofuran (anhydrous, ≥99.9%, Aldrich), cesium carbonate (Aldrich), and ethanol were used to prepare the catalyst. Fig. 6-S1 shows the catalyst preparation process. Briefly, magnesium powders were heated at 500 °C for 6 h under vacuum, then mixed with triruthenium dodecacarbonyl and tetrahydrofuran, followed by stirring at room temperature for 4 h. After that, the solvent was evaporated at 40 °C to obtain the powder. Then, the mixture was further heated to 450 °C for 2 h to decompose the carbonyl precursor and held for 3 h. Afterwards, cesium carbonate and the prepared powder were mixed and dissolved with ethanol, and the mixture was stirred at room temperature for 3 h. The solution was evaporated at 50 °C and dried under vacuum for 1 h to obtain Ru(10 wt%)/Cs/MgO catalyst. The prepared catalyst was H_2-reduced at operating temperature before use. More details of catalyst preparation can be found elsewhere. [39]

6.3.3 Gas permeation and recycle reaction experiment apparatus

Fig. 6-4 shows the experimental apparatus for evaluating membrane permeation and

NH_3 synthetic reaction combined with membrane separator. Industrial gases (He, H_2, NH_3, N_2, SF_6) were used as the feed gas. Ru (10 wt%)/Cs/MgO catalyst (total weight 10.0~11.7 g) was packed with quartz wool inside a SUS tube (inner diameter: 21.6 mm, thickness: 2 mm, length: 500 mm, 350 mm), which can be regard as a packed bed reactor with relatively large surface area (heat-transfer) compared to catalytic volume and a small conversion (~1%) reasonably make heat effect negligible. This implies a negligible thermal effect for exothermic NH_3 synthesis reactions in laboratory-scale. In the recycle experiment, the reactor was connected to the membrane module, and the gases in the retentate stream of the membrane were recycled to the inlet of the reactor using a recycle compressor (type: N828ANE, KNF Japan). The maximum pressure for the recycling reaction was set at 0.2 MPa-a due to the limitation of pressure resistance of the recycle compressor.

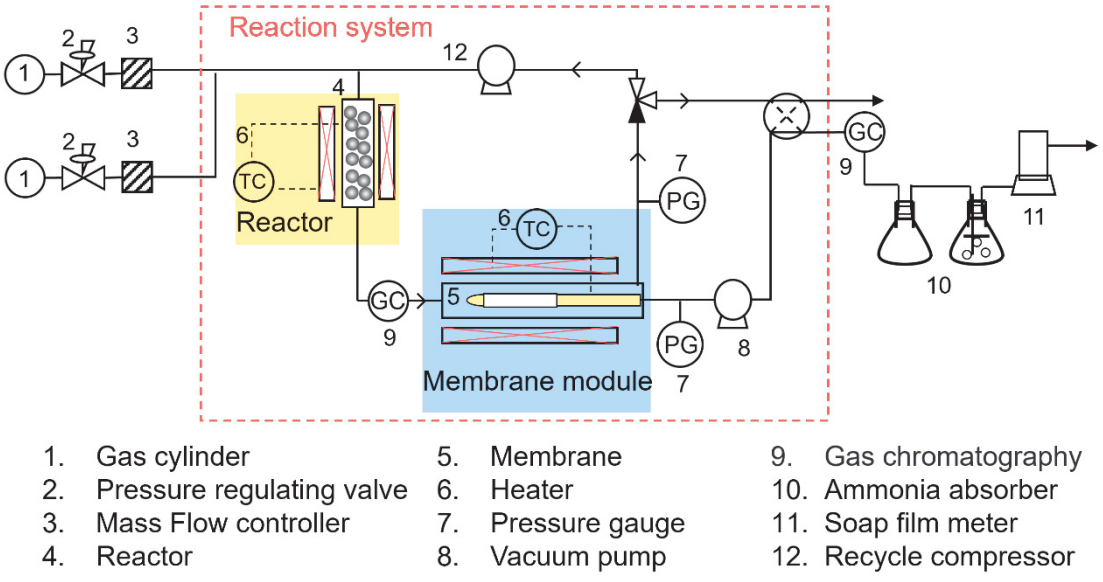

Fig. 6-4. Schematic diagram of the experimental apparatus.

6.3.3.1 Evaluation of gas permeation

For gas permeation experiments, the gas was supplied at 200 kPa-a from the outside

(upstream) of the membrane in a cylindrical module, while the inside (downstream) of the membrane was kept at atmospheric pressure. The cell temperature in the membrane was controlled at 5 to 200 °C, and a chiller for open circuit (COOLNIT CL-80R, TAITEC, Japan) is used when the desired temperature is below room temperature. The permeate flow rate of single component except NH_3 was measured using a soap film meter, while NH_3 permeate flow rate was measured using a calibrated mass flow controller by closing the retentate valve and allowing all feed to permeate.

6.3.3.2 Evaluation of plug flow reactor

For the evaluation of reaction characteristics, the temperature of the reactor was controlled at 300-400 °C and the flow rates of H_2 and N_2 were adjusted by the mass flow controller. The composition at the reactor-out was analyzed by two gas chromatographs (GC-1: Porapack N, temp. 100 °C; GC-2: Molecular Seive X, temp. 100 °C) using Ar as a carrier gas. NH_3 concentration was analyzed by GC-1, while H_2 and N_2 concentrations were analyzed by GC-2. Based on the obtained compositions and the flow rate of the reactor-in and the reactor-out, the conversion (X) was obtained using the following equation, Eq. (8).

$$X=\frac{F_{R,N_2,0}-F_{R,N_2,L}}{F_{R,N_2,0}} \quad \text{Eq. (8)}$$

For the characterization of the reaction, the operating variables were pressure (0.2~0.6 MPa-a), feed flow rate (20~100 ml/min), and ratio of feed flow rate (H_2/N_2=1/3, 1/1, 3/1). The conversion was measured for each operating variable.

6.3.3.3 Evaluation of membrane reactor with recycle flow

For the recycle membrane reactor, the reactor was controlled at 350 °C and 0.2 MPa-

a. The temperature of the membrane module was controlled at 25~100 °C, and the feed pressure was set at 200 kPa-a while the permeate stream was evacuated to an absolute pressure of 5~10 kPa-a using a vacuum pump (mini diaphragm vacuum pump, type: N810, KNF Japan). The composition at the reactor-out (membrane-in) and at the permeate stream of the membrane were analyzed by a GC, and the permeate flow rate was measured with a soap film meter after NH_3 removal by a water trap. NH_3 yield was calculated based on the following equations (Eqs. (9) and (10)), which is based on atomic balance of H_2 and N_2. Material balance of total system, based on fresh feed and membrane permeate flow, was within the maximum error of less than 10%.

$$\text{N based: } Y_N = \frac{Q_{NH_3}}{2Q_{N_2} + Q_{NH_3}} \quad \text{Eq. (9)}$$

$$\text{H based: } Y_H = \frac{3Q_{NH_3}}{2Q_{H_2} + 3Q_{NH_3}} \quad \text{Eq. (10)}$$

6.4 Results and discussion

6.4.1 Single gas permeation of membranes and performance of catalyst

Fig. 6-5 shows the temperature dependence of NH_3, H_2, and N_2 permeance for recently reported Aquivion and sulfonated MPTMS membranes. Although both Aquivion and sulfonated MPTMS contain sulfonic acid groups (-SO_3H) with acid-base interaction for NH_3, NH_3 permeance in Aquivion membrane decreased with increasing temperature while the opposite for sulfonated MPTMS membrane. [30,31] NH_3 permeance of both membranes was higher than H_2 and N_2 permeances at 5-200 °C, which can be ascribed to the fact that the acid functional group (-SO_3H) can act as an adsorption site for basic NH_3, namely adsorption-diffusion mechanism.

Moreover, NH_3 permeance was about 1.2-0.8×10^{-6} mol/(m^2 s Pa) at 5-150 °C for

Aquivion membrane, which is almost an order of magnitude higher than sulfonated MPTMS membrane. This could be due to the thicker separation layer (~900 nm) of sulfonated MPTMS membrane and a dense structure caused by the flexible propyl chains. [31] At low temperature, both membranes showed excellent NH_3 selectivity because H_2 and N_2 permeances follow an activation-diffusion and greatly decreased with decreasing temperature. Especially at 5 °C, NH_3 permeance of Aquivion membrane is 2.74×10^{-6} mol/(m^2 s Pa) with NH_3/N_2 selectivity of 2240, indicating superior NH_3 permeation performance. The performance of the two membranes approximate to those reported previously, [30,31] which can further confirm the reproducibility of the two membranes. For the simulation of the recycle reaction, the permeance obtained by regressing with the experimental results as a reference was used at each membrane temperature.

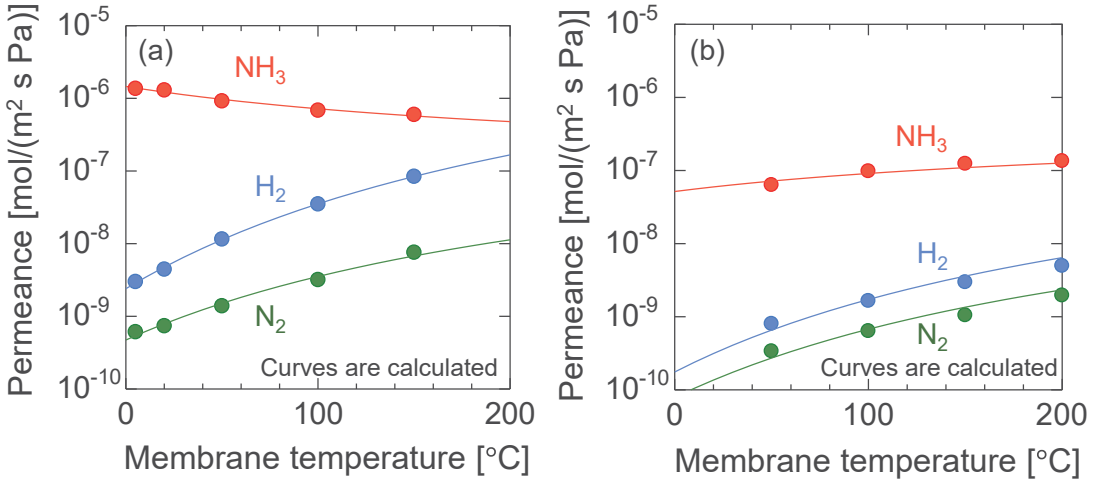

Fig. 6-5. Temperature dependence of gas permeance for Aquivion membrane (a) and sulfonated MPTMS membrane (b). Curves in the figure are calculated as shown in SI-2. The errors of the gas flowrates were less than 5% when the permeance exceeds 10^{-10} mol m^{-2} s^{-1} Pa^{-1} and less than 50% while a the permeance is below 10^{-10} mol m^{-2} s^{-1} Pa^{-1}.

Fig. 6-6 shows the conversion as a variable of reaction temperature using Ru(10

wt%)/Cs/MgO catalyst by considering heat balance at 300-400 °C. Ru-based catalysts, which are active at low temperature, were able to synthesize ammonia at temperatures below Haber-Bosch temperature (450-600 °C). Due to the limited activity of the catalyst, it exhibited very low ammonia conversion at 300 °C. As the temperature rises from 300 to 360 °C, the ammonia conversion gradually increased, reaching an equilibrium conversion at 360 °C. Above 360 °C, the reaction conversion decreased owing to the thermodynamics equilibrium limitation. Consequently, considering the reaction conversion and the applicable temperature of the catalyst in this study, the temperature of the reactor was set to 350 °C.

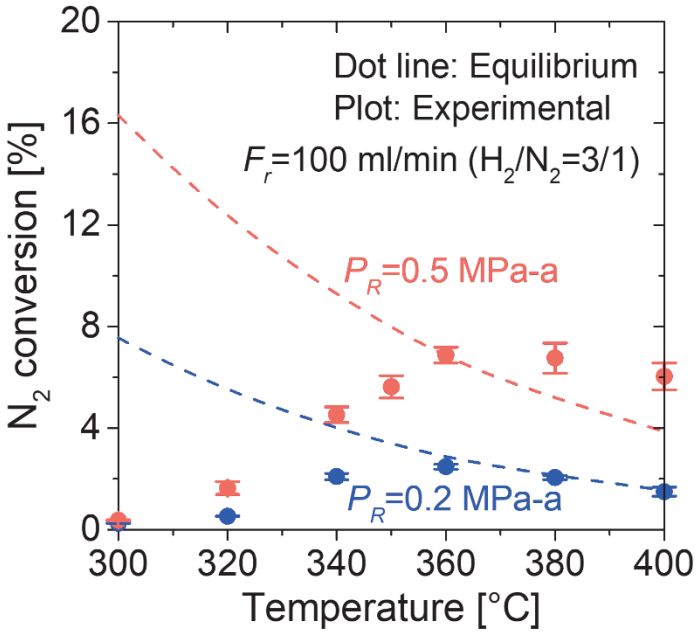

Fig. 6-6. Conversion as a function of reaction temperature. (P_R= 0.5 and 0.2 MPa-a, F_r=100 ml/min, H_2/N_2=3/1, and m_{cat}= 10 g)

Fig. 6-7 shows N_2 conversion as a function of reaction pressure, feed flow rate, and feed flow ratio of H_2/N_2. The higher the reaction pressure, the higher N_2 conversion, due to the mole number reduction toward to synthesis ammonia side, following Le Chatelier's principle. As the feed flow rate increased, N_2 conversion gradually decreased

because the residence time of the gas in the reactor decreased. N_2 conversion based on N_2 flow rate (Eq. (8)) obviously increased as the feed flow ratio of H_2/N_2. Based on experimental measurement values, the reaction rate equation of Eq. (1) can be fitted as in SI-3 in detail. Additionally, in order to explore the effect of H_2/N_2 ratio on reaction in detail, as the reaction rate (NH_3 production) and N_2 conversion as a function of H_2 mole ratio via simulation in a packed bed reactor shown in Fig. 6-7 (d). When H_2 mole ratio is around 0 (no H_2), the reaction rate is almost 0, that is, no reaction. The reaction rate and N_2 conversion increased with increasing H_2 mole ratio, the optimal H_2 mole ratio is around 0.85-0.95 although it's higher than 0.75 (3/1) of stoichiometric H_2/N_2 ratio. Further increasing H_2 mole ratio will decrease the reaction rate for the synthetic NH_3 reaction, which could be attributed to the increase in the partial pressure of H_2 promotes H_2 bonding but reduces the number of sites available for N_2 activation.

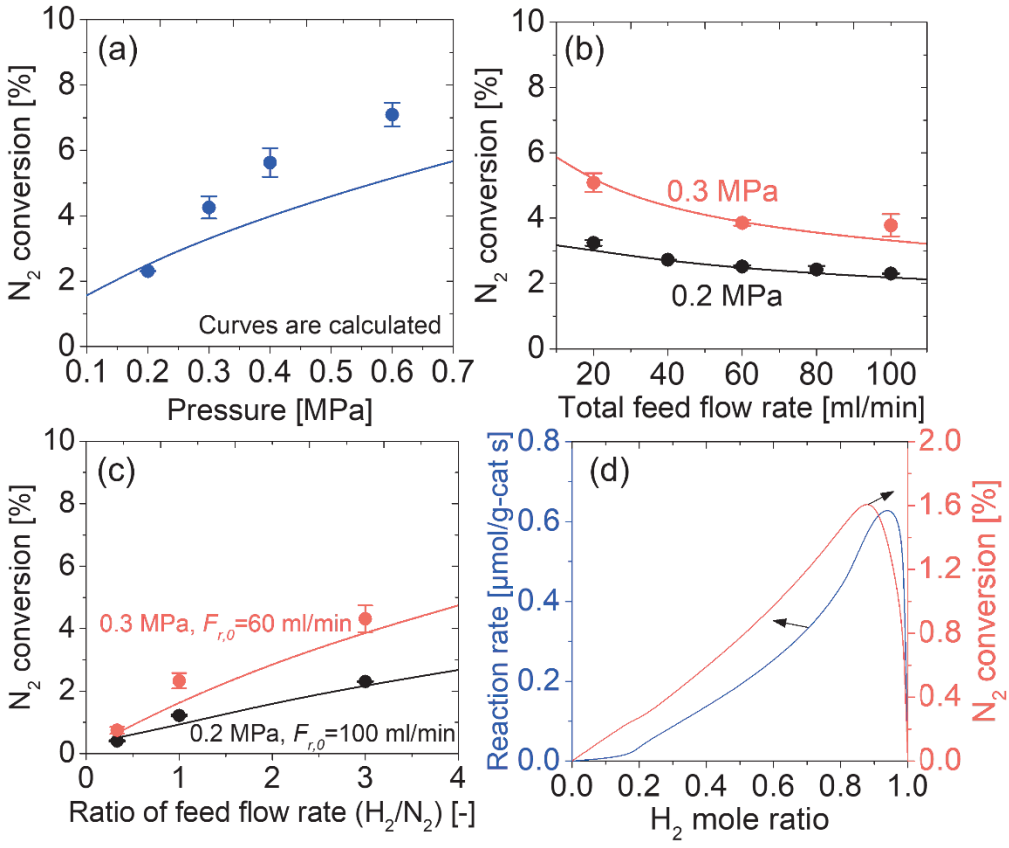

Fig. 6-7. Experimental N_2 conversion (a, b, and c) as a function of pressure, total feed flow rate, and ratio of feed flow rate (T_R=350 °C and m_{cat}= 10 g); theoretical reaction rate and N_2 conversion (d) as a function of H_2 mole ratio (T_R=350 °C, $\boldsymbol{P_R}$=0.3 MPa-a, $\boldsymbol{F_R}$=1000 ml/min and m_{cat}= 10 g).
(a) Pressure dependence: P_R=0.2~0.6 MPa-a, F_R=100 ml/min, H_2/N_2=3/1;
(b) Feed flow rate dependence: P_R= 0.2 and 0.3 MPa-a, F_R=20~100 ml/min, H_2/N_2=3/1;
(c) Ratio of feed flow rate dependence: P_R= 0.2 and 0.3 MPa-a, F_R=60 and 100 ml/min, H_2/N_2=3/1, 1/1, and 1/3.

Fig. 6-8 shows the NH_3 composition at the reactor-out as a function of Da at 0.2 MPa-a that is the pressure evaluated in the membrane and reactor. Da corresponds to the reaction rate in relation to the feed flow rate. When Da is large, meaning that the feed flow rate decreases or the amount of catalyst increases, the NH_3 composition at the reactor outlet increases because the residence time in the reactor increases and the amount of NH_3 produced increases. The NH_3 composition increases rapidly for Da=1~3, and the NH_3 composition is close to the equilibrium composition (mole fraction 0.016) for $Da \geq 5$. The experimental data are in reasonable agreement with the calculated value.

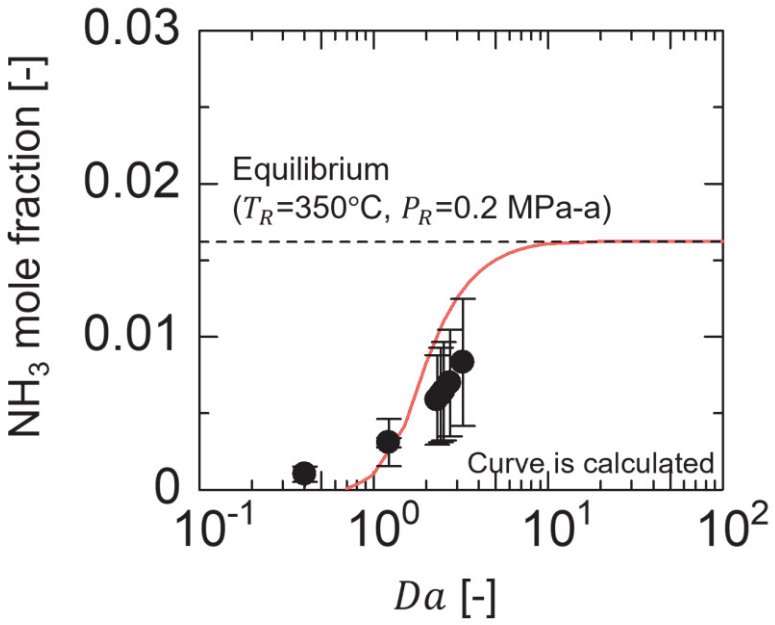

Fig. 6-8. Effect of Da on NH_3 mole fraction of reactor-in and reactor-out. (T_R=350 °C and P_R=0.2 MPa-a).

Notably, the errors in the experimental data shown above should be reasonable, which could be mainly ascribed to the errors from the GC analysis, the temperature profile along the reactor furnace (the temperature of the center was measured/controlled), and slight fluctuations in the reaction stream. According to the results, therefore, a steady reaction system and effective NH_3 conversion can be achieved, which are beneficial for further developing the recycle membrane reactor.

6.4.2 Reactor and membrane without recycle

Fig. 6-9 show the time course for a reactor combined with membrane (without recycle) at different feed flow rate (400-1200 ml/min) and the reactor temperature kept at 350 °C using Aquivion membranes. NH_3 generated in the reactor is preferentially recovered in the permeate stream of the NH_3 selective membrane. The component recovery (permeate flow rate with respect to the feed flow rate to the membrane of NH_3, H_2,

and N_2) was the highest for NH_3, reaching up to about 40%, while they were in the low single digits for H_2 and N_2. Additionally, an increase in the feed flow rate resulted in a decrease in the NH_3 composition. This decrease can be attributed to the reduction in NH_3 production caused by the decrease in gas residence time in the reactor as the feed flow rate increases. Furthermore, the increase in unreacted H_2 and N_2 feed flow rates led to an increase in the composition of H_2 and N_2. The NH_3 recovery also decreased based on the same reasons. NH_3 mole fraction and recovery at the total flow rate of 400 ml/min before and after the feed flow-swing were almost consistent, which indicates that the membrane performance is stable and reproducible.

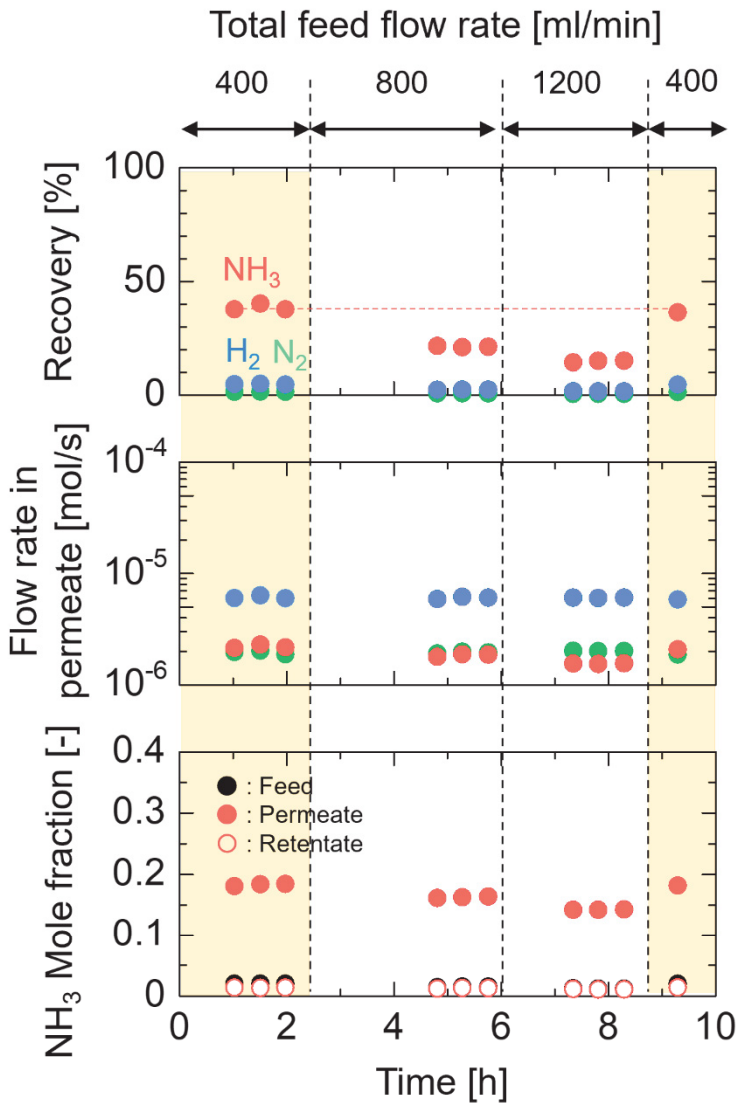

Fig. 6-9. Time course for a reactor and membrane without recycle under different feed total flow rate (F_t). (Aquivion membrane).
H_2/N_2=1/1, F_t=400~1200 ml/min, T_R=350 °C, P_R=0.3 MPa-a, T_M=25 °C, L_M=0.1 m, $p_{M,u}/p_{M,d}$= 300/30 kPa-a.

Based on the time course shown in Fig. 6-9, Fig. 6-10 summaries the recovery, NH_3 flow rate in membrane-in, and NH_3 mole fraction (feed and permeate) as a function of total feed flow rate for Aquivion membrane. The experimental NH_3 production rates and component recovery are in good agreement with simulation using Eqs. (1)-(3), which indicates that basic equations are effective for predicting the reactor/membrane-

combined system.

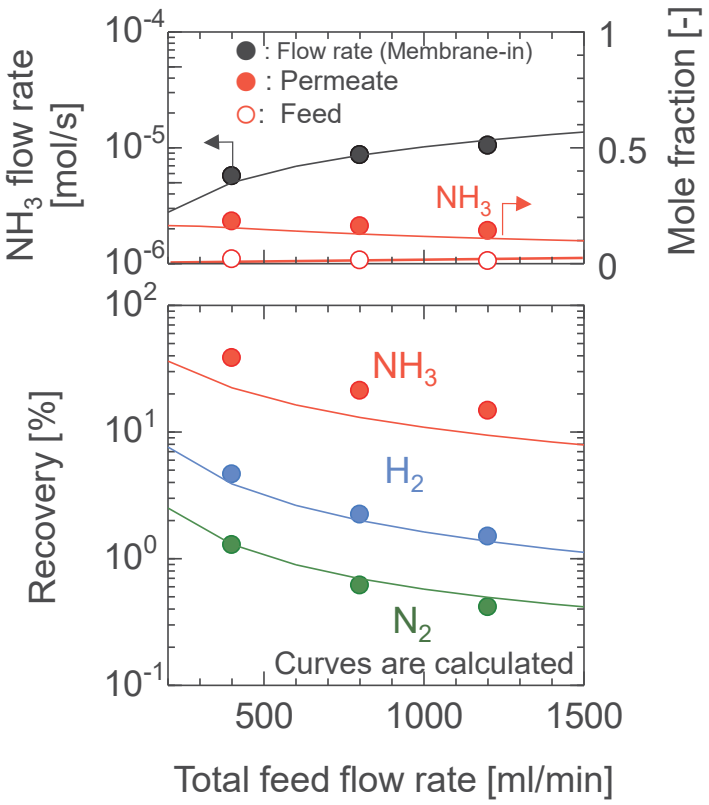

Fig. 6-10. Effect of total feed flow rate on Recovery, flow rate in membrane-in, and mole fraction of reactor-out and permeate for Aquivion membrane without recycle. Time course of the experiment is showed in Fig. 6-9 and each point is the calculated average of the data for each feed flow rate in Fig. 6-9.

6.4.3 Recycle membrane reactor

Figs. 6-11 (a) and (b) show the time course of recycle membrane reactor process with different membrane temperatures (25-100 °C) and the fixed reactor temperature of 350 °C for Aquivion and oxidized MPTMS membranes. This experiment was started by feeding only N_2 and recycling, and then it was confirmed that N_2 flow rate in permeate was stabilized. Subsequently, H_2/N_2 mixed gas with feed flow ratio of H_2/N_2 = 3/1 was supplied and the flow rate was controlled so that the feed-side pressure would reach the target pressure (0.2 MPa-a). Since H_2 preferentially permeates through the

membrane, it was difficult to control the concentration of reactor inlet due to the transient state after changing the feed gas from pure N_2 to H_2/N_2 mixture, so that different compositions were reached as a pseudo-steady-state in the initial state of membrane temperature change.

The NH_3 composition at the reactor-out was about 0.017, which is close to the equilibrium composition at 0.2 MPa-a and a reactor temperature of 350 °C. According to single H_2, N_2, and NH_3 permeation properties (Fig. 6-5), their permeate flow rates decreased with decreasing membrane temperature but NH_3 selectivity increased, resulting in NH_3 mole fraction in the permeate increased using both Aquivion and sulfonated MPTMS membranes. In addition, NH_3 mole fraction in the permeate is about 0.2-0.4 in the system of sulfonated MPTMS membrane surpass than that of Aquivion membrane (0.1-0.2). This could be ascribed to the low permeate flow rate of sulfonated MPTMS membrane, which leads to low recovery and high NH_3 concentration along the membrane from the inlet to outlet. Due to the increase in permeate NH_3 composition, NH_3 yields also increased relative to H_2 and N_2 on a permeation flow basis (Eq. (10)). Since H_2 permeates more preferentially than N_2, the yield defined by the membrane permeate composition is lower for H_2 than for N_2. Permeate flow rate in feeding only N_2 was similar before and after the long-term reaction using H_2 and N_2 mixed gases. The stability of the membrane performance was confirmed by checking N_2 flow rate before and after NH_3 production.

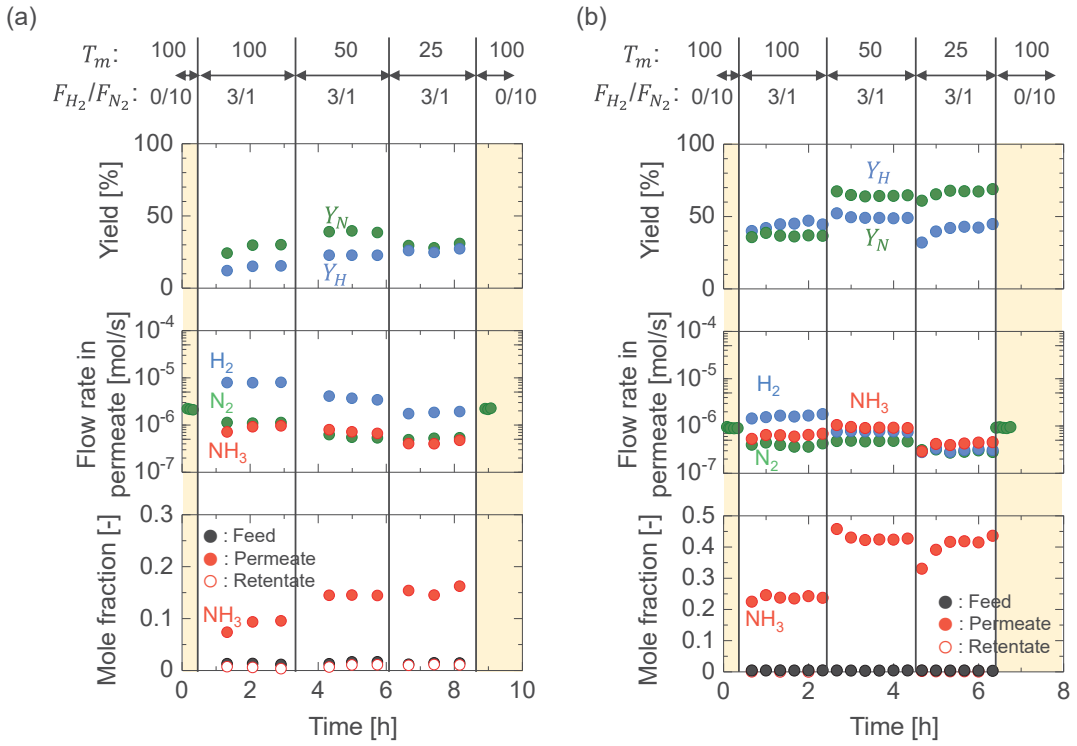

Fig. 6-11. Time course of recycle reaction under different membrane temperatures (T_M). (Aquivion membrane (a) and sulfonated MPTMS membrane (b)).

T_R=350 °C, P_R=0.2 MPa-a, R=250 ml/min, T_M=25~100 °C, L_M=0.05 m, $p_{M,u}/p_{M,d}$= 200/5 kPa-a.

A mathematical model was used to simulate recycle membrane reactor for NH_3 production, which focuses on understanding the effect of membrane temperature on permeate flow rate and mole fraction of each gas in reactor-out and permeate side. Comparing experimental and simulation results, Fig. 6-12 (a) shows the permeate flow rate and the composition of the reactor-out (membrane-in) and permeate as a function of membrane temperature for Aquivion membrane. With increasing membrane temperature, the H_2 permeate flow rate and composition increased. On the other hand, the NH_3 flow rate in permeate showed a little change because the composition of NH_3 produced was approximately 0.017 in relation to the total flow rate fed to the membrane. After an unsteady period during the transient operation, the measured H_2 compositions of the

reactor-out were 0.64 at 25 °C, 0.57 at 50 °C, and 0.42 at 100 °C, corresponding to H_2/N_2=1.42, 1.37, and 1.01, respectively. Simulations were performed based on the actual measured compositions in the reactor-out, and the simulated flow rate in permeate and compositions of each gas are shown with the solid curves in Fig. 6-12, which are in good agreement with the measured values. Fig. 6-12 (b) shows the case of oxidized MPTMS membrane. NH_3 mole fraction in permeate side was very much concentrated up to ~0.4 from low feed concentration of approximately 0.01 due to low permeance and low recovery. Although NH_3 permeance for oxidized MPTMS membrane increased with increasing membrane temperature, as opposed to that of Aquivion membrane, the permeate NH_3 molar fraction decreased using both membranes because NH_3 selectivity decreased with increasing membrane temperature. The simulated curves showed a reasonable agreement with experimental results, confirming a successful mathematical model.

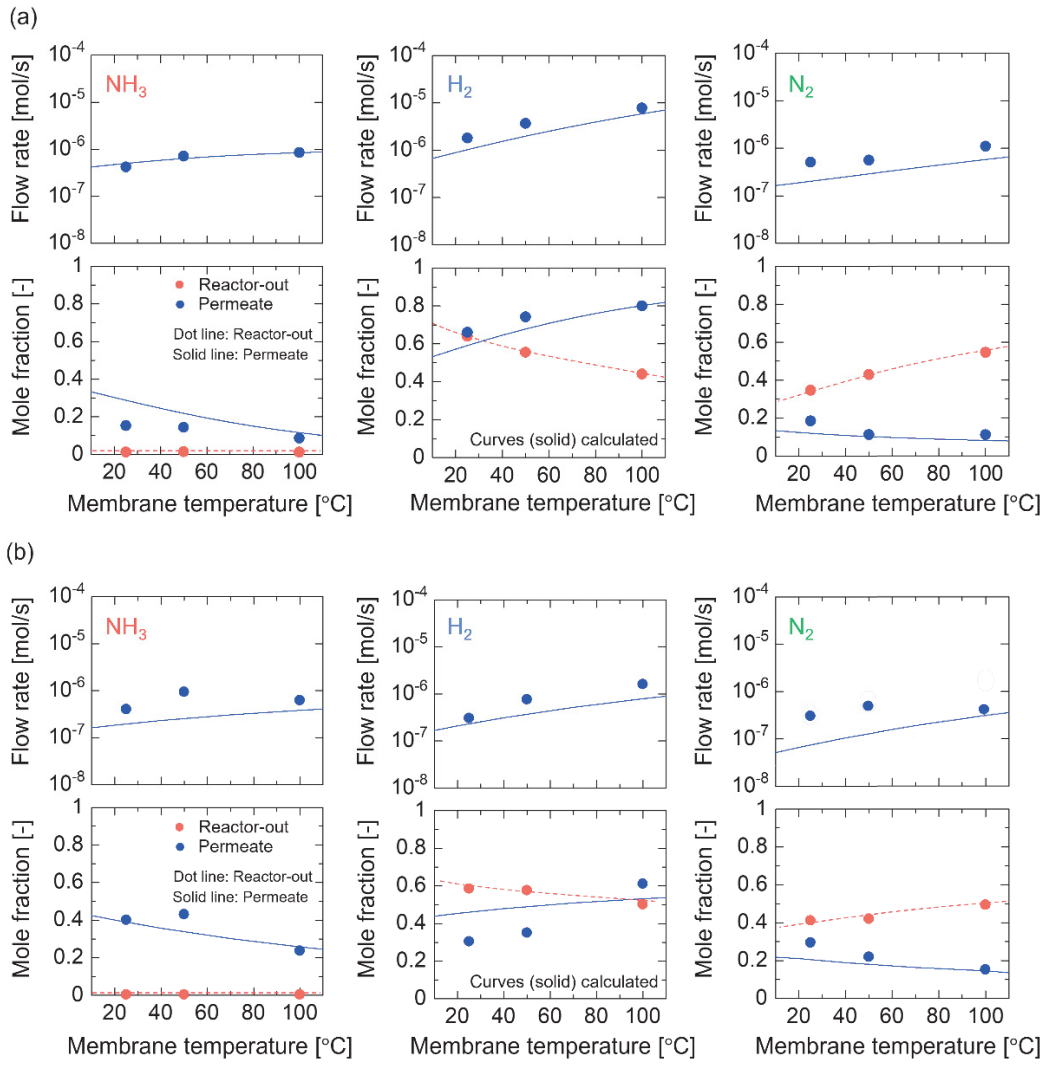

Fig. 6-12. Effect of membrane temperature on permeate flow and mole fraction of reactor-out and permeate in recycle membrane reactor: ((a) Aquivion membrane (top) and (b) sulfonated MPTMS membrane (bottom)), and each point is the calculated average of the data at each membrane temperature in Fig. 6-11.

Although the simulation results based on a mathematical model approximate the experimental results of recycle membrane reactor, several suggestions are provided for a deeper understanding of the error between simulation and experiment. First, because the activity of the catalyst currently used was still low, that is, the NH_3 conversion was only ~1%, so low NH_3 content is easy to cause large analysis errors even using GC; second, the fluctuation of membrane permeability with temperature and time; third, the assumptions in mathematical models can also cause errors between the experimental

and simulated results. Simulation results that are as close as possible to experimental results are also more conducive to using mathematical models to deeply understand the nature of the recycle membrane reactor.

6.4.4 Simulation for Green ammonia process

Wang et al. [40] proposed an electrosynthetic ammonia with a BCY15 membrane at 530 °C and atmospheric pressure. Recently, Zhang et al. [37] used a mathematical model to simulate and analyze the performance of catalytic membrane reactor with an inorganic membrane and reported that the membrane performance having NH_3/H_2 selectivity of > 4 and NH_3/N_2 selectivity of > 10 with high NH_3 permeance of ~3.4×10^{-7} mol m^{-2} s^{-1} Pa^{-1} (1000 GPU) was required to improve NH_3 production using membrane reactor. Padinjarekutt et al. reported a Na^+-gated nanochannel membrane [41] with superior NH_3/H_2 selectivity as high as 4280 and NH_3/N_2 selectivity > 10000 at 250 °C and 35 bar. The conclusion suggested that the membrane separation by replacing condensation process in HB process shows a decrease > 80% energy consumption and ~20% NH_3 production cost. [36]

As far as the authors ascertain, there is no experimental report on the recovery and recycle of ammonia produced in the reactor combined with the membrane. The recycle membrane reactor, where the catalytic reaction and the membrane separation occur in a separated equipment, cannot shift the equilibrium in the in-situ reaction system as in the catalytic membrane reactor where reaction and separation occur in one unit. However, recycle reaction can improve the overall reaction conversion and is an effective means when the reaction and separation conditions are limited. In order to reduce the

pressure of the recycle reaction from the conventional Haber-Bosch process (450 °C, 20-40 MPa) to lower pressure (1 MPa), our initial strategy is to perform lab-scale simulation and evaluate the composition and flow rate of membrane permeation.

As schematically shown in Fig. 6-2, the simulation was carried out for green ammonia production using all parameters of reactor and membrane listed in Table 6-2. The produced NH_3 is concentrated in membrane permeate, after compressing the permeate stream, NH_3 can be recovered and liquefied with a compressor and heat-exchanger. Unreacted H_2 and N_2 are recycled to the reactor together with the retentate stream (Fig. 6-2), meaning that all the inlet H_2 and N_2 as fresh feed can be converted to NH_3, that is, the whole recovery of H_2 and N_2 as NH_3 is 100%.

Table 6-2. Membrane and reactor parameters for a simulation of the theoretical system.

Membrane	Temperature: T_M	T_M=50 °C
	Pressure: $p_{M,u}/p_{M,d}$	$p_{M,u}/p_{M,d}$=200/5 kPa-a
	Permeance: P_i	P_{NH_3}=9.69×10^{-7} mol/(m^2 s Pa)
		P_{H_2}=1.13×10^{-8} mol/(m^2 s Pa)
		P_{N_2}=1.51×10^{-9} mol/(m^2 s Pa)
Reactor	Temperature: T_R	T_R=350 °C
	Pressure: P_R	P_R=0.2 MPa-a
	Reaction: Da	Equilibrium (Da=∞)

Fig. 6-13 shows the simulated flow rate (feed, permeate) and composition with membrane length (i.e. membrane area) as a variable. Notably, the flow rate to the membrane module, which corresponds to the reactor-out (membrane-in) in Fig. 6-2, is constant at 250 ml/min in the simulations. The permeate flow rates of H_2 and N_2, which occupy most composition of the reactor-out, gradually increased as the membrane length increases. On the other hand, the produced NH_3 composition at the reactor-out is set at 1%, that is the equilibrium NH_3 composition in the reactor (350 °C, 0.2 MPa-a,

H_2/N_2=3/1), and the permeate NH_3 flow rate is limited by the produced NH_3 flow rate, that is, the feed NH_3 flow rate to the membrane module.

Moreover, the mole fraction of H_2 and N_2 in permeate increased as the membrane length increases, while NH_3 rapidly decreases because NH_3 flow rate and amount to the membrane is limited (due to the low NH_3 composition of 0.017 in equilibrium conversion). As the membrane length (i.e. membrane area) increases, the membrane recovery ($\bar{Q}$, permeate flow rate to membrane feed flow rate) increases because the permeate flow rate increases, but the recycle ratio ($\bar{R}$, recycle flow rate to fresh feed flow rate) decreases because the retentate flow rate decreases. Comparing the different recycle flow ratios of H_2/N_2 in Figs. 6-13 (a) and (b), when H_2/N_2=1, N_2 feed and permeate flow rate as well as its mole fraction in the permeate are all increased, but the decrease in NH_3 mole fraction in the permeate is due to the decrease in NH_3 conversion.

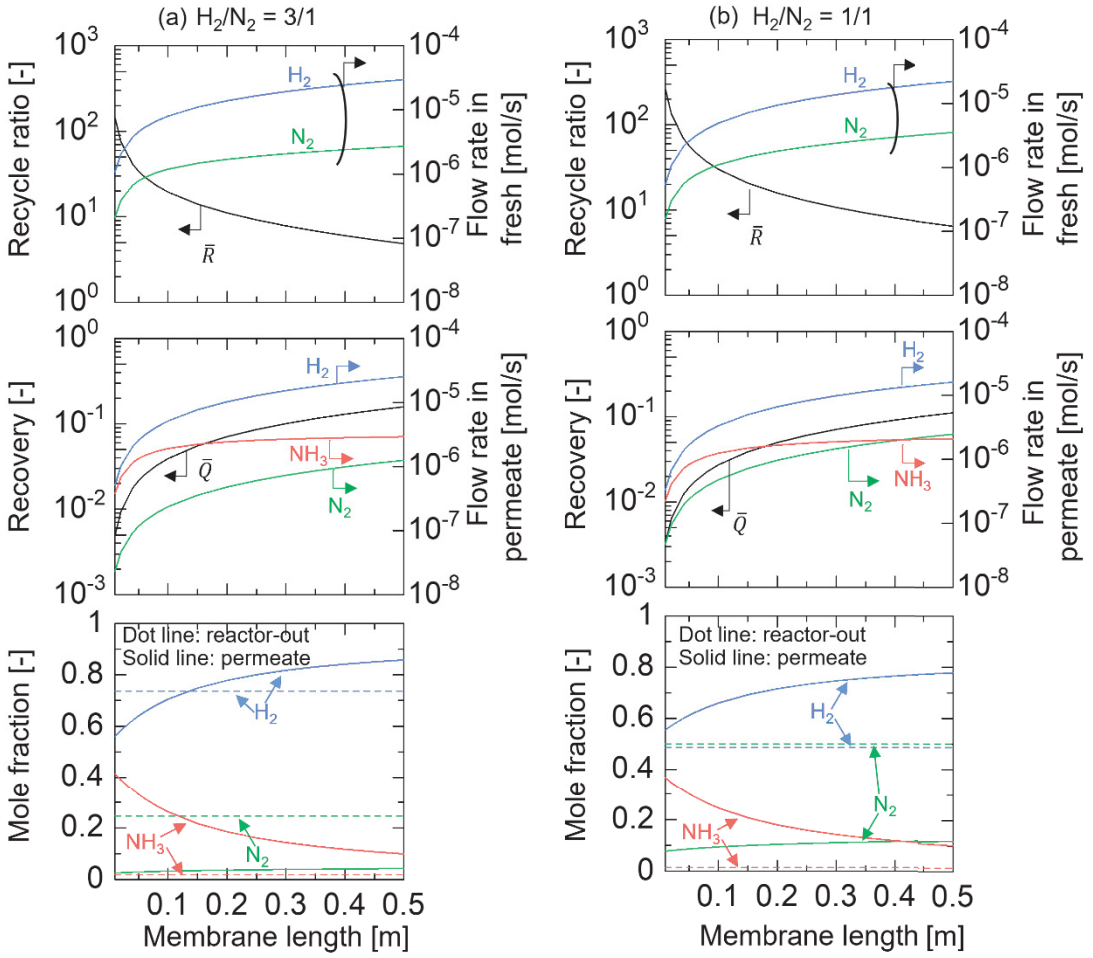

Fig. 6-13. Simulation of mole fraction, recovery, and recycle parameters as a function of membrane length. H_2/N_2=3/1 (a) and H_2/N_2=1/1 (b).
T_R=350 °C, P_R=0.2 MPa-a, $F_{M,total}$=250 ml/min, T_M=50 °C, L_M=0.01~0.5 m, $p_{M,u}/p_{M,d}$=200/5 kPa-a.

As one of the most important properties of membranes, the effect of NH_3 selectivity on molar fraction, recovery, and recycle parameters is explained in SI-5. High NH_3 selectivity can increase NH_3 composition in the permeate and promote the recycle ratio while decrease the recovery ratio.

Fig. 6-14 shows the simulations of flow rate (feed, permeate) and composition with feed pressure as a variable. When the feed pressure (the reactor pressure and the feed pressure of the membrane) increase from 0.1 to 1.0 MPa, the NH_3 mole fraction in permeate increases from 0.1 to 0.5 due to the increase in NH_3 equilibrium concentration

from the reactor. Furthermore, as the reaction pressure increases, the flow rate in permeate increases because the driving pressure required for permeation also increases. In addition, the membrane recovery gradually increased and the recycle ratio become smaller due to the increased permeate flow rate and decreased retentate flow rate.

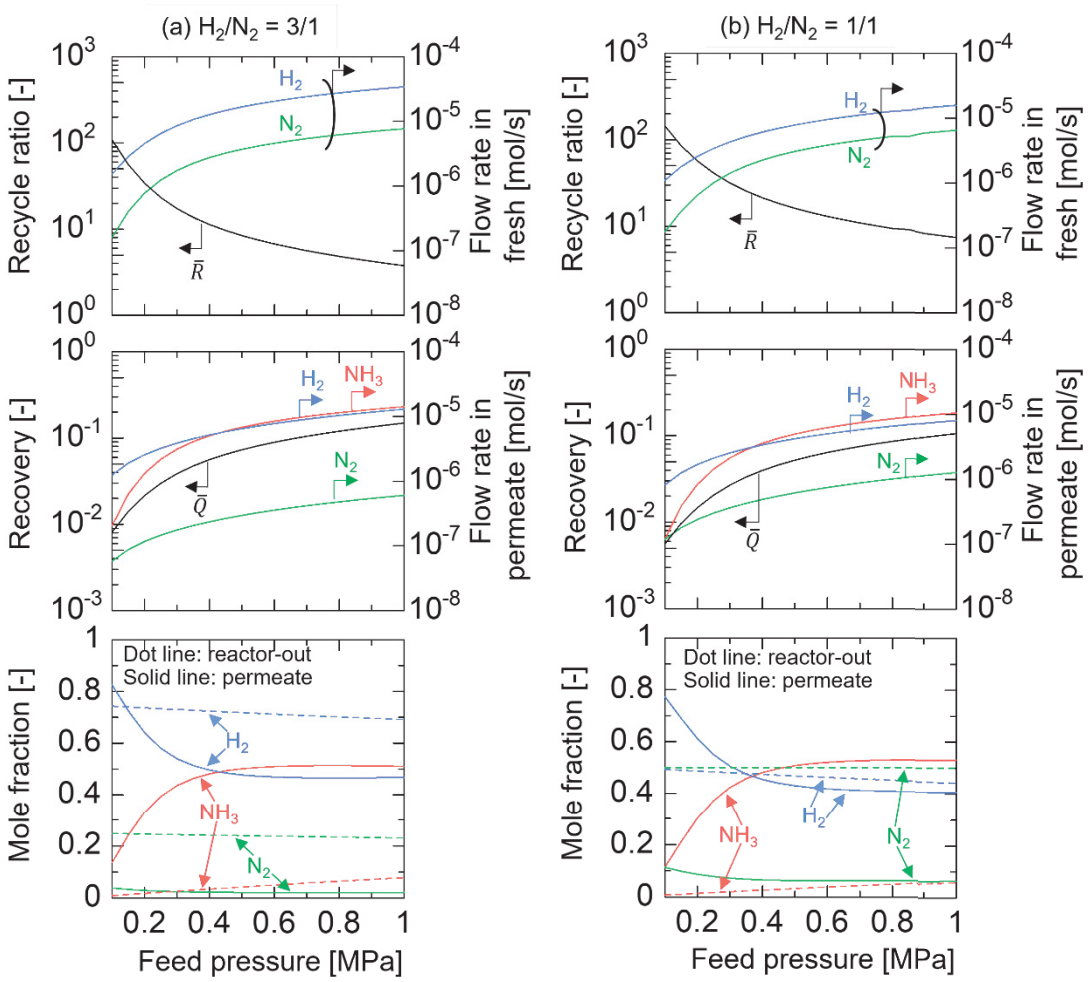

Fig. 6-14. Simulation of mole fraction, recovery, and recycle parameters as a function of feed pressure dependence. H_2/N_2=3/1 (a) and H_2/N_2=1/1 (b). T_R=350 °C, P_R=0.1~1.0 MPa-a, $F_{M,total}$=250 ml/min, T_M=50°C, L_M=0.05, $p_{M,u}/p_{M,d}$=100~1000/5 kPa-a.

The flow ratio of H_2/N_2 in the recycle ($F_{H_2,recycle}/F_{N_2,recycle}$) can be regarded as a variable as shown in Figs. 6-13 (a) and (b) as well as Figs. 6-14 (a) and (b). As the feed flow ratio of H_2/N_2 in the system changes, the H_2 and N_2 compositions at the reactor-

out are seriously affected, resulting in the different H_2 (or N_2) partial pressure difference and the H_2 (or N_2) permeate flow rates. Although the simulations of feed rate, flow rate in permeate, permeate composition, and dimensionless number showed a similar trend despite a change in the recycle flow ratio of H_2/N_2, NH_3 flow rate and mole fraction in permeate decrease mildly.

Fig. 6-15 shows the simulation of flow rate (feed, permeate), recovery, and composition as a function of the feed flow rate to the membrane. Increasing the feed flow rate to the membrane increases the retentate flow rate, while the permeate flow rate is approximately unchanged, which is determined by the membrane performance and operating condition, such as pressure. As the feed flow rate gradually increases from 100 to 400 ml/min, the NH_3 permeate flow rate increases when the equilibrium composition from the reactor outlet is assumed to be constant. However, the NH_3 permeate flow rate increases a little with further the increase in feed flow rate, while the permeate flow rates of H_2 and N_2 remain constant. The NH_3 permeate flow rate increases gradually as the feed flow rate increases from 100 to 400 ml/min, and then all gas flow rates are basically close to constant with further increasing the feed flow rate to 1000 ml/min. Therefore, the recycle ratio increases because the recycle flow rate (retentate flow rate) increases.

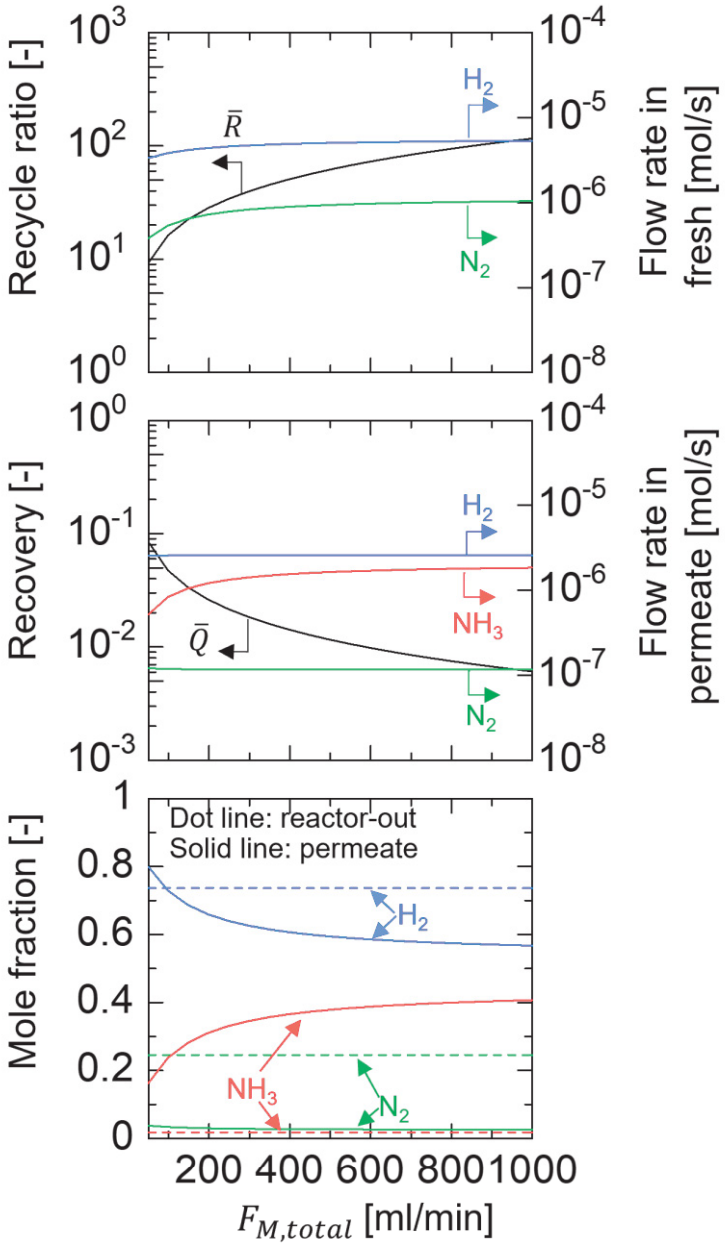

Fig. 6-15. Simulation of flow rate (feed, permeate), recovery, and composition as a function of the feed flow rate to membrane.
H_2/N_2=3/1, T_R =350 °C, P_R =0.2 MPa-a, $F_{M,total}$ =50~1000 ml/min, T_M =50 °C, L_M=0.05 m, $p_{M,u}/p_{M,d}$=200/5 kPa-a.

To generalize recycle membrane reactor for green NH_3 production, we have attempted to summarize reactor performance in dimensionless expression. Fig. 6-16 shows simulated requirement energy, recycle ratio, and compositions with θ as a variable. θ is a dimensionless number that serves as a measure of membrane performance,

and a large θ is achieved by a large membrane area or length, a high permeance, or a low feed flow rate. The NH_3 composition at the reactor outlet is again assumed to be in equilibrium at 0.017 at 0.2 MPa-a in Fig. 6-16 (a) and 0.078 at 1.0 MPa-a in Fig. 6-16 (b). As the θ increases, the H_2 mole fraction in permeate increases and the NH_3 mole fraction decreases because the H_2 permeate flow rate through membrane increases a lot. Since the most permeable NH_3 preferentially permeate at low θ, that is, the low recovery via membrane, then H_2 as the second permeable component gradually permeate through the membrane at high recovery.

The NH_3 composition on the permeate side increases to 0.87 at 1.0 MPa-a in Fig. 6-16 (b), indicating that NH_3 enrichment at high concentrations is possible even at 1.0 MPa-a, which is quite low pressure compared with the conventional Haber-Bosch process. The recycle ratio becomes smaller as the θ increases because the retentate flow rate decreases as the permeate flow rate increases. As the feed pressure increases, the recycle ratio becomes smaller because the permeate flow rate increases as shown in Figs. 6-14 (a) and (b). Importantly, the permeate NH_3 can be concentrated up to 0.5 in mole fraction. When the permeate stream is pressurized to 1.0 MPa, NH_3 partial pressure is 0.5 MPa, which means that NH_3 can be liquified at 0 °C because the saturated vapor pressure of NH_3 at 0 °C is ~0.4 MPa. For NH_3 mole fraction of 0.8, NH_3 condenses at 20 °C. This is a great advantage of recycling reaction with membranes, implying that liquid NH_3 can be obtained even at 1 MPa for reaction system and 25 °C for NH_3 liquefaction.

Under the present assumption (equilibrium composition in reactor-out), low θ

which accompanies large recycle flow is preferable for achieve the high concentration of NH_3. Therefore, energy requirement is also calculated by considering the circulating energy of retentate stream (from retentate to reactor-in) and the compressing energy of permeate stream (from permeate to reactor-in). The details can be found in SI-6. Notably, when the stream from the retentate side of the membrane is circulated to the reactor without any energy-loss (R_1 (0%)), the requirement energy of the system increases with the θ increases, regardless of pressure. However, the assumption of energy-loss for recycling should be more realistic, and 10% and 20% pressure drop along reactor and membrane module are assumed and indicated as R_1 (10%) and R_1 (20%), respectively. The energy consumption for NH_3 production shows the minimum values around 50-80 kJ/mol-NH_3, which is around 10% of the energy consumption for conventional Haber-Bosch process (9-15 MWh/t-NH_3, that is 550-920 kJ/mole-NH_3).

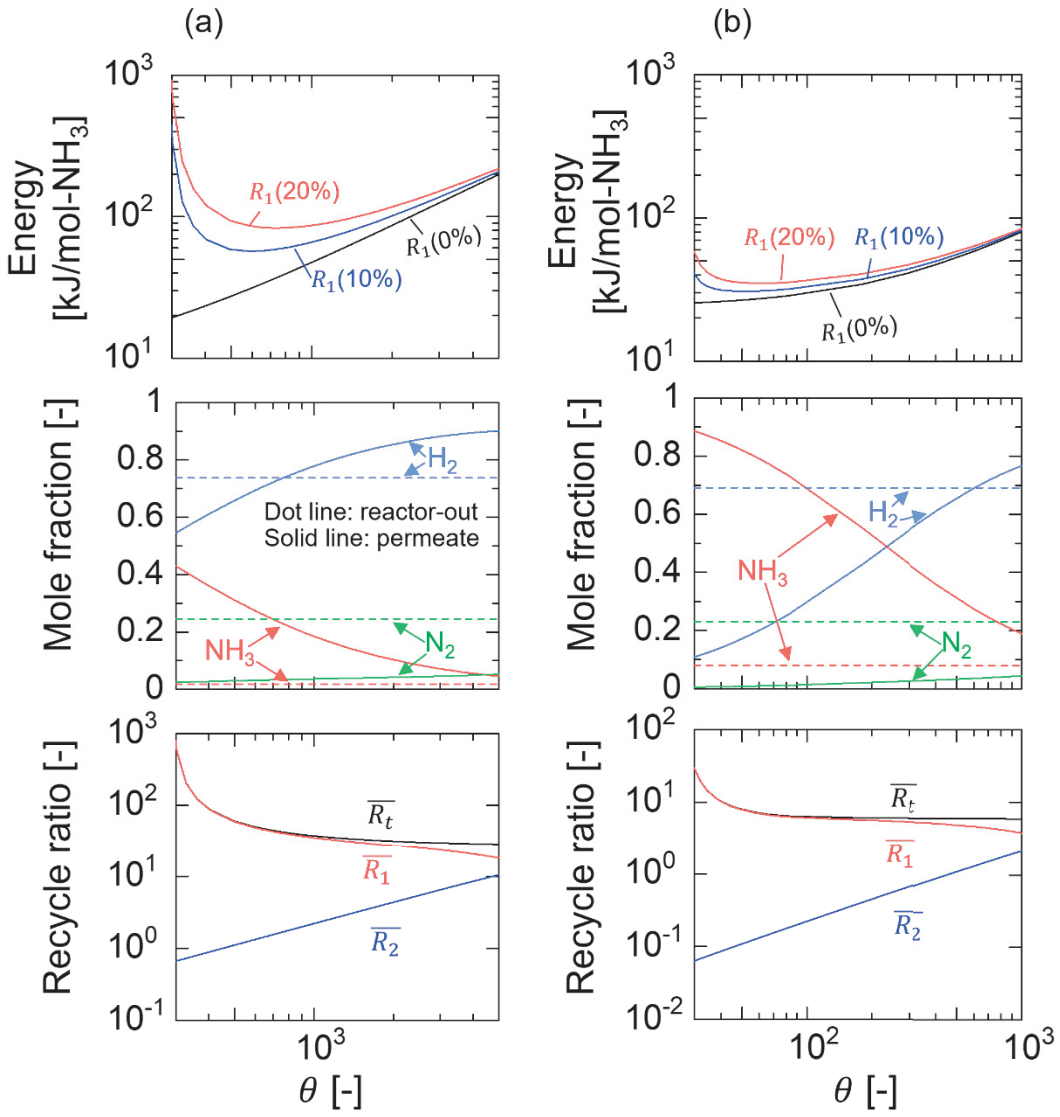

Fig. 6-16. Simulation of permeation number dependence.
(a) P_R=0.2 MPa-a, $p_{M,u}/p_{M,d}$=200/5 kPa-a
(b) P_R=1.0 MPa-a, $p_{M,u}/p_{M,d}$=1000/5 kPa-a
H_2/N_2=3/1, T_R=350 °C, $F_{M,total}$=250 ml/min, T_M=50 °C, L_M=0.05 m
$R_1 = \frac{\sum R_{i,1}}{F_{H_2}+F_{N_2}}$, $R_2 = \frac{\sum R_{i,2}}{F_{H_2}+F_{N_2}}$, $R_t = R_1 + R_2$

Figs. 6-17 (a) and (b) show the effect of NH_3 selectivity (α=NH_3/H_2) on the recycle ratio and NH_3 compositions with $\boldsymbol{\theta}$ as a variable on permeation number for feed-side pressure of 1 MPa and permeate-side pressure of 100 kPa and 5 kPa, respectively. Generally, NH_3 molar fraction increases with NH_3 selectivity of the membrane, and the increase in NH_3 selectivity of the membrane also results in less H_2 and N_2 permeate

flow rate and an increase in the recycle ratio. However, both recycle ratio and NH_3 compositions gently decrease with the $\boldsymbol{\theta}$ increases due to the increase in permeate flow rate especially for H_2 and N_2. Importantly, when using a high-selective membrane, 1 MPa and 100 kPa for feed and permeate sides, respectively, are feasible to produce high concentration of NH_3 under low energy consumption.

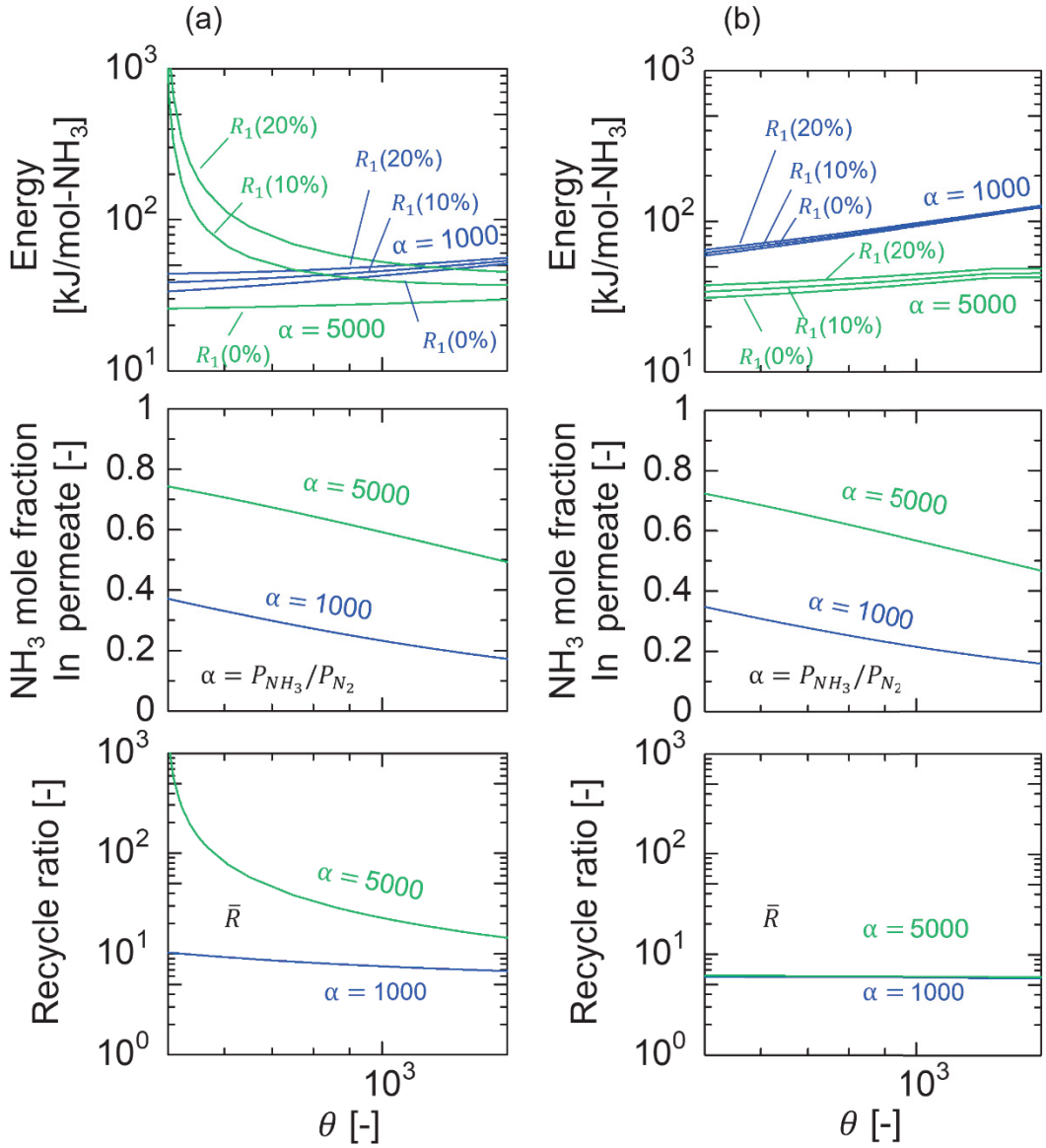

Fig. 6-17. Simulation of permeation number dependence.
(a) $p_{M,u}/p_{M,d}$=1000/100 kPa-a, (b) $p_{M,u}/p_{M,d}$=1000/5 kPa-a;
H_2/N_2=3/1, T_R=350 °C, P_R=1.0 MPa-a, P_{NH_3}=1.0×10^{-6} mol/(m^2 s Pa), P_{H_2}/P_{N_2}=10, $F_{M,total}$=250 ml/min, L_M=0.05 m.

6.5 Conclusions

Herein, a green NH_3 production system using a recycle membrane reactor was proposed and carried out, namely reactor combined with membrane separator with recycle flow, which enables the temperature of reactor and membrane separator controlled independently. The Ru (10 wt%)/Cs/MgO catalyst and two membranes with different permeation properties and NH_3 selectivity (Aquivion/ceramic composite and sulfonated MPTMS membranes) were used to produce NH_3 and selectively extract the synthesized NH_3 from feed side to permeate side. Importantly, NH_3 mole fraction was greatly increased from 0.01 of equilibrium state to 0.1-0.45 of permeate side, which is ascribed to the gas permeance and NH_3 selectivity of membrane at different temperatures. Furthermore, a one-dimensional, isothermal, and plug-flow model was proposed to simulate this system and compared with experiments. Ultimately, a mathematical model was successfully developed and applied to green NH_3 production under mild conditions, and NH_3 mole fraction, recovery, and recycle parameters as a function of membrane length, feed pressure, and feed flow rate, respectively, were systematically studied.

Notation

(1) Reaction rate:

r_{NH_3}: Reaction rate [μmol/(g-cat s)]

P_i: Pressure [bar]

θ: Surface coverage for free sites, $\theta = \left(1 + \frac{P_{NH_3}}{P_{H_2}^{1.5} K_a} + \frac{P_{H_2}^{0.5}}{K_b}\right)^{-1}$

(2) Reaction rate constant:

$N_s K_1 k_2$: [μmol/(g-cat s bar)]

K_{eq}: [bar^{-1}]

K_a: [bar$^{-0.5}$]

K_b: [bar$^{-0.5}$]

(3) Flow rate:

$F_{R,i,0}$: Feed flow rate (in) [mol/s]

$F_{R,i}$: Feed flow rate in reactor [mol/s]

$F_{M,i}$: Feed flow rate in membrane [mol/s]

R_1: Recycle flow rate from retentate stream [mol/s]

R_2: Recycle flow rate from cooler [mol/s]

Q_i: Permeate flow rate [mol/s]

$F_{recyle,i}$: Recycle flow rate [mol/s]

(4) Reactor:

T_R: Reactor temperature [°C]

P_R: Reactor pressure [MPa]

r_{NH_3}: Reaction rate [mol/(g s)]

v_i: Stoichiometric coefficient [-]

m'_{cat}: Catalyst weight per unit reactor axial length [g/m]

L_R: Reactor length [m]

z_R: Reactor axial coordinate [m]

(5) Membrane:

T_M: Membrane temperature [°C]

$p_{M,u}$: Membrane upside pressure [kPa]

$p_{M,d}$: Membrane downside pressure [kPa]

P_i: Permeance [mol/(m^2 s Pa)]

L_M: Membrane length [m]

z_M: Membrane axial coordinate [m]

s: Membrane area per unit membrane axial length [m^2/m]

α_i: NH_3 selectivity (NH_3/H_2, NH_3/N_2) [-]

β: Pressure ratio [-]

x: Mole fraction in feed side [-]

y: Mole fraction in permeate side [-]

References

[1] J.W. Erisman, M.A. Sutton, J. Galloway, Z. Klimont, W. Winiwarter, How a century of ammonia synthesis changed the world, *Nat. Geosci.* 1 (2010) 636-639.

[2] J. Humphreys, R. Lan, S. Tao, Development and recent progress on ammonia synthesis catalysts for Haber-Bosch process, *Adv. Energy Sustainability Res.* 2 (2021) 2000043.

[3] M. Blois, The industrialization of the Haber-Bosch process, *C&EN* 101 (2023) 20-21. DOI: 10.1021/cen-10126-cover2.

[4] Global ammonia annual production capacity, https://www.statista.com/statistics/1065865/ammonia-production-capacity-globally/.

[5] A.I. Amhamed, S. Shuibul Qarnain, S. Hewlett, A. Sodiq, Y. Abdellatif, R.J. Isaifan, O. Fawwaz Alrebei, Ammonia production plants—A review, *Fuels* 3 (2022) 408-435. https://doi.org/10.3390/fuels3030026.

[6] S. Chatterjee, R.K. Parsapur, K.W. Huang, Limitations of ammonia as a hydrogen energy carrier for the transportation sector, *ACS Energy Letters* 6 (2021) 4390-4394.

[7] Y. Kojima, M. Yamaguchi, Ammonia as a hydrogen energy carrier, *Int. J Hydrogen Energ.* 47 (2022) 22832-22839.

[8] R. Javaid, H. Matsumoto, T. Nanba, Influence of reaction conditions and promoting role of ammonia produced at higher temperature conditions in its synthesis process over Cs-Ru/MgO catalyst, *ChemistrySelect* 4 (2019) 2218-2224.

[9] A. Valera-Medina, F. Amer-Hatem, A.K. Azad, I.C. Dedoussi, M. de Joannon, R.X.

Fernandes, P. Glarborg, H. Hashemi, X. He, S. Mashruk, J. McGowan, C. Mounaim-Rouselle, A. Ortiz-Prado, A. Ortiz-Valera, I. Rossetti, B. Shu, M. Yehia, H. Xiao, M. Costa, Review on ammonia as a potential fuel: From synthesis to economics, *Energy Fuels* 35 (2021) 6964-7029.

[10] K. Machaj, J. Kupecki, Z. Malecha, A.W. Morawski, M. Skrzypkiewicz, M. Stanclik, M. Chorowski, Ammonia as a potential marine fuel: A review, *Energy Strategy Rev.* 44 (2022) 100926.

[11] S. Giddey, S.P.S. Badwal, C. Munnings, M. Dolan, Ammonia as a renewable energy transportation media, *ACS Sustainable Chem. Eng.* 5 (2017) 10231-10239.

[12] L. Li, Ammonia synthesis: A different route for N_2 activation on sub-nanometric Ru catalysts, *Chem* 8 (2022) 599-600.

[13] D. Wang, F. Loose, P.J. Chirik, R.R. Knowles, N−H bond formation in a manganese(V) nitride yields ammonia by light-driven proton-coupled electron transfer, *J. Am. Chem. Soc.* 141 (2019) 4795-4799.

[14] L. Forni, D. Molinari, I. Rossetti, N. Pernicone, Carbon-supported promoted Ru catalyst for ammonia synthesis, *Appl. Catal. A* 185 (1999), 269-275.

[15] B. C. McClaine, R. J. Davis, Importance of product readsorption during isotopic transient analysis of ammonia synthesis on Ba-promoted Ru/Ba*X* catalyst, *J. Catal.* 211 (2002) 379-386.

[16] Y.V. Larichev, B.L. Moroz, V.I. Zaikovskii, S.M. Yunusov, E.S. Kalyuzhnaya, V.B. Shur, V.I. Bukhtiyarov, XPS and TEM studies on the role of the support and alkali promoter in Ru/MgO and Ru-Cs^+/MgO catalysts for ammonia synthesis, *J. Phys.*

Chem. C 111 (2007) 9427-9436.

[17] L. Liu, X. Zhang, X. Ju, J. Feng, J. Wang, P. Chen, Ru nanoparticles on a Cs-loaded MgO superbase as highly efficient catalysts for ammonia synthesis, *Dalton Trans.* 50 (2021) 12074-12078.

[18] R. Javaid, T. Nanba, Stability of Cs/Ru/MgO catalyst for ammonia synthesis as a hydrogen and energy carrier, *Energies* 15 (2022) 3506. https://doi.org/10.3390/en15103506.

[19] Y.V. Larichev, Effect of Cs^+ Promoter in Ru/MgO Catalysts, *J. Phys. Chem. C* 115 (2011) 631-635.

[20] B.C. McClaine, R.J. Davis, Isotopic transient kinetic analysis of Cs-promoted Ru/MgO during ammonia synthesis, *J. Catal.* 210 (2002) 387-396.

[21] A. Yapicioglu, I. Dincer, A review on clean ammonia as a potential fuel for power generators, *Renew. Sust. Energ. Rev.* 103 (2019) 96-108.

[22] J. Sousa, W. Waiblinger, K.A. Friedrich, Techno-economic study of an electrolysis-based green ammonia production plant, *Ind. Eng. Chem. Res.* 61 (2022) 14515-14530.

[23] R. Lan, J.T.S. Irvine, S. Tao, Synthesis of ammonia directly from air and water at ambient temperature and pressure, *Sci. Rep.-UK* 3 (2013) 1145. DOI: 10.1038/srep01145.

[24] L. Paturzo, A. Basile, E. Drioli, High temperature membrane reactors and integrated membrane operations, *Rev. Chem. Eng.* 18 (2002) 511-552.

[25] T. Tsuru, K. Yamaguchi, T. Yoshioka, M. Asaeda, Methane steam reforming by

microporous catalytic membrane reactors, *AIChE J.* 50 (2004) 2794-2805.

[26] Y. Zhang, Z. Wu, Z. Hong, X. Gu, N. Xu, Hydrogen-selective zeolite membrane reactor for low temperature water gas shift reaction, *Chem. Eng. J.* 197 (2012) 314-321.

[27] L. Meng, X. Yu, T. Niimi, H. Nagasawa, M. Kanezashi, T. Yoshioka, T. Tsuru, Methylcyclohexane Dehydrogenation for hydrogen production via a bimodal catalytic membrane reactor, *AIChE J.* 61 (2015) 1628-1638.

[28] Z. Li, T.T. Tsotsis, Methanol synthesis in a high-pressure membrane reactor with liquid sweep, *J. Membrane Sci.* 570–571 (2019) 103–111.

[29] P. Rodriguez-Vega, A. Ateka, I. Kumakiri, H. Vicente, J. Ereña, A.T. Aguayo, J. Bilbao, Experimental implementation of a catalytic membrane reactor for the direct synthesis of DME from H_2+CO/CO_2, *Chem. Eng. Sci.* 234 (2021) 116396.

[30] K. Wakimoto, W.W. Yan, N. Moriyama, H. Nagasawa, M. Kanezashi, T. Tsuru, Ammonia permeation of fluorinated sulfonic acid polymer/ceramic composite membranes, *J. Membrane Sci.* 658 (2022) 120718.

[31] W.W. Yan, K. Wakimoto, N. Moriyama, H. Nagasawa, M. Kanezashi, T. Tsuru, Development of sulfonated (3-Mercaptopropyl)trimethoxysilane membranes with thermal stability and excellent NH_3 perm-selectivity at 300 °C, *J. Membrane Sci.* 696 (2024) 122535.

[32] M. Kanezashi, A. Yamamoto, T. Yoshioka, T. Tsuru, Characteristics of ammonia permeation through porous silica membranes, *AIChE J.* 56 (2010) 1204-1212.

[33] W.W. Yan, U. Anggarini, H.C. Bai, H. Nagasawa, M. Kanezashi, T. Tsuru,

Enhanced NH_3 permeation of bis[3-(trimethoxysilyl)propyl] amine membranes via coordination with metals, *J. Membrane Sci.* 678 (2023) 121665.

[34] W.W. Yan, U. Anggarini, K. Wakimoto, H.C. Bai, H. Nagasawa, M. Kanezashi, T. Tsuru, Optimization of Ni-amine coordination for improving NH_3 permeation through nickel-doped bis[3-(trimethoxysilyl)propyl] amine membranes, *Sep. Purif. Technol.* 326 (2023) 124809.

[35] Q. Wei, J.M. Lucero, J.M. Crawford, J. Douglas Way, C.A. Wolden, M.A. Carreon, Ammonia separation from N_2 and H_2 over LTA zeolitic imidazolate framework membranes, *J. Membrane Sci.* 623 (2021) 119078.

[36] S. Padinjarekutt, H. Li, S. Ren, P. Ramesh, F. Zhou, S. Li, G. Belfort, M. Yu, Na^+-gated nanochannel membrane for highly selective ammonia (NH_3) separation in the Haber-Bosch process, *Chem. Eng. J.* 454 (2023) 139998.

[37] Z. Zhang, J. Douglas Way, Colin A. Wolden, Design and operational considerations of catalytic membrane reactors for ammonia synthesis, *AIChE J.* 67 (2021) e17259.

[38] N. Moriyama, H. Nagasawa, M. Kanezashi, T. Tsuru, Improved performance of organosilica membranes for steam recovery at moderate-to-high temperatures via the use of a hydrothermally stable intermediate layer, *J. Membrane Sci.* 620 (2021)118895.

[39] M. Kitano, Y. Inoue, Y. Yamazaki, F. Hayashi, S. Kanbara, S. Matsuishi, T. Yokoyama, S.W. Kim, M. Hara, H. Hosono, Ammonia synthesis using a stable electride as an electron donor and reversible hydrogen store, *Nature Chem.* 4 (2012) 934-

940.

[40] W.B. Wang, X.B. Cao, W.J. Gao, F. Zhang, H.T. Wanga, G.L. Ma, Ammonia synthesis at atmospheric pressure using a reactor with thin solid electrolyte $BaCe_{0.85}Y_{0.15}O_{3-\alpha}$ membrane, *J. Membrane Sci.* 360 (2010) 397-403.

[41] S. Padinjarekutt, B. Sengupta, H. Li, K. Friedman, D. Behera, R. Lecaros, M. Yu, Synthesis of Na^{+}-gated nanochannel membranes for the ammonia (NH_3) separation, *J. Membrane Sci.* 674 (2023) 121512.

Supplementary Material

---------- **SI-1**: Dimensionless equation ----------

$$\frac{d(F_{R,i}/F_{N_2})}{d(z_R/L_R)}=\frac{v_i m'_{cat} r_{NH_3}}{F_{N_2}}=v_i Da\frac{r_{NH_3}}{r_{NH_3,0}}=v_i Da R^*_{NH_3}$$

$$\frac{d(F_{M,i}/F_{N_2})}{d(z_M/L_M)}=-\frac{P_i s L_M p_{M,u,i}}{F_{N_2}}(x_i-\beta y_i)=-\theta(x_i-\beta y_i)$$

--------- **SI-2**: The calculated permeances for the simulation of recycle reaction ---------

The activation energy ($E_{P,i}$) of H_2, N_2, and NH_3 permeation was calculated as following equations by the regression of permeance (P_i) as a function of temperature (T) based on the modified gas translation (m-GT) model [1-3].

$$P_i=\frac{k_{0,i}}{\sqrt{M_i RT}}\exp\left(-\frac{E_{P,i}}{RT}\right)$$

$$k_{0,i}=k_0\left(d_p-d_i\right)^3$$

P_i: permeance of the i-th component; M_i: molecular weight of the i-th component; R: gas constant; $E_{P,i}$: activation energy of permeation of the i-th component; k_0: structural constant; d_p: pore diameter; d_i: diameter of the i-th component.

---------- **SI-3**: Reaction rate constant after corrections (Fitting parameters) ----------

Reaction rate constant after corrections (Fitting parameters):

$$2N_s K_1 k_2=1.56\times10^3\left(-\frac{6.60\times10^3}{RT}\right)$$

$$K_{eq}=2.03\times10^{-12}\left(\frac{1.01\times10^{5}}{RT}\right)$$

$$K_{a}=2.73\times10^{-2}\left(-\frac{2.71\times10^{4}}{RT}\right)$$

$$K_{b}=2.16\times10^{3}\left(-\frac{4.80\times10^{4}}{RT}\right)$$

---------- **SI-4**: Catalyst preparation process ----------

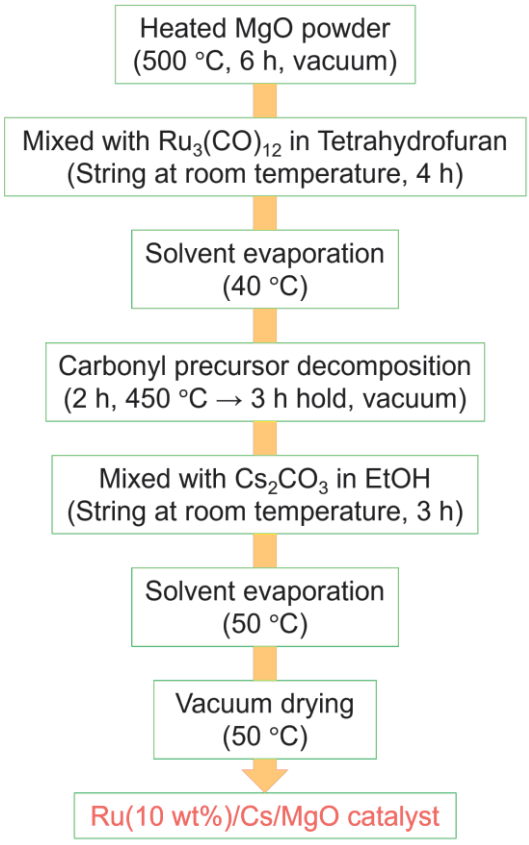

Fig. 6-S1. Catalyst preparation process.

---------- **SI-5**: Simulation of NH_3 selectivity dependence ----------

Fig. 6-S2 shows the simulation of flow rate (feed, permeate) and composition with NH_3 selectivity as a variable. The higher the NH_3 selectivity, the larger the NH_3

composition in the permeate, while the H_2 and N_2 compositions decrease due to the decrease in their flow rates in permeate. The membrane recovery ratio also decreases due to the decrease in the H_2 and N_2 flow rates in permeate, and the recycle ratio increases due to the decrease in the feed flow rate of the raw material.

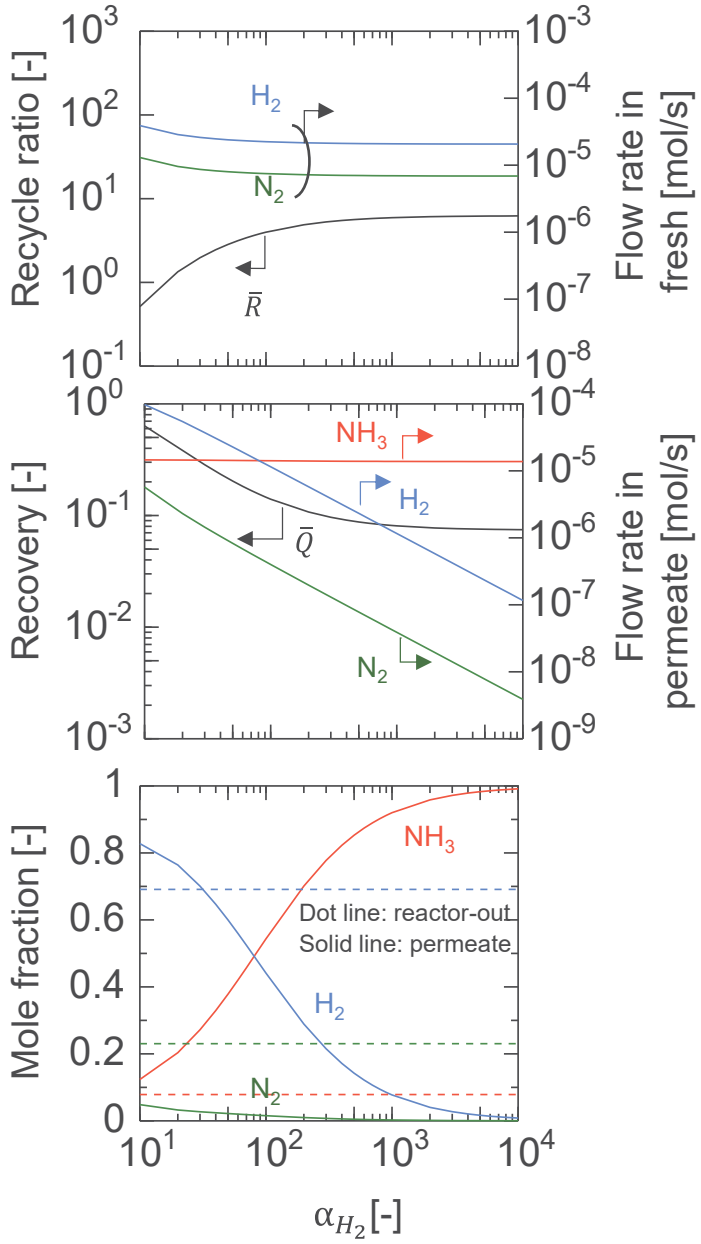

Fig. 6-S2. Simulation of NH_3 selectivity dependence.
H_2/N_2=3/1, T_R=350 °C, P_R=0.2 MPa-a, $F_{M,total}$=250 ml/min, T_M=50 °C, L_M=0.05 m, $p_{M,u}/p_{M,d}$=200/5 kPa-a, $P_{NH_3}=1.0\times10^{-6}$ mol/(m^2 s Pa), P_{H_2}/P_{N_2}=10

---------- **SI-6**: Equation of energy requirement calculation ----------

$$E = \frac{Q_F W_R + R_1 W_M + R_2 W_C}{Q_{NH_3}}$$

$$W_R = RT_R \ln \frac{P_R}{P_F} \qquad (P_R = 1.0,\ P_F = 0.1)$$

$$W_M = RT_M \ln \frac{P_{M,u,t}}{\gamma \times P_{M,u,t}} \qquad (P_{M,u,t} = 0.2,\ 1.0;\ P_{M,d,t} = 0.005;\ \gamma = 0.8,\ 0.9,\ 1.0)$$

$$W_C = RT_M \ln \frac{P_{M,u,t}}{P_{M,d,t}}$$

E: Energy per mol of NH_3 production (kJ/mol-NH_3), W_R: Compressed energy of fresh feed, W_M: Circulating energy of retentate stream (from retentate to reactor-in), W_C: Compressing energy of permeate stream (from permeate to reactor-in), γ: Pressure loss. $R_1 = \sum R_{i,1}$: Retentate flow rate; $R_2 = \sum R_{i,2}$: Permeate flow rate.

References

[1] T. Yoshioka, M. Kanezashi, T. Tsuru. Micropore size estimation on gas separation membranes: A study in experimental and molecular dynamics. *AIChE J.*, 59 (2013) 2179-2194.

[2] M. Kanezashi, T. Sasaki, H. Tawarayama, H. Nagasawa, T. Yoshioka, K. Ito, T. Tsuru, Experimental and theoretical study on small gas permeation properties through amorphous silica membranes fabricated at different temperatures. *J. Phys. Chem. C* 118 (2014) 20323-20331.

[3] H.R. Lee, M. Kanezashi, Y. Shimomura, T. Yoshioka, T. Tsuru, Evaluation and fabrication of pore-size-tuned silica membranes with tetraethoxydimethyl disiloxane for gas separation, *AIChE J.* 57 (2011) 2755-2765.

Chapter 7

Conclusions and outlook

This dissertation focused on the development of novel organosilica membranes for NH_3 separation and their application for synthetic NH_3 catalytic membrane reactors. The microporous structure and surface chemistry caused by metal coordination and functional group transformation were scientifically evaluated through a series of characterizations. The NH_3 affinity and diffusion of the metal-doped aminosilica membranes and the sulfonated organosilica membranes were elaborately improved for enhancing the NH_3 separation performance from H_2 and N_2 at high temperatures. Consequently,

The present research highlights the fabrication of novel metal-doped and sulfonated organosilica membranes and their application of catalytic membrane reactors, which may pave the way for advanced NH_3 separation and NH_3 synthesis.

7.1 Conclusions

The main conclusions of each chapter in this thesis were summarized as follows:

[1] Bis[3-(trimethoxysilyl)propyl] amine (BTPA) membranes doped with different metals, including Fe, Ni, and Ag, were applied to evaluate the permeation properties of H_2, N_2, and NH_3. All metal-coordinated BTPA gels showed superior NH_3 adsorption and desorption capacity via NH_3 temperature-programmed desorption (NH_3-TPD), which benefits from the coordination between metal and NH_3. The single-gas permeation and activation energy of permeance were measured to evaluate NH_3 separation

performance, which occurred in the following rank: Ni-BTPA > Fe-BTPA > Ag-BTPA > BTPA. These results are consistent with NH_3-TPD data. The Ni-BTPA membrane showed NH_3 permeance at ~2.8×10^{-6} and ~1.5×10^{-6} mol m^{-2} s^{-1} Pa^{-1} with ideal NH_3/H_2 selectivities of 11 and 27, and NH_3/N_2 selectivities of 102 and 277 at 200 and 50 °C, respectively. Intermolecular interaction e

[2] With an increase in the amount of nickel doping in BTPA, the coordination between nickel and propylamines is enhanced, particularly for 1.00 Ni-BTPA, as shown by FT-IR and UV-vis analysis, resulting in a weakening of the coordination between *N-H* and *N=O* that originates with an acid-base interactions. For 1.00 Ni-BTPA, the strengthening coordination between nickel and *N-H* and the interparticle pore caused by the aggregation and/or segregation of nickel nanoparticles not only negatively affects the NH_3 affinity but also weakened the molecular sieving. The results from both NH_3-TPD and simulation prove that 0.50 Ni-BTPA has sufficient coordination sites and considerable interaction intensity with NH_3, which can effectively improve the NH_3 permselectivity by balancing molecular sieving (pore size) and membrane affinity. The optimal performance was obtained with 0.50 Ni-BTPA membrane, showing NH_3 permeance of ~2.8×10^{-6} mol m^{-2} s^{-1} Pa^{-1} with ideal NH_3/H_2 selectivity of 11 and NH_3/N_2 selectivity of 102 at 200 °C.

[3] The unoxidized (3-mercaptopropyl)trimethoxysilane (MPTMS) sols were prepared, and further oxidated by H_2O_2 to improve NH_3 affinity. FT-IR and XPS analyses showed that *S-H* groups can be completely oxidized to sulfonated groups via oxidizing sol solution with H_2O_2. The thermal stability of MPTMS xerogels with and without

oxidation was proven around 300 °C via TG-MS analysis. Furthermore, the xerogel powders were always maintained a dense structure using N_2 adsorption due to the flexible and stable propyl chains, independently of H_2O_2 oxidation. Compared with unoxidized MPTMS xerogels, the oxidated xerogels expressed an intense NH_3 affinity and a large NH_3 adsorption amounts because of the improved acidity and increased acidic sites to enhance acid-base interactions from NH_3-TPD results. For single and binary gas permeation, the oxidated MPTMS membranes showed an excellent NH_3/H_2 selectivity of 6 and NH_3/N_2 selectivity of 18 with an NH_3 permeance of ~1.4×10^{-7} mol m^{-2} s^{-1} Pa^{-1} at 300 °C. This can be ascribed to the efficiently selective adsorption on the top-separation layers and the effectual diffusion through membranes.

[4] 3-(trihydroxysilyl)-1-propanesulfonic acid (TPS) was diluted to 0.1 wt% with ethanol to fabricate sulfonic silica-based membranes. The thermal stability of -*SO_3H* groups and propyl chains was proven by FT-IR analysis of TPS films calcined from 100 to 350 °C, and the siloxane network structure was formed by the self-catalyzed condensation of silanol (*Si-OH*) with the intrinsically acidic -*SO_3H* groups, as the amorphous structure shown by XRD patterns. Because of the flexibility of propyl chains and/or the filling of pores by bulky sulfonic acid groups, TPS xerogel powders calcined at 300 °C still showed a dense structure via N_2 adsorption, which further confirmed the thermal properties combined with XPS measurement. Owing to the inherently stronger proton-acidic -*SO_3H* groups in TPS, an intensive NH_3 affinity for TPS (an NH_3 adsorption amount of ~3.0 mmol g^{-1}) was observed twice higher than oxidized MPTMS by NH_3-TPD. For single and binary gas permeation, TPS-EtOH membranes showed a superior

NH_3 permeance of ~2.6 and ~1.8×10^{-7} mol m^{-2} s^{-1} Pa^{-1} with an excellent NH_3/H_2 selectivity of 7 and 165, and NH_3/N_2 selectivity of 266 and 18700 at 300 and 50 °C, respectively.

[5] A green NH_3 production system using a recycle membrane reactor was proposed and carried out, namely reactor combined with membrane separator with recycle flow, which enables the temperature of reactor and membrane separator controlled independently. The Ru (10 wt%)/Cs/MgO catalyst and two membranes with different permeation properties and NH_3 selectivity (Aquivion/ceramic composite and sulfonated MPTMS membranes) were used to produce NH_3 and selectively extract the synthesized NH_3 from feed side to permeate side. Importantly, NH_3 mole fraction was greatly increased from 0.01 of equilibrium state to 0.1-0.45 of permeate side, which is ascribed to the gas permeance and NH_3 selectivity of membrane at different temperatures. Furthermore, a one-dimensional, isothermal, and plug-flow model was proposed to simulate this system and compared with experiments. Ultimately, a mathematical model was successfully developed and applied to green NH_3 production under mild conditions, and NH_3 mole fraction, recovery, and recycle parameters as a function of membrane length, feed pressure, and feed flow rate, respectively, were systematically studied.

7.2 Outlook

This dissertation has focused on selective NH_3 separation using metal-doped and sulfonic-containing organosilica membranes and green NH_3 production utilizing a recycle membrane reactor. Firstly, although the NH_3 affinity and diffusivity were greatly

enhanced by transition metal-doping and sulfonic group-introducing, the prepared NH_3 separation membranes were only used up to 300 °C due to the limited thermal properties of the propylamine chains and propyl mercaptan chains in organosilanes. The synergistic mechanism of molecular sieving and adsorption-diffusion of NH_3 was confirmed for organosilica membranes, however, high temperature is unfavorable to NH_3 selective permeation, especially NH_3/H_2 separation. The reason why we pay attention to NH_3 membrane separation at high temperatures is mainly because of the low activity of synthetic NH_3 catalyst at low temperature, which will limit the development of catalytic membrane reactors for NH_3 synthesis.

Based on the conclusions derived from this dissertation, the referential recommendations for future work are given as follows:

(1) Enhance the thermal stability of organosilica with high NH_3 affinity at 350 °C at least.

(2) Reasonable control of network aperture derived from organosilica with thermal stability. Organosilica membranes with denser structures can be tried.

(3) Improve NH_3 affinity strength and site, including the grafting of phosphate groups, carboxylic groups, and/or the doping of bimetal.

List of publications

Journal articles

[1] Kotaro Wakimoto,[#] **Wei-Wei Yan**,[#] Masashi Hattori, Michikazu Hara, Norihiro Moriyama, Hiroki Nagasawa, Masakoto Kanezashi, Toshinori Tsuru.* Green ammonia production via recycles membrane reactor: Experiment and process simulation, *Chemical Engineering Journal* **2024**, Accepted. ((#: Equal contribution)

[2] **Wei-Wei Yan**, Kotaro Wakimoto, Norihiro Moriyama, Hiroki Nagasawa, Masakoto Kanezashi, Toshinori Tsuru.* Fabrication of 3-(trihydroxysilyl)-1-propanesulfonic acid membranes with superior affinity and selectivity for NH_3 permeation over H_2 and N_2 at 50-300 °C. *Journal of Membrane Science* **2024**, 702, 122798.

[3] **Wei-Wei Yan**, Kotaro Wakimoto, Norihiro Moriyama, Hiroki Nagasawa, Masakoto Kanezashi, Toshinori Tsuru.* Development of sulfonated (3-Mercaptopropyl)trimethoxysilane membranes with thermal stability and excellent NH_3 permselectivity at 300 °C. *Journal of Membrane Science* **2024**, 696, 122535.

[4] **Wei-Wei Yan**, Ufafa Anggarini, Kotaro Wakimoto, Hong-Cun Bai, Hiroki Nagasawa, Masakoto Kanezashi, Toshinori Tsuru.* Optimization of Ni-amine coordination for improving NH_3 permeation through nickel-doped bis[3-(trimethoxysilyl)propyl] amine membranes. *Separation and Purification Technology* **2023**, 326, 124809.

[5] **Wei-Wei Yan**, Ufafa Anggarini, Hong-Cun Bai, Hiroki Nagasawa, Masakoto Kanezashi, Toshinori Tsuru.* Enhanced NH_3 permeation of bis[3-(trimethoxysilyl)propyl] amine membranes via coordination with metals. *Journal of Membrane Science* **2023**, 678, 121665.

[6] Kotaro Wakimoto, **Wei-Wei Yan**, Norihiro Moriyama, Hiroki Nagasawa, Masakoto Kanezashi, Toshinori Tsuru.* Ammonia permeation of fluorinated sulfonic acid polymer/ceramic composite membranes. *Journal of Membrane Science* **2022**, 658, 120718.

Patent

[1] ヤンエイエイ，森山教洋，金指正言，長澤寛規，都留稔了. 分離膜及び分離膜の製造方法.（2024.04.19）

Conferences

[1] **Wei-Wei Yan**, Hiroki Nagasawa, Masakoto Kanezashi, Toshinori Tsuru.* Metal-coordinated aminosilica membranes for NH_3 separation and application to ammonia membrane reactor. *13th International Congress on Membranes and Membrane Processes (ICOM 2023)* **2023.07.07-19** Chiba, Japan (Poster).

[2] **Wei-Wei Yan**, Norihiro Moriyama, Hiroki Nagasawa, Masakoto Kanezashi, Toshinori Tsuru.* Development of functionalized organosilica membranes with high NH_3 permselectivity and their application to green NH_3 production. *14th Congress of Aseanian Membrane Society (AMS 14)*, **2024.07.23-26** Nanjing, China (Oral).

Acknowledgements

Firstly, I would like to express my deepest appreciation to my supervisors, Prof. Toshinori Tsuru (都留 稔了), and my referrer, Prof. Liang Yu (余亮) who has left for Beijing Institute of Technology, for giving me a precious opportunity to study in Hiroshima University. Especially, Prof. Toshinori Tsuru is not only a distinguished expert in membrane science who frequently gives insightful and professional comments but also an honorable elder who gives warm-hearted help and care. Sincerely, congratulations retirement for my advisor! You have enjoyed a long and productive career of which you can justly be proud. Wish you all the best in your retirement!

I am very thankful to Prof. Masakoto Kanezashi (金指 正言), Prof. Hiroki Nagasawa (長澤 寛規), and Dr. Norihiro Moriyama (森山 教洋) for sparing no efforts to provide valuable suggestions and helpful discussion on my research work. I am also grateful to Prof. Masakoto Kanezashi (金指 正言), Prof. Nakai Satoshi (中井 智司), Prof. Miyaoka Hiroki (宮岡 裕樹), and Prof. Ishigami Toru (石神 徹) in my dissertation committee for reading my thesis in their busy schedule.

I also would like to thank all members in Separation Technology Lab. for their kind helps, particularly My friend, Dr. Rana Ikram, my collaborator, Mr. Kotaro Wakimoto, and my tutor, Mr. Masahiro Sonoda.

Sincerely, I would like to thank my family and my sweetheart for their endless support and loving encouragements during the 3-year studying journey in Japan.

Lastly, I highly appreciate the financial support from the China Scholarship Council (CSC No. 202106420012) and JSPS KAKENHI (Grant No. 21H04630).

July 2024

Yan Wei-Wei (闫卫卫，ヤン・ェイェイ)